Exploration of Nucleon Structure in Lattice QCD with Chiral Quarks

by

Sergey Nikolaevich Syritsyn

Submitted to the Department of Physics
in partial fulfillment of the requirements for the degree of

Doctor of Philosophy

at the

MASSACHUSETTS INSTITUTE OF TECHNOLOGY

September 2010

Author .....
.....
Department of Physics
August 2, 2010

Certified by.....
.....
John W. Negele
William A. Coolidge Professor of Physics
Thesis Supervisor

Accepted by..
.....
Krishna Rajagopal
Associate Head for Education

Exploration of Nucleon Structure in Lattice QCD with Chiral Quarks

by

Sergey Nikolaevich Syritsyn

Submitted to the Department of Physics
on August 2, 2010, in partial fulfillment of the
requirements for the degree of
Doctor of Philosophy

Abstract

In this work, we calculate various nucleon structure observables using the fundamental theory of quarks and gluons, QCD, simulated on a lattice. In our simulations, we use the full QCD action including $N_f = 2 + 1$ dynamical quarks in the $SU(2)$ isospin limit. We compute the nucleon vector and axial vector form factors as well as the generalized form factors, and analyze the nucleon charge, magnetization, and axial radii, anomalous magnetic moment, and axial charge. In addition, we compute quark contributions to the nucleon momentum and spin.

Our calculation is novel for three reasons. It is a first full QCD calculation using both sea and valence chiral quarks with pion masses as low as $m_\pi = 300$ MeV. We develop a method to keep systematic effects in the lattice nucleon matrix elements under control, which helps us to obtain a better signal-to-noise ratio, to achieve higher precision and to test the applicability of low-energy effective theories. Finally, we compare the results from lattice QCD calculations with two different discretization methods and lattice spacings, with the rest of the calculation technique kept equal. The level of agreement between these results indicates that our calculations are not significantly affected by discretization effects.

Thesis Supervisor: John W. Negele
Title: William A. Coolidge Professor of Physics

Acknowledgments

This work would not be possible without constant support of many people. I would like to express my gratitude to my Bachelor's and Master's Thesis supervisor, Mikhail Polikarpov, who stirred my initial interest in lattice gauge theories by an opportunity to learn how quantum field theory works in practice and who inspired me with many exciting examples from quantum physics. A great deal of discussions with Andrew Pochinsky on the topics of both physics and computer science were often essential to our progress. During their stay at MIT and after, Harvey Meyer, Massimiliano Procura, and Meifeng Lin helped tremendously in understanding and interpreting our calculation results. Michael Engelhardt performed a substantial part of computer simulations for this project. I am most thankful to my teacher, John Negele, whose amazing potential to motivate and guide were enormous driving force for this work, and who has taught me, among other things, how to do Physics with passion.

And, beyond any extent, I am in debt to my family who supported me wholeheartedly on the difficult path of completing this work.

Contents

List of Figures

List of Tables

Chapter 1

Introduction: Nucleon Structure

Since the early days of hadron physics it has been known that the proton and neutron are not point-like particles, as indicated by the deviation of their magnetic moments from the Dirac equation values [Ste33]. Generally speaking, the non-elementary magnetic moments mean that there are circulating currents inside nucleons. Elastic $e-p$ and $e-n$ scattering experiments showed that their spatial electric charge distribution is also not point-like. Extensive studies of the quark density and helicity inside protons and neutrons at SLAC, Fermilab, CERN and DESY resulted in the understanding that quarks contribute only some part to the boosted nucleon momentum and spin, and also contribute only a negligible part of its mass. The rest must be carried by gluons, which are thus essential and separately relevant degrees of freedom inside a nucleon.

A new generation of dedicated experiments are planned or already underway to further explore the structure of the nucleon, including COMPASS [A+07], HERMES [A+99, KN02], CEBAF at Jefferson Lab, PANDA at FAIR [Gia10], MAMI [Are06], RHIC Spin [Vog04] and others. These experiments aim at higher levels of precision in measuring nucleon form factors, as well as mapping out the three-dimensional structure of the nucleon and resolving the long-standing "spin crisis" puzzle [A+88b], or the origin of the nucleon spin.

There is definitely a need for a theory which could explain such a rich and complicated system as a nucleon. Such a theory should be able to make predictions about

nucleon structure and constrain phenomenological analyses of experimental data. A vital example demonstrating the need for theory constraints is generalized parton distribution functions (GPDs) [Die03], which describe the contents of a boosted nucleon(see also Sec. 1.3). The GPDs F^q can be measured in inelastic scattering experiments through their convolutions with parton scattering kernels $\hat{T}$

$$\text{amplitude} \sim \int d\xi \, \hat{T}(\frac{x}{\xi}) \, F^q(\xi,)$$

and thus are not accessible directly. Dependence of GPDs $F^q(x, \xi, t)$ on its kinematic variables can reveal the full three-dimensional structure of the nucleon. However, to extract physics information from such measurements, one has to assume some functional form for the GPDs (see, e.g., Ref.[DFJK05]) inevitably introducing model dependence into experimental results. Although quite a few phenomenological models explaining certain aspects of nucleon structure have been proposed, none of them is able to solve all of the nucleon puzzles consistently. Apparently, one has to use the fundamental theory of strong interactions, quantum chromodynamics (QCD), to fully understand how nucleons and other hadrons are formed from the elementary particles, quarks and gluons.

Quantum chromodynamics has been successful in explaining high-energy processes where asymptotic freedom permits perturbative treatment of scattering events. However, the low-energy phenomena such as confinement, spontaneous chiral symmetry breaking, the light hadron spectrum and hadron structure definitely require non-perturbative methods. Numerical calculations on a lattice have proven to be the only viable tool so far to extract quantitative predictions from non-perturbative QCD. Although currently there are certain limitations in this approach, such as finite volume, finite ultraviolet cutoff and difficulties in making the pion of simulated QCD as light as the real-world pion, all these obstacles can, at least in principle, be overcome using more powerful computers. For example, recently the Budapest-Marseille-Wuppertal lattice QCD collaboration reported the first successful calculation of hadron spectrum using full QCD with three dynamical flavors [D$^+$08]. It would be fair to say that the

current predictive power of lattice QCD is limited by available computing resources, and eventually, as they advance, more accurate calculations with smaller systematic errors will be possible.

Lattice QCD is a solution of quantum field theory in Euclidean space on a discrete lattice. The transition to Euclidean space is required to make all particles "virtual" in the sense that their correlators decay exponentially along any direction. Because there are no massless particles in the spectrum of QCD, this system may be simulated in a finite box with the size limited from below by the inverse mass of the lightest particle, the pion. To study hadron structure on a lattice, one computes matrix elements of local operators between single-hadron states. For example, charge and magnetization distributions in the nucleon are extracted from the vector current; quark and gluon contributions to the nucleon momentum and angular momentum are extracted from the energy-momentum tensor. Computations with local twist-two operators that are related to the Mellin moments of the parton distribution functions (PDFs) provide theoretic constraints which complement experimental measurements. In principle, using lattice QCD methods one can "measure" any local operators that are inaccessible experimentally and fill in the gaps in our picture of nucleon properties.

Although applying brute-force calculations to lattice QCD may help to improve its results, in practice only a combination of advanced error-reduction methods and increased computer time might lead to good quantitative predictions. The main reason for this is that lattice QCD is a Monte-Carlo simulation, and the associated stochastic variation decreases only as $\sigma \sim \frac{1}{\sqrt{N}}$, where N is the number of stochastic samples. At the same time, the computational cost of each sample increases drastically with the linear size of the box and with decreasing quark masses. In addition, the size of Monte-Carlo ensembles necessary to suppress noise may vary depending on the quantity being computed. For example, in the baryon spectrum calculations many cancellations occur that aggravate their stochastic variation. This effect is even worse in the calculations of hadron structure because one has to compute three-point correlators as opposed to two-point correlators for the hadron spectrum. The development of methods to extract the answer with small stochastic uncertainty, and to

set a bound on lattice QCD-specific systematic bias constitutes a major part of this work.

In this work we study nucleon structure observables using the most advanced and systematic bias-free lattice QCD framework, calculations which only recently became feasible. To produce reliable results from lattice QCD, one has to solve a number of problems. First, as will be discussed in Chapter 2, the simulation of fermions on a lattice is difficult because simple discretizations of the fermion action break chiral symmetry. Chiral symmetry is essential if one wants to preserve the original symmetries of the theory and connect the results of simulations to low-energy effective theories such as chiral perturbation theory (ChPT). Also, it reduces dramatically the lattice-specific systematic effects, or lattice artifacts, such as unphysical mixing between operators relevant to the hadron structure. A number of approaches have been devised to avoid chiral symmetry breaking on a lattice. However, all of them increase the cost of simulations significantly. The second problem is that light quarks and, correspondingly, light pions are expensive to simulate. In addition to purely numerical handicaps, one needs larger spatial volume to preserve long-range meson dynamics. Moreover, the Monte-Carlo update is more difficult because lighter fermions produce more rigid "feedback" on the color gauge field and finer and more accurate calculations are required. Finally, as mentioned above, the stochastic variation of lattice QCD calculations grows as the pion mass decreases. All these difficulties limit the current simulations with chiral quarks[1] to pion masses $m_\pi \gtrsim 300$ MeV and finite volume $\lesssim (3.5 \text{ fm})^2$.

Because of the high cost of realistic lattice QCD simulations, we focus on reducing the uncertainty as much as possible and extracting precise results for nucleon structure by fully utilizing the statistics available from the existing lattice QCD ensembles [A$^+$08a, B$^+$09, B$^+$01]. For example, we have been able to compute the nucleon electromagnetic structure with a remarkable precision for pion masses down

[1] Lattice QCD is a rapidly changing field, which progresses *at least* as fast as computing resources. The cited limitations applied in 2007 to the generation of the gauge configurations used in this work. Lattice QCD results for nucleon structure presented here are up-to-date since they require significant additional calculations.

to 300 MeV [S$^+$10]. Currently, lattice QCD simulations are performed in the isospin limit $m_u = m_d \equiv \hat{m} \ll m_s$, and the electromagnetic interactions of quarks are neglected. We used these results to check existing predictions from Chiral Perturbation Theory with the conclusion that ChPT (at least, to the approximation order used) is not applicable in this range of the pion masses. In addition, it is very reassuring that we are able to reach the precision of existing experiments, albeit with the up and down quark masses still being too heavy for a direct comparison. Furthermore, by comparing the results from several different lattice QCD methodologies, we check whether QCD discretization has any effect on the lattice QCD predictions. Fair agreement between mixed quark action [B$^+$10] and unitary chiral quark action [LHP, S$^+$10] shows that lattice QCD gives consistent results.

The rest of this chapter is devoted to the discussion of some of the nucleon structure observables which we compute from lattice QCD and compare to experiments and other theoretical models. In Chapter 2 we briefly describe and compare the ways to implement QCD on a lattice, and discuss their respective advantages and potential problems. Chapter 3 is an overview of the methods to create nucleon states on a lattice and control related systematic effects. Good control over systematic effects allows one to reduce stochastic errors without inducing systematic bias. Since the operators computed on a lattice require renormalization, we performed such renormalization nonperturbatively and describe the methods we used in Chapter 4. Chapter 5 summarizes the most physically interesting results:

- Nucleon vector form factors for the space-like momentum transfer $0 \leq Q^2 \leq 1$ GeV^2, nucleon charge and magnetization mean squared radii, anomalous magnetic moments.

- Nucleon axial form factors, nucleon axial charge and axial r.m.s. radii.

- Quark contributions to the nucleon momentum, as well as quark spin and orbital angular momentum contributions to the spin of the nucleon.

- Nucleon generalized form factors (GFFs) for u and d quarks corresponding to

$n = 1$, 2 and 3 moments of generalized parton distributions, revealing the dependence of the latter on their kinematic parameters.

Wherever possible, we apply chiral extrapolation formulas to obtain the values at the physical pion mass $m_\pi \approx 140$ MeV which is a factor 2 less than the lightest mass in our simulations.

1.1 Electromagnetic structure

Electromagnetic form factors characterize fundamental aspects of the structure of protons and neutrons. In particular, they specify the spatial distribution of charge and magnetization. For nonrelativistic systems the electric and magnetic Sachs form factors $G_E(Q^2)$ and $G_M(Q^2)$ (see Eqs. (1.2,1.3)) would just be Fourier transforms of the charge and current densities. A probabilistic interpretation of the Dirac and Pauli form factors $F_1(Q^2)$ and $F_2(Q^2)$ (See Eq. (1.1)) can be obtained from a two-dimensional Fourier transformation to impact parameter space in the infinite momentum frame [Bur00, Bur03]. At high momentum transfer, the elastic form factor specifies the amplitude for a single quark in the nucleon to absorb a very large momentum kick and share it with the other constituents in such a way that the nucleon remains in its ground state instead of being excited. It thus describes the onset of scaling [BF75, BJY03] and the scale at which quark counting rules become applicable, which is an unresolved theoretical question in nonperturbative QCD. Given the constantly improving experimental measurements of form factors and their fundamental significance, it is an important challenge for lattice QCD to calculate them accurately from first principles.

The nucleon Dirac and Pauli form factors, $F_1(Q^2)$ and $F_2(Q^2)$, respectively, are defined as follows for each quark flavor (q):

$$\langle P', S'|\bar{q}\gamma^\mu q|P, S\rangle = \bar{U}(P', S')\Big[\gamma^\mu F_1^q(Q^2) + i\sigma^{\mu\nu}\frac{q_\nu}{2M_N}F_2^q(Q^2)\Big]U(P, S)\,, \qquad (1.1)$$

where $U(P, S)$, $\bar{U}(P', S')$ are the initial and final nucleon spinors; S, S' are the corre-

sponding spin vectors; the momentum transfer is $q = P' - P$ with $Q^2 = -q^2 \geq 0$; and M_N is the nucleon mass. The Sachs form factors $G_E(Q^2)$ and $G_M(Q^2)$ are defined by

$$G_E(Q^2) = F_1(Q^2) - \frac{Q^2}{(2M_N)^2} F_2(Q^2), \tag{1.2}$$

$$G_M(Q^2) = F_1(Q^2) + F_2(Q^2)\,. \tag{1.3}$$

Finally, it is useful to define isoscalar and isovector form factors as the sum and difference of proton and neutron form factors as follows:

$$F^v_{1,2}(Q^2) = F^p_{1,2}(Q^2) - F^n_{1,2}(Q^2) = F^u_{1,2}(Q^2) - F^d_{1,2}(Q^2) \equiv F^{u-d}_{1,2}(Q^2), \tag{1.4}$$

$$F^s_{1,2}(Q^2) = F^p_{1,2}(Q^2) + F^n_{1,2}(Q^2) = \frac{1}{3}\left(F^u_{1,2}(Q^2) + F^d_{1,2}(Q^2)\right) \equiv \frac{1}{3}F^{u+d}_{1,2}(Q^2), \tag{1.5}$$

where, according to Eq. (1.1), $F^{p,n}_{1,2}$ are the form factors of the electromagnetic current in a proton and a neutron, respectively:

$$V^\mu_{\mathrm{em},p} = \frac{2}{3}\bar{u}\gamma^\mu u - \frac{1}{3}\bar{d}\gamma^\mu d\,, \qquad V^\mu_{\mathrm{em},n} = -\frac{1}{3}\bar{u}\gamma^\mu u + \frac{2}{3}\bar{d}\gamma^\mu d\,. \tag{1.6}$$

Although proton and neutron form factors contain both connected diagrams, calculated in this work, and disconnected diagrams, which are currently omitted, the disconnected diagrams do not contribute to the isovector form factors F^v_i. Hence, we will devote particular attention in this work to the isovector form factors.

Precise experimental measurements of the set of all four nucleon form factors remains challenging, and the field is marked both by significant recent developments and open questions. Although the most straightforward measurement is $F_1(Q^2)$ for the proton, the slope at very small values of Q^2 remains controversial. Phenomenological fits to experimental form factors [FW03, AMT07] appear to be inconsistent with analyses based on dispersion theory [H$^+$76, MMD96, BHM07], with phenomenological fits yielding larger Dirac radii. Hence, a new generation of precision measurements of form factors at low momentum transfer is currently being undertaken at Mainz [Ber08]. In addition, a recent measurement of the proton charge radius using the Lamb shift in the μp system [P$^+$10] disagrees with the earlier results, which may be an indica-

tion that not all the theoretical corrections in these experiments have been assessed and confirmed. Spin polarization experiments [M$^+$98, P$^+$01, G$^+$02, G$^+$01, P$^+$05] yielded results for $F_2(Q^2)$ significantly different from traditional measurements based on Rosenbluth separation, and there is a consensus that two-photon exchange processes contribute much more strongly to the backward cross section used in Rosenbluth separation than to polarization transfer [AMT07]. However, there are not yet precise theoretical calculations of two-photon exchange that fully resolve the discrepancy between the two experimental methods, and hence experiments using positron scattering, for which the relative contribution of the two-photon term changes sign, are being prepared [A$^+$04a, OLY09]. Neutron form factors are more uncertain than proton form factors because of the need to know the nuclear wave function to go from experimental scattering results from deuterium or ^{3}He to a statement about the neutron form factor. Over the years, nuclear models and theoretical calculations have been refined, but it is still a challenge to provide a definitive estimate of the uncertainty in the claimed neutron form factors extracted from nuclear targets. Given the level of precision to which we aspire in lattice calculations, systematic uncertainties in isovector and isoscalar form factors are not necessarily negligible. In the future when lattice calculations reliably include precise calculations of disconnected contributions, it may well be that lattice calculations play a role in guiding the resolution of some of these experimental questions.

In Section 5.1 we present our results for the momentum dependence of the nucleon vector form factors $F_1(Q^2)$ and $F_2(Q^2)$, their r.m.s. radii

$$\langle r^2_{1,2} \rangle = -\frac{6}{F_{1,2}} \frac{dF_{1,2}}{dQ^2}$$

and the nucleon anomalous magnetic moment $\kappa = F_2(0)$. We apply chiral perturbation theory to extrapolate the Dirac and Pauli r.m.s. radii to the physical point. However, such extrapolation is difficult because these quantities diverge in the chiral limit.

1.2 Axial form factors

Electroweak probes such as (anti)neutrinos interacting with quarks via chiral currents give access to the nucleon axial structure [BEM02]. The nucleon axial structure is characterized by the nucleon axial form factors,

$$\langle N(P',S')|A^{a\mu}|P,S\rangle = \bar{U}(P',S')\Big[\gamma^\mu G_A(Q^2) + \frac{(P'-P)^\mu}{2M_N}G_P(Q^2)\Big]\gamma^5\tau^a U(P,S), \tag{1.7}$$

where $A^{a\mu} = \bar{q}\gamma^\mu\gamma^5\tau^a q$ is the non-singlet axial current. $G_A(Q^2)$ is called the nucleon axial form factor and $G_P(Q^2)$ the induced pseudoscalar form factor at the momentum transfer $Q^2 = -(P'-P)^2$. On a lattice we work in the isospin-symmetric limit with $M_n = M_p \equiv M_N$, and study the proton matrix elements of the isovector current $A^{3\mu} = \bar{u}\gamma^\mu\gamma^5 u - \bar{d}\gamma^\mu\gamma^5 d$ which measures the correlation between the spin and isospin distributions inside a nucleon.

In experimental measurements, the form factor $G_A(Q^2)$ in the range $Q^2 \lesssim 1$ GeV^2 is usually parameterized phenomenologically with a dipole formula,

$$G_A(Q^2) \approx \frac{g_A}{(1+Q^2/M_A^2)^2}, \tag{1.8}$$

where the dipole parameter M_A is called the axial mass. In the forward limit $Q^2 = 0$ the axial form factor gives the nucleon axial charge $g_A = 1.1267(3)$ [A$^+$08b] which is known precisely from measurements of neutron β-decay lifetime.

There are two methods to measure the nucleon axial form factor $G_A(Q^2)$ for $Q^2 \neq 0$. One method is based on (anti)neutrino scattering off protons [A$^+$88a], deuterons [K$^+$90] or nuclei [KLN$^+$69]. In the other method, $G_A(Q^2)$ is determined from charged pion electroproduction off protons (e.g., Ref. [B$^+$73]). The resulting world averages for the axial masses are

$$M_A = 1.026(21)\text{ GeV} \qquad \text{neutrino scattering},$$
$$M_A = 1.069(16)\text{ GeV} \qquad \text{pion electroproduction},$$

which disagree by $\approx 4\%$, which is approximately 1.6σ deviation with their errors. The axial mass is connected to the mean-squared axial radius, defined through the low-energy behavior of the axial form factor, assuming the dipole form (1.8) holds for $Q^2 \to 0$

$$G_A(Q^2) = g_A(1 - \frac{1}{6}\langle r_A^2\rangle Q^2 + \mathcal{O}(Q^4)), \quad \langle r_A^2\rangle = -\frac{6}{G_A(0)}\frac{dG_A(Q^2)}{dQ^2}\Big|_{Q^2=0} \tag{1.9}$$

From the two experimental values above, one can extract the axial radius,

$$\sqrt{\langle r_A^2\rangle} = 0.666(14) \text{ fm} \qquad \text{neutrino scattering,}$$
$$\sqrt{\langle r_A^2\rangle} = 0.639(10) \text{ fm} \qquad \text{pion electroproduction}$$

The induced pseudoscalar form factor $G_P(Q^2)$ is expected to receive its dominant contribution from a pion pole, which reflects the pion-mediated coupling of nucleons to the axial current:

$$G_P(Q^2) = \frac{4M_N F_\pi g_{\pi N}}{m_\pi^2 + Q^2} + \mathcal{O}(Q^0). \tag{1.10}$$

where $g_{\pi N} = g_{\pi N}(Q^2 = -m_\pi^2)$ is the pion-nucleon coupling constant in $N \to \pi N$ processes and $F_\pi \approx 93$ MeV is the pion decay constant. Because of the chiral Ward identity the induced pseudoscalar form factor is not independent of the axial form factor [BKM94]. This fact is reflected in the Goldberger-Treiman relation

$$g_A = \frac{g_{\pi N} F_\pi}{M_N}, \tag{1.11}$$

which must hold precisely in the chiral limit and approximately for $m_\pi \neq 0$ up to $\mathcal{O}(m_\pi^2)$ corrections from ChPT. Additionally, from ChPT one can find $\mathcal{O}(Q^0)$ correction to Eq. (1.10) [BKM94, BEM02]:

$$G_P(Q^2) = \frac{4M_N F_\pi g_{\pi N}}{m_\pi^2 + Q^2} - \frac{2}{3} g_A m_N^2 \langle r_A^2\rangle + \mathcal{O}(Q^2, m_\pi^2), \tag{1.12}$$

and this formula is believed to describe G_P well for small momentum transfer Q^2.

The induced pseudoscalar form factor can be determined experimentally from

ordinary muon capture (OMC) $\mu + p \to \nu_\mu + n$ in a μp "atom" at the low fixed momentum transfer $Q^2_{\text{OMC}} = 0.88 m_\mu^2$. However, because of systematic difficulties the uncertainty is quite large, constituting $\approx 30\%$ [BEM02]. In *radiative muon capture* (RMC) experiments, where an additional photon is emitted, it is possible to study timelike momentum transfer values up to $Q^2 = -m_\mu^2$, which are very close to the pion pole. However, such events are strongly suppressed by the branching ratio. Analyses based on the hypothesis of pion pole dominance give values for $G_P(Q^2 = Q^2_{\text{OMC}})$ [J$^+$96, W$^+$98, BF89] that are about 50% larger than expected from theory and determined from OMC.

Another way to determine the form factor $G_P(Q^2)$ is pion electroproduction. The results [C$^+$93] for the Q^2-dependence of G_P agree with pion-pole dominance, but the precision is not sufficient to separate the pion pole contribution from chiral perturbation theory corrections in the spirit of Eq. (1.12). Currently, the induced pseudoscalar form factor remains the least known of all electroweak nucleon form factors [BEM02], which makes its theoretical investigation very important.

We investigate the nucleon axial and induced pseudoscalar form factor on a lattice and present our results in Sec. 5.3. We compute the nucleon axial charge g_A and axial radius $\langle r_A^2 \rangle$. We also compute the momentum dependence of G_A and G_P form factors and compare them to the phenomenological expectations and experimental results discussed above. In addition, we attempt to check the pion-pole dominance hypothesis and the Goldberger-Treiman relations [GT58a, GT58b].

1.3 Generalized form factors

Generalized parton distributions (GPDs) unify and extend the notions of nucleon parton distributions and nucleon elastic form factors, the principal quantities that provide information on nucleon structure [Die03]. Compared to the ordinary parton distribution functions (PDFs), which simply count the partons with a given longitudinal momentum and polarization, GPDs parameterize scattering amplitudes in which a parton acquires some momentum from external particle(s), both in longitudinal and

transverse directions. At the same time, compared to the elastic form factors, the GPDs reveal how the nucleon charge and magnetization are distributed over partons with different longitudinal momentum fraction. As mentioned before, GPDs depend on the three kinematic parameters, x, ξ, and t, and experimental study of GPDs can potentially provide a three-dimensional image of hadron structure [Bur00]. Also, knowledge of parton distribution in the transverse plane gives access to the orbital angular momentum (OAM) of partons.

An attractive feature of the generalized parton distributions is that they occur in a range of different processes, e.g. deeply virtual Compton scattering [A$^+$01, S$^+$01, C$^+$03, A$^+$05], wide-angle Compton scattering and exclusive meson production, in addition to the classic processes that probe the forward parton distributions and form factors. The challenge of GPDs lies in their more complex structure— each generalized parton distribution is a function of three parameters rather than just one, and different experimental processes provide different constraints on their form. Typically only convolutions of these functions in the x variable are experimentally accessible.

In this work we concentrate on the valence quark GPDs of a nucleon. The GPDs are defined through matrix elements of bi-local light cone quark operators,

$$\mathcal{O}_q(x) = \int \frac{d\lambda}{2\pi} e^{2i\lambda x}\, \bar{q}(-\lambda n)\, \not{n}\, \mathcal{W}(-\lambda n, \lambda n)\, q(\lambda n), \tag{1.13}$$

$$\mathcal{O}_q^{\gamma^5}(x) = \int \frac{d\lambda}{2\pi} e^{2i\lambda x}\, \bar{q}(-\lambda n)\, \not{n}\gamma^5\, \mathcal{W}(-\lambda n, \lambda n)\, q(\lambda n), \tag{1.14}$$

where n is a light-cone vector, $n^2 = 0$, and $\mathcal{W}$ is the light-cone Wilson line connecting points $\pm\lambda n$:

$$\mathcal{W}(-\lambda n, \lambda n) = \mathcal{P}\mathrm{exp}\Big[-ig \int_{-\lambda}^{+\lambda} d\alpha\, n \cdot A(\alpha n)\Big]$$

The matrix elements of the operators (1.13,1.14) between single-nucleon states are

parameterized according to their Lorentz tensor structure [Die03]:

$$\langle P', S'|\mathcal{O}_q|P, S\rangle = \bar{U}(P', S')\Big[\not{n} H^q(x,\xi,t) + \frac{i\sigma^{\mu\alpha} n_\mu q_\alpha}{2M_N} E^q(x,\xi,t)\Big] U(P,S), \quad (1.15)$$

$$\langle P', S'|\mathcal{O}_q^{\gamma^5}|P, S\rangle = \bar{U}(P', S')\Big[\not{n}\gamma^5 \tilde{H}^q(x,\xi,t) + \frac{n\cdot q}{2M_N}\gamma^5 \tilde{E}^q(x,\xi,t)\Big] U(P,S), \quad (1.16)$$

where the frame-independent Lorentz scalars H^q, E^q are the unpolarized and $\tilde{H}^q$, $\tilde{E}^q$ are the corresponding polarized generalized parton distributions. In this work we do not analyze the so-called transversity distributions H_T^q,E_T^q, which are discussed in a different publication [Bra09]. The parameters in Eqs. (1.15,1.16) are the average longitudinal momentum fraction of the struck parton x, the longitudinal momentum transfer fraction $\xi = -n\cdot q/2 = (P-P')\cdot n/(P'+P)\cdot n$ and the total momentum transfer squared $t = -Q^2 = q^2$, where $q = P' - P$.

Since lattice calculations deal with operators and matrix elements in Euclidean space, a direct computation of non-local light-cone operators is not possible. Instead, to facilitate the lattice calculations one takes x^{n-1}-moments of Eqs. (1.15) and (1.16), yielding a tower of local operators whose matrix elements can be related to the corresponding moments of H, E, $\tilde{H}$ and $\tilde{E}$. In this study, we will compute matrix elements of the following local generalized currents,

$$\left(\mathcal{O}_q^{[\gamma^5]}\right)^{\{\mu_1\ldots\mu_n\}} = \bar{q}\gamma^{\{\mu_1}[\gamma^5] i\overleftrightarrow{D}^{\mu_2}\cdots i\overleftrightarrow{D}^{\mu_n\}} q\,, \quad (1.17)$$

Curly braces around indices represent the symmetrization of the Lorentz indices $\mu_1\cdots\mu_n$ and the subtraction of traces over pairs of these indices. The symmetric derivative is defined as $\overleftrightarrow{D} = \frac{1}{2}(\overrightarrow{D} - \overleftarrow{D})$.

Taking the x^{n-1}-moments of the GPDs we define the *generalized moments*

$$\begin{aligned} H^n(\xi,t) &\equiv \int_{-1}^{1} dx\, x^{n-1} H(x,\xi,t)\,, & \tilde{H}^n(\xi,t) &\equiv \int_{-1}^{1} dx\, x^{n-1}\tilde{H}(x,\xi,t)\,, \\ E^n(\xi,t) &\equiv \int_{-1}^{1} dx\, x^{n-1} E(x,\xi,t)\,, & \tilde{E}^n(\xi,t) &\equiv \int_{-1}^{1} dx\, x^{n-1}\tilde{E}(x,\xi,t)\,. \end{aligned} \quad (1.18)$$

The non-forward nucleon matrix elements of the local operators, Eq. (1.17), can in

turn be parametrized according to their Lorentz structure in terms of generalized form factors (GFFs) $A_{nm}(t)$, $\tilde{A}_{nm}(t)$, $B_{nm}(t)$, $\tilde{B}_{nm}(t)$, and $C_{nm}(t)$, for $n = 1, 2, 3$

$$\begin{aligned}
\langle P', S'|\mathcal{O}^{\mu_1}|P, S\rangle &= \bar{U}(P', S')\Big[\gamma^{\mu_1} A_{10}(t) + \frac{i\sigma^{\mu_1\alpha} q_\alpha}{2m} B_{10}(t)\Big] U(P, S)\,, \\
\langle P', S'|\mathcal{O}^{\{\mu_1\mu_2\}}|P, S\rangle &= \bar{U}(P', S')\Big[\bar{P}^{\{\mu_1}\gamma^{\mu_2\}} A_{20}(t) + \bar{P}^{\{\mu_1}\frac{i\sigma^{\mu_2\}\alpha} q_\alpha}{2m} B_{20}(t) \\
&\qquad + \frac{q^{\{\mu_1} q^{\mu_2\}}}{m} C_{20}(t)\Big] U(P, S)\,, \\
\langle P', S'|\mathcal{O}^{\{\mu_1\mu_2\mu_3\}}|P, S\rangle &= \bar{U}(P', S')\Big[\bar{P}^{\{\mu_1}\bar{P}^{\mu_2}\gamma^{\mu_3\}} A_{30}(t) + \bar{P}^{\{\mu_1}\bar{P}^{\mu_2}\frac{i\sigma^{\mu_3\}\alpha} q_\alpha}{2m} B_{30}(t) \\
&\qquad + q^{\{\mu_1} q^{\mu_2}\gamma^{\mu_3\}} A_{32}(t) + q^{\{\mu_1} q^{\mu_2}\frac{i\sigma^{\mu_3\}\alpha} q_\alpha}{2m} B_{32}(t)\Big] U(P, S)\,,
\end{aligned} \tag{1.19}$$

for the vector operators and

$$\begin{aligned}
\langle P', S'|\big(\mathcal{O}^{\gamma^5}\big)^{\mu_1}|P, S\rangle &= \bar{U}(P', S')\Big[\gamma^{\mu_1}\gamma^5 \tilde{A}_{10}(t) + \frac{q^{\mu_1}}{2m}\gamma^5 \tilde{B}_{10}(t)\Big] U(P, S)\,, \\
\langle P', S'|\big(\mathcal{O}^{\gamma^5}\big)^{\{\mu_1\mu_2\}}|P, S\rangle &= \bar{U}(P', S')\Big[\bar{P}^{\{\mu_1}\gamma^{\mu_2\}}\gamma^5 \tilde{A}_{20}(t) + \frac{q^{\{\mu_1}\bar{P}^{\mu_2\}}}{2m}\gamma^5 \tilde{B}_{20}(t)\Big] U(P, S)\,, \\
\langle P', S'|\big(\mathcal{O}^{\gamma^5}\big)^{\{\mu_1\mu_2\mu_3\}}|P, S\rangle &= \bar{U}(P', S')\Big[\bar{P}^{\{\mu_1}\bar{P}^{\mu_2}\gamma^{\mu_3\}}\gamma^5 \tilde{A}_{30}(t) + \frac{q^{\{\mu_1}\bar{P}^{\mu_2}\bar{P}^{\mu_3\}}}{2m}\gamma^5 \tilde{B}_{30}(t) \\
&\qquad + q^{\{\mu_1} q^{\mu_2}\gamma^{\mu_3\}}\gamma^5 \tilde{A}_{32}(t) + \frac{q^{\{\mu_1} q^{\mu_2} q^{\mu_3\}}}{2m}\gamma^5 \tilde{B}_{32}(t)\,,\Big] U(P, S)
\end{aligned} \tag{1.20}$$

for the axial vector operators. Here we have defined the average nucleon 4-momentum $\bar{P} = (P'+P)/2$. By comparing these expressions with the x^{n-1}-moments of Eqs. (1.15,1.16) and using Eq. (1.18), one finds that the ξ-dependence of the moments of the GPDs is merely polynomial[Die03],

$$\begin{aligned}
H^{n=1}(\xi, t) &= A_{10}(t)\,, & E^{n=1}(\xi, t) &= B_{10}(t)\,, \\
H^{n=2}(\xi, t) &= A_{20}(t) + (2\xi)^2 C_{20}(t)\,, & E^{n=2}(\xi, t) &= B_{20}(t) - (2\xi)^2 C_{20}(t)\,, \\
H^{n=3}(\xi, t) &= A_{30}(t) + (2\xi)^2 A_{32}(t)\,, & E^{n=3}(\xi, t) &= B_{30}(t) + (2\xi)^2 B_{32}(t)\,, \\
&\ldots
\end{aligned} \tag{1.21}$$

and

$$\begin{aligned}
\tilde{H}^{n=1}(\xi,t) &= \tilde{A}_{10}(t)\,, & \tilde{E}^{n=1}(\xi,t) &= \tilde{B}_{10}(t)\,,\\
\tilde{H}^{n=2}(\xi,t) &= \tilde{A}_{20}(t)\,, & \tilde{E}^{n=2}(\xi,t) &= \tilde{B}_{20}(t)\,,\\
\tilde{H}^{n=3}(\xi,t) &= \tilde{A}_{30}(t) + (2\xi)^2\tilde{A}_{32}(t)\,, & \tilde{E}^{n=3}(\xi,t) &= \tilde{B}_{30}(t) + (2\xi)^2\tilde{B}_{32}(t)\,,\\
&\ldots\,.
\end{aligned} \tag{1.22}$$

In the forward limit of Eqs. (1.15,1.15) with $\vec{P} = \vec{P}'$, we obtain the well-known parton distribution functions,

$$q(x) = H^q(x,\xi=0,t=0)\,, \qquad \Delta q(x) = \tilde{H}^q(x,\xi=0,t=0)\,. \tag{1.23}$$

It is interesting that in the case $\xi = 0$ and arbitrary $t = q^2$, that is when the momentum transfer is limited to the transverse direction, the GPDs and the corresponding GFFs can be interpreted as distributions in both longitudinal momentum *and* transverse position in the infinite longitudinal momentum frame [Bur00].

Taking together Eqs. (1.18,1.21,1.22) and Eq. 1.23 and setting $t = 0$ will similarly yield the PDF moments

$$\langle x^{n-1}\rangle_q = H^n(0,0) = A_{n0}(0)\,, \qquad \langle x^{n-1}\rangle_{\Delta q} = \tilde{H}^n(0,0) = \tilde{A}_{n0}(0)\,. \tag{1.24}$$

Note also that for $n = 1$ from Eqs. (1.19,1.20) we recover the nucleon vector and axial form factors introduced in Sec. 1.1 and 1.2,

$$\begin{aligned}
F_1^q(Q^2) &\equiv A_{10}^q(Q^2)\,, & G_A(Q^2) &\equiv \tilde{A}_{10}^{u-d}(Q^2)\,,\\
F_2^q(Q^2) &\equiv B_{10}^q(Q^2)\,, & G_P^q(Q^2) &\equiv A_{10}^{u-d}(Q^2).
\end{aligned}$$

On a lattice, we compute the set of polarized and unpolarized generalized form factors for $n = 1, 2, 3$[2] and present our results in Sec. 5.5. In particular, the results for

[2] Computing the generalized form factors with $n > 3$ currently presents a difficulty because of stochastic noise. The GFFs with $n > 4$ on a lattice will mix with lower-dimensional operators because of broken rotational symmetry, see Sec. 2.4.

these form factors allow us to make predictions on the transverse size of the nucleon, the dependence of GPDs on the "skewness" parameter ξ and on the validity of some phenomenological Ansätze for the functional form of GPDs. More importantly, the access to the energy-momentum tensor through $n = 2$ moments of GPDs allows us to compute quark contributions to the nucleon spin and momentum, and we present our findings in Sec. 5.4.

Chapter 2

QCD on a lattice: Overview

In this chapter we describe the methodology of simulating QCD on a lattice. Since there are many reviews of lattice QCD basics in the literature, e.g., [MM, Rot05], we only briefly discuss its formulation and simulation in Sec. 2.1. While lattice QCD reproduces well many non-perturbative phenomena, such as confinement, chiral symmetry breaking, and the hadron spectrum both qualitatively and quantitatively, using it for precise calculation of hadron structure still remains a challenge. In particular, one has been limited to pion masses significantly heavier than the physical value, and only recently the simulations close to or at physical pion mass have begun [D$^+$08]. In addition, the nucleon structure calculations may be affected by systematic effects arising from a particular way to implement the theory on a lattice, of which the most important one is the explicit chiral symmetry violation of lattice fermion actions. Both these problems arise from the fundamental difficulty in regulating any chiral fermion theory on a lattice [NN81]. We discuss different fermion action choices in Sec. 2.3.

Another problem in lattice calculations is that the lattice breaks rotational symmetry. The consequences of such symmetry breaking for nucleon structure calculations are discussed in Sec. 2.4.

2.1 Lattice gauge theory

Lattice gauge theories are formulated on a discrete Euclidean space-time grid. The purpose of introducing a grid is twofold. First, a lattice serves as an ultraviolet regulator with a cutoff $\Lambda_{\text{lat}} = a^{-1}$ where a is the lattice spacing. For free fields, the highest energy mode has momentum $p_{\text{max}} \sim \pi/a$. Such modes behave as $\phi \sim (-1)^x$, where x is a coordinate, and may potentially introduce lattice-specific artifacts because they are not smooth. Therefore, the energies of states studied on a lattice should be limited to $E \ll \pi/a$. Second, lattice quantum field theories formulated on a discrete Euclidean lattice can be simulated on a computer analogously to Statistical Mechanics systems.

The calculations consist in computing the Feynman path integral numerically,

$$Z = \int \mathcal{D}A_\mu \mathcal{D}\psi \mathcal{D}\bar{\psi} e^{-\int d^4x (\frac{1}{4g^2}(F_{\mu\nu})^2 + \sum_f \bar{\psi}_f (D(m_f)\psi_f)} \tag{2.1}$$

where $D(m_q)$ are fermion operators for each quark flavor. Then, computing v.e.v.'s of various field operators and their correlators,

$$\langle \mathcal{O}(x_1) \cdots \mathcal{O}(x_n) \rangle = \frac{1}{Z} \int \mathcal{D}A_\mu \mathcal{D}\psi \mathcal{D}\bar{\psi}\, \mathcal{O}(x_1) \cdots \mathcal{O}(x_n)\, e^{-\int d^4x (\frac{1}{4g^2}(F_{\mu\nu})^2 + \sum_f \bar{\psi}_f (D(m_f)\psi_f)} \tag{2.2}$$

one can study the spectrum of states and their matrix elements for various operators, e.g. vector charge density and energy-momentum tensor.

It is important to note that the parameters one can control while solving gauge theory in this way are the same parameters that are present in the original theory, and no model approximations are made. For QCD, they play the role of the bare coupling α_S and quark masses m_f in the lattice regularization. Doing a series of calculations at various parameter values, one can *tune* the parameters so that some selected set of computed physical observables *match* their experimental values.

2.1.1 Formulation of QCD on a lattice

In his pioneering work, Wilson [Wil74] showed how to quantize gauge field theory on a discrete lattice in Euclidean space-time preserving exact gauge symmetry.

The first step is to convert QCD to Euclidean space-time using the Wick rotation

$$\begin{cases} x^0 \equiv t & \rightarrow -ix_4 \equiv -i\tau \\ p^0 \equiv E & \rightarrow ip_4 \\ \langle N(t)\bar{N}(0)\rangle & \rightarrow e^{-E\tau} \end{cases} . \tag{2.3}$$

Note that all the correlators decay exponentially and the problem may be solved in a finite box of size $L \gtrsim \text{const} \cdot \frac{1}{m_0}$ where m_0 is the lightest excitation above the vacuum state.

Scalar and fermion fields are naturally represented by variables ϕ_x or ψ_x specified at each site. To transcribe the gauge field potential[1] $A^a_\mu(x)$ to lattice variables we note that a scalar field $\phi(x)$ in a non-trivial representation of the gauge group picks up a "color phase"

$$\phi(x) = \mathcal{P}e^{-i\int_x^y dx\cdot(A^a\lambda^a)}\phi(y) = \mathcal{W}(x,y)\phi(y) \tag{2.4}$$

when moved along a contour $\mathcal{C}(x,y)$, see Fig. 2-1(a). Therefore, it is natural to specify a gauge potential variable on each link of a lattice and treat it as an elementary gauge transporter between the two lattice sites it connects:

$$U_{x,\mu} = \mathcal{W}(x, x+\hat{\mu}) = \mathcal{P}e^{-i\int_x^{x+\hat{\mu}} dx\cdot(A^a\lambda^a)} . \tag{2.5}$$

[1] Note that we include a factor g into the definition of the gauge potential $A^a_\mu(x)$, so that $F_{\mu\nu} = \partial_\mu A_\nu - \partial_\nu A_\mu + i[A_\mu, A_\nu]$ with $F_{\mu\nu} = F^a_{\mu\nu}\lambda^a$ and $A_\mu = A^a_\mu\lambda^a$.

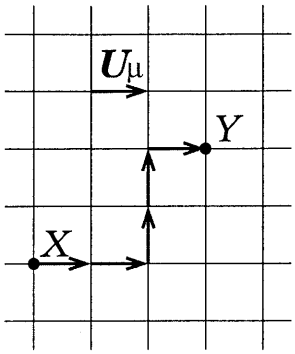

(a) Lattice Wilson lines

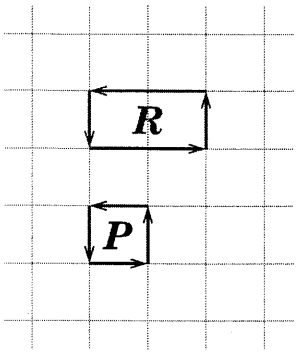

(b) [P]laquettes and [R]ectangles

Figure 2-1: Gauge links, Wilson lines and loops.

This transcription is automatically gauge invariant,

$$\begin{aligned} \phi'_y &= \Omega_y \phi_y, \\ \mathcal{W}'(x,y) &= \Omega_x \mathcal{W}(x,y) \Omega_y^\dagger, \\ \phi'_x &= \Omega_x \mathcal{W}(x,y) \Omega_y^\dagger \cdot \Omega_y \phi_y = \Omega_x \phi_x \,, \end{aligned}$$

where Ω is a local gauge transformation. In addition, this construction naturally incorporates non-perturbative fields in the sense that gauge potential is now represented by a group element instead of an algebra element. Because of this representation, instantons and other topological configurations can be and have been studied numerically on a lattice, see, for example, Refs. [ILS+86, B+91, GPGASvB94].

To finalize quantization of gauge field theory on a lattice, one has to use some form of discretized action $S = S_g[U] + S_F[U, \psi, \bar{\psi}]$ and compute a Feynman path integral,

$$Z = \int \mathcal{D}U \mathcal{D}\psi \mathcal{D}\bar{\psi} e^{-S_g[U] - S_F[U,\psi,\bar{\psi}]} \,, \tag{2.6}$$

where integration over $\mathcal{D}U$ is understood as the integration with the Haar measure and $\mathcal{D}\psi\mathcal{D}\bar{\psi}$ is the Grassman integration over fermion fields. We postpone the discussion of possible choices of lattice gauge and fermion actions to Sec. 2.2 and Sec. 2.3, respectively. One important thing to notice though is that a lattice action must

approximate the continuum action,

$$\mathcal{L}_{\text{lat}} = \mathcal{L}^{(4)} + a\mathcal{L}^{(5)} + a^2\mathcal{L}^{(6)} + \cdots \tag{2.7}$$

with the higher-order discretization terms $a\mathcal{L}^{(5)} + a^2\mathcal{L}^{(6)} + \cdots$ vanishing in the continuum limit $a \to 0$. A good discretization of the continuum action must suppress the contribution of the first correction terms $\mathcal{L}^{(5)}, \mathcal{L}^{(6)}$ to the Lagrangian to guarantee fast approach to the continuum limit.

2.1.2 Numerical simulation

Over the years, simulating QCD on a lattice has developed into a highly technical field. For comprehensive overviews of algorithms and related theory, interested readers are referred to Refs. [MM, Rot05, Gup97] and references therein. In this section we briefly discuss the main obstacles preventing lattice QCD theorists from making predictions exactly at the physical values of all the parameters.

The lattice version (2.6) of Feynman integrals (2.1,2.2) is computed by the Monte-Carlo method as a statistical average over a set of gauge field configurations $\{U_{x,\mu}\}$ that sample the distribution of the action e^{-S}. This set may be generated using the Metropolis accept-reject algorithm.

One important remark concerns the simulations of dynamic fermions $\{\psi_f, \bar{\psi}_f\}$ which are integrated implicitly using the rules of Grassman variable integration,

$$\int \mathcal{D}U\mathcal{D}\psi_f\mathcal{D}\bar{\psi}_f\, e^{-S_g[U]-\bar{\psi}_f M\psi_f} \to \int \mathcal{D}U\, \det M_f\, e^{-S_g[U]}. \tag{2.8}$$

Computing the determinant $\det M_f$ exactly is a formidable task. Instead, this determinant is estimated using "pseudofermion" fields $\phi, \phi^\dagger$,

$$\det M_f \to \int \mathcal{D}\phi^\dagger\mathcal{D}\phi e^{-\phi^\dagger[M_f]^{-1}\phi} \tag{2.9}$$

and the inverse of the operator M_f arises because of different statistics of fermions and pseudofermions.

The fact that one has to invert the lattice Dirac operator M_f is the main reason why simulating QCD with dynamical fermion fields is very expensive. Basically, for each step of the Metropolis accept-reject algorithm, one has to solve the equation

$$M_f \psi = \chi \tag{2.10}$$

many times, which is a very expensive task. Inverting the lattice Dirac operator is also required for computing correlators involving quark fields, i.e. any hadron correlator. This fact can be illustrated with the simplest case of a quark propagator, which, according to (2.8), is equal to[2]

$$\langle \psi_x \bar{\psi}_y \rangle = \int \mathcal{D}U \mathcal{D}\psi_f \mathcal{D}\bar{\psi}_f \, \psi_x \bar{\psi}_y e^{-S_g - \bar{\psi}_f M_f \psi_f} \rightarrow \int \mathcal{D}U \, [M_f]^{-1}_{xy} \det M_f \, e^{-S_g[U]}. \tag{2.11}$$

Correlators of composite fields such as hadrons must be evaluated according to Wick contraction rules and may require computing separate solutions of Eq. (2.10).

Below we summarize the main factors contributing to the cost of solving QCD on a lattice.

1. The light quark mass is so far the most difficult obstacle to overcome. The lattice Dirac operator M_f in Eq. (2.10) has a bad condition number as the quark mass approaches zero, and its inversion demands significant computational resources.

2. Finite lattice volume presents a difficulty because increasing the linear size of the box entails increase of the number of lattice sites to the fourth power.

3. A lattice spacing should be small enough to suppress the discretization effects. Smaller lattice spacings, or denser grids, evidently lead to increased computational complexity, if one keeps physical volume fixed.

Presently, lattice QCD calculations approach the physical pion mass. Chirally-symmetric fermions, however, are more expensive to simulate on a lattice, and so far

[2] A quark propagator is a gauge-dependent quantity. Computing the lattice ensemble average in Eq. (2.11) requires gauge fixing. We discuss the quark propagator merely for the illustration purpose.

thorough studies have been performed only for $m_\pi \gtrsim 300$ MeV and current simulations are performed with the pion masses down to $m_\pi \approx 180$ MeV. An approximate scaling formula used recently [RBC07] predicts simulation costs with chiral fermions in fixed physical volume

$$\text{Cost} \sim \left(\frac{L}{\text{fm}}\right)^5 \cdot \left(\frac{\text{fm}}{a}\right)^7 \cdot \left(\frac{\text{MeV}}{m_\pi}\right), \tag{2.12}$$

where L is the box dimension, a is the lattice spacing and m_π is the pion mass. Although superficially it seems that the cost depends on the pion mass much weaker than on the box size or the lattice spacing, finite volume effects require increasing the box size L with decreasing m_π as $L \sim 1/m_\pi$.

One must also take the continuum limit $a \to 0$ to get rid of discretization effects. Practically, one has to perform simulations at a few values of a and extrapolate the results to $a \to 0$. Fortunately, with properly chosen chiral fermion action,the limits $a \to 0$ and $m_\pi \to 0$ are independent [A$^+$08a], and chiral extrapolations may be performed independently of taking the continuum limit.

2.2 Discretization of gauge action

Because the gauge action must be gauge-invariant, it can be built only from closed loops $\mathcal{W}(x,x)$ [Gup97]. The simplest gauge action consisting of 1×1 lattice Wilson loops, so-called "plaquettes" (see Fig. 2-1(b)),

$$S \sim \sum \text{ReTr}(1 - U^P), \quad U^P_{x,\mu\nu} = U_{x,\mu} U_{x+\hat{\mu},\nu} U^\dagger_{x+\hat{\nu},\mu} U^\dagger_{x,\nu}, \tag{2.13}$$

approximates the continuum gauge action up to $\mathcal{O}(a^2)$ corrections, which can be seen from the Taylor expansion of a plaquette $U^P_{x,\mu\nu}$,

$$U^P_{x,\mu\nu} = 1 - ia^2 F_{\mu\nu} - \frac{a^4}{2}(F_{\mu\nu})^2 + \mathcal{O}(a^6) + \cdots, \tag{2.14}$$

where $F_{\mu\nu} = \partial_\mu A_\nu - \partial_\nu A_\mu + i\big[A_\mu, A_\nu\big]$ and $F_{\mu\nu}$ and A_μ are matrices representing elements of the algebra of the gauge group.

$$S_g[U] = \frac{2}{g^2} \sum_x \sum_{\mu<\nu} \mathrm{ReTr}\big(1 - U^P_{x,\mu\nu}\big) \to \frac{1}{4} \int d^4x \, (F_{\mu\nu})^2, \quad a \to 0\,. \tag{2.15}$$

To bring the lattice theory closer to the continuum, one can eliminate the effect of the $\mathcal{O}(a^6)$ terms in the expansion (2.14). This can be done by combining 1×1 (*plaquettes*) and 1×2 (*rectangles*) Wilson loops (see Fig. 2-1(b))

$$S_{g,\mathrm{imp.}}[U] = \frac{2}{g^2} \sum_x \Big[(1 - 8c_1) \sum_{\mu<\nu} \mathrm{ReTr}\big(1 - U^P_{x,\mu\nu}\big) + c_1 \sum_{\mu\neq\nu} \mathrm{ReTr}\big(1 - U^R_{x,\mu\nu}\big)\Big] \tag{2.16}$$

with coefficients chosen so that the leading nontrivial term in Eq. (2.14) reproduces the continuum action term $\sim (F_{\mu\nu})^2$. The value of the parameter c_1 can be fixed from the Taylor expansions of U^P and U^R Wilson loops. Such gauge action is called Symanzik, or *tree level*, improved gauge action.

However, the tree-level Symanzik improvement does not take into account quantum fluctuations. The optimal value of c_1 must be computed either perturbatively [Iwa85] or non-perturbatively [dF+00], with the criterion that the *couplings* c_1 and $c_2 = 1 - 8c_1$ stay on the same trajectory $c_1(c_2)$ under renormalization or blocking, i.e., with changing the cutoff scale $\Lambda = a^{-1}$. Such choice guarantees faster approach to the continuum limit and restoration of the rotation symmetry even on coarse-grained lattices [HN94].

2.3 Discretization of fermion action

2.3.1 Chiral symmetry on a lattice

As mentioned before, one wants to preserve as many symmetries as possible in lattice formulation of QCD. One important symmetry is the chiral symmetry of quarks. Unfortunately, when fermions are regularized on a lattice, chiral symmetry can be

preserved only at the expense of introducing so-called *doublers* [NN81][3]. On a 4D hypercubic lattice, one obtains $2^4 - 1 = 15$ additional fermion species with *naive* discretization of the Dirac operator,

$$\not{D}_{\text{naive}} = \sum_{\mu} \gamma_\mu \nabla_\mu + m\,, \tag{2.17}$$

in which the continuum derivatives are replaced with the finite differences $[\nabla_\mu \psi]_x = \frac{1}{2a}(\psi_{x+\hat{\mu}} - \psi_{x-\hat{\mu}})$. These species appear as poles of the Dirac operator (2.17) at the wave numbers $k_\mu = \left\{0, \frac{\pi}{a}\right\}$ with $k^2 \neq 0$.

Evidently, one must have the correct number of fermion species in order to have the correct QCD low-energy dynamics. Below in this section, we will discuss the methods to amend this problem. However, one must realize that this problem has no simple solution, and avoiding the *no-go theorem* [NN81] either breaks chiral symmetry explicitly (Section 2.3.2) or is expensive (introducing additional dimension, Section. 2.3.3). Other solutions, so-called *overlap fermions* [NN93], are currently even more expensive and prohibit dynamical fermion simulations unless the volume is unphysically small.

Despite the difficulties involved, it is important to preserve the chiral symmetry of fermion action for a number of reasons. First and foremost, it is the fundamental symmetry of the QCD Lagrangian, which is spontaneously broken by QCD vacuum structure. In order to guarantee the correct chiral dynamics, our simulations must reproduce this feature. Second, chiral symmetry prevents occurrence of some discretization error terms in a Lagrangian. For example, an $\mathcal{O}(a)$ term in a fermion action cannot be chirally symmetric because of its mass dimension, and must disappear provided the Lagrangian does not contain any *hard* chiral symmetry breaking terms. Therefore, lattice QCD with a chirally-symmetric Lagrangian will be automatically $\mathcal{O}(a^2)$ improved. Third, in a chirally-symmetric lattice theory, renormalization

[3] In fact, the theorem proved in Ref. [NN81] states that *any* regularization of chiral (Weyl) fermions must break one of the following conditions: (1) invariance under gauge symmetry, (2) different number of left- and right-handed fermion species, (3) correct ABJ anomaly or (4) action being bilinear in the Weyl field.

and mixing of operators built of quark fields are significantly simpler.

2.3.2 Wilson fermions

In agreement with Eq. (2.7), one may add irrelevant terms to the lattice QCD Lagrangian that will disappear in the continuum limit. Wilson [Zic77] suggested a solution to the fermion doubling problem by adding a dimension five operator

$$a\,\delta\mathcal{L}^{(5)}_{\text{Wilson}} = -a\,r\bar{\psi}\Delta\psi\,, \tag{2.18}$$

where Δ is a lattice Laplacian. Doubler fermion poles appear at the wave numbers $k_\mu \sim \frac{1}{a}$ in a naive lattice fermion propagator (2.17), and the term (2.18) lifts the doubler degeneracy so that their energy is $\sim \frac{1}{a}$ and they decouple from the only *physical* propagator pole at the wave number close to $k_\mu = 0$. With the commonly used value $r = 1$, the final form of the Wilson action is

$$S_W[\psi,\bar{\psi}] = \frac{1}{a}\bar{\psi}_x\Big[(am_q+4)\delta_{xx'} - \sum_\mu\big(\frac{1-\gamma_\mu}{2}U_{x,\mu}\delta_{x+\hat{\mu},x'} + \frac{1+\gamma_\mu}{2}U^\dagger_{x-\mu,\mu}\delta_{x-\hat{\mu},x'}\big)\Big]\psi_{x'}\,. \tag{2.19}$$

The Wilson fermion action is easy to simulate on a lattice and many calculations with heavy pion masses have been performed with it. As the pion mass goes down, simulations become more expensive (with any fermion action) because of the cost of inverting the Wilson-Dirac operator, although the Wilson action (2.19) is still significantly cheaper than chirally-invariant actions (see Sec. 2.3.3).

However, the term (2.18) breaks the chiral symmetry explicitly. This term generates $\sim \frac{1}{a}$ additive correction to the quark mass, so that the bare quark mass must be tuned to cancel this effect. Also, the Wilson action has $\mathcal{O}(a)$ discretization effects and requires calculations with very small lattice spacing values to keep systematic errors under control. A way to get rid of $\mathcal{O}(a)$ effects while keeping only one fermion species [SW85] is to add another dimension five operator,

$$S_{SW} = S_W - \frac{iaC_{SW}}{4}\bar{\psi}_x\sigma_{\mu\nu}F_{\mu\nu}\psi_x \tag{2.20}$$

with $C_{SW} = 1$ from tree-level perturbative analysis. This additional, so-called *Clover*, term is site-local and adds negligible incremental cost to simulations with the Wilson-Clover action. With careful tuning, about an order of magnitude reduction of systematic effects is possible [EHK98].

This type of action allowed the *BMW* collaboration to succeed in calculating the hadron spectrum from lattice QCD [D$^+$08]. We perform initial calculations for several pion masses using gauge configurations generated by the *BMW* collaborations (see Appendix A.3) and report preliminary results in Sec. 5.1 and Sec. 5.3.

2.3.3 Domain wall fermions

The domain wall fermions (DWF) [Kap92] and its variation [Sha93] is a method to simulate chirally-symmetric fermions on a lattice with finite lattice spacing at the expense of introducing an additional discrete dimension s, sometimes misleadingly called a "flavor" dimension:

$$S_{\mathrm{DW}} = \bar{\Psi} D_{\mathrm{DW}} \Psi = \bar{\Psi}_{x,s} \Big[+ \delta_{ss'} \big[D_W(-M_5) \big]_{xx'} + \delta_{xx'} \big[D_\perp(m_q) \big]_{ss'} \Big] \Psi_{x's'} \,, \qquad (2.21)$$

where D_W is a Wilson fermion operator

$$\big[D_W(-M_5) \big]_{xx'} = 4 - M_5 - \sum_\mu \Big[\frac{1+\gamma_\mu}{2} U^\dagger_{x-\hat{\mu},\mu} \delta x - \hat{\mu}, x' + \frac{1-\gamma_\mu}{2} U_{x,\mu} \delta_{x+\hat{\mu},x'} \Big] \,,$$

and $D_\perp$ is a finite-difference "differential" operator in the fifth dimension with a defect at $s = 0$,

$$\big[D_\perp(m_q) \big]_{ss'} = \begin{cases} m_q P_+ \delta_{L_5-1,s'} - P_- \delta_{1,s'} \,, & s = 0 \,, \\ -P_+ \delta_{s-1,s'} - P_- \delta_{s+1,s'} \,, & 1 \le s \le L_5 - 2 \,, \\ -P_+ \delta_{L_5-2,s'} + m_q P_- \delta_{0,s'} \,, & s = L_5 - 1 \,, \end{cases} \quad ,$$

$$\text{where} \quad P_\pm = \frac{1 \pm \gamma^5}{2} \,.$$

Because the action is asymmetric with respect to left-handed and right-handed fermions, the light boundary states that appear at $s = 0$ and $s = L_5 - 1$ are left- and right-handed, respectively. These chiral modes are thus separated in the fifth dimension and do not interact with each other. The physical chiral 4D fermion fields are related to the 5D fermions as

$$\begin{aligned} q_R &= P_+ \Psi_{L_5-1}\,, \qquad & q_L &= P_- \Psi_0\,, \\ \bar{q}_R &= \bar{\Psi}_{L_5-1} P_-\,, \qquad & \bar{q}_L &= \bar{\Psi}_0 P_+\,, \end{aligned} \tag{2.22}$$

The chiral symmetry is exact (up to the mass term $\sim m_q$) in the limit of infinite extent of the fifth dimension, $L_5 \to \infty$, at which the boundary states can decay completely in the bulk in the 5th direction. Because of the $\sim m_q$ mass term in $D_\perp$, right- and left-handed modes can "talk" to each other with the term

$$\mathcal{L}_m \approx m_q \left[\bar{q}_R q_L + \bar{q}_L q_R\right]. \tag{2.23}$$

However, in practice one has to limit the extent of the fifth dimension (an often used value is $L_5 = 16$), and carefully tune the other parameters such as M_5 and gauge field parameters to maximize the localization of chiral modes at the boundaries. The residual interaction of left- and right-handed modes is parameterized as additional "residual" quark mass,

$$\delta\mathcal{L}_m \approx m_{\text{res}} \left[\bar{q}_R q_L + \bar{q}_L q_R\right]. \tag{2.24}$$

and can be extracted as using an analog of PCAC relation for 5D fermions, see below. Because the interesting states are boundary states decaying exponentially in the 5th dimension away from the walls, the residual mass, with careful choice of parameters is decaying as $m_{\text{res}} \sim e^{-\alpha L_5}$ with L_5.

Essentially, the domain wall operator (2.21) is a 5D Wilson operator with a defect in the fifth dimension. Similarly to Wilson fermions, the domain wall fermions have $U(1)_V$ symmetry that generates the 5D conserved current that, after the summation

over s provides the 4D vector current

$$\mathcal{V}_{x,\mu} = \sum_s \left[\bar{\Psi}_{x+\hat{\mu},s} \frac{1+\gamma_\mu}{2} U^\dagger_{x,\mu} \Psi_{x,s} - \bar{\Psi}_{x,s} \frac{1-\gamma_\mu}{2} U_{x,\mu} \Psi_{x+\hat{\mu},s} \right] \tag{2.25}$$

We are, however, more interested in the (partially) conserved axial current that is constructed by the transformation [B+02]

$$\delta_A \Psi_{x,s} = i\epsilon_{x,s} \Psi_{x,s}\,, \quad \delta_A \bar{\Psi}_{x,s} = -i\epsilon_{x,s} \bar{\Psi}_{x,s}$$

and $\epsilon_{x,s}$ has *opposite* signs in the "left-handed" $0 \le s < L_5/2$ and "right-handed" $L_5/2 \le s < L_5$ halves along the 5th dimension,

$$\epsilon_{x,s} = \begin{cases} -\epsilon_x\,, & 0 \le s < L_5/2\,, \\ +\epsilon_x\,, & L_5/2 \le s < L_5\,, \end{cases}$$

The axial current is then

$$\mathcal{A}_{x,\mu} = -\sum_{0 \le s < L_5/2} \mathcal{A}_{x,\mu,s} + \sum_{L_5/2 \le s < L_5} \mathcal{A}_{x,\mu,s}\,, \tag{2.26}$$

$$\text{where} \quad \mathcal{A}_{x,\mu,s} = \left[\bar{\Psi}_{x+\hat{\mu},s} \frac{1+\gamma_\mu}{2} U^\dagger_{x,\mu} \Psi_{x,s} - \bar{\Psi}_{x,s} \frac{1-\gamma_\mu}{2} U_{x,\mu} \Psi_{x+\hat{\mu},s} \right]$$

Computing the divergence of such current, we arrive at the Ward identity

$$\nabla^-_\mu \mathcal{A}_{x,\mu} \doteq \sum_\mu \left(\mathcal{A}_{x,\mu} - \mathcal{A}_{x-\hat{\mu},\mu} \right) = 2m_q \left[\bar{q}\gamma^5 q \right]_x + 2J^{5q}_x \tag{2.27}$$

where $\nabla^-_\mu \mathcal{A}_{x,\mu} = \sum_\mu (\mathcal{A}_{x,\mu} - \mathcal{A}_{x-\hat{\mu},\mu})$ is a lattice vector field divergence and

$$J^{5q}_x = -\bar{\Psi}_{x,L_5/2-1} \frac{1-\gamma_5}{2} \Psi_{x,L_5/2} + \bar{\Psi}_{x,L_5/2} \frac{1+\gamma_5}{2} \Psi_{x,L_5/2-1}\,. \tag{2.28}$$

The second term in Eq. (2.27) plays a role of residual mass mentioned before. Its modifies the bare quark mass $m_q \to m_q + m_{\text{res}}$ according to Eq. (2.24) and it can be

estimated from its matrix elements including the pion,

$$m_{\text{res}} = \frac{\langle 0|J^{5q}|\pi\rangle}{\langle 0|\bar{q}\gamma^5 q|\pi\rangle} \tag{2.29}$$

Similarly, because the axial current (2.26) satisfies the Ward identity (2.27), its renormalization constant $Z_{\mathcal{A}} \equiv 1$[4] and it can be used to renormalize the local axial current $\left[\bar{q}\gamma_\mu\gamma^5 q\right]_x$. One usually computes the following ratio using the

$$\frac{Z_A}{Z_{\mathcal{A}}} = \frac{\langle 0|\mathcal{A}_0|\pi\rangle}{\langle 0|\bar{q}\gamma_0\gamma^5 q|\pi\rangle}. \tag{2.30}$$

2.3.4 Mixed action

Simulating dynamical fermions is expensive because one has to invert the fermion operator many times to generate the next sample of a Monte-Carlo sequence. Therefore, using chiral fermions described in Sec. 2.3.3 can be prohibitively expensive. At the same time, cheaper actions that break chiral symmetry allow one to accumulate substantial statistics. Thus, the MILC collaboration have generated large ensembles at light pion masses and large spatial volumes [B$^+$01] using so-called *Asqtad* improved staggered quarks [B$^+$98, OT99, OTS99], which are now freely available to the lattice community.

It is natural to assume that the type of valence quark action has more influence on the nucleon observables than the type of sea quarks. For example, the valence quark-bilinear operators will have the symmetry governed by the symmetry of valence quarks, and must renormalize accordingly at least at one-loop level. Therefore, a hybrid scheme of calculations, in which we simulate chiral valence quarks in the gauge background with the inclusion of non-chiral sea quarks, is advantageous, because we combine the symmetries of chiral valence quarks and the availability of non-chiral sea quarks.

We have performed extensive calculations with mixed action where sea (dynamical) quarks are staggered *Asqtad* quarks and valence quarks are chiral (*Domain Wall*).

[4] See also the discussion in Sec. 4.1.3.

The summary tables of the ensembles used are collected in Appendix A.2. Because the operators we compute are constructed from valence, hence chirally-symmetric, quarks, we use the same renormalization procedures as in the *Domain Wall* calculations, e.g., Eqs. (2.29,2.30).

Low-energy theory analysis, however, is generally more complicated because one has to use so-called Partially-Quenched Chiral Perturbation Theory (PQChPT) to take into account the difference between valence and sea quark actions in the lattice theory. Doing so would require tracking the dependence of lattice QCD results on both sea and valence quark masses separately, which is computationally demanding. Instead, since we do not focus on any aspects of PQChPT, we tune the *Domain Wall* valence quark masses to reproduce the pseudoscalar meson mass for each value of *Asqtad* quark mass. Then we use the conventional chiral perturbation theory to analyze our results and extrapolate them to the physical pion mass. One must be aware, however, that the low-energy constants extracted from such hybrid lattice QCD calculations may not be directly related to calculations with unitary quark action (in which $S_{F,\text{sea}} \equiv S_{F,\text{valence}}$), thus making *simultaneous* chiral fits with *Domain Wall* results impossible.

2.4 Rotation symmetry on a lattice

Introducing a discrete space-time grid breaks the $O(4)$ symmetry, the rotation symmetry of 4D Euclidean space. It has been shown that rotation symmetry is restored in long-range lattice QCD; one can also choose an action discretization that reduces rotation symmetry breaking [HN94]. However, short-range effects such as operator mixing generally cannot be avoided because the rotation symmetry is reduced from the continuous group $O(4)$ to the discrete hypercubic group $H(4)$, which leads to complicated operator renormalization and mixing.

This statement can be illustrated with tensors on a lattice. In the continuum, tensors of any rank n constitute a direct sum of irreducible representations of the rotation group $O(4)$. All (symmetric traceless) tensors belong to different representations of

the $O(4)$ group, which protects them from mixing with each other. There are infinitely many irreducible representations of $O(4)$. On the contrary, all tensors on a hypercubic lattice are sums of a finite number of irreducible representations of $H(4)$ [G+96a]: 4 one-dimensional, 2 two-dimensional, 4 three-dimensional, 4 four-dimensional, 4 six-dimensional, and 2 eight-dimensional. For example, the $O(4)$ vector corresponds to the $\mathbf{4}_1$ representation. Tensors of rank $n = 2$ and $n = 3$ are [Dol00]

$$(\mathbf{4}_1)^{\otimes 2} = 1 \cdot \mathbf{1}_1 \oplus 1 \cdot \mathbf{3}_1 \oplus 1 \cdot \mathbf{6}_1 \oplus 1 \cdot \mathbf{6}_3 \,,$$
$$(\mathbf{4}_1)^{\otimes 3} = 4 \cdot \mathbf{4}_1 \oplus 1 \cdot \mathbf{4}_3 \oplus 1 \cdot \mathbf{4}_4 \oplus 3 \cdot \mathbf{8}_1 \oplus 2 \cdot \mathbf{8}_2 \,.$$

One important consequence of the rotation symmetry breaking is that the number of operators that can be calculated on a lattice is limited. For example, the twist-two operators (1.17) discussed in Sec. 1.3 can be computed only up to some rank, because the remnant $H(4)$ symmetry does not discriminate higher-rank operators from low-rank operators.

Chapter 3

Nucleon Matrix Elements on a Lattice

In this chapter, we describe the methodology of computing nucleon structure observables on a lattice. This chapter is based on the analysis performed in [S+10] where the nucleon electromagnetic form factors were calculated, but the methodology is applicable to any hadron three-point correlator calculation. We begin with the discussion of nucleon creation and annihilation operators in Sec. 3.1. In the fundamental theory we are simulating, the correlation functions may contain any physical states permitted by the symmetries, not just nucleons. Hence, to keep systematic errors under control it is essential to choose nucleon operators properly.

To extract the nucleon form factors reliably, we have to compute large sets of nucleon three-point correlators. In Section 3.2 we summarize the common method [BDHS] to minimize the number of required quark propagator inversions. We also present a general method to derive the required valence quark field contractions and illustrate it with an appropriate example.

The nucleon (generalized) form factors are extracted from the nucleon matrix elements by solving overdetermined systems of equations, see Sec. 3.3. Finally, in Section 3.4 we discuss our methodology to set bounds on the contamination from the excited states accompanying a nucleon on a lattice.

3.1 Creating nucleon states on a lattice

Nucleon matrix elements $\langle N|\mathcal{O}|N\rangle$ are computed on a lattice from the three-point correlators of nucleon fields $N, \bar{N}$ and the operator $\mathcal{O}$. Thus, we have to introduce appropriate nucleon interpolating fields that create and annihilate the nucleon states on a lattice.

In the Euclidean quantum field theory all on-shell states are exponentially decaying with the (Euclidean) time, and heavy states decay faster than light ones. Hence, the propagation in Euclidean time can be thought of as a filter selecting the lightest (ground) state from a set with given quantum numbers. However, for the precise calculations to be possible, the nucleon field operator must be as close as possible to the "ideal" one, creating ground states with little admixture of excited states.

3.1.1 Basic nucleon operator

First of all, the nucleon interpolating field should possess correct spin (reduced to the hypercubic group representations), isospin, parity and be a color singlet. Starting from the nonrelativistic quark model wave function for an $I = \frac{1}{2}, S = \frac{1}{2}$ baryon $N_\uparrow^{\mathrm{NRQM}} = \epsilon^{abc} u_\uparrow^a [u_\uparrow^b d_\downarrow^c - u_\downarrow^b d_\uparrow^c]$, one has a relativistic generalization [D$^+$02] using bispinors

$$N_\alpha(u,u,d) = \epsilon^{abc} u_\alpha^a [(u^b)^T C\gamma_5 d^c] \tag{3.1}$$

where $C = \gamma_4\gamma_2$ and $\gamma_5 = \gamma_1\gamma_2\gamma_3\gamma_4$[1]. However, such a generalization is not unique. In particular, one may drop the lower (antiquark) components completely without significant reduction of the overlap with a nucleon ground state [Gra92] by using the projected quark fields

$$q_P = \frac{1+\gamma_4}{2} q. \tag{3.2}$$

Such a choice may be beneficial for the two reasons discussed below.

One reason is that it automatically projects the nucleon operator (3.1) on the positive-parity component, thus removing the negative-parity partner of the nucleon

[1] Here and below we use Euclidean conventions for gamma-matrices, $\gamma_\mu^\dagger = \gamma_\mu$.

(corresponding to the ground state with $I(J^P) = \frac{1}{2}(\frac{1}{2}^-)$, $N(1535)$ [A$^+$08b]) from the state at rest and also reducing its component in the state moving with small velocity $\frac{v}{c} = \frac{p}{E} \ll 1$. The degree of this suppression in a moving nucleon state can be estimated from the ratio of the upper and lower bispinor components in the Dirac plane wave u_p, $(\not{p} - m)u_p = 0$:

$$\frac{|u_p^-|}{|u_p^+|} = \frac{|(1-\gamma_4)u_p|}{|(1+\gamma_4)u_p|} = \frac{\sqrt{E-m_N}}{\sqrt{E+m_N}} \approx \frac{|\vec{p}|}{2m_N}, \tag{3.3}$$

and for a realistic lattice computation with $(am_N) \sim 0.5$ and $(a\vec{p}) = \frac{2\pi}{L} \approx 0.2$ (for $L = 32$) the suppression of the negative-parity state amplitude is $\frac{|\langle N^-|N\rangle|}{|\langle N^+|N\rangle|} \approx 0.2$.

The other reason to use the projected quark fields in Eq. (3.1) is that such projection reduces the number of Dirac operator inversions required to compute nucleon correlators. For example, computing a general hadron two-point correlator requires solving the Dirac equation for each of the $N_s \cdot N_c = 12$ components. If the projection (3.2) is used, only six of these components participate in the nucleon field and thus the cost of the calculation is reduced by a factor of two.

In the discussion of baryon two- and three-point correlators below we will use the following convenient parameterization of baryon operators [Ren04]:

$$B_\delta(u,u,d) = \epsilon^{abc} f^B_{\alpha\beta\gamma\delta} u^a_\alpha u^b_\beta d^c_\gamma \tag{3.4}$$

where $f_{\alpha\beta\gamma\delta}$ is the spin tensor determining the quantum numbers of the field B. From Eq.(3.1) with parity-projected quarks, for the nucleon operator we have

$$f^N_{\alpha\beta\gamma\delta} = (\frac{1+\gamma_4}{2})_{\alpha\delta}(\gamma_1\gamma_3\frac{1+\gamma_4}{2})_{\gamma\beta} = (\frac{1+\gamma_4}{2})_{\alpha\delta} S_{\gamma\beta}, \tag{3.5}$$
$$\text{where } S_{\gamma\beta} = (\gamma_1\gamma_3\frac{1+\gamma_4}{2})_{\gamma\beta}.$$

For completeness, we add the expression for the antibaryon field:

$$\begin{aligned}\bar{B}_{\delta'} &= (N)^{\dagger}_{\delta}(\gamma_4)_{\delta\delta'} = (f^{B}_{\alpha\beta\gamma\delta}u_{\alpha}u_{\beta}d_{\gamma})^{\dagger}_{\delta}(\gamma_4)_{\delta\delta'} \\ &= \bar{f}^{B}{}_{\alpha'\beta'\gamma'\delta'}\bar{d}_{\gamma'}\bar{u}_{\beta'}\bar{u}_{\alpha'},\end{aligned} \tag{3.6}$$

$$\text{where} \quad \bar{f}^{B}{}_{\alpha'\beta'\gamma'\delta'} = (f^{B}_{\alpha\beta\gamma\delta})^{*}(\gamma_4)_{\alpha'\alpha}(\gamma_4)_{\beta'\beta}(\gamma_4)_{\gamma'\gamma}(\gamma_4)_{\delta\delta'} \tag{3.7}$$

and the antisymmetrization over the color indices is implied.

3.1.2 Suppression of excited states

The operator in Eq. (3.1) creates a superposition of states with the same quantum numbers. Let $|\Psi\rangle = \mathcal{C}^{-1/2}\bar{N}|\Omega\rangle$ denote the normalized state obtained by the action of the nucleon interpolation field on the vacuum, and $|n\rangle$ denote the n^{th} eigenstate of the system. In addition to the nucleon ground state, there are nucleon excited states as well as multiparticle (scattering) states, for example $\pi + N$ with the pion in a p-wave to preserve positive parity. These states contaminate the relevant ground-state nucleon signal and introduce systematic bias to the nucleon matrix elements being computed. According to the transfer matrix formalism, the contributions of different states to the three-point function are

$$\langle N(t_3)\mathcal{O}(t_2)N(t_1)\rangle = \mathcal{C}\sum_{n,m}\langle\Psi|n\rangle\langle n|\mathcal{O}|m\rangle\langle m|\Psi\rangle e^{-E_n(t_3-t_2)-E_m(t_2-t_1)}, \tag{3.8}$$

In principle, one can rely on the Euclidean time propagation to filter out wrong states since they have higher energy, $E_n > E_0$, $n \geq 1$. However, doing so requires increasing the distance in the corresponding three-point correlation functions. The ratio of the signal to stochastic noise in the case of a nucleon falls off with distance as [Lep]

$$\frac{\text{signal}}{\text{noise}} \sim e^{-(m_N - \frac{3}{2}m_\pi)t}. \tag{3.9}$$

We have two objectives while choosing the nucleon interpolating fields appropriate for accurate lattice calculations of hadronic matrix elements. The first one is to

minimize the overlap with excited states $\left(1-|\langle 0|\Psi\rangle|^2\right)$. Since we cannot construct the nucleon ground state precisely without knowing its structure, which itself is studied in this work, we can only attempt to *suppress* excited states as much as possible using some general assumptions. So, it is reasonable to assume that quarks in the ground state are smoothly distributed over the size of the nucleon. As we do not know these distributions precisely, we *approximate* them with spatially smeared quark fields and construct the nucleon interpolating field from them. Our second objective is to minimize the fluctuations arising from the nucleon interpolating field itself. Such fluctuations arise because extended (smeared) quark fields must be constructed in a gauge-covariant way, thus entangling the gauge noise into the nucleon fields.

The extended (smeared) quark fields are created with some smooth kernel $K(x)$,

$$\tilde{q}(x) = \int dx\, K(x-x')q(x'), \tag{3.10}$$

where $q(x)$ is regular quark field, and the smeared nucleon field is then

$$\tilde{N}(x) = N\big(\tilde{u}(x), \tilde{u}(x), \tilde{d}(x)\big). \tag{3.11}$$

Note that a nucleon field has the serious limitation that spatial quark wave functions in the state created with it are independent, i.e. the 3-quark state wave function is factorizable into the spatial distributions of separate quarks. We will discuss an attempt to overcome this limitation in Sec. 3.1.3.

While different choices for the kernel $K(x-x')$ are possible, for example, using wave functions from non-relativistic potential models [PS], the one whose use is most wide spread is the Wuppertal [G$^+$89, G9̈0], or equivalently, Gaussian form,

$$\tilde{q}(x) = \Big[(1+\frac{\sigma^2}{4N}\Delta)^N q\Big](x), \tag{3.12}$$

where Δ is the gauge-covariant spatial Laplacian. This form is very easy to implement on a lattice in a gauge-covariant way and it is hard to outperform in terms of suppression of excited states [PS]. Another advantage is that Gaussian smearing has

effectively only one parameter, the width $\sim \sigma$, while the number of iterations N is chosen so that (3.12) is numerically stable. Finally, this construction is spherically-symmetric after averaging over a gauge configuration ensemble, which corresponds to an S-wave distribution of quarks inside the nucleon, and suppresses any states in which quarks have non-zero orbital angular momentum. Again, it is not given that quarks in the nucleon are only in the S-wave state, but it is reasonable to assume that in the nucleon *ground state* quarks have less angular momentum than in nucleon excited states.

The first objective of optimizing the nucleon operator is met by using smeared propagators and treating the r.m.s. radius of the smearing kernel as a variational parameter,

$$r_{\rm rms} = \langle r^2 \rangle^{\frac{1}{2}} = \left[\frac{\int d^3x |\vec{x}|^2 |q(\vec{x})|^2}{\int d^3x |q(\vec{x})|^2} \right]^{1/2} . \tag{3.13}$$

It is clear that the point-like nucleon field $N_x = N(u_x, u_x, d_x)$ may have significant overlap with various excited states in the spectrum. For example, if the quark wave function is too narrow, it will have significant overlap with wave functions having nodes and corresponding to radially-excited nucleon-like states. In the other extreme case, if the quark wave function is too wide, because of its tails it is likely to have significant overlap with states including pion(s). Clearly, there must exist an optimal value for the width of the quark wave function or, equivalently, r.m.s. radius (3.13).

To attain our second objective of minimizing the fluctuations arising from the source itself, it is highly advantageous to perform so-called APE smearing of the gauge links [FPPT85] used in generating the source on the time slice of the source. In each iteration of APE smearing, each link is replaced by a linear combination of itself and the sum of staples within that time slice, and projected back onto $SU(3)$ as follows

$$U_{x,i}^{(N)} = {\rm Proj}_{SU(3)} \left[U_{x,i}^{(N-1)} + \beta \sum_{j \neq i}^{3} U_{x,j}^{(N-1)} U_{x+j,i}^{(N-1)} U_{x+i,j}^{(N-1)\,\dagger} \right] , \tag{3.14}$$

where $U^{(0)}$ is the original field and $U^{(N_{\rm APE})}$ is used in the covariant Laplacian in

Eq. (3.12). Applying the APE smearing has the effect of suppressing ultraviolet fluctuations of the gauge field and thus reducing the noise in the operators constructed with it. At the same time, this procedure is gauge-covariant and thus does not require any gauge fixing to build extended color fields.

A simple measure of the noise introduced by the gauge field into the nucleon field is its fractional fluctuation $\frac{\delta\mathcal{O}}{\mathcal{O}} = \frac{\langle(\mathcal{O}-\langle\mathcal{O}\rangle)^2\rangle^{\frac{1}{2}}}{\langle\mathcal{O}\rangle}$, where $\mathcal{O}$ is the norm of the state $\left|\langle 0|\bar{N}|\Omega\rangle\right|^2$ created by the nucleon field. Figure 3-1(b) shows the dramatic effect that the APE smearing has on reducing these fluctuations for both lattice spacings. Since the incremental benefit of successive smearing becomes small beyond 25 smearing steps, we have chosen to use 25 steps throughout. Note that for the largest number of Wuppertal smearing steps, this reduces the noise by a factor of more than 5 in each case.

We can control the r.m.s. radius (3.13) of smeared sources through the smearing parameters, however, only the r.m.s. radius has physical sense. Because the APE smearing smooths the gauge links, the r.m.s. radius for given Gaussian smearing parameters increases slightly with the number of APE smearing steps. We performed a scan of the parameter region shown in Fig. 3-1(a)

In lattice gauge theories for which one can construct a transfer matrix and quarks and antiquarks are properly normal ordered at zero time separation in the quark propagator [Lus77], the source may be optimized straightforwardly by maximizing the overlap between the normalized state created by the action of the source $|\Psi^{(r)}\rangle = \mathcal{C}^{-1/2}\bar{N}^{(r)}|\Omega\rangle$, where the source $\bar{N}^{(r)}$ has r.m.s. radius r, and the normalized ground state of the nucleon $|0\rangle$. Denoting the momentum projected normalized eigenstates of the nucleon by $|n\rangle$ and their energies by E_n, the momentum projected two-point correlation function may be expanded:

$$C^{(r)}(t) = \int d^3x \langle N^{(r)}(x,t)\bar{N}^{(r)}(0,0)\rangle = \mathcal{C}\sum_n \left|\langle\Psi^{(r)}|n\rangle\right|^2 e^{-E_n t}, \tag{3.15}$$

where $\mathcal{C}$ is an unknown normalization constant. Since one can directly measure the

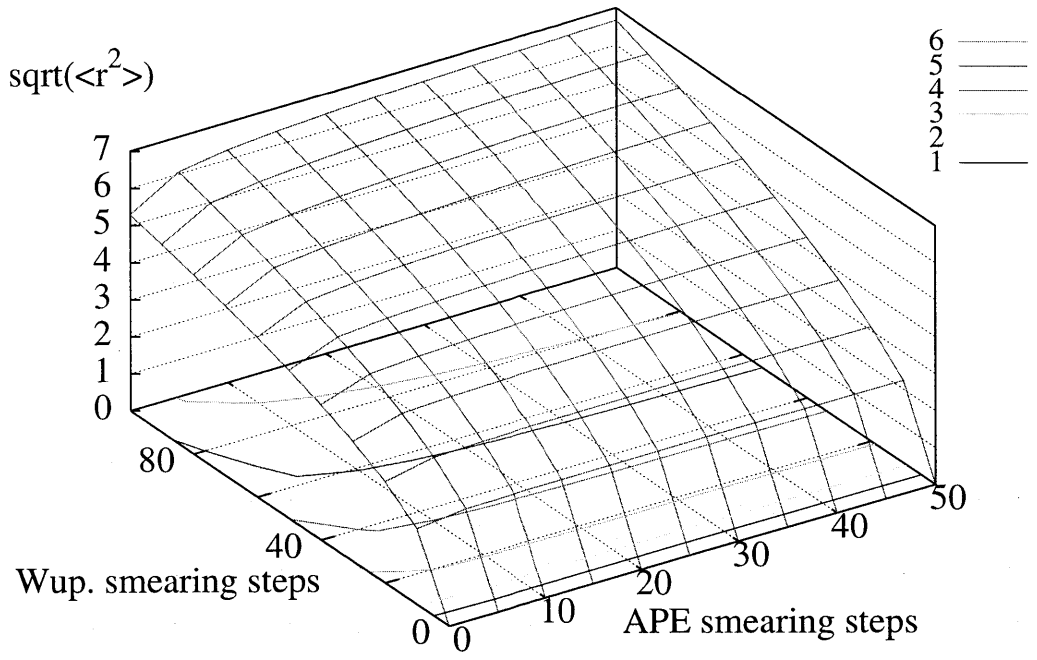

(a) R.m.s radius (3.13) of Wuppertal-smeared (3.12) sources as a function of the coefficient $\alpha = (4N/\sigma^2 - 6)^{-1}$ and the number of smearing steps N

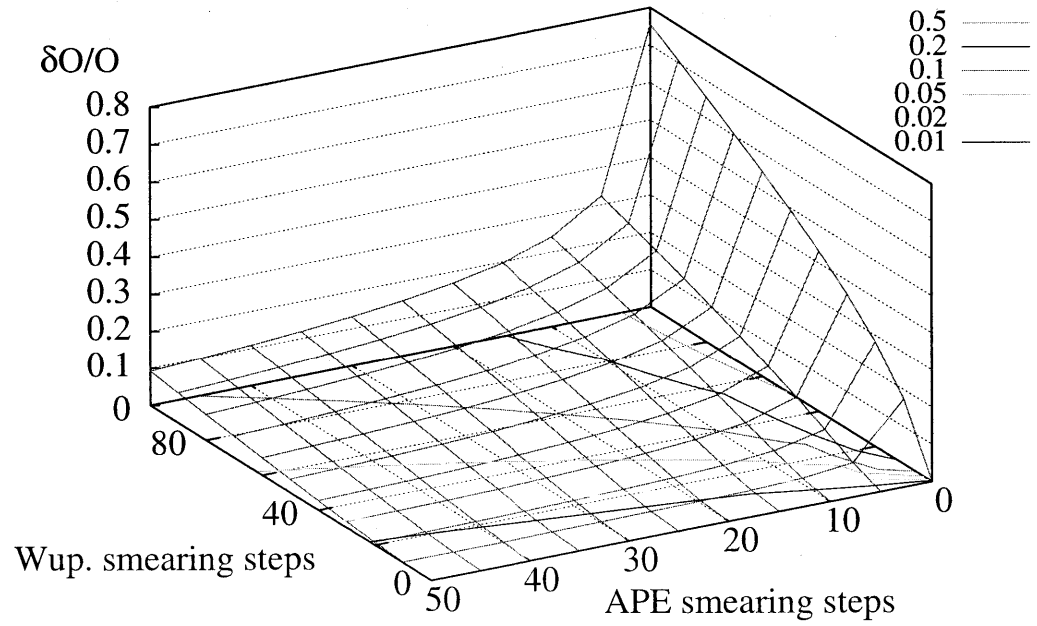

(b) Fractional variation of the nucleon state norm created with operator (3.11).

Figure 3-1: Scan of the Wuppertal and APE smearing parameter space.

correlation function at zero time separation

$$A^{(r)} = C^{(r)}(0) = \mathcal{C} \sum_n \left| \langle \Psi^{(r)} | n \rangle \right|^2 , \tag{3.16}$$

and reliably fit the large t behavior of the correlation function to extract the ground state contribution

$$B^{(r)} = \mathcal{C} \left| \langle \Psi^{(r)} | 0 \rangle \right|^2, \tag{3.17}$$

the probability that the source contains the nucleon ground state may be calculated by

$$\mathcal{P}^{(r)} = \frac{B^{(r)}}{A^{(r)}} = \left| \langle \Psi^{(r)} | 0 \rangle \right|^2. \tag{3.18}$$

For domain wall fermions, which do not have a local transfer matrix, we consider the following generalization of Eqs. (3.16-3.18), which compares the ratio of the correlation function and the extrapolated ground state contribution at time t instead of time $t = 0$:

$$A^{(r)}(t) = C^{(r)}(t), \tag{3.19}$$

$$B^{(r)}(t) = \mathcal{C} \left| \langle \Psi^{(r)} | 0 \rangle \right|^2 e^{-E_0 t}, \tag{3.20}$$

$$\mathcal{P}^{(r)}(t) = \frac{B^{(r)}(t)}{A^{(r)}(t)}. \tag{3.21}$$

This ratio, $\mathcal{P}^{(r)}(t)$, ranges from the overlap $\mathcal{P}^{(r)}$ at $t = 0$ to 1 in the limit $t \to \infty$. We expect that for small t, it is still a good measure of the presence of excited state components in the source and should have a maximum close to the maximum in $\mathcal{P}^{(r)}$. This expectation is borne out in the case of Wilson fermions, and we note that this criterion gets even better as the lattice spacing decreases. Since we are only interested in the dependence of $\mathcal{P}^{(r)}(t)$ on the r.m.s. radius r and the absolute normalization for $t \neq 0$ has no physical significance, it suffices to calculate the following ratio for large t_0

$$\frac{C^{(r)}(t_0)}{C^{(r)}(t)} \xrightarrow{t_0 \to \infty} \frac{\mathcal{C} |\langle \Psi^{(r)} | 0 \rangle|^2 e^{-E_0 t_0}}{C^{(r)}(t)} = \mathcal{P}^{(r)}(t) e^{E_0 (t_0 - t)}. \tag{3.22}$$

For each value of t, it is convenient to normalize the curve such that its maximum value is unity. Hence, defining the r.m.s. radius at the maximum as r^*, our final

criterion for optimizing the smearing is the ratio

$$R^{(r)}(t) = \frac{C^{(r)}(t_0)/C^{(r)}(t)}{C^{(r^*)}(t_0)/C^{(r^*)}(t)}. \tag{3.23}$$

Equation (3.23) has the computational advantages that all oscillating terms in the time dependence of the correlation functions cancel out of the ratios and that jackknife or bootstrap resampling analysis enables accurate measurements on small ensembles.

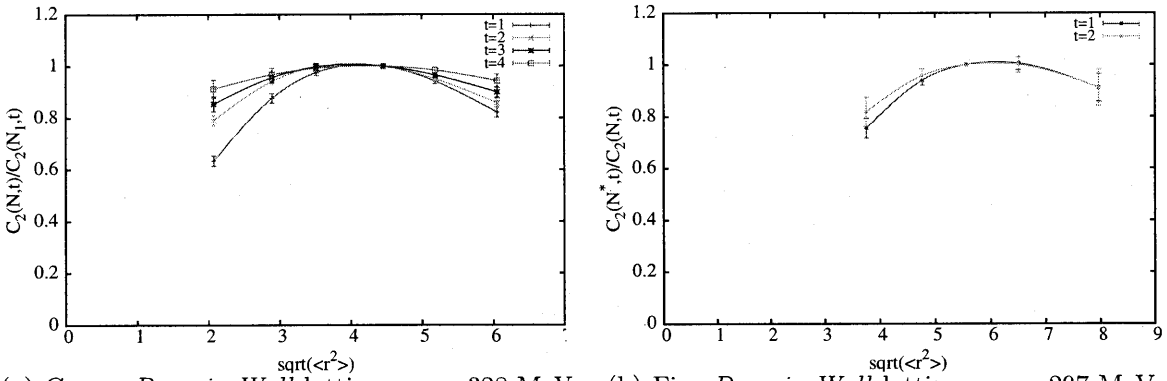

(a) Coarse *Domain Wall* lattice, $m_\pi = 328$ MeV (b) Fine *Domain Wall* lattice, $m_\pi = 297$ MeV

Figure 3-2: Source optimization criterion (3.23) vs smeared source r.m.s. radius (3.13).

Figure 3-2 shows the primary result of the calculation for both lattice spacings. The solid curves are splines passing through the mean values to guide the eye. For the coarse lattice, the ratio $R^{(r)}(t)$ is calculated at six values of the number of Wuppertal steps, $N = 10, 20, 30, 50, 70, 100$, corresponding to r.m.s. radii, $r =$ 2.07, 2.89, 3.51, 4.46, 5.19, and 6.06 lattice units respectively. We chose $r^* = 4.46$ fm and calculated bootstrap error bars using 32 configurations. Instead of normalizing at a single value of t_0 as in Eq. (3.23), the errors in the ratios in Fig. 3-2 were further reduced by normalizing to an exponential fit to each correlation function in the region $t = [6 - 12]$. These results are completely consistent with those of a single t_0, but display the shape of the maxima more precisely. Note that for all four values $t = 1, 2, 3$, and 4, the curves are accurately determined and the ratio $R^{(r)}(t)$ has a maximum at approximately the same point, $r = 4.0$, corresponding to $N = 40$. Thus, we believe our optimization criterion is robust and statistically accurate for domain

wall fermions.

For the fine lattices, the ratio $R^{(r)}(t)$ is calculated at 5 values of the number of Wuppertal steps, $N = 30, 50, 70, 100$, and 150, corresponding to r.m.s. radii $r = 3.76, 4.77, 5.56, 6.51$, and 7.77 lattice units respectively. We chose $r^* = 5.56$, normalized by exponential fits to each correlation function in the region $t = [6 : 12]$, calculated error bars with jackknife resampling method, and only included $t = 1$ and 2 to avoid making the graph confusing due to the larger error bars. The maximum occurs at approximately $r = 6.0$ lattice units, corresponding to 84 Wuppertal smearing steps. This result appears reasonable, since assuming a constant r.m.s. radius in physical units would imply that the r.m.s. radius on the coarser lattice of 4.0 lattice units would scale to $4.0 \times 0.114/0.084 = 5.4$ lattice units on the present lattice, and the pion mass on the finer lattice is somewhat lighter.

Table 3.1: Parameters for optimal sources as defined in Eq. (3.14) and (3.24).

lattice	APE smearing			Wuppertal smearing			Size
a [fm]	β	$A = 1/\beta$	$N_{\rm APE}$	α	σ	N_W	$\langle r^2 \rangle^{1/2}$
0.114	0.3509	2.85	25	3	5.026	40	4.0
0.084	0.3509	2.85	25	3	7.284	84	6.0

We summarize the final parameters for optimal sources used in this work in Table 3.1. The definitions of Wuppertal smearing in different parameterizations are given by

$$\begin{aligned}\psi(x,t) &= \left(1 + \alpha \sum_{i=1}^{3} \left[U(x,i)\delta_{x+\hat{i},y} + U^\dagger(x-\hat{i},i)\delta_{x-\hat{i},y}\right]\right)^N \delta_{y,0} = \left(1 - \frac{\sigma^2\nabla^2}{4N}\right)^N \delta_{y,0} \\ &\equiv \left(1 - \frac{3\sigma^2}{2N}\right)^N \left(1 + \frac{\sigma^2/4N}{1 - 3\sigma^2/2N} \sum_{i=1}^{3} \left[U(x,i)\delta_{x+\hat{i},y} + U^\dagger(x-\hat{i},i)\delta_{x-\hat{i},y}\right]\right)^N \delta_{y,0}\end{aligned} \tag{3.24}$$

and the parameters are related by

$$\alpha = \frac{\sigma^2/4N}{1 - 3\sigma^2/2N}, \qquad \sigma^2 = \frac{2N\alpha}{3\alpha + 1/2}.$$

3.1.3 Composite nucleon operators

In the conclusion of this section, we discuss a method to tune the nucleon interpolating field [PS] that could potentially perform better than those discussed in Sec. 3.1.2. This method is not used for calculations in the present work, however, it may be vital for the future studies.

As pointed out after Eq. (3.11), its main disadvantage is that the quark wave functions are independent. A simple way to improve this is to construct a "composite" nucleon operator

$$\tilde{N}(x) = \sum_i \alpha_i N\big(\tilde{u}^{(A_i)}(x), \tilde{u}^{(B_i)}(x), \tilde{d}^{(C_i)}(x)\big), \tag{3.25}$$

where $\{A, B, C\}_i$ denote the combinations of different types of spatial smearing of the quark fields. Then, our goal is to tune the smearing combinations $\{A, B, C\}_i$ and their coefficients α_i so that the interpolating field creates a state which is orthogonal to a number of the lowest excited states[2].

In principle, one can combine Gaussian smeared quarks (3.12) with different width parameters. However, a series of Gaussian-smeared nucleon operators tends to create states which are very close to being "collinear" in the Hilbert space. For example, if the nucleon operators smeared with two different values σ_1 and σ_2 create states

$$\begin{aligned} \tilde{N}_1|\Omega\rangle &= A(|0\rangle + \alpha_1|1\rangle) + \text{other exc. states}, \\ \tilde{N}_2|\Omega\rangle &= B(|0\rangle + \alpha_2|1\rangle) + \text{other exc. states}, \end{aligned} \tag{3.26}$$

with the main contamination given by the state $|1\rangle$ *and* α_1 is close to α_2, the linear combination of these states canceling the $|1\rangle$ state will be very noisy. Instead, one can try adding node(s) to the quark wave functions used in Eq. (3.11) to create a different superposition of $|0\rangle$ and $|1\rangle$ states and combine it with one of Eq. (3.26). Further, a number of such operators constitutes a basis of states in which the orthogonalization

[2] We emphasize that one has to suppress the excited states that are separated by the smallest gap from the ground state. The rest of the contamination will be suppressed by the evolution factor $e^{-\Delta E_{n0} t}$

procedure is more stable and reliable, especially when noisy lattice data are used for source optimization.

For example, if some potential model is taken as a crude description of a nucleon, the simplest form one may try is

$$\tilde{N}(x) = A\,N\big(\tilde{u}^{(0)},\tilde{u}^{(0)},\tilde{d}^{(0)}\big)+B\left[N\big(\tilde{u}^{(1)},\tilde{u}^{(0)},\tilde{d}^{(0)}\big)+N\big(\tilde{u}^{(0)},\tilde{u}^{(1)},\tilde{d}^{(0)}\big)+N\big(\tilde{u}^{(0)},\tilde{u}^{(0)},\tilde{d}^{(1)}\big)\right], \tag{3.27}$$

where $\tilde{q}^{(0)}$ is the spherically-symmetric ground state wave function (without nodes) of a quark in some model potential and $\tilde{q}^{(1)}$ is the first excited state (with one node). By tuning A and B one may obtain better overlap with the ground state than by tuning the first term alone.

As a preliminary study, we compute an 8×8 two-point nucleon correlator matrix $\langle\tilde{N}_i(t)\overline{\tilde{N}}_j(0)\rangle$ corresponding to eight different nucleon operators at the source and the sink using the *BMW* ensemble,

$$\begin{aligned}
\tilde{N}_0 &= N\big(\tilde{u}^{(0)},\tilde{u}^{(0)},\tilde{d}^{(0)}\big),\\
\tilde{N}_1 &= N\big(\tilde{u}^{(1)},\tilde{u}^{(0)},\tilde{d}^{(0)}\big),\\
\tilde{N}_2 &= N\big(\tilde{u}^{(0)},\tilde{u}^{(1)},\tilde{d}^{(0)}\big),\\
&\cdots\\
\tilde{N}_7 &= N\big(\tilde{u}^{(1)},\tilde{u}^{(1)},\tilde{d}^{(1)}\big),
\end{aligned} \tag{3.28}$$

where $\tilde{q}^{(0)}$ is the Gaussian-smeared quark field (3.12) and $\tilde{q}^{(1)}$ is the same profile with the covariant Laplacian applied,

$$\tilde{q}^{(1)} = \Delta\Big[(1+\frac{\sigma^2}{4N}\Delta)^N q\Big](x). \tag{3.29}$$

Applying the Laplacian to the Gaussian distribution should produce a profile with a node, as indicated by the free-field case

$$\Delta e^{-\frac{r^2}{2\sigma^2}} = \frac{r^2-3\sigma^2}{\sigma^4}e^{-\frac{r^2}{2\sigma^2}}.$$

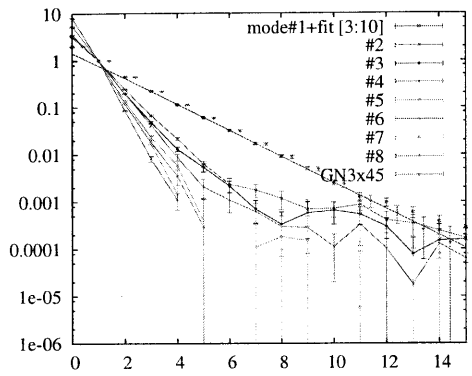

(a) Gaussian $\oplus$ Δ·Gaussian smearing

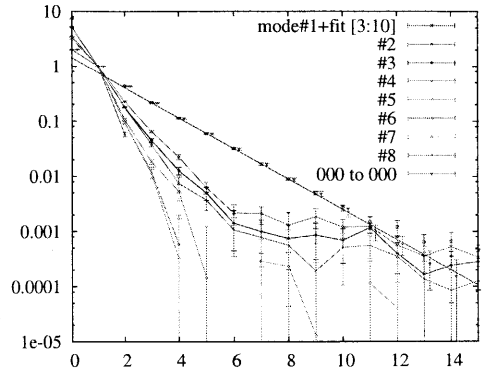

(b) $|0\rangle \oplus |1\rangle$ in the linear potential

Figure 3-3: Eigenvalues extracted from the nucleon correlator matrix with 8 composite sources and sinks (3.28).

Analyzing the data using traditional variational method [LW90], we extract eigenvalues of the 8×8 correlator matrix with the sources and sinks (3.28) described above. We show the results in Fig. 3-3 for both Gaussian $\oplus$ Δ·Gaussian smearing and $|0\rangle \oplus |1\rangle$ states in the linear potential. It is notable that in both methods we obtain very similar results, and they *do not* improve the overlap compared to the factorizable nucleon operator with the optimal choice of the smearing parameters. This may be explained by potentially suboptimal choice of basis in Eq. (3.28), and further study is required to clarify this.

An additional important observation from Fig. 3-3 is that the gaps between the ground state and the excited states are significant and are of the order of the mass of the ground state so that $m_{\text{exc}} \sim m_N$. This result is reassuring because it indicates that our operators create little or no admixture of "scattering" $N + \pi$ states which may have much smaller energy gaps from the ground state. This observation will be used in the discussion in Sec. 3.4.

3.2 Three-point correlators on a lattice

3.2.1 Quark-bilinear operators

Computing three-point correlators of nucleons with quark-bilinear operators on a lattice

$$C^{\Gamma}_{3\mathrm{pt}}(x,y) = \langle N(x)\big[\bar{q}\Gamma q\big](y)\bar{N}(0)\rangle \tag{3.30}$$

requires pairing all quark fields with antiquark fields in all possible ways and substituting lattice quark propagators for each pair. There are two types of contractions, connected and disconnected (see Fig. 3-4). Disconnected contractions give non-trivial contributions because the quark loop in Fig. 3-4(b) is evaluated in the presence of the gluon background that connects this loop with the valence quark lines by virtual gluon exchanges.

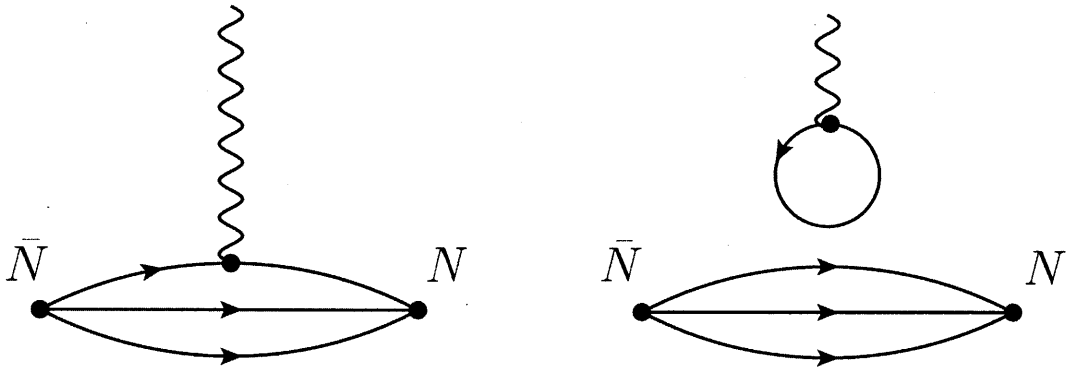

(a) Connected (b) Disconnected

Figure 3-4: Wick contractions of quark fields in three-point correlators.

The disconnected contribution is very hard to calculate. Generally, one needs to compute momentum-projected correlators and thus has to sum over the position y in Eq. (3.30). Doing so requires inverting the Dirac operator for all the L_s^3 lattice sites in the spatial volume. Although there is some progress in such computations (most notably, see Refs. [D$^+$09, BCS09a, BCS09b]), they are still limited to heavy pion masses and non-chiral fermions.

It is worth noting that the calculation of disconnected contractions is crucial for

such problems as the strange quark content of the nucleon, quark spin contributions to the nucleon spin and, in general, any isosinglet nucleon structure observables or observables associated with one specific flavor. Computing connected contractions gives the complete result only for flavor-nonsinglet contributions, for example, the axial charge and the isovector form factors. However, even if advanced techniques or resources to compute the disconnected contractions become available, one will still have to reduce the noise in MC simulations and contaminations from excited states. Therefore, in this work we focus mostly on isovector observables as a test case to understand the precision that is possible to achieve, and lay the foundations for complete nucleon structure calculations in the future.

3.2.2 Connected three-point quark correlators

In our calculations we use the so-called sequential source method [BDHS]. The sequential source method in this work is motivated by the same reason as in Ref. [H+08, D+02]: it allows one to compute quark-bilinear operators with any Dirac matrix insertion in Eq. (3.30) as well as covariant derivatives. However, when using the sequential source method, one has to fix the time locations of the nucleon source and sink, thus making studying the systematic dependence on the source-sink separation prohibitively expensive. Thus, a separate study of this potential source of systematic effects is necessary, see Sec. 3.4.

Inversion of the Dirac operator on a lattice is a costly procedure, and, unless one uses special stochastic estimator techniques [D+09], one can only compute a small number of fermion propagators $x \leftarrow y$ where y is a fixed point on a lattice:

$$\left[\not{D}^{-1}\right]^{ab}_{\alpha\beta}(x,y) = \langle q^a_\alpha(x)\bar{q}^b_\beta(y)\rangle, \tag{3.31}$$

In addition, one can use the so-called γ_5-hermiticity of Dirac operators, $\gamma_5 \not{D} \gamma_5 = \not{D}^\dagger$ (the conjugation is applied to all the pairs of "indices", spin, color and coordinate),

to obtain the propagator $x \leftarrow y$ where x is a fixed point:

$$\left[\not{D}^{-1}(x,y)\right]^{ab}_{\alpha\beta} = \left[\gamma_5 \left[\not{D}^{-1}(y,x)\gamma_5\right]^\dagger\right]^{ab}_{\alpha\beta}. \tag{3.32}$$

Every lattice propagator (3.31) or (3.32) requires 12 inversions of the Dirac operator $\not{D}$ on a lattice to compute all the combinations of spin and color indices.

The main idea of the sequential propagator method is to represent the three-point correlator (3.30) as a trace of the product,

$$C^{\bar{q}\Gamma\mathcal{U}q}_{\text{3pt}}(x,y) = \text{Tr}_{\text{spin,color}}\left[S^{N\bar{N}}_q(0;x)\,\not{D}^{-1}(x,y')\,\Gamma\,\mathcal{U}(y',y)\,\not{D}^{-1}(y,0)\right], \tag{3.33}$$

where $\mathcal{U}(y,y')$ is the product of the gauge links along some path $y \rightarrow y'$ [3] and $S^{N\bar{N}}_q(0;x)$ is the sequential source for the pair of a nucleon source and a sink at points 0 and x, respectively. On a lattice, one successively computes the forward propagator $\not{D}^{-1}(\bullet,0)$ [4], the sequential source $S^{N\bar{N}}_q(0;x)$, the backward propagator $S^{N\bar{N}}_q(0;x)\not{D}^{-1}(x,\bullet)$ and, finally, the three-point function(s) $C^{\bar{q}\Gamma\mathcal{U}q}_{\text{3pt}}(x,y)$.

A sequential source $S^{N\bar{N}}_q$ depends on a particular type of the nucleon interpolating field, the source and sink locations, the nucleon polarization matrix, and the quark flavor q. One may think of a sequential source as a two-point correlator with one of the valence quark lines in Fig. 3-4(a) cut to insert an operator. Symbolically, one can express a sequential source as

$$\left[S^{N\bar{N}}_q(0;x)\right]^{ab}_{\alpha\beta} = \Gamma^{\text{pol}}_{\delta\delta'}\left\langle\!\left\langle \left(N_{\delta'}(x)\frac{\overleftarrow{\delta}}{\delta q^b_\beta(x)}\right)\cdot\left(\frac{\overrightarrow{\delta}}{\delta\bar{q}^a_\alpha(0)}\bar{N}_\delta(0)\right)\right\rangle\!\right\rangle, \tag{3.34}$$

where the angular brackets $\langle\langle\cdots\rangle\rangle$ denote (connected) contractions of the remaining valence quarks. One usually computes three-point correlators with a momentum-projected sink, summing $S(0;x)$ over $\vec{x}$ with an appropriate phase factor $e^{-i\vec{P}'\vec{x}}$, and

[3] These link paths allow one to construct the finite differences approximating covariant derivatives on a lattice. Computing the three-point correlators with the full set of link paths up to some length ("building blocks") was first used in Ref. [Ren04] and allows efficient computation of a number of point-split quark-bilinear operators in a single run.

[4] The dot "$\bullet$" here and below denotes any point on the lattice. Thus, $\not{D}^{-1}(\bullet,0)$ is a lattice "vector" of fermion matrices.

using the fact that doing so commutes with the rest of the computation of three-point functions.

If the nucleon interpolating fields are constructed from smeared quark fields one has to apply the smearing kernel from Eq. (3.10)

- to both sides of the lattice quark propagators $\mathcal{U}$ and $\mathcal{D}$, $\mathcal{Q}(x,y) \rightarrow \tilde{\mathcal{Q}}(x,y) = \int dx'\, dy' K(x-x')\mathcal{Q}(x',y')K(y'-y)$
- and to the sequential source, $S(0;x) \rightarrow \tilde{S}(0;x) = \int dx'\, S(0;x')K(x'-x)$.

Finally, to illustrate the sequential source method, we derive explicitly the expression for the sequential source $S^{n\bar{p}}_{\bar{d}u}$ corresponding to the matrix element $\langle n|\bar{d}\Gamma u|p\rangle$ between proton and neutron states. Since we are working in the isospin limit, this matrix element is equivalent to the $(u-d)$ combination of the proton matrix elements,

$$S^{n\bar{p}}_{\bar{d}u} = S^{p\bar{p}}_{\bar{u}u} - S^{p\bar{p}}_{\bar{d}d}\,. \tag{3.35}$$

This derivation is useful for calculations with so-called twisted boundary conditions (TwBC) in which the spatial boundary conditions on a lattice are non-trivial and different for the u and d quarks allowing one to have fractional (with respect to the lattice momentum quantization) momentum transfer values $Q^2 = -(P'-P)^2$.

We use the definition for the proton and neutron interpolating fields as

$$p = N(u,u,d)\,, \quad n = N(d,d,u)\,. \tag{3.36}$$

The variations of the proton and neutron fields with respect to the quark fields are equal to

$$\begin{aligned}
\frac{\overrightarrow{\delta}}{\delta \bar{u}^a_\alpha}\bar{p}_\delta &= \epsilon^{abc}\left[\bar{f}_{\alpha\beta\gamma\delta} + \bar{f}_{\beta\alpha\gamma\delta}\right]\bar{d}^c_\gamma \bar{u}^b_\beta\,, \\
n_{\delta'}\frac{\overleftarrow{\delta}}{\delta d^a_\alpha} &= \epsilon^{a'b'c'}\left[f_{\alpha'\beta'\gamma'\delta'} + f_{\beta'\alpha'\gamma'\delta'}\right]d^{b'}_{\beta'}u^{c'}_{\gamma'}\,.
\end{aligned}$$

Substituting the above expressions into Eq. (3.34) and using $f_{\alpha\beta\gamma\delta} = (\frac{1+\gamma_4}{2})_{\alpha\delta}S_{\gamma\beta}$ and

$\frac{1+\gamma_4}{2}\Gamma^{\rm pol} = \Gamma^{\rm pol}\frac{1+\gamma_4}{2} = \Gamma^{\rm pol}$, we get

$$\begin{aligned}\left[S^{n\bar{p}}_{\bar{d}u}(0;x)\right]^{aa'}_{\alpha\alpha'} &= \Gamma^{\rm pol}_{\delta\delta'}\epsilon^{a'b'c'}\epsilon^{abc}\left[f_{\alpha'\beta'\gamma'\delta'} + f_{\beta'\alpha'\gamma'\delta'}\right]\left[\bar{f}_{\alpha\beta\gamma\delta} + \bar{f}_{\beta\alpha\gamma\delta}\right]\Big(- \mathcal{U}^{c'b}_{\gamma'\beta}\mathcal{D}^{b'c}_{\beta'\gamma}\Big) \\ &= \epsilon^{a'b'c'}\epsilon^{abc}\Big[\Gamma^{\rm pol}_{\alpha\alpha'}\big(S\mathcal{U}\big)^{bc}_{\beta\gamma}\big(\mathcal{D}S^*\big)^{bc}_{\beta\gamma} + \big(S\mathcal{U}\Gamma^{\rm pol}\big)^{ba'}_{\beta\alpha'}\big(\mathcal{D}S^*\big)^{ba}_{\beta\alpha} \\ &\quad - \big(S\mathcal{U}S^*\big)^{a'b}_{\alpha'\beta}\big(\Gamma^{\rm pol}\mathcal{D}\big)^{ab}_{\alpha\beta} + \big(S\mathcal{U}\Gamma^{\rm pol}\mathcal{D}S^*\big)^{a'a}_{\alpha'\alpha} + \big(S\mathcal{U}\big)^{a'b}_{\alpha'\beta}\big(\Gamma^{\rm pol}\mathcal{D}S^*\big)^{ab}_{\alpha\beta}\Big],\end{aligned}$$

where $\mathcal{U} = \langle u_x\bar{u}_0\rangle = \not{D}_u^{-1}(x,0)$ and $\mathcal{D} = \langle d_x\bar{d}_0\rangle = \not{D}_d^{-1}(x,0)$.

We leave it to the reader to check that the relation (3.35) holds.

3.2.3 Composite sources

In this section we would like to summarize briefly the problems of computing three-point functions with the composite sources discussed in Sec. 3.1.3. As we have described in Sec. 3.2.2 one must plan carefully the order of computing quark propagators and contracting them into two- and three-point correlators to maximize the useful output of a calculation. Generally, with simple ("factorizable") sources one has to compute one forward propagator and, separately, one backward propagator for each flavor and sink position (or, equivalently, sink spatial momentum). The parity projection $\frac{1+\gamma_4}{2}$ further reduces the number of inversions by a factor of two.

However, if one constructs a nucleon state with a composite nucleon operator, each term in Eq. (3.25) requires the calculation of a separate full set of inversions and contractions multiplying the cost by an integer factor. It is remarkable that the composite nucleon sink does not require additional computations except for smearing and computing contractions in the sequential sources $S_q^{(i)}$.

Thus, the most effective strategy is to use a composite nucleon sink and a simple nucleon source. Unfortunately, such approach will result in asymmetric plateaus even for forward matrix elements which are usually the "gold-plated" quantities computed on a lattice. One needs to implement a convoluted fitting procedure to extract nucleon matrix elements from such plateaus that takes into account the fact that the data points closer to the sink are more credible than those closer to the source.

In practice, however, calculations with an asymmetric source-sink pair may be the only reasonable choice to study the nucleon form factors at non-zero momentum transfer. According to the recent study in Ref. [LCE+10], optimal source parameters may depend on the momentum of a nucleon state. However, in the present calculations momentum projection is performed for sink and operator locations while the position of a source is fixed and thus contains all possible momenta. Hence, it is impossible to tune both the source and the sink to suppress the most dangerous excited states. Instead, tuning of the sink can be performed at each sink momentum separately with negligible additional cost required for separate smearing of quark propagators.

3.3 Form Factors

3.3.1 Transfer matrix expressions

In order to calculate nucleon matrix elements, we compute the three-point polarized nucleon correlators involving the vector current, along with the two-point correlators [H+08]:

$$C_{2\mathrm{pt}}(t,P) = \sum_{\vec{x}} e^{-i\vec{P}\cdot\vec{x}} \sum_{\alpha\beta} (\Gamma_{\mathrm{pol}})_{\alpha\beta} \langle N_\beta(\vec{x}\,,t)\bar{N}_\alpha(0\,,0)\rangle, \tag{3.37}$$

$$C^{\mathcal{O}}_{3\mathrm{pt}}(\tau,T;P,P') = \sum_{\vec{x},\vec{y}} e^{-i\vec{P}'\cdot\vec{x}+i\left(\vec{P}'-\vec{P}\right)\cdot\vec{y}} \sum_{\alpha\beta} (\Gamma_{\mathrm{pol}})_{\alpha\beta} \langle N_\beta(\vec{x}\,,T)\mathcal{O}(\vec{y},\tau)\bar{N}_\alpha(0,0)\rangle \tag{3.38}$$

where N_β, $\bar{N}_\alpha$ are the lattice nucleon operators; $\langle\Omega\,|N_\alpha(x)|\,P,\sigma\rangle = \sqrt{Z(P)}U^{(\sigma)}_\alpha(P)e^{-iPx}$, with $Z(P)$ parameterizing the overlap with the nucleon ground state; $(\Gamma_{\mathrm{pol}})_{\alpha\beta} = \frac{1+\gamma_4}{2}\frac{1-i\gamma_3\gamma_5}{2}$ is the spin and parity projection matrix[5]; and $\mathcal{O}$ is the operator in ques-

[5] In this subsection, we use Euclidean γ-matrices, $(\gamma^\mu)^\dagger = \gamma^\mu$, $\{\gamma^\mu,\gamma^\nu\} = 2\delta^{\mu\nu}$.

tion. In the transfer matrix formalism, these correlators take the form

$$C_{\text{2pt}}(t,P) = \frac{Z(P)e^{-Et}}{2E}\text{Tr}\left[\Gamma_{\text{pol}}\left(i\not{P}+M_N\right)\right] + \text{excited states}, \tag{3.39}$$

$$\begin{aligned} C^{\mathcal{O}}_{\text{3pt}}(\tau,T;P,P') = &\frac{\sqrt{Z(P')\cdot Z(P)}e^{-E'(T-\tau)-E\tau}}{2E'\cdot 2E}\times \\ &\times \text{Tr}\left[\Gamma_{\text{pol}}\left(i\not{P}'+M_N\right)\Gamma\left(P',P\right)\left(i\not{P}+M_N\right)\right] \\ &+ \text{excited states}, \end{aligned} \tag{3.40}$$

where E and E' are the ground state energies of the initial and final nucleon states and $\Gamma\left(P',P\right)$ is the vertex corresponding to an operator $\mathcal{O}$,

$$\langle N(P',S')|\mathcal{O}(0)|N(P,S)\rangle = \bar{U}(P',S')\Gamma(P',P)U(P,S), \tag{3.41}$$

which is parameterized with corresponding form factors, e.g. Dirac and Pauli form factors for the electromagnetic current operator. Excited state contributions have generally similar forms with different Z-factors, vertices and higher energies $E_{\text{exc}} > E$. The systematic effects related to them will be discussed in Sec. 3.4.

Equations (3.39,3.40) describe the evolution of an on-shell particle with energy $E = \sqrt{\vec{P}^2 + M_N^2}$ with the Euclidean time. After the Wick rotation, the Euclidean 4-momentum P must have an imaginary time component, resulting in

$$P^{\text{Euc}} = (\vec{P}, -iE) = (\vec{P}, -i\sqrt{\vec{P}^2 + M_N^2}). \tag{3.42}$$

Note that the polarization matrix $\left(i\not{P}+M_N\right)$ constructed with Euclidean γ-matrices (3.43) directly corresponds to the polarization matrix $\left(\not{P}^{\text{Mink}}+M_N\right)$ constructed from Minkowski 4-momentum and γ-matrices,

$$(\gamma_{1,2,3})^{\text{Euc}} = i(\gamma^{1,2,3})^{\text{Mink}}, \quad (\gamma_4)^{\text{Euc}} = (\gamma^4)^{\text{Mink}}, \quad (\gamma_5)^{\text{Euc}} \equiv \Gamma(15) \equiv (\gamma_1\gamma_2\gamma_3\gamma_4)^{\text{Euc}} = (\gamma_5)^{\text{Mink}}, \tag{3.43}$$

$$i\not{P}^{\text{Euc}} \equiv i(\sum_i P_i^{\text{Euc}}\gamma_i^{\text{Euc}}) = \not{P}^{\text{Mink}} \equiv (P^\mu\gamma_\mu)^{\text{Mink}} \equiv (E\gamma^0 - \vec{P}^{\text{Mink}}\cdot\vec{\gamma}^{Mink}) \tag{3.44}$$

3.3.2 Nucleon matrix elements

In order to extract nucleon matrix elements (3.41) we combine lattice nucleon correlators (3.39, 3.40) into the usual ratio of three- and two-point correlation functions [H+08], which we find useful to write in a convenient and illuminating new form as follows. First, we define two ratios, a *normalization ratio*, R_N, and an *asymmetry ratio*, R_A,

$$R_N \equiv \frac{C^{\mathcal{O}}_{3\text{pt}}(\tau, T; P, P')}{\sqrt{C_{2\text{pt}}(T, P) C_{2\text{pt}}(T, P')}}, \tag{3.45}$$

$$R_A \equiv \sqrt{\frac{C_{2\text{pt}}(T-\tau, P) C_{2\text{pt}}(\tau, P')}{C_{2\text{pt}}(T-\tau, P') C_{2\text{pt}}(\tau, P)}}. \tag{3.46}$$

The physical matrix element is then given by the product

$$\begin{aligned} R^{\mathcal{O}} \equiv R_N R_A &= \frac{C^{\mathcal{O}}_{3\text{pt}}(\tau, T; P, P')}{\sqrt{C_{2\text{pt}}(T, P) C_{2\text{pt}}(T, P')}} \sqrt{\frac{C_{2\text{pt}}(T-\tau, P) C_{2\text{pt}}(\tau, P')}{C_{2\text{pt}}(T-\tau, P') C_{2\text{pt}}(\tau, P)}} \\ &\xrightarrow{\{T,\, \tau,\, T-\tau\} \to \infty} \frac{\sum_{S,S'} \left(\bar{U}(P,S) \Gamma_{\text{pol}} U(P',S') \right) \cdot \langle P', S' | \mathcal{O} | P, S \rangle}{\sqrt{2E(E+M_N) \cdot 2E'(E'+M_N)}}. \end{aligned} \tag{3.47}$$

The normalization ratio R_N has the property that all the lattice-dependent overlap factors Z for the ground state cancel out, which motivates its name, and in the case of *forward* matrix elements $P = P'$ it yields the final result for the corresponding matrix element. The asymmetry ratio R_A compensates the asymmetric exponential τ dependence of the three-point correlator, thus motivating its name. In the absence of excited states, it would be equal to $\exp\left[-(E'-E)(\tau - T/2)\right]$ and in the forward case, $P' = P$, this ratio is trivial and equal to one, $R_A(\tau)\big|_{P'=P} \equiv 1$. In the general case, $P' \neq P$, this ratio is still identically one in the center of the plateau, $\tau = T/2$, and by construction possesses the following symmetry around the plateau center: $R_A(T-\tau) = 1/R_A(\tau)$.

The limits $\{T,\ \tau,\ T-\tau\} \to \infty$ should be taken to get rid of excited state contaminations. In practice, this requires adopting a value of source-sink separation T large enough so that the excited state contributions to Eq. (3.47) are negligible com-

pared to the other sources of errors and using only points that are close to the center of plateaus. We will explicitly explore the contributions of excited states to $R^{\mathcal{O}}$ in Sec. 3.4, where the decomposition into the product $R_N R_A$ will prove extremely useful.

Table 3.2: A set of momentum combinations satisfying $|p_i| \leq 1$ for the high precision form factors.

#	$\langle$out$\|$in$\rangle$	Q^2 [GeV^2]
1	$\langle 0,0,0\|0,0,0\rangle$, $\langle -1,0,0\|-1,0,0\rangle$	0.0
2	$\langle 0,0,0\|1,0,0\rangle$, $\langle -1,0,0\|0,0,0\rangle$	0.203
3	$\langle -1,0,0\|-1,0,1\rangle$	0.204
4	$\langle 0,0,0\|1,1,0\rangle$	0.391
5	$\langle -1,0,0\|-1,1,1\rangle$	0.395
6	$\langle -1,0,0\|0,0,1\rangle$	0.422
7	$\langle 0,0,0\|1,1,1\rangle$	0.568
8	$\langle -1,0,0\|0,1,1\rangle$	0.626
9	$\langle -1,0,0\|1,0,0\rangle$	0.844
10	$\langle -1,0,0\|1,1,0\rangle$	1.048

In order to obtain the most precise information on the form factors, one may constrain the in- and out- lattice nucleon momenta to have components $0, \pm 1$. A list of such momentum combinations (one representative for each group with respect to spatial symmetry) is given in Table 3.2, together with the corresponding momentum transfer values Q^2 for the fine *Domain Wall* lattice with $m_\pi = 297$ Mev. Higher momentum components are subject to stronger finite lattice spacing effects, i.e., discretization errors and dispersion relation deviations from the continuum expression. There is also an indication (see Sec. 3.4.1) that such states have larger excited state contaminations.

3.3.3 Overdetermined analysis of form factors

The nucleon matrix elements computed in Sec. 3.3.2 are parameterized by linear combinations of form factors. These form factors depend only on Lorentz-invariant momentum transfer $Q^2 = -(P' - P)^2$. At any fixed Q^2, there is usually a set of nucleon matrix elements corresponding to different in- and out-momenta and/or operator components, e.g., the four components of the vector current. Hence, for this

usual case of multiple matrix elements, one can extract form factor values by solving an overdetermined system of equations. This is best demonstrated with the vector current form factors, Dirac F_1 and Pauli F_2,

$$\Gamma^{\mu}(P', P) = F_1(Q^2)\gamma^{\mu} + F_2(Q^2)\frac{i\sigma^{\mu\nu}q_{\nu}}{2M_N}, \quad q = P' - P, \quad Q^2 = -q^2. \tag{3.48}$$

Transforming the above expression to Euclidean space and substituting it into Eq. (3.40) and then Eq. (3.47) and neglecting the excited states, we obtain an overdetermined system of equations for the form factors $F_{1,2}(Q^2)$:

$$A_{\alpha 1}F_1 + A_{\alpha 2}F_2 = R_{\alpha}^{V_{\mu}}, \tag{3.49}$$

where α is a composite index specifying the component of the current, "μ", and the initial and final nucleon momenta. The right-hand side in Eq. (3.49), R_{α}, is a set of matrix elements evaluated using Eq. (3.47) from nucleon correlators computed on a lattice.

We find the solution of the overdetermined system (3.49) from a linear fit, which minimizes the functional

$$\mathcal{F} = \sum_{\alpha\beta} \left(A_{\alpha i}F_i - R_{\alpha}\right) C^{-1}_{\alpha\beta} \left(A_{\beta j}F_j - R_{\beta}\right), \tag{3.50}$$

where $C_{\alpha\beta}$ is the estimation of the covariance matrix of R_{α},

$$C_{\alpha\beta} = \frac{1}{N-1}\left(\langle\langle R_{\alpha}R_{\beta}\rangle\rangle - \langle\langle R_{\alpha}\rangle\rangle\langle\langle R_{\beta}\rangle\rangle\right), \tag{3.51}$$

with the double brackets denoting an ensemble average. Using the covariance matrix is crucial because the lattice correlation functions are often correlated.

Since the estimated covariance matrix may be ill-determined, it can introduce uncontrollable errors into the extracted form factors. In general, a covariance matrix is notoriously difficult to estimate reliably in statistical analyses. To make sure the linear fitting gives correct result, we repeat the analysis with only the diagonal elements of

the covariance matrix $C_{\alpha\alpha}$, which is equivalent to an uncorrelated linear fit. The comparison of these two schemes is presented in Fig. 3-5, for a fine *Domain Wall* lattice with $m_\pi = 297$ MeV. We find that the form factors determined with the uncorrelated fit ("*uncorr*") are consistent with the results from the correlated fits ("*full*").

The overdetermined system (3.49) contains a subclass of equations which have an exactly zero left-hand side: $A_{\alpha i} = 0$, $i = 1, 2$. The computed lattice value of the right-hand side R_α is not required to be zero identically. In an uncorrelated fit, such equations decouple and do not contribute to the solution. In contrast, the correlated fit result depends on the r.h.s. of such equations because of the correlation matrix, and thus utilizes the input from lattice calculations better. In addition, by fitting the equations with a vanishing left-hand side, we check the symmetries of the electromagnetic vertex (3.48) statistically. Figure 3-5 also shows the agreement of the full overdetermined system solution ("*full*") and the system without zero left-hand side equations ("*non-zero*"), confirming the consistency of our analysis.

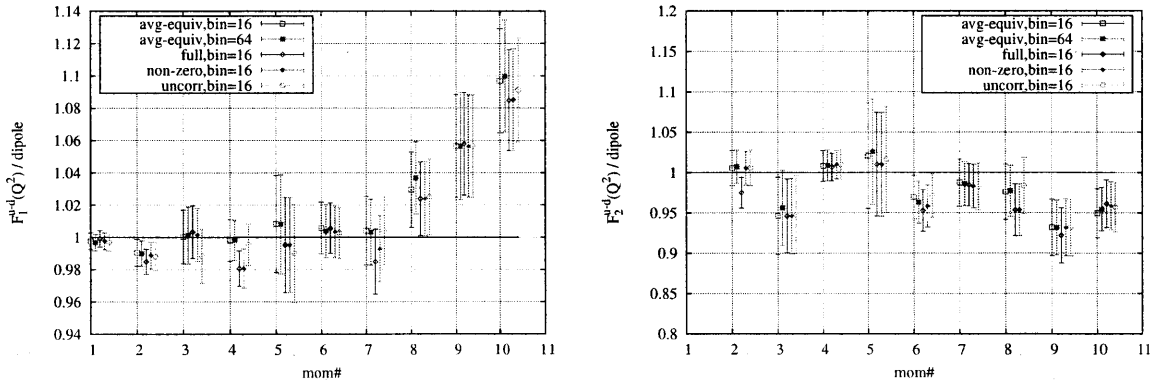

(a) Dirac F_1 form factor

(b) Pauli F_2 form factor

Figure 3-5: Comparison of the nucleon isovector form factors extracted from the *full* overdetermined system, only *nonzero* equations, *uncorrelated* fit the system with averaged equivalent equations (*avg-equiv*), for the momentum combinations listed in Tab. 3.2. These types of analysis are also described in the text.

The dimension of the overdetermined system may be large, especially when many momentum combinations are included. For example, the most precise point for $Q^2 > 0$ corresponds to the matrix element $\langle 0,0,0 | V^\mu(0) | 1,0,0 \rangle$. Including all V^μ

components, together with spatial rotations and reflections gives 48 equations, only 16 of which are nonzero. It is useful to combine all the nucleon matrix elements for each fixed Q^2 into equivalence classes based on the spatial (rotational and reflection) symmetry. We adopted the following heuristic *equivalence* criteria[6] for three-point functions:

1. The momenta of in- and out-states must be equivalent under the spatial symmetry.

2. The corresponding coefficients $A_{\alpha i}$ in Eq. (3.49) must be equal up to an overall sign.

3. The components of the current operator must be both temporal or both spatial and both real or both imaginary parts of a matrix element.

Blocking the three-point correlators within equivalence classes is advantageous for two reasons. First, this reduces the dimension of the system of equations (3.49) and the covariance matrix we need to estimate, and we note that blocking strongly correlated values improves the covariance matrix condition number. Second, we may block the three- and two-point correlators separately *before* computing the ratio (3.47). Doing so improves the ratio method in Eq. (3.47) by reducing the fluctuations of the denominator because of the two-point correlators. We compare the form factor extraction results using this method ("*avg-equiv*") to other methods in Fig. 3-5 and find that this averaging does not introduce any systematic errors.

The main method we use to extract the final set of the form factors is the correlated fit to the reduced (i.e., the system with no equations whose left-hand side is zero) overdetermined system with blocked equivalent equations.

[6] We did not classify the matrix elements according to the hypercubic lattice symmetry. Instead we use the relations derived in the continuum theory. Thus these criteria may be thought of as numerical means to improve the condition number of a linear system we need to solve.

3.4 Role of excited states

The lattice matrix elements may have systematic bias due to the excited and/or unphysical oscillating states [SN07, LBO+08, OY08] present in two- and three-point correlators. The oscillating states appear because there is no transfer matrix for the *Domain Wall* action [SN07]. To control it, we solve the overdetermined system separately for each location of the operator and examine the plateau for the extracted form factors. Examples are shown in Fig. 3-6. Because of the tuning of the quark sources, the contributions from contaminating states to the matrix element plateaus close to their centers are suppressed and very small.

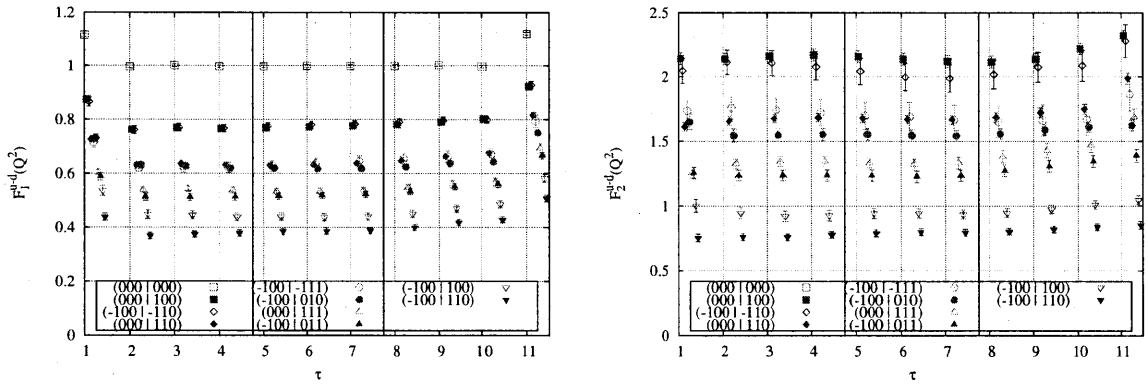

(a) Dirac form factor F_1

(b) Pauli form factor F_2

Figure 3-6: Nucleon isovector form factor plateaus for the lightest $m_\pi = 297\,\mathrm{MeV}$ ensemble.

Analyzing plateaus is usually reduced to observing that they have little curvature from decaying "tails" from the source and the sink. This method has two problems. First, there is no figure of merit that could tell us if a particular plateau is good enough to be credible. Second, the form of the plateau provides little information about contributions which are not tail-like but are suppressed by the total separation between nucleon operators, $\sim e^{-aT}$, $T = t_{\mathrm{snk}} - t_{\mathrm{src}}$.

A method to ensure that excited state contaminations present no problem is to compute three-point correlators with a number of different separations $T = t_{\mathrm{snk}} - t_{\mathrm{src}}$. However, doing so requires proportional increase in the cost of the calculations. In addition, the discrepancy between the results with different separations T can

be hidden by larger stochastic errors at larger T, and one will have to quote the uncertainties from the calculation with the largest separation, thus making precise, small separation calculations useless.

Instead of comparing different separations T, we analyze the lattice data at a fixed separation to understand how big the excited contaminations are. In Section 3.4.1 we estimate such contaminations from a simple model and in Section 3.4.2 we fit the plateaus directly.

3.4.1 Two-state model

To put quantitative bounds on excited state contributions to the matrix elements, we study first the excited states in the nucleon correlators. The nucleon two-point correlation functions have less stochastic variation and thus can provide very precise information on the presence of states other than ground. For example, with our current statistics the parameters of a fit with three states can be constrained very well:

$$C_{2\mathrm{pt}}(t;P) = Z_0(P)e^{-E_0 t} + Z_1(P)e^{-E_1 t} + (-1)^t Z_{\mathrm{osc}}(P)e^{-E_{\mathrm{osc}} t}, \quad Z_{0,1} > 0, \qquad (3.52)$$

where Z_0, Z_1, and Z_{osc} denote the overlaps of the nucleon interpolating field with the ground, the first excited and the unphysical oscillating states, respectively. Having estimated the energy gap $\Delta E_{10}(P) = E_1(P) - E_0(P)$ and the magnitude of the contamination $Z_1(P)/Z_0(P)$, one can put bounds on the excited state contribution to the matrix elements computed from the two- and three-point lattice nucleon correlators.

The ratio formula (3.47) for physical matrix elements has two factors: $R^{V^\mu} \equiv R_N R_A$. Excited states can potentially contribute to either one. First, we study the asymmetry ratio, R_A, defined in Eq. (3.46). As was pointed out above, this factor compensates the asymmetric τ dependence in R_N, and in the absence of excited states it would be equal to $\exp\left[-(E' - E)(\tau - T/2)\right]$. Although this factor involves different two-point functions, their excited state contributions appear to cancel each other to a large extent, as shown in Fig. 3-7. Figure 3-7(a) shows the ratio of R_A to

the exponential result in the absence of excited states

$$\frac{R_A(\tau)}{e^{-(E'-E)(\tau-T/2)}} = \frac{\sqrt{\frac{C_{2\mathrm{pt}}(T-\tau,P)C_{2\mathrm{pt}}(\tau,P')}{C_{2\mathrm{pt}}(T-\tau,P')C_{2\mathrm{pt}}(\tau,P)}}}{e^{-(E'-E)(\tau-T/2)}}, \tag{3.53}$$

where $(E'-E)$ in the denominator is determined by the best fit to R_A in the range $3 \leq \tau \leq 6$. The fact that this ratio is unity within 1% over the plateau in the range $3 \leq \tau \leq 9$ indicates that excited state contributions are negligible. Furthermore, Figure 3-7(b) shows the effective ground state energy difference

$$\delta E^{\mathrm{eff}}(t) = \log\left[\frac{C_{2\mathrm{pt}}(t,P')}{C_{2\mathrm{pt}}(t+1,P')} \Big/ \frac{C_{2\mathrm{pt}}(t,P)}{C_{2\mathrm{pt}}(t+1,P)}\right], \tag{3.54}$$

which in the absence of any excited state contaminants, would simply be $\delta E^{\mathrm{eff}}(t) = (E'-E)$. For comparison, the values of $E'-E$ determined above are plotted on the same graph, and agree nicely in the fiducial range $2 \leq \tau \leq 10$. Thus, we neglect small contaminations from this factor.

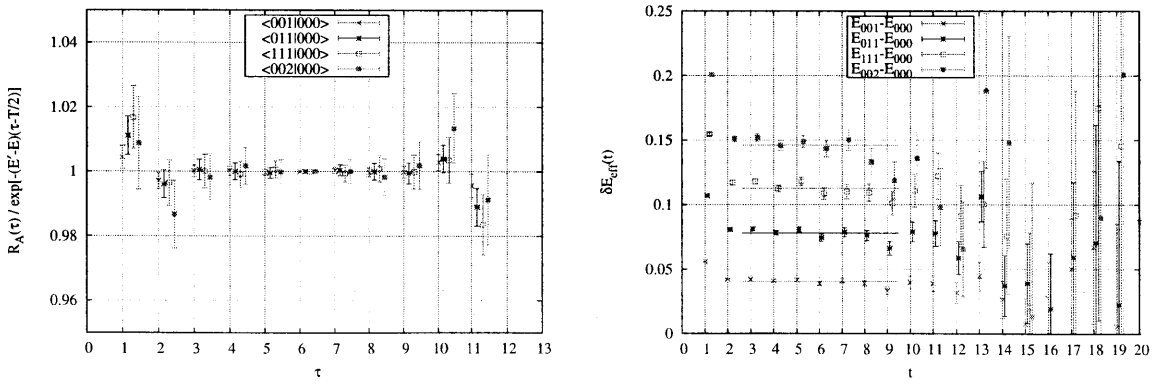

(a) Ratio $A(\tau)$ in Eq. (3.53)

(b) Effective energy difference (3.54) in lattice units and the fit values of $E'-E$ used in panel (a)

Figure 3-7: Illustration of remarkable cancellation between contaminations in all $\vec{P}' \neq \vec{0}$ and $\vec{P} = \vec{0}$ two-point correlators.

Second, we estimate the contribution to R_N defined in Eq. (3.45) assuming only

one excited state and no oscillating term[7]:

$$C_{3\mathrm{pt}}(\tau,T) \approx C_{3\mathrm{pt}}(\tau,T)|_0 \left[1+\sqrt{\frac{Z_1}{Z_0}}\frac{\mathcal{O}_{0'1}}{\mathcal{O}_{0'0}}e^{-\Delta E\tau}+\sqrt{\frac{Z_1'}{Z_0'}}\frac{\mathcal{O}_{1'0}}{\mathcal{O}_{0'0}}e^{-\Delta E'(T-\tau)}\right.$$
$$\left.+\sqrt{\frac{Z_1'Z_1}{Z_0'Z_0}}\frac{\mathcal{O}_{1'1}}{\mathcal{O}_{0'0}}e^{-\Delta E'(T-\tau)-\Delta E\tau}\right],$$
$$\frac{C_{3\mathrm{pt}}(\tau,T)}{\sqrt{C_{2\mathrm{pt}}(T)C'_{2\mathrm{pt}}(T)}} \approx \left(\frac{C_{3\mathrm{pt}}(\tau,T)}{\sqrt{C_{2\mathrm{pt}}(T)C'_{2\mathrm{pt}}(T)}}\right)_0 \times \left[1+\frac{\mathcal{O}_{0'1}}{\mathcal{O}_{0'0}}\delta R_{10}(\tau)+\frac{\mathcal{O}_{1'0}}{\mathcal{O}_{0'0}}\delta R'_{10}(T-\tau)\right.$$
$$\left.+\frac{\mathcal{O}_{1'1}}{\mathcal{O}_{0'0}}\delta R_{10}(\tau)\delta R'_{10}(T-\tau)-\frac{1}{2}\left(\delta R_{11}+\delta R'_{11}\right)\right], \tag{3.55}$$

where

$$\delta R_{10}^{(\prime)}(\tau)=\sqrt{\frac{Z_1^{(\prime)}}{Z_0^{(\prime)}}}e^{-\Delta E^{(\prime)}\tau}, \qquad \delta R_{11}^{(\prime)}=\frac{Z_1^{(\prime)}}{Z_0^{(\prime)}}e^{-\Delta E^{(\prime)}T}=\left[\delta R_{10}^{(\prime)}(T/2)\right]^2, \tag{3.56}$$

and we have expanded Eq. (3.45) assuming that $\delta R_{11}^{(\prime)} \ll 1$. The value of the suppression factor $\delta R_{10}^{(\prime)}(\tau)$ is shown in Fig. 3-8. Its values are estimated using parameters $Z_{0,1}$, $E_{1,0}$ from the fit using Eq. (3.52), and the errors are computed using the jackknife procedure. It is remarkable that $\delta R_{10}^{(\prime)}(\tau)$ falls off steeply with τ. As a result, its contribution can be easily detected and removed by fitting the plateau with

$$R^{\mathcal{O}}(\tau) \approx C_0 + C_1 e^{-\Delta E\tau} + C_1' e^{-\Delta E'(T-\tau)}. \tag{3.57}$$

From Fig. 3-8 one may estimate the last two terms in the contamination formula (3.55), suppressed by $\delta R_{11}^{(\prime)}$ and $\delta R_{10}(\tau)\delta R'_{10}(T-\tau)$. If one assumes further that the excited state matrix elements are at most of the same order as the ground state matrix elements, $\frac{\mathcal{O}_{1'1}}{\mathcal{O}_{0'0}} \lesssim 1$, the effect of the last two terms in Eq. (3.55) is well below 1%. It is also worth noting that higher momentum matrix elements with $\vec{p}=(0,0,2)$ may contain substantially larger contamination, as compared to lower momentum matrix

[7] We neglect the contribution of oscillating states because they decay even faster than excited states.

elements. Such matrix elements are excluded from our analysis.

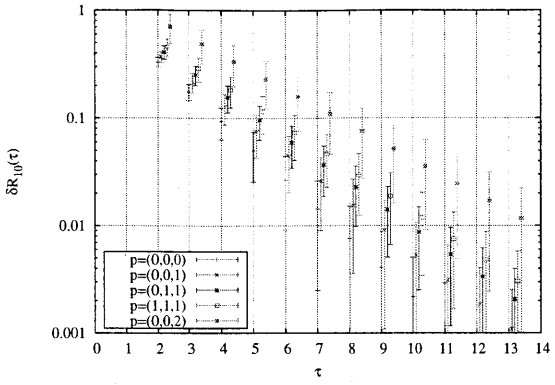

Figure 3-8: Suppression factor for the excited state contributions $\delta R_{10}(\tau)$ (3.56), as estimated from fitting the two-point function.

3.4.2 Plateau fits

Finally, we compare the form factors extracted using the plateau average with those from fitting the τ dependence to Eq. (3.57). Because of the uncertainty in the two-point correlator fitting parameters, we perform fits for a range of mass gaps $\Delta M_N =$ 0.4, 0.6 and 0.8 (see also Sec. 3.1.3), which bracket the fitted values from different fitting ranges and fitting with or without the oscillating term in Eq. (3.52). The energy gaps ΔE for the $\vec{P} \neq 0$ states are computed using the continuum dispersion formula $E = \sqrt{M_N^2 + \vec{P}^2}$ for both the ground and the excited states. The result is statistically independent of the mass gap value used (see Fig. 3-9) and is stable when fitting inside the region $2 \leq \tau \leq 10$. The complete consistency between conventional plateau averages and results from the analysis with excited state contaminants separated from the physical ground state contribution clearly indicates the absence of systematic errors from excited state contaminants in our present results.

In addition, we also compare the results of the calculations with two different source-sink separations, $T = 12$ and $T = 14$. We expect that the noise from the coherent sink technique [B$^+$10], if any, is worse for the larger T, for which an unwanted adjacent sink is closer. Hence, in the case of $T = 14$, we have used independent backward propagators to check that this is not a problem. The typical plateaus for

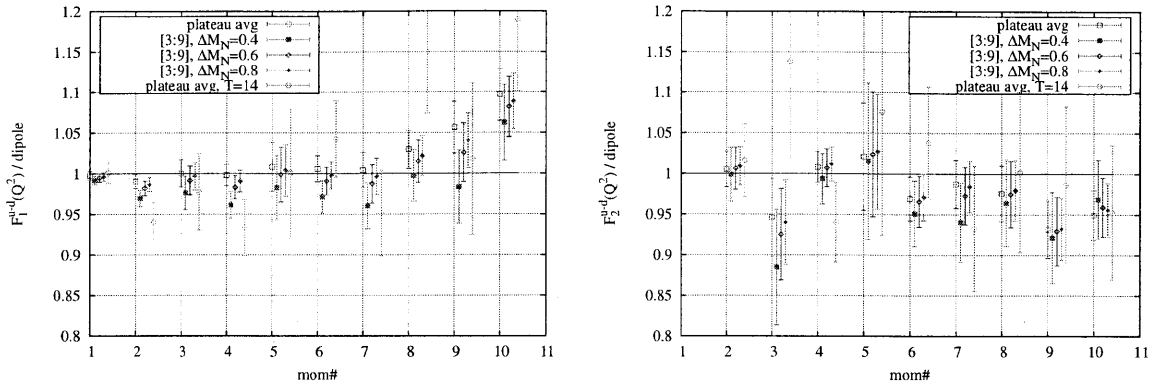

(a) Dirac F_1 form factor

(b) Pauli F_2 form factor

Figure 3-9: Comparison of the isovector nucleon form factors extracted from plateau averages and from fitting plateaus to the formula (3.57). Results are computed on a fine *Domain Wall* lattice with $m_\pi = 297$ MeV, with $T = 12$ and $T = 14$ Euclidean time separations. Horizontal axis corresponds to momentum combinations listed in Tab. 3.2.

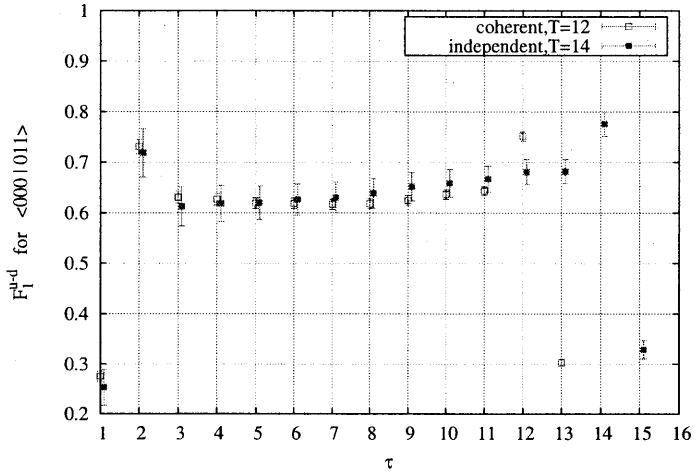

Figure 3-10: Comparison of F_1^{u-d} plateau using coherent backward propagators with $T = 12$ and independent backward propagators with $T = 14$. The momentum transfer Q^2 corresponds to $\langle 000|011\rangle$.

$T = 12$ and $T = 14$ separations computed on a subset of the fine *Domain Wall* lattice with $m_\pi = 297$ MeV ensemble are shown in Fig. 3-10 and they demonstrate agreement within statistics. The results (plateau averages) for the vector form factors for different momentum transfer Q^2 with separations $T = 12$ and 14 are also compared in Fig. 3-9 above. The agreement of results using two different separations and techniques directly indicates that our method does not suffer from the systematic

effects due to excited states or the coherent propagator technique [B+10].

Summary

The procedure summarized above enables construction of states on a lattice that reproduce the nucleon ground state to the precision necessary for computing nucleon matrix elements. We find out that nucleon excited states and states with wrong quantum numbers can be suppressed by a combination of methods, and the parameters can be tuned for each gauge configuration ensemble. In addition, we can estimate and set an upper bound on the systematic errors coming from excited states. Finally, we point out that development of additional techniques to create nucleon states on a lattice may be required as lattice calculations approach the physical pion mass.

Chapter 4

Renormalization of Lattice Quark-Bilinear Operators

In this section we discuss how the nucleon structure observables calculated on a lattice should be renormalized before comparing with experimental results. Generally, it requires matching between lattice and continuum calculations quark correlators. In Section 4.1 we discuss some general aspects of renormalization of lattice observables. We mention briefly the renormalization using lattice perturbation theory in Sec. 4.1.1, and proceed to the nonperturbative renormalization methods in Sec. 4.2, which is used as the main method in this work. We present the details of matching between continuum and lattice observables in Section 4.3, and analyze possible sources of systematic bias arising from this matching. The final numbers for lattice renormalization coefficients are collected in Appendix C.

4.1 General aspects of renormalization

4.1.1 Linking lattice calculations and experiment

Lattice QCD is a gauge theory regularized by the introduction of a space-time lattice, making path integrals finite-dimensional. Generally an operator constructed on a lattice requires renormalization since their computed matrix elements are bare values

with fixed ultraviolet cutoff determined by the inverse lattice spacing $\Lambda_{\rm lat} = a^{-1}$. To make comparisons to experimental values possible, one has to convert these values to an appropriate renormalization scheme, which is usually the $\overline{\rm MS}$ scheme at the scale $\mu^2 = (2{\rm GeV})^2$ widely used in phenomenology.

One possible approach to this problem is to compare perturbative calculations in lattice and continuum theories. While the perturbation theory in continuum QCD is well-developed and boasts calculations up to four loops, the perturbative computations in lattice QCD are much more complex. So far, most of lattice perturbative calculations are limited to one loop. This limitation is especially bad because one usually has a rather small ultraviolet cutoff; current lattice simulations are performed with lattice spacing values $a^{-1} \lesssim 4$ GeV. One might worry that the strong coupling α_S at this scale is large, and the convergence of lattice perturbation calculations is expected to be slow, invalidating one-loop calculations. In addition, it is very hard to estimate the systematic effects due to perturbative series truncation [B$^+$10].

The convergence of perturbative renormalization factors may be improved by the tadpole improvement of perturbation theory [LM93]. For example, the one-loop perturbative renormalization factors were computed for mixed action calculations [Bis05]. Below in this chapter we will compare the calculation in Ref. [Bis05] to the nonperturbative calculation (see Sec. 4.4).

4.1.2 Mixing of lattice operators

Under renormalization, different lattice operators can mix with each other. In this section we discuss what consequences this mixing may have for our calculations and how it can be avoided.

Firstly, there is *physical* mixing between flavor-singlet quark and gluon contributions to the nucleon structure observables, e.g., nucleon momentum, angular momentum and structure functions. In the DGLAP evolution equations this corresponds to the mixing of quark and gluon distribution functions, if the former are not protected by conservation laws[1]. For proper renormalization of the quark contribution

[1] This is not the case for the isovector components, e.g. $u(x) - d(x)$ which is protected by the

to the nucleon structure the gluon counterpart which mixes with it must also be computed. However, because of the stochastic noise associated with fluctuations in the gluon field, the gluon contributions requires roughly the same computational resources as disconnected diagrams and therefore have been neglected in this work. Therefore, presently we have to *neglect* the mixing of quark and gluon observables. The uncertainty because of quark-gluon mixing is relevant only to isosinglet quark observables. Since the isosinglet channel has also uncertainty from the disconnected contractions (see Sec. 3.2), we find it useful to concentrate on isovector observables, which do not have such complications, and treat the results for isoscalar observables as approximate.

Secondly, the lattice regularization reduces the rotational symmetry, as was discussed in Sec. 2.4. This results in irreducible "spin" representations of $SO(4)$ breaking up into a finite number of representations of the hypercubic group $H(4)$ [G$^+$96a]. If operators of different spins and/or dimensions have components in the same $H(4)$ representation they can mix; this mixing is unphysical and a pure lattice artifact. In our study, we compute the matrix elements of twist-2 operators, which are the series of operators with growing dimension and spin. In the continuum, these operators are protected from mixing because they belong to different representations of $SO(4)$. On a lattice, however, the number of representations of the lattice "rotation group" $H(4)$ is finite, and the higher-dimensional operators will imminently mix with lower-dimensional operators. The mixing coefficient is necessarily dimensionful and determined by the lattice cutoff $\Lambda_{\text{lat}} = a^{-1}$ and it diverges in the continuum limit [BBCR95, G$^+$96b] prohibiting reliable calculation of higher-dimensional operators on a lattice [G$^+$96a]. Practically, we are limited to computing the twist-2 operators up to dimension $d = 6$. For the operators with $d \leq 6$ we have to choose carefully the $H(4)$ representations to avoid mixing [D$^+$02, H$^+$03].

In principle, it is possible to find the mixing coefficients nonperturbatively and subtract the lower-dimensional contributions as was done in Ref. [G$^+$05a].

---

isospin conservation.

4.1.3 Special cases of lattice renormalization

In some special cases the renormalization of lattice operators is not required or is very simple. For example, in the computation of vector form factors one can use the forward value of the Dirac form factor as the renormalization factor. Because the vector current is conserved, the total charge $g_V = F_1^{\rm ren}(0)$ is determined by the number of valence quarks. Thus, renormalizing the vector current $\bar{q}\gamma^\mu q$ is trivial:

$$\langle N|J^\mu_{\rm ren}|N\rangle = \frac{Q_{\rm val}}{F_1^{\rm lat}(0)}\langle N|\left[\bar{q}\gamma^\mu q\right]_{\rm lat}|N\rangle, \tag{4.1}$$

where $Q_{\rm val}$ is the total charge of the valence quarks in the state $|N\rangle$. Although we say that the vector current is conserved, its particular lattice representation may still have multiplicative renormalization. There is, of course, the *true* conserved current generated by the $U(1)_V$ symmetry of the action, but it usually involves fermion fields from several lattice sites, i.e., it is not *site-local*, and it is inconvenient for numerical reasons. Instead of it, one usually employs the *site-local* current $\bar{\psi}_x\gamma^\mu\psi_x$ and renormalizes it with Eq. (4.1).

In the case of Wilson(-Clover) fermions, the conserved current has the form

$$\mathcal{V}^{Wilson}_{x,\mu} = \bar{\psi}_{x+\hat{\mu}}U^\dagger_{x,\mu}\frac{1+\gamma_\mu}{2}\psi_x - \bar{\psi}_x U_{x,\mu}\frac{1-\gamma_\mu}{2}\psi_{x+\hat{\mu}}, \tag{4.2}$$

for which one may directly check using the equations of motion for ψ following from Wilson(-Clover) action (2.19,2.20) that its divergence is zero,

$$(\nabla_\mu\mathcal{V}_\mu)_x = \sum_\mu\left[\mathcal{V}_{x,\mu} - \mathcal{V}_{x-\hat{\mu},\mu}\right] = 0, \qquad \text{[eqn. of motion]} \tag{4.3}$$

and the correlators with this current operator satisfy the corresponding Ward identity. Using the Ward identity for the conserved current, one can show that $Z_\mathcal{V} \equiv 1$ in the lattice gauge theory with Wilson(-Clover) fermion action. As we will see below in Sec. 4.2, in the nonperturbative renormalization method one can extract the quark field renormalization Z_ψ using the fact that the conserved current is not renormalized.

Another important case of renormalization is the 5D partially-conserved axial current of domain wall fermions. As we have seen in Sec. 2.3.3, one can construct the axial current $\mathcal{A}_\mu$ which is partially conserved. This current should also satisfy the corresponding Ward identity and have no renormalization, $Z_\mathcal{A} \equiv 1$. However, because of an effect of the residual mass, this equality is not satisfied identically [Sha07]. In Ref. [A$^+$08a] this effect was analyzed and it was found that $|Z_\mathcal{A} - 1| \lesssim 1\%$. For our current level of precision of results discussed in Chapter 5 such accuracy is definitely adequate.

4.2 Nonperturbative approach to renormalization

The main idea of nonperturbative renormalization is to compute the Green functions of operators and quark fields both in the continuum and lattice field theory with *the same renormalization condition.* Since the $\overline{\text{MS}}$ scheme is tied with dimensional regularization and cannot be realized on a lattice, a special (modified) momentum subtraction-like scheme is used for transformation from the lattice to the continuum.

This scheme, called RI′-MOM [MPS$^+$95], has been well described in the literature [MPS$^+$95, B$^+$02]. In addition to fixing the external bare quark and operator momenta, one fixes the Landau gauge. Both these conditions are easy to implement on a lattice. The matching coefficients between RI′-MOM and $\overline{\text{MS}}$ schemes in the continuum field theory have been computed with 3 loops of perturbation theory [Gra03a]. Thus, the final matching between the operators renormalized in RI′-MOM and $\overline{\text{MS}}$ schemes is straightforward, and will be discussed in Sec. 4.3.

In this section we summarize the nonperturbative renormalization method and illustrate it with the calculations on a *Domain Wall* ensemble configurations.

4.2.1 Rome-Southampton method

First, we summarize our conventions for the renormalization coefficients:

$$\mathcal{O}^R(\mu) = Z_{\mathcal{O}}(\mu, a)\mathcal{O}^{\text{lat}}(a), \tag{4.4}$$

$$\psi^R(\mu) = \sqrt{Z_\psi(\mu, a)}\psi^{\text{lat}}(a), \tag{4.5}$$

$$m_q^R = Z_m(\mu, a)m_q^{\text{lat}}(a). \tag{4.6}$$

Note that these definitions agree with [Gra03a, Gra06] for operator and renormalization constants $Z_{\mathcal{O}}$. This choice also agrees with the conventions adopted in the initial [MPS+95] and subsequent works on the nonperturbative renormalization in lattice QCD.

To find the nonperturbative renormalization constants for lattice operators, one has to compute on a lattice their amputated correlators with quark fields following the prescription of RI′-MOM-scheme. In this scheme, the in- and out-quarks have the same off-shell momentum[2] $p = p'$ determining the scheme scale, $\mu^2 = p^2$. It is understood that the scale is in the window $\Lambda^2_{QCD} \ll \mu^2 \ll \Lambda^2_{\text{lat}} = a^{-2}$ because, on one hand, the scale must be above the non-perturbative regime and, on the other hand, low enough to suppress discretization errors. As we will see in Sec. 4.4, sometimes such a window does not exist.

[2] Note that in such a scheme the operator insertion momentum is zero. This may lead to ill-behaved correlators, for example, pseudoscalar density $\bar{q}\gamma_5 q$ [S+09]. In this work we neglect such effects because we renormalize only the twist-two Wilson operators.

One proceeds by computing the following Fourier-transformed correlators:

$$S^{\text{lat}}(x,p) = \sum_y \langle q_x \bar{q}_y \rangle e^{ipy} = \sum_y \langle \not{D}^{-1}(x,y) \rangle e^{ipy}, \tag{4.7}$$

$$S^{\text{lat}}(p) = \frac{1}{V} \sum_{x,y} \langle q_x \bar{q}_y \rangle e^{ip(y-x)} = \frac{1}{V} \sum_{x,y} \langle \not{D}(x,y) \rangle e^{ip(y-x)}, \tag{4.8}$$

$$G_\Gamma^{\text{lat}}(p) = \frac{1}{V} \sum_{x,y,z} \langle q_x \left[\bar{q}\Gamma q\right]_z \bar{q}_y \rangle e^{ip(y-x)} = \frac{1}{V} \sum_{x,y,z} \langle \gamma_5 \left[\not{D}^{-1}(z,x)\right]^\dagger \gamma_5 \Gamma \not{D}^{-1}(z,y) \rangle e^{ip(y-x)}, \tag{4.9}$$

$$\Lambda_\Gamma^{\text{lat}}(p) = (S^{\text{lat}})^{-1}(p) G_\Gamma^{\text{lat}}(p) (S^{\text{lat}})^{-1}(p), \tag{4.10}$$

where Λ^{lat} is the amputated Green function for off-shell quarks. The propagator $z \leftarrow e^{ipx}$ with a plane-wave source is reused to compute both correlators (4.8,4.9). In such a computational scheme we have to compute a separated propagator for each momentum p, however the gain in statistics from the volume averaging is so large that 20-50 gauge configurations are sufficient to achieve negligible stochastic variation. In addition, the correlators with non-site-local operators can be computed.

Remembering the definitions in Eqs.(4.4-4.6), for a simple site-local operator $\mathcal{O}_\Gamma = \bar{q}\Gamma q$ we obtain the following renormalization condition:

$$\frac{Z_\Gamma}{Z_\psi} \Lambda_\Gamma^{\text{lat}}(p) = \Gamma, \quad \left(\frac{Z_\psi}{Z_\Gamma}\right)_p^{\text{lat}} = \frac{\text{Tr}\left[\Lambda_\Gamma^{\text{lat}}(p) \cdot \Gamma\right]}{\text{Tr}\left[\Gamma \cdot \Gamma\right]}. \tag{4.11}$$

For a multi-component operator $\mathcal{O}_{\Gamma,i} = \bar{q}\Gamma_i q$ (e.g., the vector current with $\{\Gamma_i\} = \{\gamma_\mu\}$ or any other lattice symmetry multiplet) there is a straightforward generalization that averages over current components,

$$\left[\frac{Z_\psi}{Z_\Gamma}\right]^{\text{lat}}(p) = \Pi_\Gamma = \frac{\sum_i \text{Tr}\left[\Lambda_{\Gamma,i}^{\text{lat}}(p) \cdot \Gamma_i\right]}{\sum_i \text{Tr}\left[\Gamma_i \cdot \Gamma_i\right]}. \tag{4.12}$$

4.2.2 Operators with derivatives

Operators with derivatives require more complicated treatment than Eq. (4.12) for a few reasons. First, a lattice vertex function (4.10) may have a correction with

different (non-Born) spin structure. For example, the Green function of the one-derivative operator $\mathcal{O}_{n=2} = \bar{q}\gamma_{\{\mu} iD_{\nu\}} q$ can have two possible structures [Gra03b],

$$[\Lambda^{\rm lat}_{n=2}]_{\mu\nu}(p) = \Pi^{(11)}_{n=2}(p^2) \cdot [\Lambda^{\mathcal{T}(1)}_{n=2}]_{\{\mu\nu\}} + \Pi^{(12)}_{n=2}(p^2) \cdot [\Lambda^{\mathcal{T}(2)}_{n=2}]_{\{\mu\nu\}}, \tag{4.13}$$

where the tree-level structures are

$$\begin{aligned} \left[\Lambda^{\mathcal{T}(1)}_{n=2}\right]_{\{\mu\nu\}} &= \gamma_{\{\mu} p_{\nu\}} - \frac{1}{4}\not{p}\delta_{\mu\nu}, \\ \left[\Lambda^{\mathcal{T}(2)}_{n=2}\right]_{\{\mu\nu\}} &= \not{p}\frac{p_\mu p_\nu}{p^2} - \frac{1}{4}\not{p}\delta_{\mu\nu}\,. \end{aligned} \tag{4.14}$$

In perturbation theory [Gra03b], $\Pi^{(12)}$ appears only as an $\mathcal{O}(\alpha)$ finite correction. One has to solve the equation system (4.13) to project on the correct vertex structure and extract the relevant renormalization factor $\Pi^{(11)}$. Similar mixing may occur for other operators, e.g., the $n = 3$ twist-two operator can have two terms while transversity operators can have tree terms. The corresponding spin structures are given in the Appendix C.1.

The second problem is that the components of the same tensor on a lattice may renormalize differently if they belong to different $H(4)$ representations. The running with the scale is the same and should agree with perturbation theory, but the matching coefficients may differ. We solve this problem by extracting separate matching coefficients for each representation. We renormalize components of each representation separately before substituting them into the right-hand side of Eq.(3.49) or its analog to extract form factors.

Equation (4.12) should be modified to extract the relevant components of operator vertices (4.13). We introduce a "scalar product" in each particular $H(4)$ representation,

$$\sum_i \mathrm{Tr}\left[\Lambda^{\rm lat}_{\Gamma,i}\Lambda^{\mathcal{T}}_{\Gamma,i}\right] = \langle \Lambda^{\rm lat}_{\Gamma}, \Lambda^{\mathcal{T}}_{\Gamma}\rangle \tag{4.15}$$

where i enumerates the elements of a given $H(4)$ irreducible representation. Using

this product, one can write the equations for $\Pi^{(a)}$ as follows:

$$\sum_b \mathcal{A}^{ab}\Pi^b_{\mathcal{O}} = \langle \Lambda^{\mathcal{T}(a)}_{\mathcal{O}}, \Lambda^{\text{lat}}_{\mathcal{O}} \rangle, \tag{4.16}$$

$$\text{where} \quad \mathcal{A}^{ab} = \langle \Lambda^{\mathcal{T}(a)}_{\mathcal{O}}, \Lambda^{\mathcal{T}(b)}_{\mathcal{O}} \rangle \tag{4.17}$$

The linear equations (4.16) are fully determined and can be solved directly.

Finally, in the spin structure of operator (4.13), the derivative gets replaced with the quark field momentum. It is not clear what momentum, lattice $\hat{p}_\mu = \sin(k_\mu)$ or continuum $p_\mu = k_\mu$, one should use to reproduce the spin structure (4.14). On one hand, the discretization of the derivative in the operator is a hint that the *lattice* quark momentum $\hat{p}_\mu = \sin(k_\mu)$ should be used in its Fourier transformed vertex; on the other hand, the quark off-shell momentum,

$$\tilde{p}_\mu = \frac{1}{4N_c}\text{Tr}\left[\gamma_\mu (S^{\text{lat}}(p))^{-1}\right], \tag{4.18}$$

is more natural for the quark polarization matrix $\not{p}$ and thus is an additional vector not necessarily equal to $\hat{p}$ that can generate other terms in addition to those in Eq. (4.13). Because we have to match the perturbative RG behavior, we have to use large momentum $p \gg \Lambda_{QCD}$ comparable to the lattice cutoff leading to the sizable difference between p_μ, $\hat{p}_\mu$ and $\tilde{p}_\mu$ representing discretization effects. We will study the "quark polarization" momentum $\tilde{p}_\mu$ in Sec. 4.2.3. Unfortunately, we cannot resolve this issue unambiguously, and we use an extrapolation procedure to get rid of possible discretization effects (see Sec. 4.3).

4.2.3 Quark field renormalization

A traditional way to compute the lattice quark field renormalization is from the inverse of a lattice quark propagator [G+10],

$$Z_q(p) = \frac{-i\sum_\mu \text{tr}\left[\gamma_\mu \hat{p}_\mu (aS^{\text{lat}})^{-1}(p)\right]}{12\sum_\mu \hat{p}^2_\mu} \tag{4.19}$$

where $\hat{p}_\mu = \frac{1}{a}\sin(k_\mu)$ is the lattice momentum and k_μ is the dimensionless lattice wave number. This method is based on the assumption that the lattice quark propagator has the form

$$(aS^{\text{lat}}(p))^{-1} = Z_\psi(i\sum_\mu \gamma_\mu \hat{p}_\mu + Z_m m) + O(a^2). \tag{4.20}$$

However, as we will see below, this is not necessarily the case.

To explore the dependence of the quark propagator on the quark wave number k_μ and the scale $(a\mu)^2 = k^2$ we study the numerical value of $\tilde{p}_\mu$ defined as

$$Z_\psi \tilde{p}_\mu = \frac{1}{12i}\text{Tr}[\gamma_\mu (aS^{\text{lat}})^{-1}]. \tag{4.21}$$

Because the renormalization constant Z_ψ also depends on the scale μ^2, the $\tilde{p}_i$ value itself cannot be isolated without additional data. However, using different orientations of the wave vector k_i we can still draw conclusions about the relation of $\tilde{p}_i$ and k_i.

In Figure 4-1(a) we show the ratio $Z_\psi(\mu)\tilde{p}_i/k_i$ for different momentum components and values of the total momentum k^2. From this ratio at fixed k_i we can extract the running of the quark field renormalization $Z_\psi(\mu)$. We observe that the Z_ψ running deviates strongly from both the perturbative running and the non-perturbative running computed using Ward identities, which are also shown on the figure. In addition, it is clear that the naive continuum relation $\tilde{p}_i = \frac{1}{a}k_i$ does not hold and there is no linear relation between $\tilde{p}_i$ and k_i.

In Figure 4-1(b) we explore further the relation between $\tilde{p}_i$ and k_i. In the double ratio $\frac{\tilde{p}_i}{k_i}/\frac{\tilde{p}_j}{k_j}$ the field renormalization Z_ψ cancels, and we can test our expectations for the relation between $\tilde{p}_i$ and k_i against the numerical results. First, Figure 4-1(b) indicates that the lattice momentum $\hat{p}_i = \frac{1}{a}\sin(ak_i) \neq \tilde{p}_i$ and the assumption (4.20) is not correct. Indeed, the plotted values of the double ratio disagree with horizontal lines representing $\frac{\sin k_i}{k_i}/\frac{\sin k_j}{k_j}$. Finally, we observe small ($\approx 1\%$) deviations of the double ratios from being horizontal. This fact indicates that there is no unique dependence between $\tilde{p}_i$ and k_i, and $\tilde{p}_i$ also weakly depends on the total momentum k^2.

Note that each branch in both Figures 4-1(a) and 4-1(b) corresponds to varying

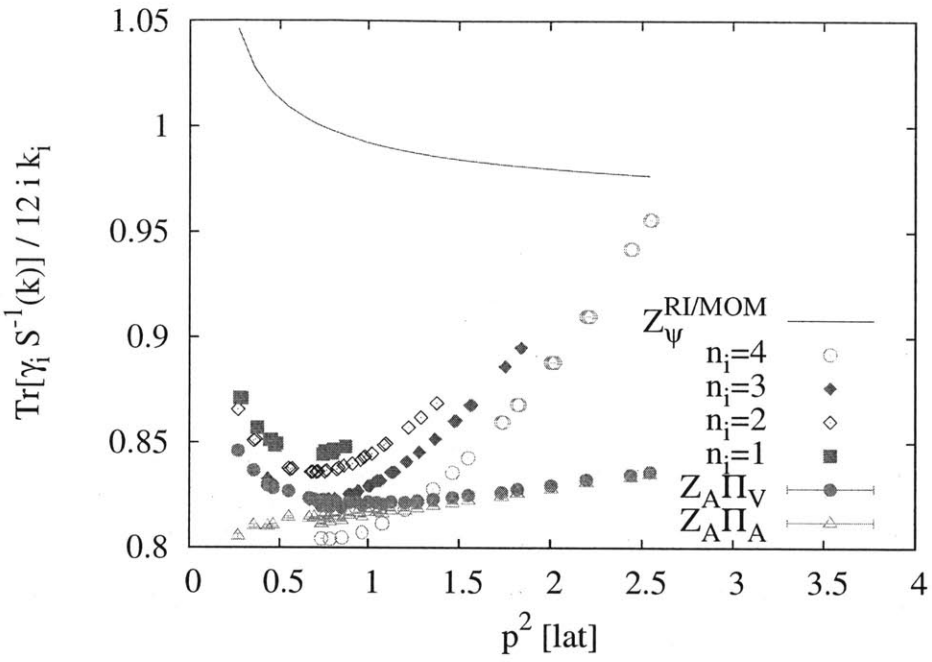

(a) Ratio $\frac{Z_\psi \tilde{p}_i}{k_i}$. Also shown is the quark field renormalization Z_ψ extracted from the (axial) vector current $\mathcal{A}$ and the perturbative running of $Z_\psi(\mu)/Z_\psi(\mu_0)$

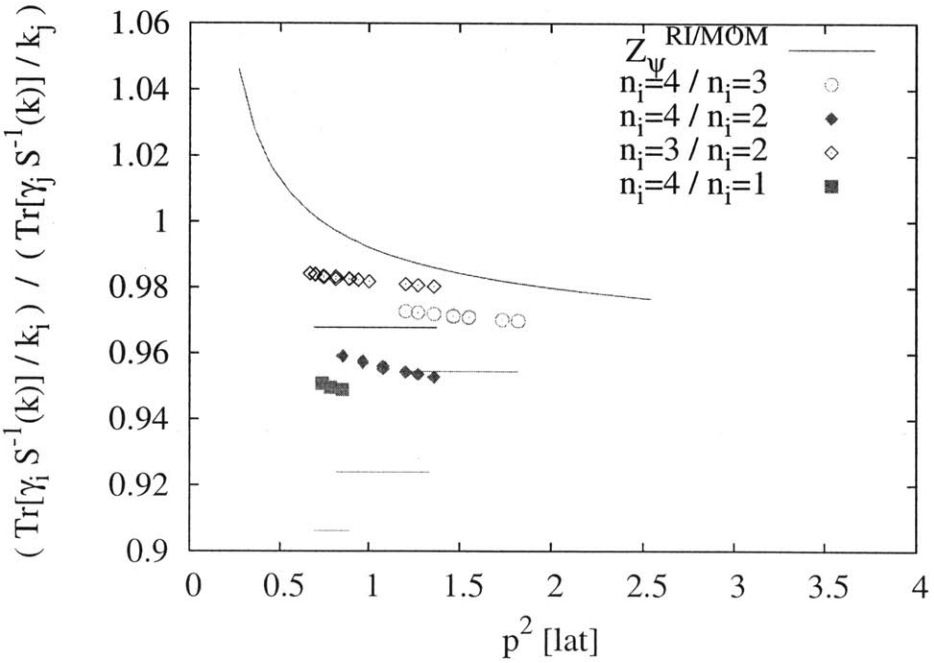

(b) Double ratio $\frac{\tilde{p}_i}{k_i} / \frac{\tilde{p}_j}{k_j}$. If the relation (4.20) held, the data points would lie on a horizontal line. The horizontal segments of the same color show this ratio assuming $\tilde{p}_i = \sin(k_i)$.

Figure 4-1: Analysis of quark momentum components extracted from quark propagators using Eq. (4.21)

wave number components k_j, $j \neq i$, thus demonstrating that these branches are universal and that $\tilde{p}_i$ depends on k_j, $j \neq i$ only through the total momentum k^2. This dependence cannot be represented through the common factor $Z_\psi(k^2)$, and the general form of a lattice quark propagator is:

$$(aS^{\text{lat}}(p))^{-1} = Z_\psi(k^2)(i\sum_\mu \gamma_\mu \tilde{p}_\mu(k_i, k^2) + Z_m(k^2)m) + O(a^2), \tag{4.22}$$

where the dependence of $\tilde{p}_\mu$ on k^2 is weak but not trivial. Whether this can be understood as an $O(a^2)$ effect is not clear.

Motivated by our findings above, in this work we extract the quark field renormalization from vertex functions of operators which satisfy Ward identities and are not renormalized, instead of Eq. (4.19). In the case of domain wall fermions, we use the local axial current operator,

$$A_\mu = \bar{q}\gamma_\mu\gamma_5 q \tag{4.23}$$

Because it is only a discretized version of the true partially conserved axial current $\mathcal{A}$, it is renormalized with a scale-independent factor $Z_A/Z_\mathcal{A} = \frac{\langle\pi|\mathcal{A}_0|\Omega\rangle}{\langle\pi|A_0|\Omega\rangle}$ and $Z_\mathcal{A} \equiv 1$ (see also Sec. 2.3.3, 4.1.3) also determined from lattice calculations. In the case of Wilson fermions, there is no conserved axial current, and we have to use the point-split vector current (4.2) with $Z_\mathcal{V} \equiv 1$. In both cases, we extract (eliminate) the quark field renormalization [B$^+$02, B$^+$04] Z_ψ as

$$Z_\psi = Z_{A,V}\Pi_{A,V}, \quad Z_\mathcal{O} = Z_{A,V}\frac{\Pi_{A,V}}{\Pi_\mathcal{O}}. \tag{4.24}$$

4.2.4 Vector and axial currents renormalization

Since Domain Wall fermions possess good chiral symmetry, it is instructive to compare the vertices of local vector and axial vector currents Π_A and Π_V. They are expected to agree as $\mu^2 \to \infty$ and chiral symmetry breaking effects become less relevant. Figure 4-2 shows $\Pi_{A,V}$ and their ratio for three quark masses and extrapolation $m_q \to 0$. The

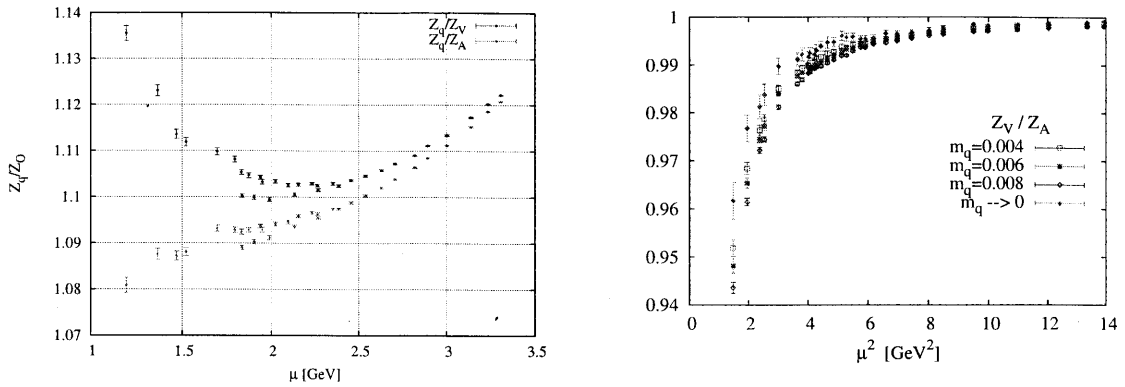

(a) $\Pi_{A,V}$ for the lightest pion mass $m_\pi \approx$ 300 MeV

(b) $Z_V/Z_A = \Pi_A/\Pi_v$ for three pion masses and extrapolation $(m_q + m_{\text{res}}) \to 0$

Figure 4-2: Comparison of vector and axial vector renormalization constants in the *Domain Wall* calculations.

main working region, as we will see below, will be limited to $\mu^2 \gtrsim 6$ GeV^2 or $(ap)^2 \gtrsim 1$. In Section 4.3.3 we will implicitly use $Z_A \cdot \frac{1}{2}(\Pi_A + \Pi_V)$ as an estimate of $Z_\psi(\mu)$, and from Fig. 4-2 its error is

$$\frac{\delta Z_\psi}{Z_\psi} \approx \frac{\delta(\Pi_A + \Pi_V)}{\Pi_A + \Pi_V} \approx \frac{|\Pi_A - \Pi_V|}{\Pi_A + \Pi_V} \lesssim 0.25\% \tag{4.25}$$

because the relative error in Z_A is negligible.

Figure 4-3(a) shows ratios of renormalization constants for helicity-dependent and helicity-independent operators. Because of chiral symmetry, these coefficients must be equal. All ratios in Fig. 4-3(a) are very close to one indicating that chiral symmetry breaking effects in the renormalization are negligible. In the following sections, both helicity-independent and helicity-dependent operators will be renormalized with the same sets of coefficients.

4.3 Matching to the $\overline{\text{MS}}$ scheme

In order to extract the coefficients which transform the lattice operators to the $\overline{\text{MS}}$ scheme, we have to

1. Extract the scale-independent (SI) factors between the lattice and RI′-MOM-

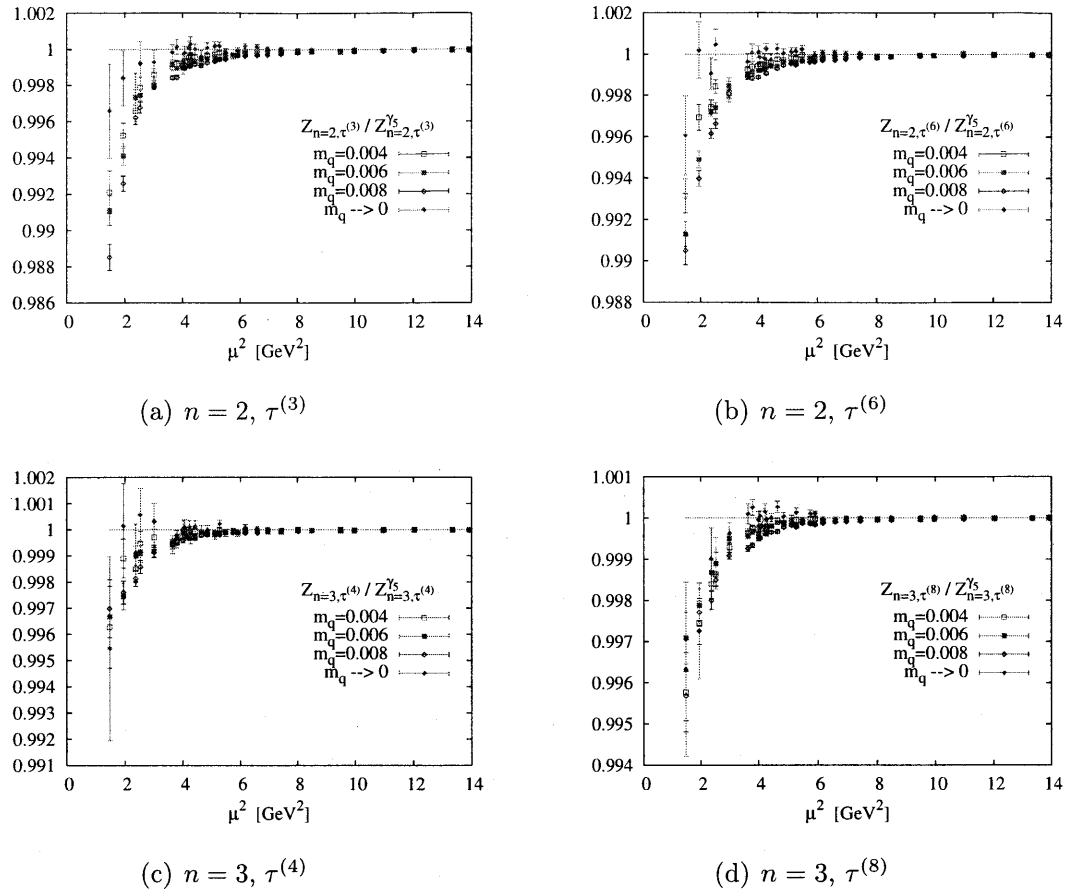

(a) $n = 2$, $\tau^{(3)}$ (b) $n = 2$, $\tau^{(6)}$

(c) $n = 3$, $\tau^{(4)}$ (d) $n = 3$, $\tau^{(8)}$

Figure 4-3: Comparison of helicity-dependent and helicity-independent renormalization coefficients for Wilson twist-2 operators.

renormalized perturbative Green functions.

2. Transform the RI′-MOM to $\overline{\text{MS}}$ operators.

3. Convert the $\overline{\text{MS}}$ values to our reference scale $\mu_0^2 = (2\text{ GeV})^2$.

In this section we summarize each of these steps in detail. In addition, in Sec. 4.3.4 we carefully analyze the systematic errors arising from both lattice and perturbative calculations involved.

4.3.1 Perturbative running of renormalization factors

The 3-loop perturbative anomalous dimensions and matching coefficients between $\overline{\text{MS}}$ and RI′-MOM are given in [Gra03a, Gra06]. For consistency, we continue to use our

conventions in Eq. (4.4-4.6)[3].

We integrate the differential equations for the anomalous dimensions and the running of the coupling constant

$$\frac{d\alpha_S}{d\ln\mu^2} = -\beta^{\overline{\rm MS}}(\alpha_S) < 0, \tag{4.26}$$

$$\frac{d\ln Z_X^{(\rm scheme)}}{d\ln\mu^2} = -\gamma^{(\rm scheme)}(\alpha_S) \tag{4.27}$$

with initial conditions $Z_X(\mu_0 = 2\ \text{GeV}) = 1$. Such starting values are convenient for eventual rescaling of the operators to the reference scale $\mu_0 = 2$ GeV. The results for the RI′-MOM scheme are shown in Fig. 4-4. The γ and β functions are computed with $N_f = 3$ flavors to correspond to the simulated lattice QCD with $N_f = 2$ light + 1 heavy flavors. Note also that the running of α_S is identical in $\overline{\rm MS}$ and RI′-MOM schemes [Gra03a].

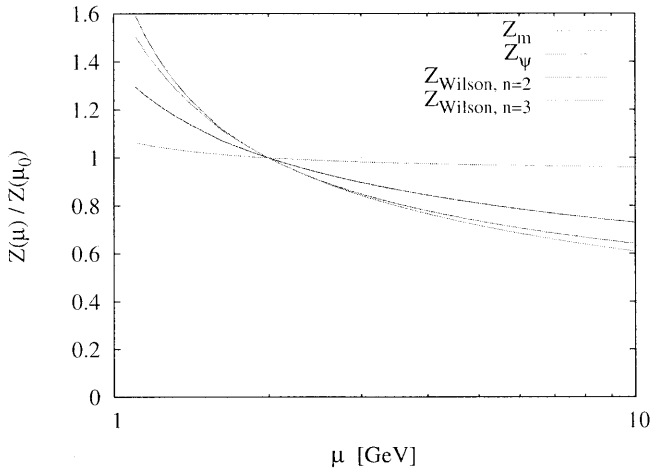

Figure 4-4: Perturbative 3-loop running of renormalization coefficients in the RI′ scheme.

Since the perturbative renormalization factors depend on α_S its uncertainty can contribute to final results. Therefore, we describe in detail how the $\alpha_S(\mu_0)$ value is obtained and where its uncertainty comes from. We take the global fit value

[3] Note that our definitions for Z_m and Z_ψ disagree with [CR00] for the mass and wave function renormalization factors.

$\alpha_S^{\overline{\rm MS}}(m_Z)$ [Bet09] and integrate the β-function with $N_f = 5$ in $m_b < \mu < m_Z$ and with $N_f = 4$ in $m_c < \mu < m_b$[4] to find $\alpha_S^{\overline{\rm MS}}(m_c)$. Then, $\alpha_S^{\overline{\rm MS},N_f=3}(2\text{ GeV}) = 0.295(5)$ is found by integrating the β-function with $N_f = 3$ in $m_c < \mu < \mu_0$ to mimic the simulated QCD. The values of quark masses used as matching thresholds are taken from Ref. [A+08b]:

$$m_c = 1.25^{+0.07}_{-0.11}\text{ GeV}, \tag{4.28}$$

$$m_b = 4.20^{+0.17}_{-0.07}\text{ GeV}, \tag{4.29}$$

$$m_Z = 91.188\text{ GeV}, \tag{4.30}$$

$$\alpha_S(m_Z) = 0.1184 \pm 0.0007 \tag{4.31}$$

The variation of $\alpha_S^{\overline{\rm MS},N_f=3}(2\text{ GeV})$ corresponding to the above uncertainties is

$$\alpha = 0.2956^{+0.0010}_{-0.0017}(m_c)^{+0.0004}_{-0.0002}(m_b)^{+0.0048}_{-0.0047}(\alpha_S(m_Z)) \tag{4.32}$$

For the rest of this work, the coupling constant is fixed at $\alpha_S(2\text{ GeV}) = 0.295(5)$.

4.3.2 Extraction of scale-independent factors

The scale-independent (SI) matching coefficients between the operators in the lattice and perturbative calculations are extracted by extrapolating the ratios

$$\left[\left(\frac{Z_\mathcal{O}}{Z_A}\right)^{\rm lat}_{p^2=\mu^2} \cdot \left(\frac{Z_\mathcal{O}^{\rm RI'}(\mu_0)}{Z_\mathcal{O}^{\rm RI'}(\mu)}\right)\right] \approx Z_\mathcal{O}^{\rm SI} + A \cdot (a\mu)^2, \tag{4.33}$$

with $\mu^2 \to 0$, where in the left-hand side the "anomalous" μ-dependence of renormalization coefficients should cancel between $Z_\mathcal{O}^{\rm lat}$ and $Z^{\rm RI'}$, the ratio $Z_\mathcal{O}/Z_A$ eliminates the field renormalization Z_ψ (4.24) and the second term $\sim (a\mu)^2$ in the right-hand side represents finite lattice spacing effects.

[4] The correct procedure is to match some scheme-independent observable [CKS97] instead of a scheme-dependent coupling constant; however, the corresponding change in α_S from matching at m_b is only 0.2% [Bet09], which is negligible compared to the uncertainty in α_S itself, nonperturbative matching coefficients, and the lattice scale determination.

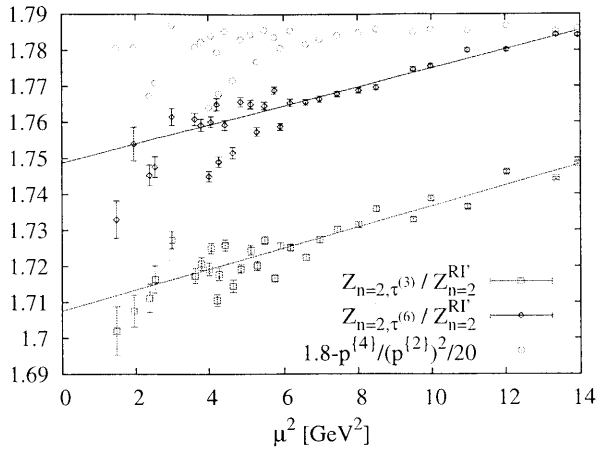

Figure 4-5: Determination of the scale-independent coefficient (4.33) for the Wilson twist-2, $n = 2$ operator, $\tau^{(3)}$ and $\tau^{(6)}$ representations.

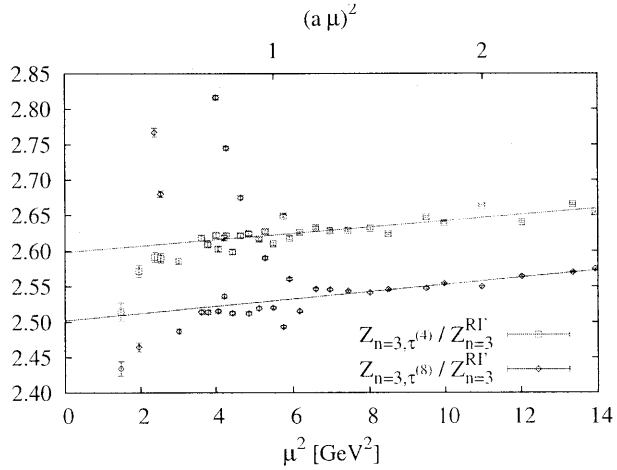

Figure 4-6: Determination of the scale-independent coefficient (4.33) for the Wilson twist-2 $n = 3$ operator, $\tau^{(4)}$ and $\tau^{(8)}$ representations.

The numerical values (4.33) and their extrapolations are shown in Fig. 4-5 for the Wilson twist-2 $n = 2$ operator and in Fig. 4-6 for the $n = 3$ operator. Extrapolation is linear in $(a\mu)^2$ in the region $\mu^2 \geq 6$ GeV^2. Judging from the spread of points the systematic error of estimating Z^{lat}/Z^{pert} is below 0.2% for $n = 2$ and below 1% for $n = 3$ operators. The results and their estimated uncertainties are collected in Tab. 4.1.

In addition, we attempt to trace the origin of the discretization errors with a

Table 4.1: Results for the renormalization factors $Z_{\mathcal{O}}^{\text{final}}$ (4.35) in the *Domain Wall* calculations.

$\mathcal{O}$	$H(4)$	$Z_{\mathcal{O}}^{\text{SI}}$ (4.33)	ϵ^{lat}	ϵ^{pert}	$\left(\frac{Z^{\overline{\text{MS}}}}{Z^{\text{RI}'}}\right)_{2\text{ GeV}}$	$Z_{\mathcal{O}}^{\text{final}}$
$\bar{q}\gamma_{\{\mu}i\overleftrightarrow{D}_{\nu\}}q$	$\tau^{(3)}$	1.708(4)	0.0020	0.0002	0.8414(42)	1.070(6)
	$\tau^{(6)}$	1.749(2)	0.0014	0.0002	0.8414(42)	1.096(6)
$\bar{q}\gamma_{\{\mu}i\overleftrightarrow{D}_{\nu}i\overleftrightarrow{D}_{\rho\}}q$	$\tau^{(4)}$	2.598(17)	0.0064	0.0002	0.7496(68)	1.450(17)
	$\tau^{(8)}$	2.502(8)	0.0033	0.0002	0.7496(68)	1.397(14)

simple model, Testing different models of discretization effects is plausible because of the extremely small stochastic variation of nonperturbative quark correlators with volume sources. An example of quantity which characterizes the rotational symmetry-breaking on a cubic lattice can be generated by higher orders in the expansion of the lattice momentum $\tilde{p}_\mu$ (cf. Ref [B$^+$08a]). Since the magnitude of the effect is not known, it is preferable to normalize this quantity so that it is dimensionless:

$$\begin{aligned} \tilde{p}_\mu \approx k_\mu + Ca^2k_\mu^3, \qquad & \text{(e.g., from } \hat{p}_\mu = \frac{1}{a}\sin(ak_\mu) \approx k_\mu - \frac{a^2}{6}k_\mu^3\text{)} \\ \Delta_{\text{discr}} \sim \frac{\tilde{p}^2 - k^2}{a^2(k^2)^2} \sim \frac{k^{\{4\}}}{(k^{\{2\}})^2} &= \frac{1}{(k^2)^2}\sum_\mu k_\mu^4, \\ \text{where } k^{\{n\}} &= \sum_\mu k_\mu^n. \end{aligned} \tag{4.34}$$

We plot this quantity (vertically offset and scaled for convenience) in Fig. 4-5 and compare it to the irregular behavior of $Z^{\text{lat}}/Z^{\text{pert}}$ at small momentum k^2. We observe that it resembles the plot for the $\tau^{(6)}$ (off-diagonal) irreducible representation, while we see no resemblance with the $\tau^{(3)}$ (diagonal) representation.

4.3.3 Final renormalization coefficients

In this section we summarize the results for overall renormalization constants relating lattice operators and operators normalized at $\mu_0 = 2$ GeV in the $\overline{\text{MS}}$-scheme,

$$\mathcal{O}^{\overline{\text{MS}}(2\text{ GeV})} = Z_{\mathcal{O}}^{\text{final}}\ \mathcal{O}^{\text{lat}}, \tag{4.35}$$

for the quark-bilinear operator studied in Chap. 5. The overall renormalization constant is computed as the combination

$$Z_{\mathcal{O}}^{\text{final}} = Z_A^{\text{lat}} \cdot \left(\frac{Z_{\mathcal{O}}^{\overline{\text{MS}}}}{Z_{\mathcal{O}}^{\text{RI}'}}\right)_{\mu_0} \cdot \underbrace{\left[\left(\frac{Z_{\mathcal{O}}}{Z_A}\right)^{\text{lat}} \left(\frac{Z_{\mathcal{O}}^{\text{RI}'}(\mu_0)}{Z_{\mathcal{O}}^{\text{RI}'}(\mu)}\right)\right]_{(a\mu)^2\to 0}}_{\text{scale-independent } Z_{\mathcal{O}}^{\text{SI}}}, \tag{4.36}$$

where the first factor $Z_A = 0.74470(6)$ was determined in Ref. [S+10], the second factor is a 3-loop conversion function $[C^{\text{RI}'}(\alpha_S(\mu_0))]^{-1} = (Z^{\overline{\text{MS}}}/Z^{\text{RI}'})_{\mu_0}$ and the third factor is extracted as described in Sec. 4.3.2. The final results for renormalization coefficients in the *Domain Wall* calculations are collected in Tab. 4.1. Column ϵ^{lat} shows fractional error from lattice calculations, and column ϵ^{pert} shows fractional error from perturbative anomalous dimensions. The latter will be discussed in detail in Sec. 4.3.4. The error from the conversion function $C^{\text{RI}'}(\alpha_S(\mu_0))$ is given below in Tab.4.2. All the uncertainties including δZ_ψ (4.25) are added in quadrature and shown in the last column $Z_{\mathcal{O}}^{\text{final}}$.

4.3.4 Systematic errors

There are several different sources of uncertainty in the determination of non-perturbative renormalization factors. We study each source separately to find out which has the most influence. First of all, we note that the stochastic fluctuation of the lattice correlators is negligible, compared, for example, to the nonlinearity of $(Z^{\text{lat}}/Z^{\text{RI}'})$ in $(a\mu)^2$, and it will not be discussed further. The other sources of errors fall into the following categories:

- irregular (nonlinear) dependence of $(Z^{\text{lat}}/Z^{\text{RI}'})$ on $(a\mu)^2$;
- uncertainty in the strong coupling α_S;
- perturbative series truncation.

Note that the uncertainty in α_S and the truncation of perturbative series contribute to $Z_{\mathcal{O}}^{\text{final}}$ in two distinct ways. First, the variation in the slope of $(Z^{\text{lat}}/Z^{\text{RI}'})$

vs $(a\mu)^2$ leads to the variation in the extrapolated value $Z_{\mathcal{O}}^{\rm SI}$ 4.33. Second, the conversion coefficients $C = Z^{\rm RI'}/Z^{\overline{\rm MS}}$ computed to the same order as the anomalous dimensions are additional multiplicative factors in $Z_{\mathcal{O}}^{\rm final}$. Contributions from each source are collected in Tab. 4.2. Rows $Z_{\mathcal{O}}^{\rm RI'}$ show the uncertainties from the extrapolation $(a\mu)^2 \to 0$ because of RG running, and rows $C_{\mathcal{O}}^{\rm RI'}$ show the uncertainties of the conversion functions. The columns indicate the contribution from the uncertainty of α_S as well as the series truncation at $\mathcal{O}(\alpha_S^2)$ and $\mathcal{O}(\alpha_S^3)$ compared to $\mathcal{O}(\alpha_S^4)$[5].

Table 4.2: Comparison of different sources of uncertainty contributing to the determination of lattice renormalization factors. Quoted numbers are fractional errors.

$\mathcal{O}$	$\delta\alpha_S = 0.005$	$O(\alpha_S^4)$ vs $O(\alpha_S^3)$	$O(\alpha_S^4)$ vs $O(\alpha_S^2)$	$Z^{N_f=4}/Z^{N_f=3}$
$Z^{\rm RI'}_{\bar{q}\gamma_{\{\mu}i\overleftrightarrow{D}_{\nu\}}q}$	$^{+0.00003}_{-0.00004}$	0.00015	$\approx 10^{-5}$	1.0026
$C_{\bar{q}\gamma_{\{\mu}iD_{\nu\}}q}$	± 0.0042	—	-0.028	—
$Z^{\rm RI'}_{\bar{q}\gamma_{\{\mu}i\overleftrightarrow{D}_{\nu}i\overleftrightarrow{D}_{\rho\}}q}$	$^{+0.00004}_{-0.00006}$	0.00023	0.00002	1.0041
$C_{\bar{q}\gamma_{\{\mu}iD_{\nu}iD_{\rho\}}q}$	± 0.0068	—	-0.046	

It is interesting that the highest-order terms in $C_{\mathcal{O}}$ that come from the $\mathcal{O}(\alpha_S^3)$ terms in the perturbative Green functions and are neglected in the anomalous dimensions contribute to the renormalization coefficients at a few percent level. Potentially, the perturbative series truncation has the largest effect on the renormalization coefficients, although it is hard to estimate properly its uncertainty.

We estimate separately the dependency of the matching coefficients on the number of flavors in the perturbative calculations. This is relevant because lattice data are matched at all scales using $N_f = 3$ QCD, while the QCD phenomenology may take into account the number of active flavors. To estimate such discrepancies, we compare $\overline{\rm MS}$ anomalous dimensions integrated in the region $m_c < \mu < \mu_0$ with $N_f = 3$ and $N_f = 4$ flavors in the last column of Tab. 4.2. In all cases the difference in the final renormalization factors remains below a fraction of a percent (see Tab. 4.2).

[5] In the comparison of the series truncation at $O(\alpha_S^4)$ and $O(\alpha_S^3)$ only the QCD β-function gets changed because only $\beta^{\overline{\rm MS}}$ is known up to four loops.

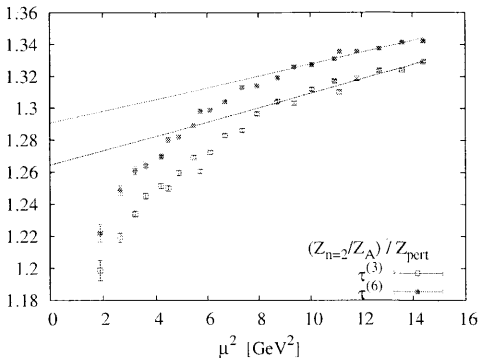

(a) $n = 2$ Wilson operator

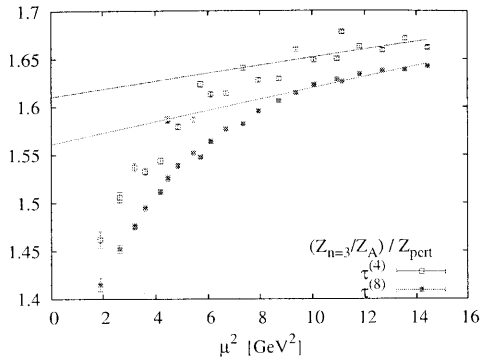

(b) $n = 3$ Wilson operator

Figure 4-7: Determination of scale-independent renormalization coefficients in the *Hybrid* ensemble. See explanations in the text.

4.4 Comparison of perturbative and nonperturbative renormalization

In this section we briefly summarize the effort to compute the non-perturbative renormalization for the *Hybrid* ensemble. We have applied the strategy described in Sec. 4.2 and 4.3 to this ensemble. The preliminary results are shown in Fig. 4-7 In the *Hybrid* calculations the lattice spacing $a = 0.124$ fm is substantially larger than in the *Domain Wall* calculations. Therefore, we expect larger discretization effects in all our calculations. In addition, as discussed in Chap. 2, the mixed action does not such good symmetry as the domain wall fermion action, for which the symmetry automatically reduces the discretization errors to $\mathcal{O}(a^2)$.

In Figure 4-7 we show the scale-independent ratio (4.33) for the $n = 2$ Wilson operator (1.19) in $\tau^{(3)}$ (diagonal) and $\tau^{(6)}$ (off-diagonal) representations, as well as the $n = 3$ Wilson operator (1.19) in $\tau^{(8)}$ (diagonal) and $\tau^{(4)}$ (off-diagonal) representations. The straight lines show extrapolations according to Eq. (4.33) It is clear that the systematic uncertainty is so large that there is even no approximate plateau, in contrast with Figs. 4-5 and 4-6. Thus, we cannot use such renormalization constants for our calculations. One possible way to amend large discretization effects is to subtract the $\mathcal{O}(a^2)$ corrections computed in lattice perturbation theory [G+10]. However,

such calculation is beyond the scope of the present work.

Instead, we use the perturbative renormalization constants $Z_{\mathcal{O}}^{\rm pert}$ computed in Ref. [Bis05]. In addition, because the quark field renormalization enters implicitly all the operator renormalization factors, we correct them as [H$^+$08, B$^+$10]

$$Z_{\mathcal{O}} = Z_{\mathcal{O}}^{\rm pert} \frac{Z_A^{\rm lat}}{Z_A^{\rm pert}} \tag{4.37}$$

where $Z_A^{\rm lat}$ is determined from the 5D partially-conserved axial current on each gauge configuration ensemble and $Z_A^{\rm pert} = 0.964$ was computed in Ref. [Bis05].

Table 4.3: Comparison of perturbative and non-perturbative renormalization factors for *Hybrid* ensemble.

$\mathcal{O}$	$H(4)$	$Z_{\mathcal{O}}^{\rm pert}(\Lambda_{\rm lat})$ [H$^+$08]	$\gamma_{\mathcal{O}}^{\text{1-loop}}$	$Z_{\mathcal{O}}(\mu_0)$	$Z_{\mathcal{O}}^{\rm NPR}(\mu_0)$
$\bar{q}[\gamma^5]\gamma^{\{\mu}i\overleftrightarrow{D}^{\nu\}}q$	$\tau_1^{(3)}$	0.962	-8/3	1.047	1.139
	$\tau_1^{(6)}$	0.968		1.054	1.174
$\bar{q}[\gamma^5]\gamma^{\{\mu}i\overleftrightarrow{D}^{\nu}i\overleftrightarrow{D}^{\rho\}}q$	$\tau_2^{(4)}$	0.980	-25/6	1.053	1.268
	$\tau_1^{(8)}$	0.982		1.055	1.259

In Table 4.3 we summarize the perturbative renormalization factors at the lattice scale $a_{Hybrid}^{-1} = 1.591$ GeV as well as the final renormalization factors at the reference scale $\mu = 2$ GeV corrected with Eq. (4.37) using the massless limit axial renormalization constant $Z_A^{\rm lat} = 1.075$ at $(m_q + m_{\rm res}) \to 0$.. The transformation between scales follows from the formula [Bis05]

$$Z_{\mathcal{O}}^{\rm pert} = 1 + \frac{g^2 C_F}{16\pi^2}\left(\gamma_{\mathcal{O}} \log(a^2\mu^2) - (B^{\rm lat} - B^{\overline{\rm MS}})\right) \tag{4.38}$$

where $B^{\rm lat,\overline{MS}}$ are the finite parts of loop diagrams and the 1-loop coupling evaluated from the lattice plaquette calculation is $\frac{g^2 C_F}{16\pi^2} = 1/53.64$ [Bis05].

In the last column of Tab. 4.3 we collect the estimates of renormalization factors computed using extrapolations shown in Fig. 4-7. The comparison of fully non-perturbative and perturbative renormalization factors provides a way to estimate the uncertainty of computing the twist-2 operators on a lattice because of renormalization

in *Hybrid* calculations:

$$\begin{aligned} n = 2 \quad & \delta Z_{\mathcal{O}} / Z_{\mathcal{O}} \approx 6\% \,, \\ n = 3 \quad & \delta Z_{\mathcal{O}} / Z_{\mathcal{O}} \approx 10\% \,. \end{aligned} \tag{4.39}$$

Summary

In this section, we have calculated the renormalization constants for the twist-two lattice operators of rank $n = 2$ and $n = 3$ nonperturbatively for the *Domain Wall* lattices. We use the standard procedure described in the literature on lattice operator renormalization, which provides precise determination of lattice renormalization factors even with small statistics.

We repeated a similar calculation for the *Hybrid* lattices, for which perturbative calculation of renormalization constants previously existed, to compare the lattice and analytic determinations. Nonperturbative renormalization is problematic because the scale window $\Lambda_{QCD} \ll \mu \ll a^{-1}$ may not exist or very narrow. Nevertheless, the results of the perturbative and lattice calculations agree within $\approx 10\%$ and allow us to estimate the systematic error because of the renormalization of lattice operators in the *Hybrid* calculations.

Chapter 5

Select Results

Equipped with the methods summarized in the previous chapters, we can compute a wide array of nucleon structure observables. To demonstrate how these calculations compare to experiments, in this section we present our results, including vector form factors and charge/magnetization radii in Sec. 5.1 for isovector and 5.2 for isoscalar components, axial charge and form factors in Sec. 5.3, quark contributions to nucleon momentum and spin in Sec. 5.4, and generalized form factors in Sec. 5.5. In addition, we can assess the systematic uncertainties of our calculations by comparing the results obtained using different lattice QCD discretizations listed in Appendix A.

Since our calculations are done with pion masses $m_\pi \gtrsim 300$ MeV we use chiral extrapolations to obtain physical observables at the physical pion mass $m_\pi \approx 140$ MeV. Generally, there is little understanding of whether a particular formulation of baryon ChPT is adequate for the range of pion masses we are working with. In addition, the applicability of different formulations of baryon ChPT may depend on nucleon structure observables in question. Throughout this section we will use the following baryon ChPT formulations:

- CBChPT , [covariant] baryon chiral perturbation theory, in which baryons and mesons are relativistic [GSS88];
- HBChPT , heavy baryon chiral perturbation theory, additional expansion in m_π/M_N with consistent power counting demonstrated in Ref. [BKKM92];

- HBChPT+Δ , heavy baryon chiral perturbation theory including the $\Delta(1232)$ degree of freedom, also called Small Scale Expansion (SSE) [HHK98].

For completeness, we summarize the details of these formulations in Appendix D. Although we perform full QCD simulations with dynamical $N_f = 2 + 1$ flavors, in all our ensembles the s-quark has a fixed mass near its physical value. Therefore, we have no means to study how the chiral dynamics changes with the s-quark mass and constrain the ChPT parameters related to the $SU(3)_f$ symmetry breaking. For this reason, we resort to $SU(2)_f$ chiral perturbation theory to analyze our data.

5.1 $I = 1$ vector form factors

In this section we present our results for the isovector Dirac and Pauli form factors and the corresponding r.m.s. radii. After discussing the momentum transfer dependence of the form factors, we compare the chiral extrapolations for the nucleon radii using the SSE (HBChPT+Δ) and covariant baryon chiral perturbation theory (CBChPT) .

5.1.1 Momentum transfer dependence

As will be discussed in the following section, ChPT describes the Q^2-dependence of the form factors for values of Q^2 much less than the chiral symmetry breaking scale (typically of the order of the nucleon mass). Lacking a model-independent functional form applicable in the large-Q^2 region, we study the Q^2 dependence using the phenomenological dipole and tripole formulas. Although there is no theoretical understanding of this fact, the dipole formula (5.1,5.3) is used to fit experimental results for the form factors. We also use fits to the tripole formula to show that the dependence of the extracted radii and the anomalous magnetic moment on the functional form is irrelevant at our level of precision.

The Dirac form factor is fixed to 1 at $Q^2 = 0$ under our renormalization scheme, and we use the following one-parameter dipole or tripole formula to describe the Q^2

dependence:

$$F_1(Q^2) = \frac{1}{(1+\frac{Q^2}{{M_D}^2})^2} \qquad \text{(one-parameter dipole)}, \tag{5.1}$$

$$F_1(Q^2) = \frac{1}{(1+\frac{Q^2}{{M_T}^2})^3} \qquad \text{(one-parameter tripole)}. \tag{5.2}$$

The Pauli form factor at $Q^2 = 0$, $F_2(0)$, cannot be measured on the lattice directly. We thus fit the data using the two-parameter dipole or tripole formula,

$$F_2(Q^2) = \frac{F_2(0)}{(1+\frac{Q^2}{{M_D}^2})^2} \qquad \text{(two-parameter dipole)}, \tag{5.3}$$

$$F_2(Q^2) = \frac{F_2(0)}{(1+\frac{Q^2}{{M_T}^2})^3} \qquad \text{(two-parameter tripole)}. \tag{5.4}$$

We are interested in mean squared Dirac and Pauli radii, which are defined by the slope of the form factors at small Q^2:

$$F_{1,2}(Q^2) = F_{1,2}(0)\left[1 - \frac{1}{6}\left(r_{1,2}\right)^2 Q^2 + \mathcal{O}(Q^4)\right], \tag{5.5}$$

and are related to the pole masses by

$$\left(r\right)^2 = \frac{12}{{M_D}^2}, \tag{5.6}$$

for the dipole fits, and

$$\left(r\right)^2 = \frac{18}{\left(M_T\right)^2}, \tag{5.7}$$

for the tripole fits.

Note that results at different Q^2 from the same ensemble may be highly correlated [B$^+$08b], therefore we perform *correlated* least-χ^2 fits to the data. We investigate the extent to which the dipole and tripole Ansätze describe our data and the stability of the fits by varying the maximum Q^2 values included in the fits.

In Table 5.1 we show the fit results for $F_1^{u-d}(Q^2)$ using the one-parameter dipole and tripole formulas in Eqs. (5.1) and (5.2) for the fine *Domain Wall* lattice with

Table 5.1: Comparison of different fits to the isovector Dirac form factors F_1^{u-d} with different Q^2 cutoffs for the fine *Domain Wall* lattice, $m_\pi = 297$ MeV.

	Dipole		Tripole	
$Q^2_{\max}$ [GeV^2]	χ^2/dof	M_D^{-2} [GeV^{-2}]	χ^2/dof	M_T^{-2} [GeV^{-2}]
0.3	0.2(6)	0.670(22)	0.2(6)	0.436(14)
0.4	0.3(6)	0.659(19)	0.8(9)	0.424(12)
0.5	0.5(6)	0.653(17)	1.0(9)	0.418(11)
0.6	0.4(5)	0.652(17)	1.0(8)	0.417(11)
0.7	0.5(5)	0.649(17)	1.2(8)	0.414(11)
0.9	0.9(7)	0.638(16)	1.9(1.0)	0.404(10)
1.1	1.4(8)	0.632(16)	3.0(1.1)	0.398(10)

$m_\pi = 297$ MeV. Comparing the χ^2/dof for the dipole and tripole fits, we see that the dipole fits are slightly preferred when larger Q^2 values are included in the fits. However, the Dirac radii determined from both the dipole and tripole fits agree within errors. In general, the dipole form describes the data reasonably well throughout the whole Q^2 range. We see the general trend that when large Q^2 points are included in the fits, the χ^2/dof becomes slightly worse, while the fit parameters do not depend significantly on the choice of the Q^2 cutoff, indicating that the dipole fits are stable.

Table 5.2: Comparison of different fits to the isovector Pauli form factors F_2^{u-d} with different Q^2 cutoffs for the fine *Domain Wall* lattice, $m_\pi = 297$ MeV.

	Dipole			Tripole		
$Q^2_{\max}$ [GeV^2]	χ^2/dof	$F_2(0)$	M_D^{-2} [GeV^{-2}]	χ^2/dof	$F_2(0)$	M_T^{-2} [GeV^{-2}]
0.5	1.2(1.3)	2.89(12)	0.820(70)	1.2(1.3)	2.85(11)	0.505(40)
0.6	1.1(1.1)	2.92(11)	0.846(63)	1.0(1.0)	2.87(10)	0.516(36)
0.7	0.9(8)	2.93(11)	0.847(60)	0.8(8)	2.87(10)	0.513(33)
0.9	0.9(8)	2.98(9)	0.888(46)	0.7(7)	2.89(8)	0.526(15)
1.1	0.8(7)	2.97(9)	0.881(41)	0.9(7)	2.85(8)	0.509(21)

We do the same comparison for $F_2^{u-d}(Q^2)$ as shown in Table 5.2. Judging from the χ^2/dof values, we do not see significant differences between the dipole and tripole fits. Since the Pauli form factor is not constrained at $Q^2 = 0$, including larger Q^2 in the fits does not seem to affect the quality of the fits significantly. The fit parameters $F_2(0)$ and $M_{D,T}$ prove not to be affected as well.

As an example, we show the dipole fit curves with a Q^2 cutoff at 0.5, 0.7 and

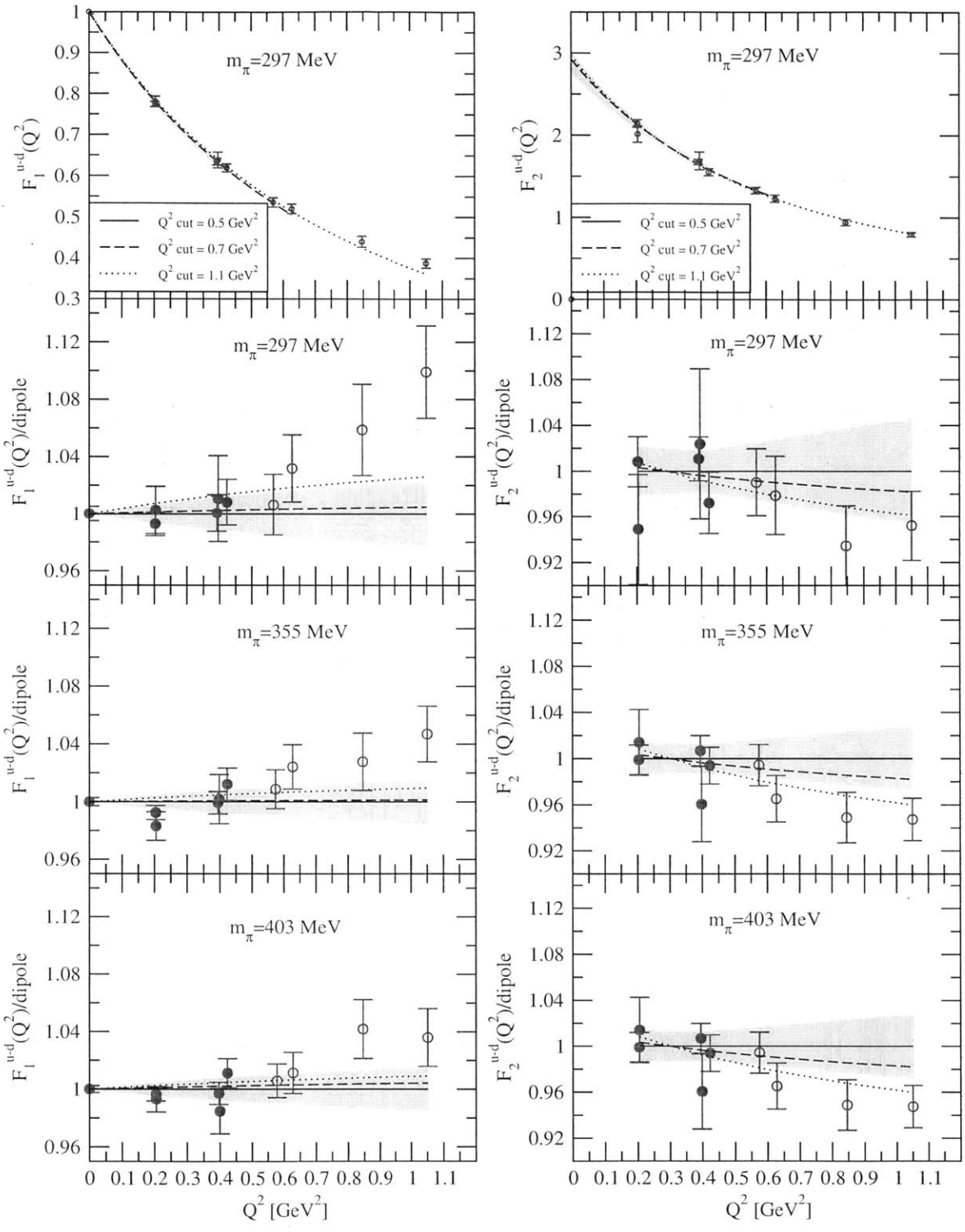

Figure 5-1: Results for $F_{1,2}^{u-d}(Q^2)$ at $m_\pi = 297$ MeV and the dipole fits with three different Q^2 cutoffs (top panels). The ratios of the lattice results for $F_{1,2}^{u-d}$ to the dipole fits using Eq. (5.1) (three bottom panels).

1.1 GeV^2 for the $m_\pi = 297$ MeV ensemble in the top panel of Fig. 5-1. To show the quality of the fits more clearly, we plot the ratios of the form factor data to the dipole fit with the Q^2 cutoff at 0.5 GeV^2 in the bottom three panels of Fig. 5-1. The error bands reflect the jackknife errors in the dipole fit parameters. We see that although the data included in the fits can be described reasonably well by the dipole formula with discrepancies that are generally within 2 to 3 standard deviations, the clear systematic tendency indicates that the dipole Ansatz is not a good description of the data over the whole momentum transfer region. In particular, for F_1^{u-d}, the precisely measured points in the region of 0.2 GeV^2 are systematically lower than the dipole fit, whereas at high Q^2, the lattice data are systematically higher. For F_2^{u-d}, the high Q^2 lattice data are systematically lower than the dipole fit. This is consistent with the empirical fits to the experimental data in Refs. [FW03, AMT07], where the phenomenological corrections to the dipole form are negative in the region of 0.2 GeV^2 and positive at about 0.4 GeV^2. For comparison, we also plot the dipole fits with Q^2 cutoffs at 0.7 GeV^2 (dashed line) and 1.1 GeV^2 (dotted line) relative to the 0.5 GeV^2 dipole fit (solid line). The differences between different Q^2 cutoffs are small, indicating that the fits are stable.

It is worth noting that the Dirac and Pauli radii, r_1^v and r_2^v, and the anomalous magnetic moment, κ_v, are defined in the $Q^2 = 0$ limit. We thus restrict the fits to the smallest Q^2 points possible to extract these quantities while still including enough data points to constrain the fits. For uniformity we choose to determine these quantities from the one-parameter dipole fits for F_1^{u-d}, and the two-parameter dipole fits for F_2^{u-d}, with a Q^2 cutoff at 0.5 GeV^2.

We also perform dipole fits to $G_E(Q^2)$ and $G_M(Q^2)$ to see how well the dipole Ansatz describes the data. We find that the dipole fits to G_E^{u-d} and G_M^{u-d} are qualitatively similar to F_1^{u-d} and F_2^{u-d}. However, it appears that the fits are even more stable over the whole range of Q^2 than Dirac and Pauli form factors. This is indicated by little change in the ratio plots in Fig. 5-2 with different Q^2 cutoffs.

Figure 5-3 shows a comparison of the lattice results for G_E at three different pion masses from the fine ensembles (the lattice spacing $a = 0.084$ fm) and one pion mass

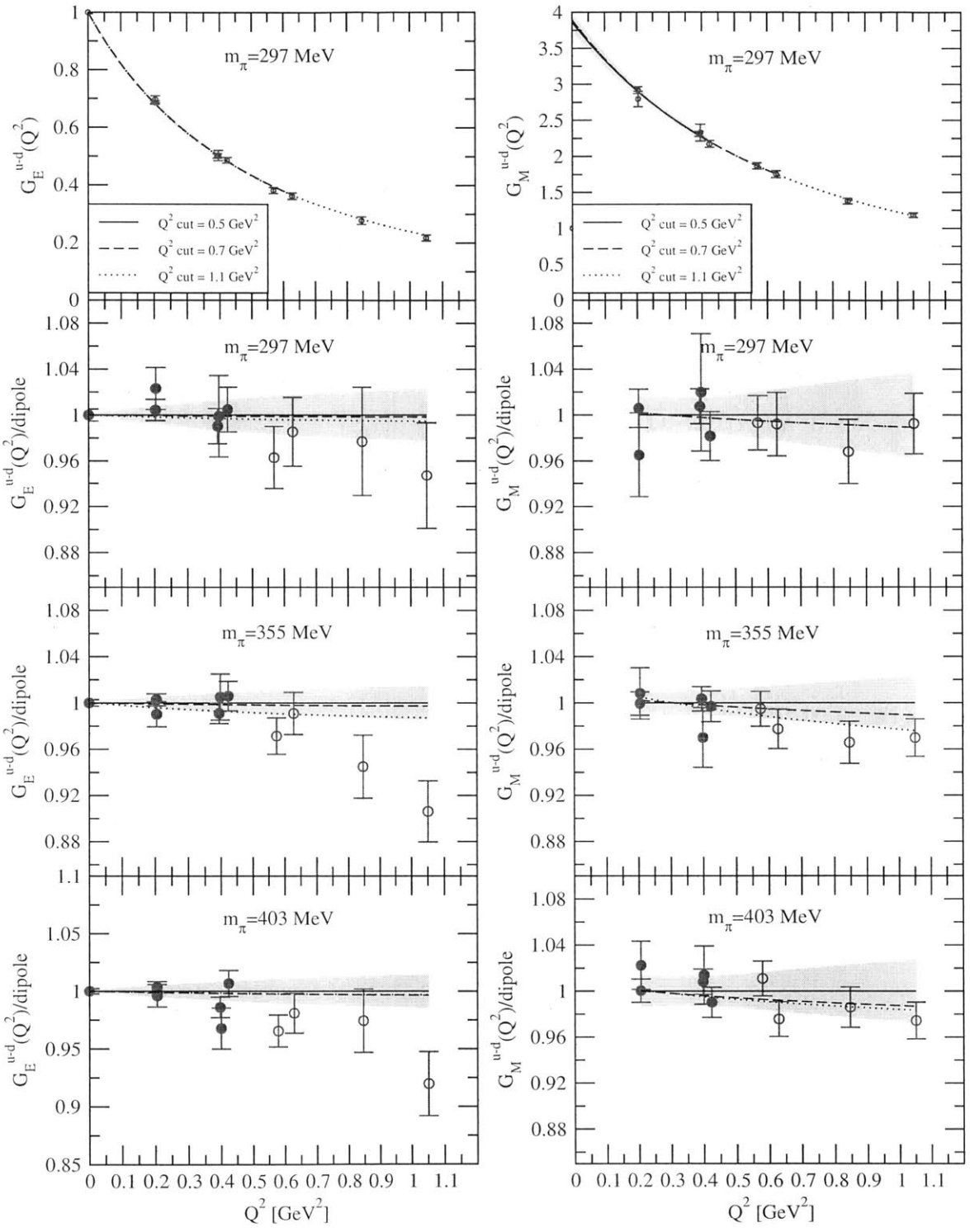

Figure 5-2: Results for $G_{E,M}^{u-d}(Q^2)$ at $m_\pi = 297$ MeV and the dipole fits with three different Q^2 cutoffs (top panels). The ratios of the lattice results for $G_{E,M}^{u-d}$ to the dipole fits using Eq. (5.1) (three bottom panels).

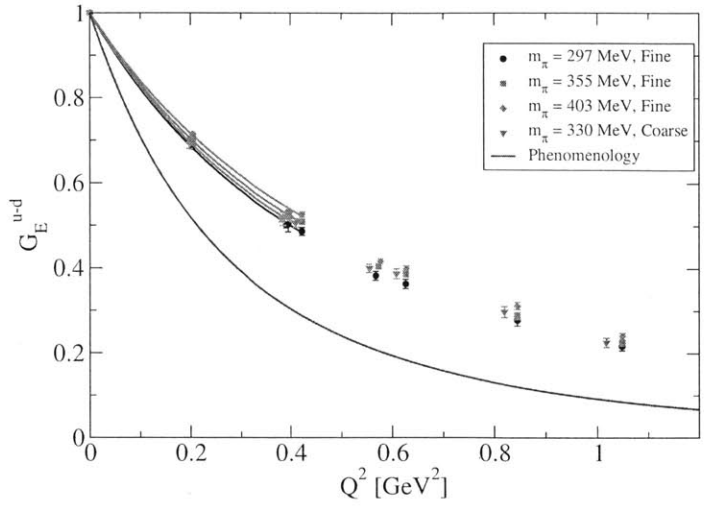

Figure 5-3: Lattice results for G_E^{u-d} for the fine and coarse *Domain Wall* ensembles, compared with a phenomenological fit [Kel04] to experimental data.

from the coarse ensemble (the lattice spacing $a = 0.114$ fm) with a phenomenological fit to the experimental data using the parameterization in Ref. [Kel04] (with no indication of the experimental errors). The solid curves are dipole fits to the form factor results with the Q^2 cutoff at 0.5 GeV^2. As the pion mass decreases, the slope of the form factors at the small momentum transfer monotonically increases. The results from the coarse ensemble at $m_\pi = 330$ MeV is nicely surrounded by the results from the fine ensembles at $m_\pi = 297$ and $m_\pi = 355$ MeV, indicating that the effect of the finite lattice spacing error should be small.

5.1.2 Chiral extrapolations using HBChPT+Δ

To compare the lattice results for the nucleon form factors at finite momentum transfer with the experimental results, we need to do extrapolations for both the m_π and Q^2 dependence using baryon chiral perturbation theory. This combined dependence has been worked out both in SSE at leading one loop accuracy and in BChPT up to NNLO order in Ref. [BFHM98] for both Dirac and Pauli form factors.

ChPT describes the Q^2 dependence of the form factors for values of Q^2 much less than the chiral symmetry breaking scale and Q^2 counts as a small quantity, of the order of m_π^2. In fact, we have attempted simultaneous fits to both the m_π and Q^2

dependences of F_1^{u-d} using the SSE formula in Ref. [BFHM98], and found that the fits fail to describe data even with $Q^2 \leq 0.4$ GeV^2 (χ^2/dof ≈ 10). This is consistent with the findings of Ref. [BFHM98], where the applicability of the $\mathcal{O}(\epsilon^3)$ SSE results for the isovector nucleon form factors at physical pion mass was found to be limited to $Q^2 < 0.2$ GeV^2. Lacking a model-independent functional form applicable in the large-Q^2 region, we resort to studying the pion-mass dependence of the mean squared Dirac radius, $(r_1^v)^2$, Pauli radius, $(r_2^v)^2$, and the anomalous magnetic moment, κ_v, as obtained from the dipole fits discussed in Sec. 5.1.1. We tabulate these values in Table 5.3.

Table 5.3: Results for the isovector Dirac and Pauli radii and anomalous magnetic moment from dipole fits with $Q^2 \leq 0.5$ GeV^2.

m_π [MeV]	$(r_1^v)^2$ [fm^2]	$(r_2^v)^2$ [fm^2]	$\kappa_v^{\text{norm}} \cdot (r_2^v)^2$ [fm^2]	κ_v^{norm}
297	0.305(8)	0.382(33)	0.938(117)	2.447(99)
355	0.281(5)	0.372(18)	0.938(66)	2.518(57)
403	0.272(5)	0.379(16)	0.954(58)	2.508(51)
330	0.290(9)	0.445(26)	1.230(105)	2.758(84)

Our results for the form factor F_2 and κ_v are given in terms of a nucleon (hence, quark) mass-dependent "magneton" $\frac{1}{2M_N^{\text{lat}}}$ (see Eq. (1.1)), which is not accounted for in SSE at the order at which we are working (see Eq. (D.2) in the Appendix). Therefore, in order to fit our lattice data to the SSE predictions, we follow Refs.[G$^+$05b, AKNT06] and define κ^{norm} measured relative to the physical magneton $\frac{1}{2M_N^{\text{phys}}}$:

$$\kappa^{\text{norm}} = \frac{M_N^{\text{phys}}}{M_N^{\text{lat}}}\kappa^{\text{lat}} = \frac{M_N^{\text{phys}}}{M_N^{\text{lat}}}F_2(0). \tag{5.8}$$

We then identify M_N in the SSE expressions as the physical nucleon mass. In the following comparisons of our results with chiral perturbation theories, the normalized magnetic moment κ_v^{norm} will be used throughout, and we drop the superscript "norm" unless there is an ambiguity.

As specified in Appendix D.1.1, at the order $\mathcal{O}(\epsilon^3)$ all the couplings in Eqs. (D.2 D.4) are meant to be taken in the chiral limit. Replacing them with the corresponding quantities at the physical point amounts to the inclusion of higher-order effects. As

long as the deviation between the values in the chiral limit and at the physical point is small, one expects such a replacement to yield little effect. To test this statement, in some cases we have performed the chiral fits using both the physical values and the chiral limit values for the low-energy constants and found no significant differences. In the following we will only present results obtained using the chiral limit values as inputs, which are summarized in Table 5.4.

Table 5.4: Input values for the low-energy constants in the fits: the nucleon axial charge g_A, the pion decay constant F_π and the mass difference $\Delta = M_\Delta - M_N$. These values correspond to the chiral limit $m_\pi \to 0$.

g_A	F_π [GeV]	Δ [GeV]
1.2	0.0862	0.293

Among the low-energy constants discussed in Appendix D.1.1, c_A and c_V are the two least known. In addition, we have little knowledge of the counterterms, $B_{10}^r(\lambda)$ and $E_1^r(\lambda)$, as well as the anomalous magnetic moment in the chiral limit, κ_v^0, from phenomenology. Lattice calculations in the chiral regime have the potential to constrain these parameters to unprecedented accuracy. Our attempt here is to check the consistency of our data with the predictions of chiral effective field theories, to estimate the range of applicability of the ChPT formulas, and to determine these low-energy constants when the formulas are applicable. To disentangle the investigation of the applicability of the ChPT formula from the possible discretization effects, we only include the results from the three fine ensembles in the chiral extrapolations discussed below. However, we want to point out that including the coarse results in the extrapolations does not change the central values of the fit parameters significantly, nor does it reduce the errors on the parameters since it only adds an additional interpolating point and does not provide a much stronger constraint on the parameters.

Since c_A appears in the formulas (D.2,D.3,D.4) for $(r_1^v)^2$, $(r_2^v)^2$ and κ_v, a simultaneous fit to all these three quantities would give a better constraint for the value of c_A. However, we have only three data points for each of these quantities, and κ_v alone has four parameters, three of which [c_V, $E_1^r(\lambda)$ and κ_v^0] are not constrained by any

other quantity. Thus the quark-mass dependence of κ_v cannot be used to constrain c_A. Therefore we choose to fit simultaneously[1] only $(r_1^v)^2$ and $\kappa_v \cdot (r_2^v)^2$ to determine c_A and $B_{10}^r(\lambda)$, and then use the resulting c_A as an input for the fit to κ_v. This way the three free parameters in κ_v are exactly specified by the three data points.

Table 5.5: Fit parameters from the SSE fits to the isovector Dirac radius $(r_1^v)^2$, Pauli radius $(r_2^v)^2$ and the anomalous magnetic moment κ_v. The HBChPT+Δ scale is $\lambda = 600$ MeV.

	χ^2/dof	c_A	c_V [GeV^{-1}]	κ_v^0	$B_{10}^r(\lambda)$	$E_1^r(\lambda)$ [GeV^{-3}]	$\mathcal{C}$ [GeV^{-3}]
No $\mathcal{C}$	17.0(4.0)	1.54(6)	8.7(5.8)	4.13(95)	1.20(17)	−4.67(42)	
With $\mathcal{C}$	3.8(2.2)	1.97(7)	7.5(4.5)	4.32(95)	2.58(25)	−5.58(42)	−0.51(7)

We present the resulting χ^2/dof and fit parameters normalized at scale $\lambda = 600$ MeV in the first row of Table 5.5 and plot the fit curves as the solid lines in Fig. 5-4. As indicated by a χ^2/dof of 17, the simultaneous fit to $(r_1^v)^2$ and $\kappa_v \cdot (r_2^v)^2$ does not describe the data. The problem is that our results for $(r_1^v)^2$ and $\kappa_v \cdot (r_2^v)^2$ favor different values for c_A. In fact, an independent fit to $(r_1^v)^2$ yields $c_A = 1.98(7)$, while an independent fit to $\kappa_v \cdot (r_2^v)^2$ gives $c_A = 1.39(10)$. The tension between these two quantities results in the large χ^2/dof in the simultaneous fit, indicating that the formulas given in Eqs. (D.3) and (D.4) do not describe our data consistently. As we can see from Fig. 5-4(b), the solid fit curve lies systematically higher than the data points, which then motivates us to use the $\mathcal{O}(m_\pi^0)$-corrected result in Eq. (D.5) instead of Eq. (D.4). With this modification, the simultaneous fit to $(r_1^v)^2$ and $\kappa_v \cdot (r_2^v)^2$, now using Eqs. (D.3,D.5), appears to describe the average value of the data much better, but still not the pion-mass dependence. We show the results in the second row of Table 5.5, and the fit curves (dashed lines) in Fig. 5-4. The fit describes $(r_1^v)^2$ very well, but c_A turns out to be larger than the range discussed earlier, which, not

[1] We note however, that in Ref. [G$^+$05b] it was already observed that the leading one-loop SSE formula for $(r_1^v)^2$ [Eq. (D.3)] is dominated by the leading chiral logarithm and dropped below the level of the lattice data available at that time for values of the pion mass as low as $m_\pi < 200$ MeV. This prompted the authors of Ref. [G$^+$05b] to exclude the isovector Dirac radius from the simultaneous fit. Likewise, the authors of Ref. [AKNT06] obtained huge, unrealistic values for the isovector Dirac radius when trying to enforce a fit of the logarithm-dominated behavior onto their data. Given these two negative precedents, we consider our "fit" to the isovector Dirac radius data to be of exploratory nature, testing the limits of applicability of the leading one-loop SSE results given in Eq. (D.3).

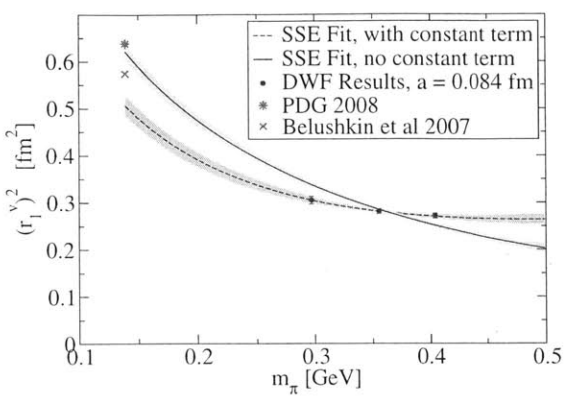

(a) Dirac radius $(r_1^v)^2$

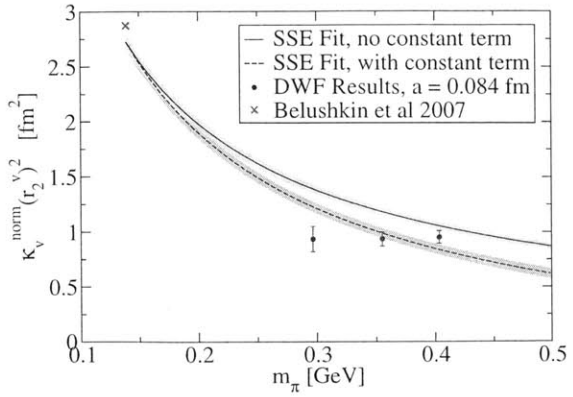

(b) Pauli radius $\kappa_v \cdot (r_2^v)^2$

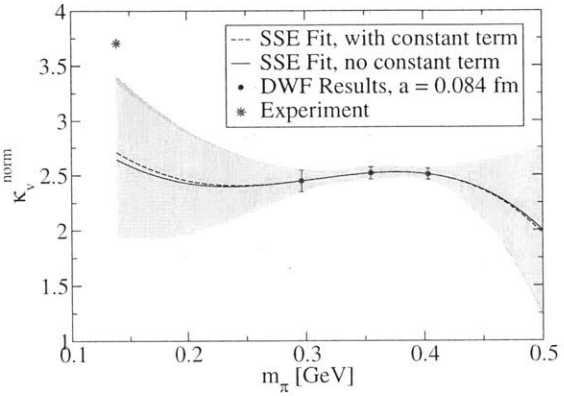

(c) anomalous magnetic moment κ_v

Figure 5-4: Chiral extrapolations for the isovector radii and the anomalous magnetic moment using the $\mathcal{O}(\epsilon^3)$ SSE formula, with (solid curves) or without (dashed curves) the constant term in Eq. (D.5). $(r_1^v)^2$ and $\kappa_v \cdot (r_2^v)^2$ are fit simultaneously, and κ_v is fit separately with c_A determined from the simultaneous fit.

surprisingly, gives rise to a smaller extrapolated value for $(r_1^v)^2$ than the experiments. Our new *Domain Wall* data extend the trend of the weak pion-mass dependence in $(r_2^v)^2$ observed in Refs. [G$^+$05b, AKNT06] now down into the range of pion masses ~ 300 MeV. The appearance of such a "plateaulike" behavior down to such light pion masses, which was also observed in Ref. [Y$^+$09], is surprising. The leading one-loop SSE formulas (D.4, D.5) for this radius cannot accommodate such a behavior, with or without the inclusion of the higher-order core term.

Using c_A determined from the above fits either with or without the constant term in Eq. (D.4) to $(r_1^v)^2$ and $\kappa_v \cdot (r_2^v)^2$, we fit κ_v to Eq. (D.2) with three unknown parameters, κ_v^0, c_V and $E_1^r(\lambda)$. The results are shown in Table 5.5. The value for

c_V from our fit turns out to have a different sign from that determined in [DMW91, HHK97] mentioned earlier. This is not surprising given that we only have three data points, which have little or no pion-mass dependence. We do not have the freedom to check the consistency of the fit, and we do not expect to obtain a reliable estimation for c_V, which, judging from Eq. (D.2), is very sensitive to the curvature of the data.

To compare chiral extrapolations with experiment, we have also plotted selected experimental data in Fig. 5-4. As noted in the introduction, there are still unresolved experimental questions, and we have indicated the range of possible values of $(r_1^v)^2$ that can be extracted from present experiments by showing two extreme results from the literature. The highest value is from PDG 2008 [A$^+$08b] and the lowest value is from a dispersion analysis including meson continuum contributions [BHM07]. We note that none of the chiral fits simultaneously yields a good fit to the lattice data while also agreeing with experiment within statistical errors.

To see how strongly the lattice results deviate from the SSE formulas, we also try to determine some of the low-energy constants using experimental results at the physical pion mass. We use the values in Table 5.4 as input, and also set $c_A = 1.5$ and $c_V = -2.5$ GeV^{-1}. Now for $(r_1^v)^2$, we have only the counter-term B_{10}^r to determine. Constraining the curve to go through the higher experimental value of $(r_1^v)^2 = 0.637$ fm^2 gives $B_{10}^r(\lambda = 600 \text{ MeV}) = 1.085$, resulting in the solid curve shown in Fig. 5-5(a). For comparison, we also plot the dashed curve that is fixed to go through the lower experimental value $(r_1^v)^2$. The curve rises much more rapidly than the lattice data as the pion mass decreases. From the slope of the leading one-loop SSE curve near the physical point and the weak pion-mass dependence displayed by our data we estimate that the applicability of Eq. (D.3) for $(r_1^v)^2$ may be much less than 300 MeV.

Without the constant term in Eq. (D.5), $\kappa_v \cdot (r_2^v)^2$ does not have any free parameters, which yields the solid curve in Fig. 5-5(b). The curve undershoots the physical point by about 5%, which may be well accounted for by the uncertainties in the chosen values of the low-energy constants. Including the higher-order term $\mathcal{C}$ of Eq. (D.5) can of course shift the curve up to exactly reproduce the product of physical Pauli radius and anomalous magnetic moment. However, the departure of the quark-mass

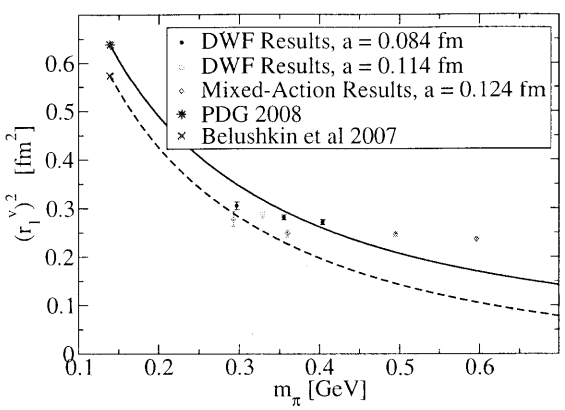

(a) Dirac radius $(r_1^v)^2$

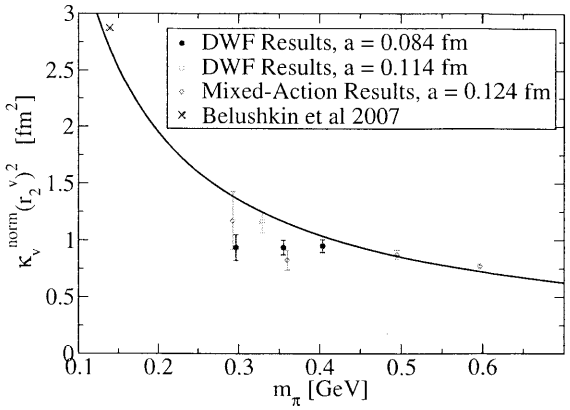

(b) Pauli radius $\kappa_v \cdot (r_2^v)^2$

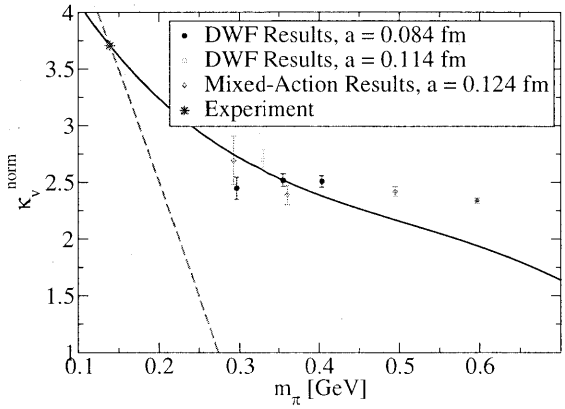

(c) anomalous magnetic moment κ_v

Figure 5-5: SSE chiral fits to the isovector radii and the anomalous magnetic moment constrained to go through the physical points using the input in Table 5.4 as well as $c_A = 1.5$ and $c_V = -2.5$ GeV^{-1}. The mixed-action results at $m_\pi = 355$ MeV are shifted slightly to the right for clarity.

dependent curve from the lattice data displayed in Fig. 5-5(b) indicates that the leading one-loop SSE formula for $\kappa_v \cdot (r_2^v)^2$ of Eqs. (D.4, D.5) should only be trusted for pion masses much less than the currently available 300 MeV. Judging from the steep slopes displayed by both the curves for the Dirac and Pauli radii as opposed to the almost mass-independent nature of the lattice data, it is conceivable that the leading one-loop SSE formulas may only be applicable at pion masses well below 300 MeV, as already suggested in Ref. [G$^+$05b].

The anomalous magnetic moment still has two free parameters, E_1^r and κ_v^0. In addition to the physical point, we need another data point to determine both parameters. We choose to use our $m_\pi = 355$ MeV result in the determination, since this

point is the most accurately calculated and its relatively large pion mass makes it less susceptible to finite-volume effects. The resulting curve (the solid line) is given in Fig. 5-5(c). For comparison, we also show the curve using the leading-order SSE formula in Eq. (D.1) (the dashed line). In this case, only the experimental point is included to determine κ_v^0. We can see that the dashed line deviates greatly from the lattice data. This is not surprising, as the dominating contribution to κ_v is the term linear in m_π, the coefficient of which is determined by $\frac{g_A^2 M_N}{4\pi F_\pi^2}$. This is clearly not the case in our data. Regarding the limit of applicability of Eq. (D.2) [which includes the dominant next-to-leading one-loop corrections to the strict $\mathcal{O}(\epsilon^3)$ SSE result of Eq. (D.1)], the plot in Fig. 5-5(c) does not give us a clear indication up to which pion mass the formula can be quantitatively employed. Furthermore, we observe that the "normalized" anomalous magnetic moments display a flat pion-mass dependence around 2.5 nuclear magnetons. The new dynamical *Domain Wall* data extend this "plateau" of the *normalized* magnetic moments – which was already observed at much larger pion masses in the quenched simulation of Ref. [G$^+$05b] – now into the region of pion masses as low as 300 MeV. Surprisingly, we can find no indication of a rise in the magnetic moment at these low pion masses, although the onset of such a rise had been anticipated for pion masses around 300 MeV in the fit results of Ref. [G$^+$05b] (see Fig. 11).

Overall, these curves show much stronger curvatures than our lattice results. Even with pion masses as light as 300 MeV, the $\mathcal{O}(\epsilon^3)$ SSE formulas do not seem to be consistent with our data. There are several possible explanations for the inconsistencies. One is that the pion masses in our simulations are still too heavy for the SSE formula at this order to be applicable, and the higher-order contributions may not be negligible in this range. The other possibility is that our results still suffer from uncontrolled systematic errors, such as finite-volume effects, especially at the light pion masses. We want to point out that our limited number of data points is not sufficient to constrain the chiral fits, which clearly demonstrates the need for calculations at lighter pion masses. Thus we do not regard our results in Table 5.5 as conclusive. Rather, we take it as an indication of the difficulty of chirally extrapolating currently

available lattice data.

Also plotted in Fig. 5-5 are our domain wall results at $m_\pi = 330$ MeV at a coarser lattice spacing [A$^+$08a] ($a \approx 0.114$ fm), as well as our updated mixed-action calculations [B$^+$10] at a lattice spacing of about 0.124 fm. These results are roughly consistent with the fine domain wall results, indicating that the discretization errors are small.

5.1.3 Chiral extrapolations using CBChPT

In this section we perform chiral extrapolations based on a formulation of $SU(2)$ baryon chiral effective field theory without explicit $\Delta(1232)$ degrees of freedom but treating both the nucleon and pion as relativistic particles. The chiral extrapolation formulas are collected in Appendix D.1.2.

In our chiral extrapolations, we treat g_A, F_π, c_2, c_3 and c_4 in Eqs. (D.20,D.22,D.21,D.23) as input parameters. The available information about the chiral limit values of g_A and F_π is discussed in Sec. D.1.1. We set the second-order couplings consistently with Refs. [BKM97, FMS98, EM02][2]. We summarize these values in Table 5.6.

Table 5.6: Input values for the covariant baryon chiral fits.

g_A	F_π [GeV]	c_2 [GeV^{-1}]	c_3 [GeV^{-1}]	c_4 [GeV^{-1}]
1.2	0.0862	3.2	-3.4	3.5

We determine M_0, c_1 and $e_1^r(\lambda)$ appearing in $M_N(m_\pi)$ by fitting the nucleon masses from the three fine *Domain Wall* ensembles to Eq. (D.21). The fit values are tabulated in Table 5.7 and the resulting fit curve is shown in Fig. 5-6. The fit (denoted as "Lattice only" in the table) is in excellent agreement with the physical nucleon mass, but the small number of data points included in the fit gives substantial statistical errors. To better constrain the value of M_0, which is needed in the subsequent fits, we also fit the data with the experimental point as a constraint (denoted as "Lattice+Exp."). The results are again shown in Table 5.7. The two fits give consistent results, and we

[2] For a discussion about the value of c_3 see [PMW$^+$06, AK$^+$04].

will use central values of M_0, c_1 and $e_1^r(\lambda)$ determined from the "Lattice+Exp." fit subsequently.

Table 5.7: Low-energy constants from the $\mathcal{O}(p^4)$ BChPT fit to the fine *Domain Wall* lattice results of the nucleon mass. In the "Lattice+Exp" fit we also impose that the curve goes through the physical point.

Fit	M_0 [GeV]	c_1 [GeV^{-1}]	$e_1^r\lambda = 1$ GeV)[GeV^{-3}]
Lattice only	0.883(79)	−1.01(26)	1.1(1.3)
Lattice + Exp.	0.8726(29)	−1.049(40)	0.90(32)

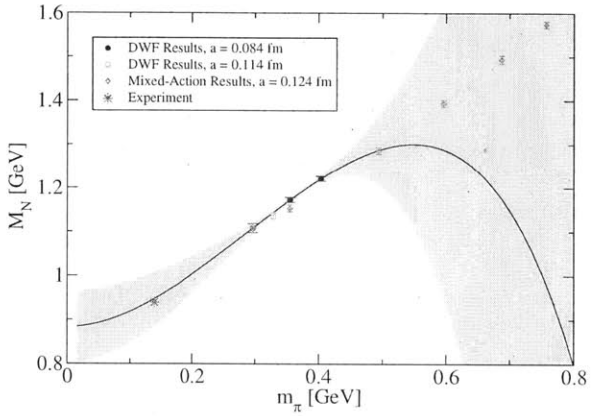

Figure 5-6: Chiral extrapolation for the nucleon mass using the $\mathcal{O}(p^4)$ BChPT formula in Eq. (D.21). The solid line is the fit to only the fine domain wall data (solid circles). The square is the coarse domain wall result, and the diamonds are the mixed-action results from Ref. [WL$^+$09].

For comparison, we also plot the coarse ($a = 0.114$ fm) domain wall result at $m_\pi \approx 330$ MeV, as well as the mixed-action results [WL$^+$09] at $a = 0.124$ fm in Fig. 5-6. We see that these results are qualitatively consistent, indicating the discretization errors are small.

Table 5.8: Fit parameters for the simultaneous fit to $(r_1^v)^2$, $\kappa_v \cdot (r_2^v)^2$ and κ_v using the $\mathcal{O}(p^4)$ CBChPT formulas. The scale is set to $\lambda = M_0$.

χ^2/dof	c_6	$d_6^r(\lambda)$ [GeV^{-2}]	e_{74}^r (λ) [GeV^{-2}]	e_{106}^r (λ) [GeV^{-3}]
7.3(2.4)	4.290(46)	0.839(7)	1.350(45)	−0.132(37)

We determine the remaining four low-energy constants, c_6, $d_6^r(\lambda)$, $e_{74}^r(\lambda)$, and $e_{106}^r(\lambda)$, from a simultaneous fit to $(r_1^v)^2$, $\kappa_v \cdot (r_2^v)^2$ and κ_v using $\mathcal{O}(p^4)$ BChPT expressions (D.20,D.22,D.23) presented in Appendix D.1.2, with the results shown in

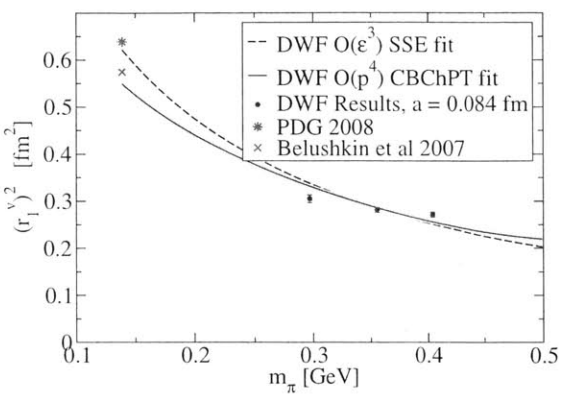

(a) Dirac radius $(r_1^v)^2$

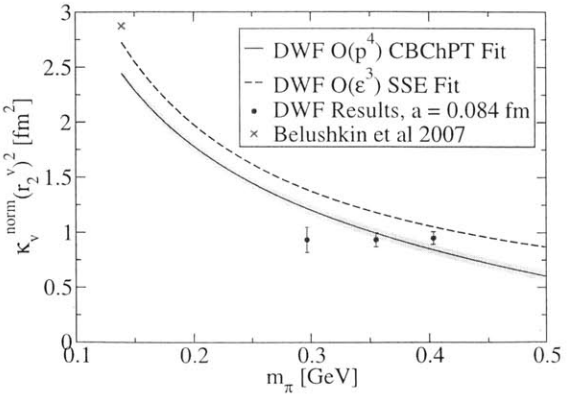

(b) Pauli radius $\kappa_v \cdot (r_2^v)^2$

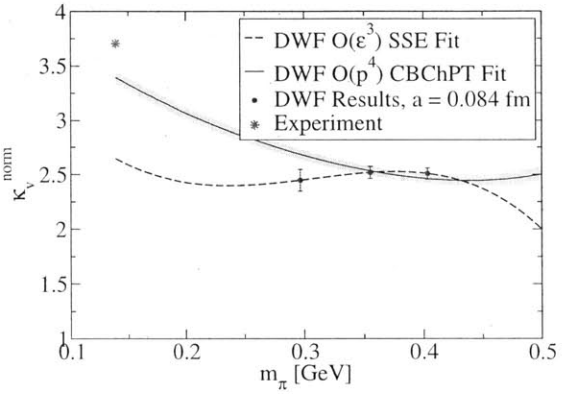

(c) anomalous magnetic moment κ_v

Figure 5-7: Simultaneous fit to the isovector radii and anomalous magnetic moment using the CBChPT formula (solid lines). The SSE formula fits without the constant term for $\kappa_v \cdot (r_2^v)^2$ (dashed line).

Table 5.8. The large χ^2/dof value indicates that the $\mathcal{O}(p^4)$ BChPT does not describe our data either. We compare the chiral extrapolations using both the BChPT formula and the $\mathcal{O}(\epsilon^3)$ SSE formula in Fig. 5-7. The solid curves with error bands are the results of the BChPT simultaneous fit, and the dashed curves are the SSE fits using Eqs. (D.3), (D.4) and (D.2) as described in Sec. 5.1.2. It appears that both the SSE and BChPT expressions are not compatible with our data, but since many of the low-energy constants in BChPT are fixed from phenomenology or the nucleon mass, the fit is better constrained than that using the $\mathcal{O}(\epsilon^3)$ SSE expressions. This is especially important for κ_v, for which the SSE expression involves more parameters than currently available lattice data. Nevertheless, both formulations fail to describe our data at this mass range.

5.2 $I = 0$ vector form factors

Although the isoscalar components of the nucleon form factors may contain unknown contributions from disconnected diagrams, we currently neglect them. In this section we give results for the isoscalar form factors as defined in Eq. (1.5) from the connected diagrams only. First, we study the Q^2 dependence of both the isoscalar Dirac and Pauli form factors using phenomenological models, and then discuss briefly the chiral extrapolations of the results.

5.2.1 Momentum transfer dependence

We perform dipole fits to $F_1^{u+d}(Q^2)$ separately for each ensemble using the formula in Eq. (5.3). Similar to the isovector case (see Sec. 5.1.1), the dipole Ansatz describes the data reasonably well at small Q^2 values, typically below 0.6 GeV^2. As large Q^2 values are included in the fit, the fit quality becomes worse, but the fit parameters do not change significantly. Furthermore, the fitted values of $F_1^{u+d}(0)$ are consistent with the expected value of 3.

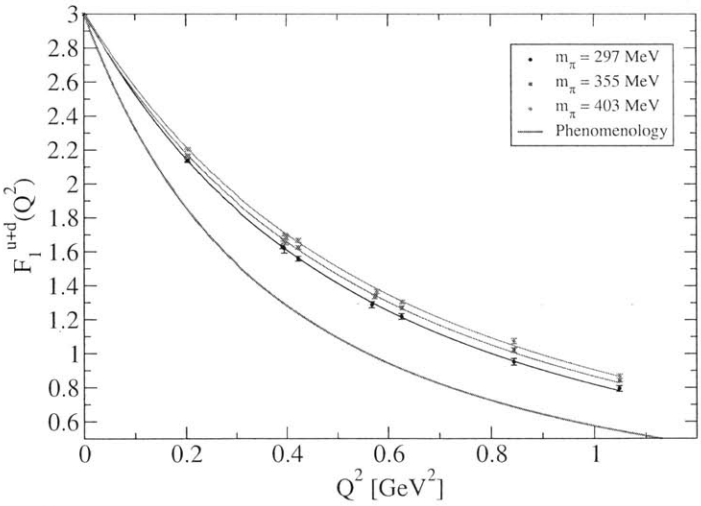

Figure 5-8: The lattice isoscalar Dirac form factor, $F_1^{u+d}(Q^2)$, dipole fits to it and the phenomenological fit [Kel04] to experimental data.

To demonstrate the quality of the fits, in Fig. 5-8 we show the dipole fits to all the Q^2 values. One can see that the data are reasonably well described by the

fit curves. Also plotted is the phenomenological fit to experimental data using the parameterization in Ref. [Kel04], although we note that no error estimate is provided and the empirical analysis involves many potential systematic errors discussed in the introduction. To determine the isoscalar mean squared Dirac radii, we follow the same reasoning as in Sec. 5.1.1 and obtain them from the dipole fits with a cut at $Q^2 \leq 0.5$ GeV^2. The results are shown in Table 5.9.

Table 5.9: Results for the isoscalar Dirac and Pauli mean squared radii and the anomalous magnetic moment from dipole and linear fits.

m_π [MeV]	χ^2/dof	$(r_1^s)^2$ [fm^2]	χ^2/dof	$\kappa_s^{\text{norm}} \cdot (r_2^s)^2$ [$\mu^{\text{phys}} \cdot$ fm^2]	κ_s^{norm} [μ^{phys}]
297	0.12(35)	0.428(5)	3.3(2.1)	−0.021(21)	−0.038(37)
355	0.97(98)	0.403(3)	1.4(1.4)	−0.015(11)	−0.030(22)
403	1.7(1.3)	0.385(3)	2.2(1.7)	−0.003(11)	0.011(21)

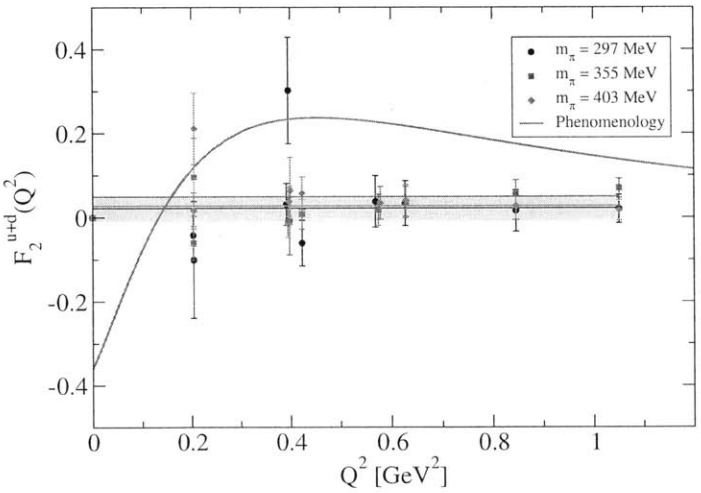

Figure 5-9: The isoscalar Pauli form factor, $F_2^{u+d}(Q^2)$, const(Q^2) fits and the phenomenological fit [Kel04] to experimental data.

In experiments, the isoscalar Pauli form factor shows a notable bump at $Q^2 \approx 0.4$ GeV^2 (solid curve in Fig. 5-9), although again there are no error estimates. Our data are too noisy to distinguish this feature at this moment. In fact, the results, shown in Fig. 5-9, are rather flat. We show the constant fits to each ensemble separately, and find that the constants are consistent with zero within 2 standard deviations. The error band corresponds to the constant fit to the $m_\pi = 297$ MeV data.

If we restrict the fits to only the small Q^2 region (≤ 0.5 GeV^2), we are able to

perform linear fits to the data and obtain both $\kappa_s \cdot (r_2^s)^2$ (from the slope) and κ_s (from the intercept), the results of which are also shown in Table 5.9[3].

5.2.2 Chiral extrapolations using HBChPT+Δ

As is well known in ChPT (e.g. see the discussion in [BFHM98]), chiral dynamics in the isoscalar form factors of the nucleon starts at the 3-pion cut, i.e. at two-loop level, corresponding to $\mathcal{O}(\epsilon^5)$ in the power-counting of SSE. Hence, the $\mathcal{O}(\epsilon^3)$ SSE expressions (D.6) have trivial pion-mass dependence and cannot be used for chiral extrapolations. Therefore, in this section, we simply extrapolate linearly in m_π^2 the mean squared Dirac radius to the physical point. This is shown in Fig. 5-10(a), where we can see that the linear extrapolation gives a result at the physical pion mass which is much lower than the empirical value. Similarly, we perform a linear extrapolation for $\kappa_s \cdot (r_2^s)^2$, which is shown in Fig. 5-10(b).

For κ_s beyond order ϵ^3, additional terms arise including a term linear in the quark mass. Following Ref. [HW02], we write

$$\kappa_s \;=\; \kappa_s^0 - 8E_2 M_N m_\pi^2, \tag{5.9}$$

where κ_s^0 and E_2 are two unknown LECs. This linear dependence describes our data well, as is shown in Fig. 5-10(c).

5.2.3 Chiral extrapolations using CBChPT

The BChPT formulas up to $\mathcal{O}(p^4)$ for $(r_1^s)^2$, $(r_2^s)^2$ and κ_s have also been derived in [Gai07, GH]. We collect them here for completeness in Appendix D.1.2. We note, however, that the next-to-leading one-loop BChPT results for the isoscalar form factors of the nucleon as presented in this section just as in the case of the leading one-loop SSE-analysis discussed in the previous section do not contain their dominant chiral dynamics arising from the 3-pion cut. Such effects would only become

[3] Like in the isovector case, the anomalous magnetic moment quoted here is normalized to the physical nuclear magneton according to Eq.(5.8).

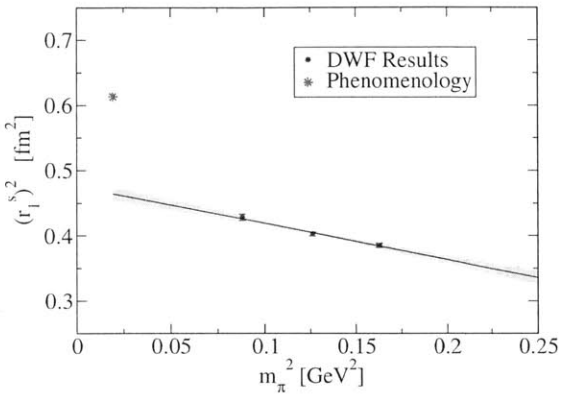

(a) Dirac radius $(r_1^s)^2$

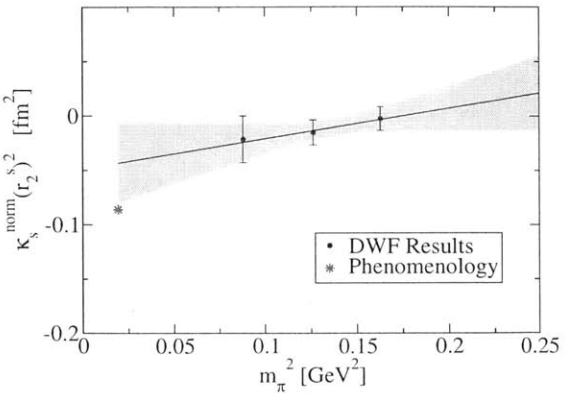

(b) Pauli radius $\kappa_s(r_2^s)^2$

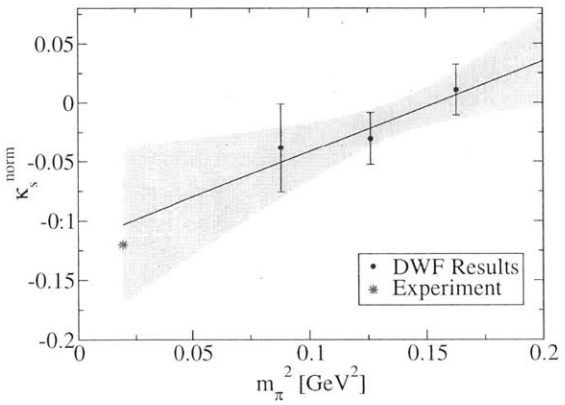

(c) anomalous magnetic moment κ_s

Figure 5-10: Linear extrapolations for the isoscalar radii and the anomalous magnetic moment. Shown also are the phenomenological values for radii obtained in Ref. [MMD96] and the experimental value [A$^+$08b] for κ_s (stars).

visible at the two-loop level, i.e. starting at $\mathcal{O}(p^5)$ in BChPT. The results presented here are therefore to be interpreted with care, as several important contributions with potentially large impact on the chiral extrapolation functions are not included at this order. For the isoscalar mean squared Dirac radius, Pauli radius and anomalous magnetic moments are given by Eqs. (D.24,D.25,D.26)

Table 5.10: Fit parameters from the *simultaneous* fit to $(r_1^s)^2$, $\kappa_s \cdot (r_2^s)^2$ and κ_s using Eqs. (D.24), (D.25) and (D.26).

χ^2/dof	κ_s^0	d_7	e_{54}	$e_{105}^r(\lambda = M_0)$
8.5(2.6)	−0.172(23)	−0.458(24)	−0.0159(41)	0.598(26)

As in the isovector case, we use the values in Table 5.6 as input in the extrapola-

Table 5.11: Fit parameters from *independent* fits to $(r_1^s)^2$, $\kappa_s \cdot (r_2^s)^2$ and κ_s using Eqs. (D.24), (D.25) and (D.26).

	χ^2/dof	κ_s^0	d_7
$(r_1^s)^2$	0.2(9)	2.67(44)	−0.581(19)
	χ^2/dof	κ_s^0	e_{54}
$\kappa_s \cdot (r_2^s)^2$	0.08(55)	1.6(2.0)	−0.055(44)
	χ^2/dof	κ_s^0	$e_{105}^r(\lambda = M_0)$
κ_s	0.4(1.3)	−0.247(53)	0.506(63)

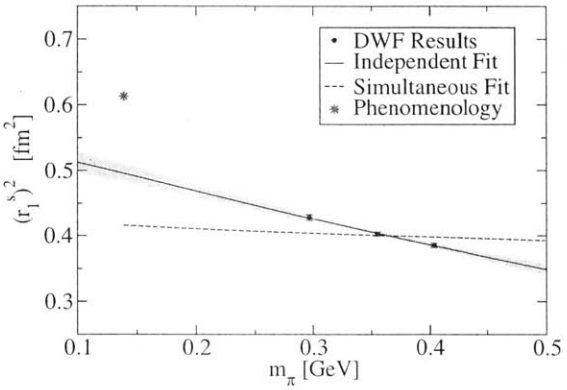

(a) Dirac radius $(r_1^s)^2$

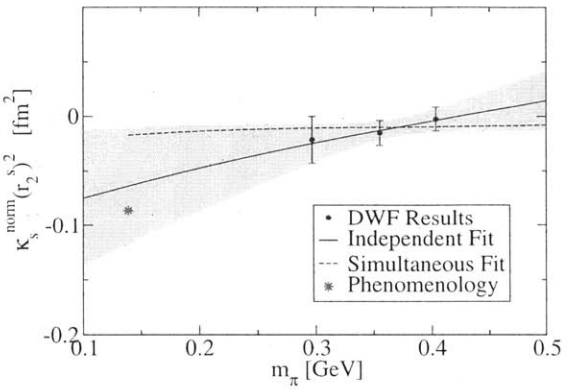

(b) Pauli radius $\kappa_s(r_2^s)^2$

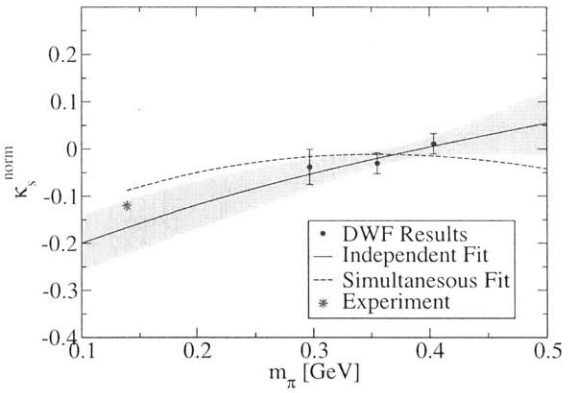

(c) anomalous magnetic moment κ_s

Figure 5-11: Simultaneous(dashed lines) and independent(solid lines) $\mathcal{O}(p^4)$ BChPT fits to the isoscalar radii and anomalous magnetic moment.

tions, leaving κ_s^0, d_7, e_{54} and $e_{105}^r(\lambda)$ as free parameters. Since $(r_1^s)^2$, $\kappa_s \cdot (r_2^s)^2$ and κ_s all contain the low-energy constant κ_s^0, naively we should perform a simultaneous fit to all three quantities, as we have done for the isovector case. However, as stated earlier, the dominant chiral dynamics for the isoscalar quantities only appears at $\mathcal{O}(p^5)$. We do not expect these $\mathcal{O}(p^3)$ expressions to describe our data. In fact, the simultaneous

fit to these three quantities gives a χ^2/dof of about 9 (see Table 5.10), showing the difficulty in fitting these quantities consistently. Looking closely at each quantity separately, we find that independent fits to $(r_1^s)^2$, $\kappa_s \cdot (r_2^s)^2$ and κ_s lead to an inconsistency in the estimation of the common parameter κ_s^0, as shown in Table 5.11. For demonstrative purposes, we compare the resulting fit curves from the simultaneous fit and the independent fits in Fig. 5-11, from which we see that the independent fits provide reasonable extrapolations for the data, while the simultaneous fit misses the data points badly, indicating inconsistencies of the BChPT expressions at this order. We also note that the extrapolated value for $(r_1^s)^2$ at the physical pion mass is about 20% lower than the phenomenological value. These observations lead us to conclude that the BChPT expressions at $\mathcal{O}(p^3)$ are not applicable in the pion-mass range of our calculation. Of course, since we have not included the disconnected diagrams in our calculations, there are uncontrolled systematic errors which may also affect the pion-mass dependence. Further investigations are required to draw definitive conclusions for these isoscalar quantities.

5.3 Axial form factors

5.3.1 Axial charge

The nucleon axial charge is an important phenomenological quantity, which, for example, determines the rate of the neutron β-decay (see Sec. 1.2). The lattice axial current operator $\left[\bar{q}\gamma_\mu\gamma^5 q\right]_x$ must be renormalized, and the renormalization procedure for Wilson-clover quarks is different from that for domain wall quarks. We have not renormalized the axial current. However, we can study the ratios in which the renormalization constant cancels to extract, for example, the axial radius in Section 5.3.2.

In order to compare our three calculations, in Figure 5-12 we show the ratio of the nucleon axial charge to the pion decay constant g_A/F_π, in which the axial current renormalization Z_A is canceled. The values for F_π are taken from Ref. [col]. On a small panel within Fig. 5-12 we show the ratio g_A/g_V that will give the renormalized

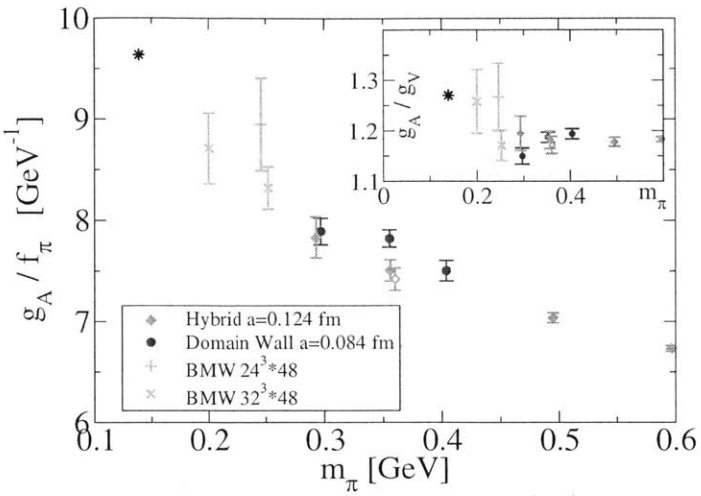

Figure 5-12: Nucleon axial charge to pion decay constant ratio, g_A/F_π for *Domain Wall* , *Hybrid* and *BMW* calculations. The upper right panel shows bare g_A/g_V ratio.

axial charge value in the chiral limit. Physical values are marked with black stars. It is notable that the data points for *Hybrid* and *Domain Wall* calculations lie approximately on the same line going towards a point slightly below the physical value. Although the uncertainty for small pion masses is still significant, it is reassuring that the newer calculations with *BMW* action (see Appendix A.3) continue the same trend. Note also that the two data points for *Hybrid* $m_\pi = 356$ MeV calculations in Fig. 5-12 correspond to the two different spatial volumes, $\approx (2.5 \text{ fm})^3$ (filled diamonds) and $\approx (3.5 \text{ fm})^3$ (open diamonds) and they are very close. The agreement between the results for different spatial volumes demonstrates that the finite volume effects are small. This fact also provides somewhat more optimistic estimate for the finite volume effects in g_A calculations compared to that in Ref. [Y$^+$09]: in our calculations the difference between the small volume ($m_\pi L \approx 4.5$) and large volume($m_\pi L \approx 6.3$) is equal to $\approx 0.006(22)$, while the authors in the reference above state that one has to have the spatial size of the box at least $L \gtrsim 6m_\pi^{-1}$ in order to have finite volume effects $\lesssim 1\%$. On the other hand, the value for the *Domain Wall* lattice with the lowest pion mass $m_\pi = 297$ MeV lies significantly below the heavier pion masses and may signal that the finite volume effects start to contribute to our calculations at the corresponding value of $m_\pi L \approx 4.05$. Thus, the question whether finite volume affects calculations of g_A remains to be understood, and one has to do calculations with two

different volumes at the same small pion mass to do a direct comparison.

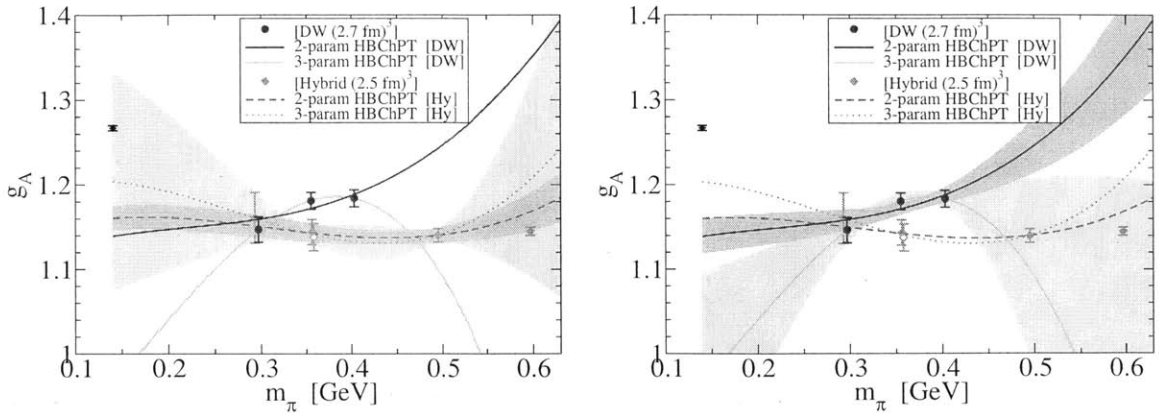

(a) *Hybrid* data extrapolation

(b) *Domain Wall* data extrapolation

Figure 5-13: Chiral extrapolations of the nucleon axial charge for the *Domain Wall* and *Hybrid* calculations. In the two-parameter HBChPT fit $g_1 = 2.5$ is set.

The renormalized g_A results enable a direct comparison between *Hybrid* and *Domain Wall* calculations. In Figure 5-13 we show data for both ensembles and perform a chiral extrapolation using the HBChPT prediction [HPW03]

$$\begin{aligned} g_A(m_\pi) = g_A &- \frac{g_A^3 m_\pi^2}{16\pi^2 F_\pi^2} + 4m_\pi^2\Big\{C(\lambda) + \frac{c_A^2}{4\pi^2 F_\pi^2}[\tfrac{155}{972}g_1 - \tfrac{17}{36}g_A] + \gamma \log\frac{m_\pi}{\lambda}\Big\} \\ &+ \frac{4c_A^2 g_A}{27\pi F_\pi^2 \Delta} m_\pi^3 + \frac{8c_A^2 g_A m_\pi^2}{27\pi^2 F_\pi^2}[1 - \tfrac{m_\pi^2}{\Delta^2}]^{\frac{1}{2}} \log R(m_\pi) \\ &+ \frac{c_A^2 \Delta^2}{81\pi^2 F_\pi^2}(25g_1 - 57g_A)\Big\{\log\tfrac{2\Delta}{m_\pi} - [1 - \tfrac{m_\pi^2}{\Delta^2}]^{\frac{1}{2}} \log R(m_\pi)\Big\}, \\ \text{where} \quad \gamma &= \frac{1}{16\pi^2 F_\pi^2}\Big[\frac{50}{81}c_A^2 g_1 - \frac{1}{2}g_A - \frac{2}{9}c_A^2 g_a - g_A^3\Big] \end{aligned} \tag{5.10}$$

The choice for the chiral limit parameters F_π, $\Delta = m_\Delta - m_N$, $c_A = g_{\pi N\Delta}$ is discussed in Sec. D.1.1. In addition, to perform the fits, we have to fix

$$c_A = 1.5,$$

for a three-parameter fit and also

$$g_1 = 2.5 \approx \frac{9}{5} g_A \quad \text{[quark-flavor symmetry]}$$

for a two-parameter fit. The only remaining parameters are the chiral limit value g_A^0 the counterterm $C(\lambda)$. The two-parameter fit is more reliable because there are data only three distinct values of $m_\pi \leq 500$ MeV in both *Domain Wall* and *Hybrid* calculations, and applying the HBChPT+Δ formula for $m_\pi > 500$ MeV is questionable. From the two-parameter fits we extract the values of extrapolated axial charge $g_A(m_\pi \approx 140 \text{ MeV})$,

$$g_A^{\text{phys}} = 1.160(14) \qquad [\textit{Hybrid }],$$
$$g_A^{\text{phys}} = 1.139(20) \qquad [\textit{Domain Wall }],$$

in our two calculations. Both results underestimate the experimental value $g_A = 1.126(3)$. This disagreement may be the result of the following:

1. heavy pion mass data points used for chiral extrapolations,

2. insufficient order of approximation in HBChPT+Δ

3. finite-volume effects contributing to the lightest pion mass values $m_\pi \approx 300$ MeV, to which the chiral extrapolations are most sensitive.

5.3.2 Momentum transfer dependence

From our lattice calculations we can also extract dependence of the nucleon axial form factors on the momentum transfer Q^2. Currently, the form factor results only for the *Domain Wall* and *Hybrid* calculations are available, because additional work to renormalize the axial current in the *BMW* calculation is required.

In Figure 5-14 we show our results for the G_A form factor from both *Domain Wall* and *Hybrid* calculations with the two lightest pion masses approximately equal to $m_\pi = 300$ and 350 MeV. Additionally, we show the results for the second (larger) volume $V \approx (3.5 \text{ fm})^3$ from *Hybrid* lattice with $m_\pi = 350$ MeV, which indicate no noticeable difference from the other (smaller) volume $V \approx (2.5 \text{ fm})^3$. This agreement demonstrates that the finite volume effects are small and negligible at our current

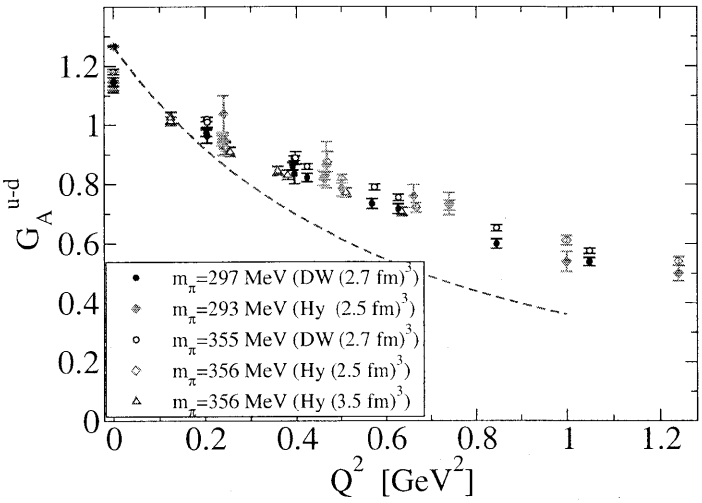

Figure 5-14: Q^2-dependence of the nucleon isovector axial form factor $G_A^{u-d}(Q^2)$.

level of precision. For comparison we also show the phenomenological dependence $G_A^{u-d}(Q^2)$,

$$G_A^{u-d}(Q^2) = \frac{g_A}{1 + Q^2/M_A^2}, \tag{5.11}$$

where the axial mass M_A is obtained from neutrino scattering experiments. It is clear that our lattice data points disagree with the phenomenology, both in the slope $G'_A(0)$ and the forward value $G_A(0) = g_A$. The disagreement in the slope may be ascribed to the pion mass being heavier than the physical pion.

Despite the disagreement with phenomenology, it is useful to check whether the lattice dependence of G_A on Q^2 is similar to the phenomenological dipole form (5.11). Therefore, we fit our data to the dipole form and present the results for the axial mass and the radius in Tab. 5.12. Because the axial current renormalization is multiplicative, we can also extract the axial mass M_A for the *BMW* ensemble calculations.

In Figure 5-15 we show the axial radius

$$\langle r_A^2 \rangle = -\frac{1}{6G_A(0)} \frac{dG_A(Q^2)}{dQ^2}\Big|_{Q^2=0} = \frac{12}{M_A^2} \tag{5.12}$$

for our three different calculations and the pion masses $300 \lesssim m_\pi \lesssim 600$ MeV. It is clear that the axial radius is significantly underestimated in our lattice calculations, which is also apparent from Fig. 5-14. However, the results from different lattice

Table 5.12: Dipole mass for lattice axial form factor $G_A^{u-d}(Q^2)$.

Ensemble	m_π [MeV]	V [fm^3]	M_A [GeV]	r_A [fm]
Domain Wall	297(5)	$(2.7)^3$	1.55(4)	0.441(10)
	355(6)	$(2.7)^3$	1.58(2)	0.432(6)
	403(7)	$(2.7)^3$	1.55(2)	0.441(6)
Hybrid	293	$(2.5)^3$	1.57(6)	0.436(15)
	356	$(2.5)^3$	1.66(3)	0.411(8)
	356	$(3.5)^3$	1.59(3)	0.431(7)
	495	$(2.5)^3$	1.65(2)	0.413(4)
	597	$(2.5)^3$	1.69(1)	0.405(3)
BMW	200	$(3.7)^3$	1.42(8)	0.482(27)
	250	$(3.7)^3$	1.50(6)	0.455(18)
	250	$(2.8)^3$	1.38(11)	0.495(40)

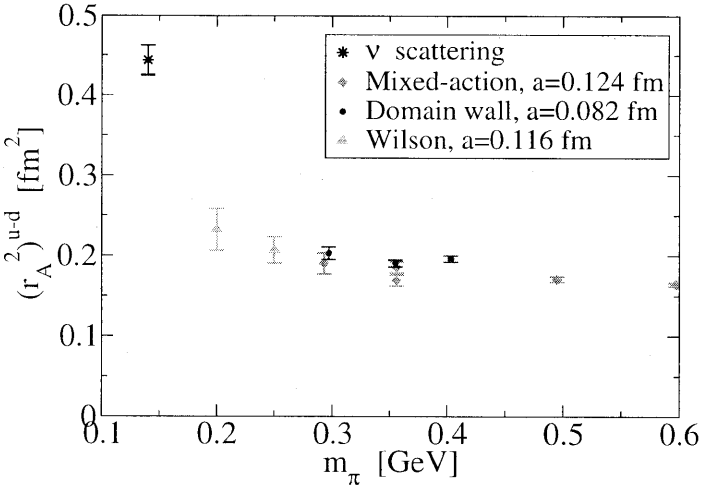

Figure 5-15: Nucleon isovector axial radius $\langle r_A^2 \rangle$.

methodologies agree demonstrating that this is a systematical trend, and the small values for $\langle r_A^2 \rangle$ are the consequence of simulating QCD with heavy pion masses. Moreover, our lattice results for the axial radius $\langle r_A^2 \rangle$ show very little dependence on the pion mass. It is worth noting that the prediction of heavy-baryon ChPT at next-to-leading order (NLO HBChPT+Δ) does not contain dependence of $\langle r_A^2 \rangle$ on m_π whatsoever [BFHM98],

$$G_A^{u-d}(Q^2) \approx g_A(m_\pi) - \tilde{B}_3 \frac{Q^2}{(4\pi F_\pi)^2}, \quad \langle r_A^2 \rangle^{u-d} = \frac{6\tilde{B}_3}{(4\pi F_\pi)^2}, \tag{5.13}$$

where $\tilde{B}_3$ is a low-energy constant. This prediction is in a striking disagreement with

the need to continue the accurate lattice data points to the physical pion mass value that is also shown in Fig. 5-15. Simulations at the lighter pion masses are necessary to reveal the $\langle r_A^2 \rangle$ dependence on the pion mass and to provide a basis to extend chiral perturbation theory accordingly.

In addition, in Fig. 5-15 we show the results for two different volumes for *Hybrid* lattices with $m_\pi = 350$ MeV, which disagree for less than 2 sigma. This disagreement is insufficient to state that we have significant finite volume effects, although we cannot exclude such possibility. Note that the larger volume corresponds to $m_\pi L > 6$ which is believed [Y+09] to be sufficient for finite volume effects in the nucleon axial charge calculations to be negligible.

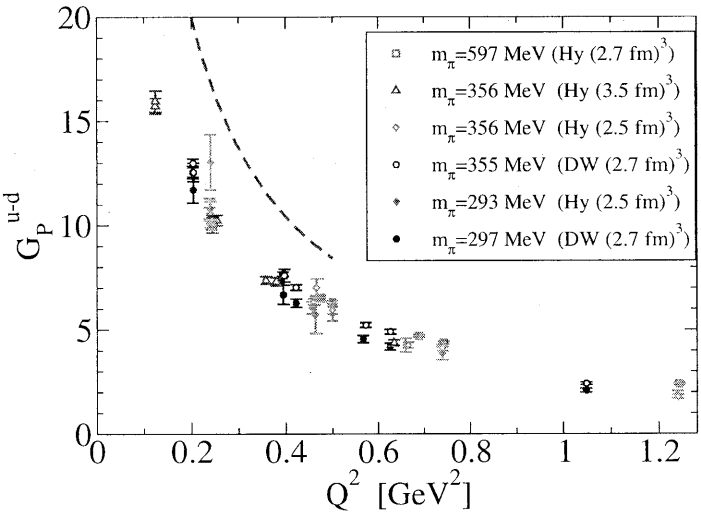

Figure 5-16: Nucleon isovector induced pseudoscalar form factor $G_P^{u-d}(Q^2)$.

The induced pseudoscalar form factor $G_P(Q^2)$ has an important phenomenological meaning. As was discussed in Sec. 1.2, this form factor is expected to be dominated by the pion pole. Hence, this is an important check for lattice QCD calculations at because one should observe significant variation of the Q^2-dependence of this form factor with the pion mass. In Figure 5-16 we show the $G_P(Q^2)$ for the two lightest pion masses, and one heavy pion mass from the *Hybrid* calculation. Unfortunately, it is not possible to compute G_P in the forward case $Q^2 = 0$ on a lattice. Our lowest Q^2 data point corresponds to $Q^2 \approx 0.2$ GeV^2. Without small $Q^2 \lesssim m_\pi^2$ data points, it is hard to check whether the data agrees with the pion-pole prediction or not.

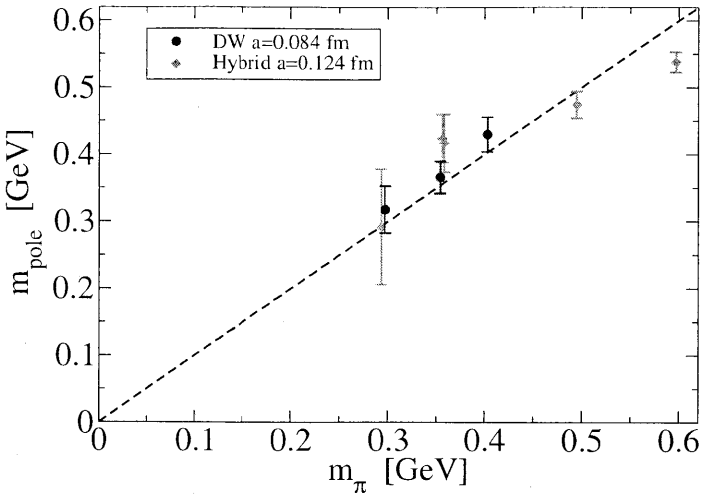

Figure 5-17: Pole mass from a fit using Eq. (5.14) and $m_{\text{pole}} = m_\pi$.

To answer this question, we fit our lattice data to a pole form

$$G_P(Q^2) = \frac{a}{m_{\text{pole}}^2 + Q^2} + b, \tag{5.14}$$

where a, b and m_{pole} are free fit parameters. The results of the fits for all ensembles and pion masses are presented in Fig. 5-17. Our lattice data for G_P form factor shows fair agreement with the pion pole model: the pole masses from the fit lie on the line $m_{\text{pole}} = m_\pi$ with the exception of the heaviest pion mass $m_\pi \approx 600$ MeV.

To conclude the discussion of the nucleon axial form factors, we attempt to check the Goldberger-Treiman relation $g_{\pi NN}(Q^2 = 0) = \frac{M_N}{F_\pi} g_A$ that must hold in (or close to) the chiral limit. Away from the chiral limit, the chiral perturbation theory predicts [BFHM98] that

$$G_P(Q^2) = \frac{4M_N^2}{m_\pi^2 + Q^2}\left[g_A - \frac{2m_\pi^2}{(4\pi F_\pi)^2}\tilde{B}_2\right] - \tilde{B}_3\frac{4M_N^2}{(4\pi F_\pi)^2}, \tag{5.15}$$

and the residue at the pole is determined by the axial charge $g_A = G_A(0)$ up to a correction proportional to m_π^2,

$$1 - \frac{g_{\pi NN}}{g_{\pi NN}^{\text{GT}}} \sim m_\pi^2, \quad \text{where } g_{\pi NN}^{\text{GT}} = \frac{M_N}{F_\pi} g_A. \tag{5.16}$$

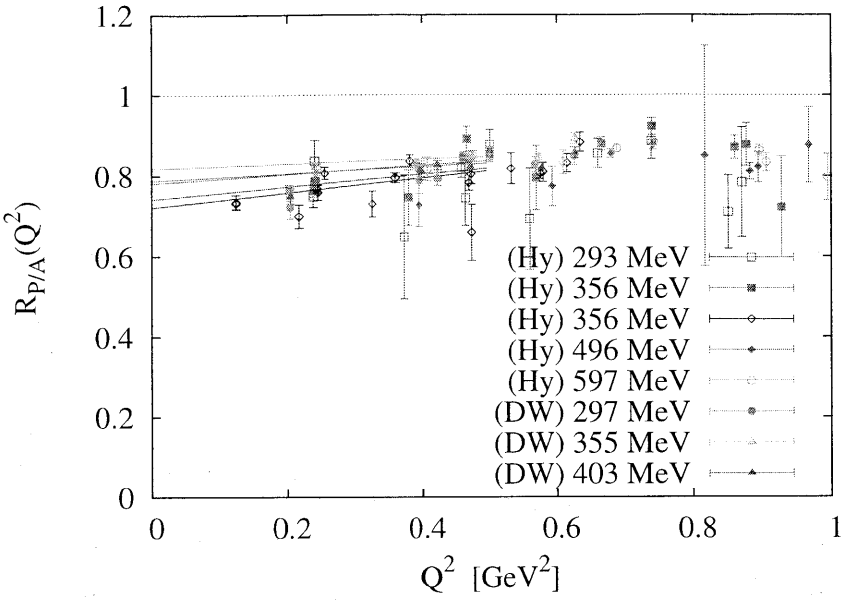

Figure 5-18: Check of GT relation. $R_{P/A}(Q^2)$ from Eq. (5.17) should be extrapolated to $Q^2 \to 0$ to obtain $g_{\pi N}/g_{\pi N}^{\rm GT}$. NLO Chiral perturbation theory predicts that $1 - g_{\pi N}/g_{\pi N}^{\rm GT} \sim m_\pi^2$.

Using only our lattice data, we cannot check this relation because direct calculation of the forward value $G_P(0)$ is not possible. In addition, because of the strong pole dependence of G_P on Q^2, the extrapolation $Q^2 \to 0$ is not reliable. Instead, we study the ratio

$$R_{P/A}(Q^2) = \frac{m_\pi^2 + Q^2}{4m_N^2} \cdot \frac{G_P(Q^2)}{G_A(Q^2)} \quad \underset{Q^2 \to 0}{\longrightarrow} \quad \frac{g_{\pi NN}(0)}{g_{\pi NN}^{\rm GT}}, \tag{5.17}$$

that should give the ratio$(g_{\pi NN}(0)/g_{\pi NN}^{\rm GT})$ in the limit $Q^2 \to 0$. Indeed, as Fig. 5-18 shows, this ratio depends weakly on the momentum transfer Q^2 and thus it is a good way to do the extrapolations and check the GT relation. However, the extrapolated values deviate significantly from one, indicating the violation of the Goldberger-Treiman relation by $\approx 20\%$. Furthermore, comparing the results for the pion masses $\approx 300 \div 600$ MeV, we observe *no dynamics* with decreasing m_π, and the NLO HBChPT+Δ prediction (5.16) does not agree with our data. This apparent violation may result either because the pion masses are too high or the method to do $Q^2 \to 0$ extrapolations is not correct. We definitely need to calculate the $G_P(Q^2)$ form factor for smaller non-zero values of Q^2 than performed in our work to control

Q^2 extrapolations better.

5.4 Quark energy-momentum tensor

As has been discussed in Sec. 1.3, one can compute quark contributions to the nucleon energy-momentum tensor by evaluating matrix elements of the twist-two Wilson $n = 2$ operator,

$$T_q^{\mu\nu} = \bar{q}\big[\gamma^{\{\mu} i\overleftrightarrow{D}^{\nu\}}\big]q\,, \tag{5.18}$$

which can be parameterized with three generalized form factors, A_{20}, B_{20} and C_{20} [Die03]:

$$\begin{aligned}\langle P'|\bar{q}\big[\gamma^{\{\mu} i\overleftrightarrow{D}^{\nu\}}\big]q|P\rangle = \bar{U}(P')\Big[&A_{20}^q(Q^2)\gamma^{\{\mu}\bar{P}^{\nu\}} \\ &+ B_{20}^q(Q^2)\frac{i}{2M_N}\bar{P}^{\{\mu}\sigma^{\nu\}\alpha}q_\alpha \\ &+ C_{20}^q(Q^2)\frac{1}{M_N}q^{\{\mu}q^{\nu\}}\Big]U(P).\end{aligned} \tag{5.19}$$

In order to compute quark momentum fraction and angular momentum, we need to extrapolate A_{20} and B_{20} form factors to $Q^2 \to 0$ and $m_\pi \to m_\pi^{\text{phys}}$.

5.4.1 CBChPT fits of generalized form factors

For our extrapolations we use relativistically-covariant chiral perturbation theory (CBChPT) calculations [DGH08] for the nucleon $n = 2$ generalized form factors that have recently become available. Although Ref. [DGH08] provides the formulas for the full Q^2 and m_π^2 dependence of the generalized form factors, we do not use them to fit our data with $Q^2 \gtrsim 0.2$ GeV^2 because they can be outside of the ChPT applicability range. Instead, we extrapolate our lattice data to the point $Q^2 = 0$ and fit the forward values of these generalized form factors. In addition to the form factors themselves, we include their slopes $\rho_{A,B,C}$

$$\rho_X = -\frac{d\,X}{d\,Q^2}\Big|_{Q^2=0} \tag{5.20}$$

into our chiral fits to impose further constraints on fit parameters. Formulas for $\rho_{A,B,C}$ are also available in Ref. [DGH08]. This approach is slightly different from Ref. [B$^+$10] where $Q^2 \neq 0$ points were also included into fits. However, because the data for GFFs with small momentum transfer are scarce (2 or 3 distinct Q^2 points), one can actually extract only *slopes* and *intercepts* of A_{20}, B_{20} and C_{20} dependence on the momentum transfer; more detailed structure of GFF dependence on Q^2 is not revealed by our current level of precision. We also find that including the GFF *slopes* $\rho_{A,B,C}$ to our chiral fits has very limited impact on constraining the fit parameters. Therefore, we conclude that the outcome of our procedure should be very close to the one used in Ref. [B$^+$10].

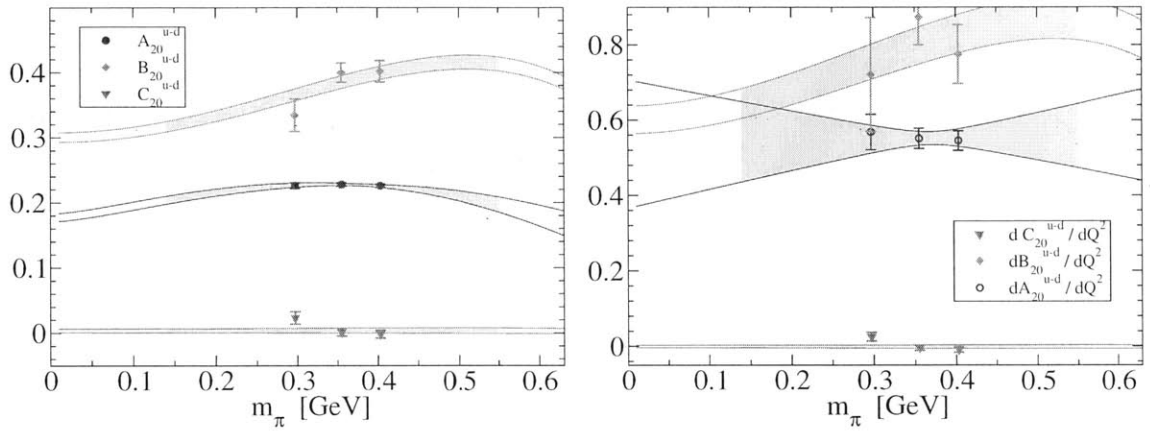

(a) Generalized form factors

(b) GFF slopes

Figure 5-19: Chiral extrapolations of the isovector generalized form factors A_{20}^{u-d}, B_{20}^{u-d}, A_{20}^{u-d} and their slopes $\rho_{A,B,C}$ using the *Domain Wall* calculations.

Table 5.13: Covariant chiral perturbation theory fits to the forward values of $n = 2$ generalized form factors at $\mu^2 = (2\text{ GeV})^2$, using the *Domain Wall* calculations.

GFF	$Q^2 \to 0$ extrapolation	$m_\pi = 140$ MeV	chiral limit	chi^2/ndf
A_{20}^{u-d}	dipole $Q^2 \leq 0.5$ GeV^2 †	0.204(6)	0.177(6)	
B_{20}^{u-d}	dipole $Q^2 \leq 0.5$ GeV^2	0.317(8)	0.306(7)	≈ 1.50
C_{20}^{u-d}	linear $Q^2 \leq 0.5$ GeV^2	0.0036(31)	0.0037(29)	
A_{20}^{u+d}	dipole $Q^2 \leq 0.5$ GeV^2 †	0.539(12)	0.531(13)	
B_{20}^{u+d}	linear $Q^2 \leq 0.5$ GeV^2	$-0.021(31)$	$-0.030(10)$	≈ 0.48
C_{20}^{u+d}	linear $Q^2 \leq 0.5$ GeV^2	$-0.123(26)$	$-0.131(38)$	

† Extrapolation is used only to extract the slope $\rho_A = -A'_{20}(0)$.

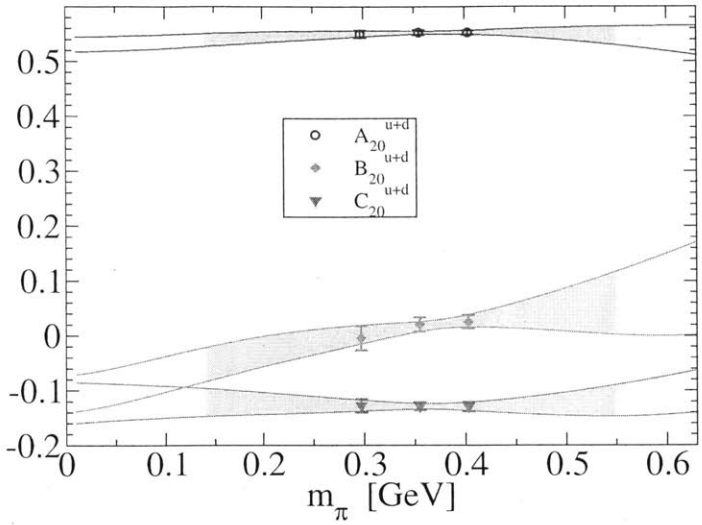

Figure 5-20: Chiral extrapolations of the isoscalar generalized form factors A_{20}^{u+d}, B_{20}^{u+d}, A_{20}^{u+d} using the *Domain Wall* calculations.

To extrapolate the GFFs to the point $Q^2 = 0$, we use a dipole form and switch to a linear form for form factors that are close to zero. The methods used in each case are listed in Tab. 5.13. Best fit curves to $A_{20}^{u\pm d}(Q^2)$, $B_{20}^{u\pm d}(Q^2)$ and $C_{20}^{u\pm d}(Q^2)$ data are shown in Fig. 5-29 and Fig. 5-30 for the *Domain Wall* and *Hybrid* calculations, respectively. The dependence of the $Q^2 \to 0$ extrapolated values on fit forms used is not significant, because the estimated uncertainties of the data points are dominated by their stochastic variations.

We perform a simultaneous fit to the isovector generalized form factors A_{20}^{u-d}, B_{20}^{u-d} and C_{20}^{u-d} and their slopes $\rho_{A,B,C}$ using Eq. (28,31,32) and Eq. (34-36) of Ref. [DGH08], which include the $\mathcal{O}(p^2)$ terms in the effective Lagrangian. In addition, these formulas include terms that "estimate" $\mathcal{O}(p^3)$ corrections. Our numerical analysis shows that these terms are important, in agreement with the results in Ref.[DGH08]. We fix the value of the parameter $\Delta a_{2,0}^v = 0.165$, which is known from the analysis of other lattice data [E$^+$06a], and the other 8 fit parameters

$$a_{2,0}^v,\ b_{2,0}^v,\ c_{2,0}^v,\ c_8^r,\ c_{12},\ \delta_A^t,\ \delta_B^t,\ \delta_C^t, \tag{5.21}$$

are free. The results of the fits to the *Domain Wall* data are shown in Fig. 5-19. In

this fit we use 18 data points and have 10 degrees of freedom. As indicated by the value $\chi^2/\text{dof} \approx 1.5$, our data are described well by the chiral perturbation theory. We summarize the physical and chiral limit values of GFFs at $Q^2 = 0$ in Tab. 5.13.

We also perform a simultaneous fit to the isoscalar generalized form factors A_{20}^{u+d}, B_{20}^{u+d} and C_{20}^{u+d} using Eq. (44,46,47) of Ref. [DGH08] and varying six parameters

$$a_{2,0}^{s},\ b_{2,0}^{s},\ c_{2,0}^{s},\ c_9,\ \delta_B^0,\ \delta_C^0, \tag{5.22}$$

where δ_B^0 and δ_C^0 also parameterize the $\mathcal{O}(p^3)$ contributions to the generalized form factors. Our data agree with the chiral perturbation theory results as indicated by the value $\chi^2/\text{dof} \approx 0.1$. Judging from such a small χ^2/dof value, we conclude that additional data and/or higher precision are required to constrain the fit parameters better. The physical and chiral limit values of the GFF at $Q^2 = 0$ are collected in Tab. 5.13.

Table 5.14: Covariant chiral perturbation theory fits to the forward values of $n = 2$ generalized form factors at $\mu^2 = (2\ \text{GeV})^2$ using the *Hybrid* calculations.

GFF	$Q^2 \to 0$ extrapolation	$m_\pi = 140$ MeV	chiral limit	chi^2/ndf
A_{20}^{u-d}	dipole $Q^2 \leq 0.5$ GeV^2 †	0.186(4)	0.159(4)	
B_{20}^{u-d}	dipole $Q^2 \leq 0.5$ GeV^2	0.292(7)	0.283(7)	≈ 1.25
C_{20}^{u-d}	linear $Q^2 \leq 0.5$ GeV^2	0.0027(48)	0.0028(45)	
A_{20}^{u+d}	dipole $Q^2 \leq 0.5$ GeV^2 †	0.500(8)	0.488(8)	
B_{20}^{u+d}	linear $Q^2 \leq 0.5$ GeV^2	−0.022(27)	−0.067(28)	≈ 1.4
C_{20}^{u+d}	linear $Q^2 \leq 0.5$ GeV^2	−0.125(28)	−0.118(39)	

† Extrapolation is used only to extract the slope $\rho_A = -A'_{20}(0)$.

We perform the same analysis for the *Hybrid* calculations results. The corresponding physical and chiral limit values are collected in Tab. 5.14.

5.4.2 Quark momentum fraction

In this section we present our results for the quark momentum fraction $\langle x \rangle$ determined from the GFF $A_{20}(0) \equiv \langle x \rangle$. We use the methods outlined in the previous section to extrapolate lattice results to the physical point for both the *Domain Wall* and *Hybrid* calculations.

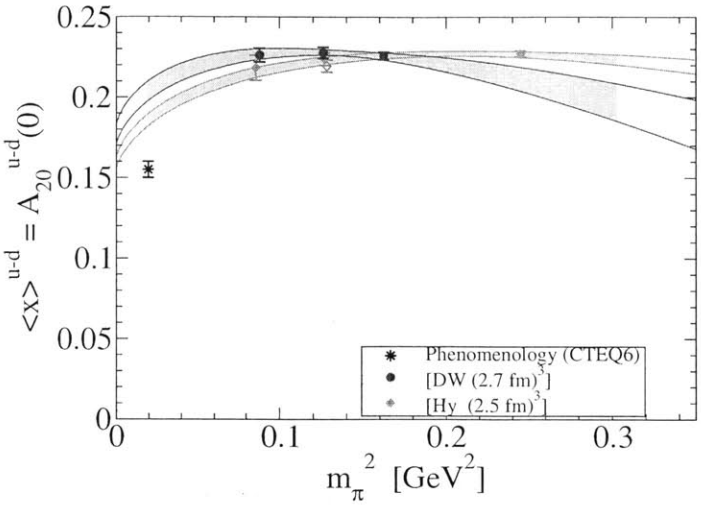

Figure 5-21: Comparison of the isovector quark momentum fraction from the *Domain Wall* and *Hybrid* calculations.

Figure 5-21 shows the isovector quark momentum fraction $\langle x \rangle_{u-d}$. In addition to our lattice results, we show the CTEQ6 PDF-parameterization result [DDG] $\langle x \rangle_{u-d}^{\text{CTEQ6}} = 0.155(5)$. Both the *Domain Wall* and the *Hybrid* results overshoot the phenomenological value significantly. As one can see from Fig. 5-21, chiral perturbation theory predicts rapid change of $\langle x \rangle_{u-d}$ as the pion mass approaches the physical pion mass. For this reason, more precise simulations at the lighter pion masses are required to resolve this disagreement.

Both lattice calculations lead to extrapolated values which are ≈ 2.5 standard deviations apart. This deviation can be explained either by discretization effects or by the perturbative renormalization used in the *Hybrid* calculations. Nevertheless, the agreement within $\approx 10\%$ between these independent lattice calculations is reassuring.

Figure 5-22 shows the isoscalar quark momentum fraction $\langle x \rangle_{u-d}$. In addition to our lattice results, we show the CTEQ6 PDF-parameterization result [DDG] $\langle x \rangle_{u+d}^{\text{CTEQ6}} = 0.537(22)$. Note that the *disconnected* contractions are omitted from our results presented in Fig. 5-22. Therefore, the apparent agreement between lattice and phenomenology must be taken as qualitative, potentially indicating that the disconnected contributions to the quark momentum fraction are small. As in the case of the isovector $\langle x \rangle_{u+d}$, two our lattice calculations agree within $\approx 8\%$, indicating that both lattice

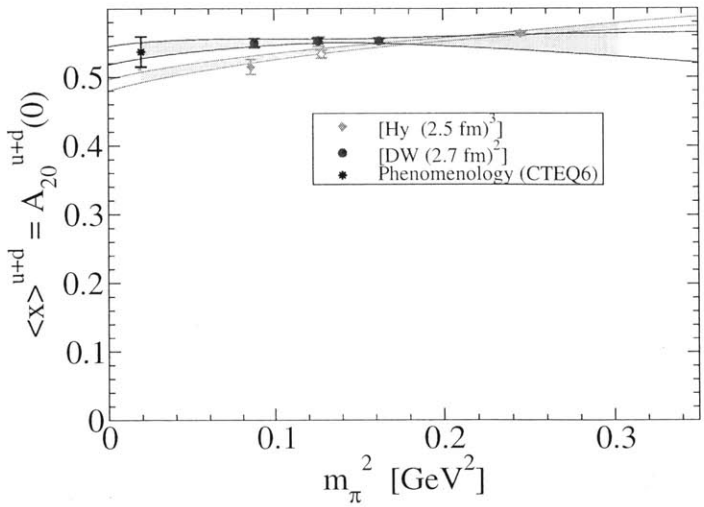

Figure 5-22: Comparison of the isoscalar quark momentum fraction from the *Domain Wall* and *Hybrid* calculations. Disconnected contractions are not included.

methodologies lead to reasonable results.

5.4.3 Quark angular momentum

The quark angular momentum inside the nucleon is a very important nucleon structure observable. As has been observed in DIS experiments, the quark spin contributes only $30 - 50\%$ to the nucleon spin [FJ01]. The rest must come from the quark *orbital angular momentum* and the gluon *total angular momentum*. On a lattice, the quark angular momentum is accessible through the matrix elements of the energy-momentum form factors A^q_{20} and B^q_{20}. According to Ji's sum rule [Ji97],

$$J^q = \frac{1}{2}\big(A^q_{20}(0) + B^q_{20}(0)\big). \tag{5.23}$$

The same is true for the gluon angular momentum,

$$J^g = \frac{1}{2}\big(A^g_{20}(0) + B^g_{20}(0)\big), \tag{5.24}$$

and the evident sum rule for the nucleon spin $J_q + J_g = \frac{1}{2}$ leads to an estimate for the gluon angular momentum, which has not been constrained experimentally. Furthermore, the sum rule for the momentum fraction carried by quarks and gluons

$\langle x \rangle_q + \langle x \rangle_g = A_{20}^q(0) + A_{20}^g(0) = 1$ automatically leads to another sum rule [Die03]

$$B_{20}^q(0) + B_{20}^g(0) = 0. \tag{5.25}$$

This sum rule has also been understood in terms of light-cone wave functions [BHMS01]. For future lattice calculations of nucleon structure the sum rule (5.25) may be useful because the direct computation of gluon contribution to the nucleon structure is difficult.

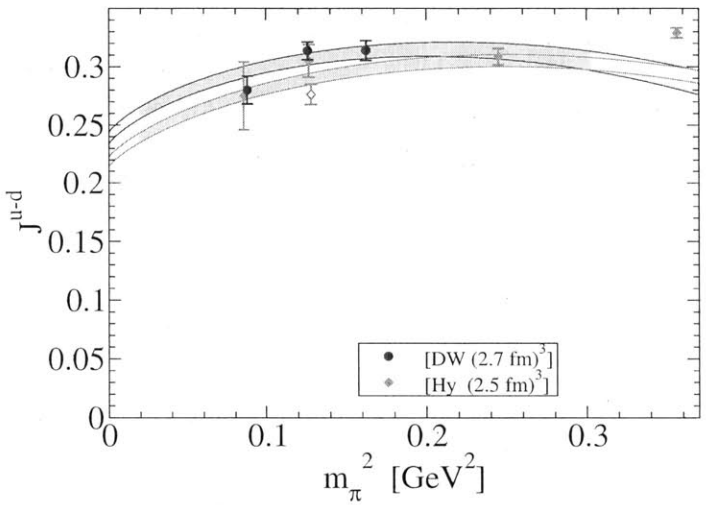

Figure 5-23: Comparison of the isovector quark angular momentum J^{u-d} from the *Domain Wall* and *Hybrid* calculations.

Table 5.15: Covariant chiral perturbation theory extrapolations of the quark angular momentum contributions to the nucleon spin. The renormalization scale is $\mu^2 = (2\ \text{GeV})^2$.

	Domain Wall		*Hybrid*	
	$m_\pi = 140$ MeV	chiral limit	$m_\pi = 140$ MeV	chiral limit
J^{u-d}	0.260(5)	0.239(5)	0.239(4)	0.219(4)
J^{u+d}	0.243(16)	0.213(17)	0.239(13)	0.212(14)
J^u	0.252(9)	0.226(10)	0.239(8)	0.215(8)
J^d	−0.009(8)	−0.013(9)	0.000(7)	−0.003(7)

Using the chiral extrapolations of our data in Sec. 5.4.1, we determine the angular momenta carried by quarks in the chiral limit and at the physical pion mass. The results are summarized in Tab. 5.15 for the u and d quarks as well as for the isovector

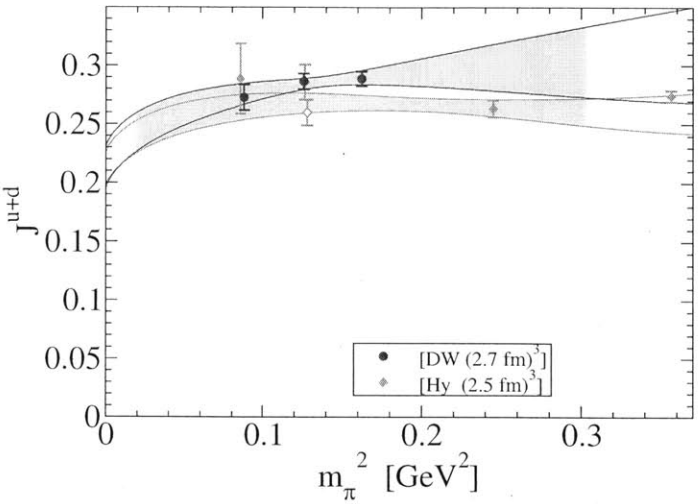

Figure 5-24: Comparison of the isoscalar quark angular momentum J^{u+d} from the *Domain Wall* and *Hybrid* calculations. Disconnected contractions are not included.

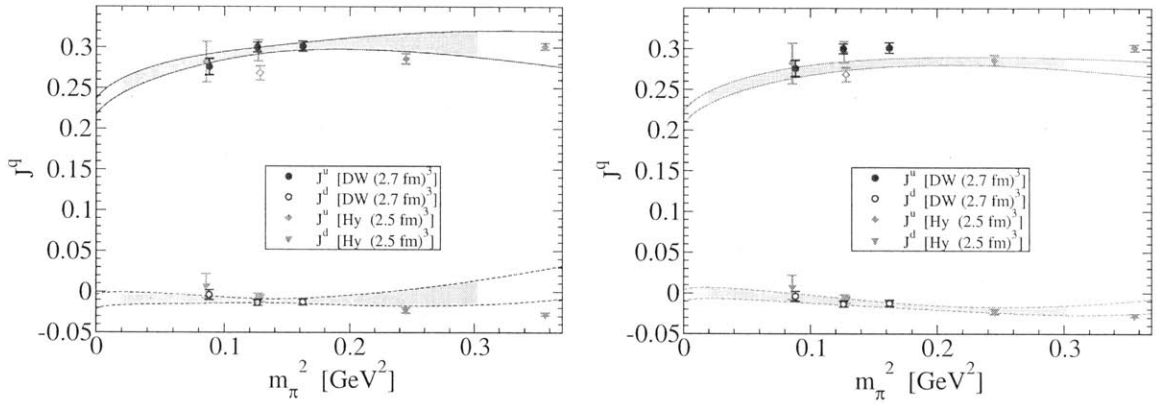

(a) *Domain Wall* data extrapolation

(b) *Hybrid* data extrapolation

Figure 5-25: Separate u and d quark contributions to the nucleon spin and their chiral extrapolations. Disconnected contractions are not included.

$u - d$ and isoscalar $u + d$ combinations.

The isoscalar angular momentum J^{u+d} represents the full contribution of quarks to the proton nucleon spin[4]. We determine this contribution at the physical pion mass as $J^q \equiv J^{u+d} = 0.24(1)$, or approximately 48% of the total nucleon spin. Although this result must be taken with some caution because of omitted contributions and disagreement of chiral extrapolations of isovector calculations with experiment, we note that it is in very close agreement with an estimation based on the QCD sum

[4] We emphasize once again that in this work we do not study the s quark contribution, as well as disconnected lattice field contractions (see Sec. 3.2).

rules [BJ97]. The determinations from the *Domain Wall* and *Hybrid* calculations agree perfectly, as illustrated by the comparison of their chiral extrapolations in Fig. 5-24.

In Figure 5-23 we show the isovector component of the quark angular momentum $J^{u-d} = J^u - J^d$. The results of the *Domain Wall* and *Hybrid* calculations for J^{u-d} disagree by $\approx 8\%$. We note that this disagreement is of the same order as the estimate of the uncertainty in the perturbative renormalization of *Hybrid* results (see Sec. 4.4). On the other hand, this disagreement may arise from different fermion actions used in the *Domain Wall* and *Hybrid* calculations.

Note that the values of J^{u+d} and J^{u-d} are very close. Correspondingly, the main contribution to J^q comes from the u quark, while the angular momentum of d quark is negligible. We show separate contributions of u and d quarks in Fig. 5-25. Although disconnected contractions are not included in $J^{u,d}$, the presented result is a strong indication that the major contribution to the nucleon spin as seen at our working scale $\mu^2 = (2\ \mathrm{GeV})^2$ comes from u quarks and gluons and not d quarks. For the d-quarks, as our investigation shows, the spin and the OAM cancel each other almost precisely, and this remarkable feature remains to be understood in nucleon models.

5.4.4 Quark spin and OAM

Finally, we want to discuss the decomposition of the quark angular momentum in terms of the quark spin and the quark orbital angular momentum (OAM) inside the nucleon. As it has been shown in Ref. [Ji97, Ji98], such decomposition is gauge-invariant:

$$J_q = S_q + L_q = \int d^3x \left[\frac{1}{2} q^\dagger \sigma^{12} q + q^\dagger \left(x^1\, iD^2 - x^2\, iD^1\right) q\right], \tag{5.26}$$

where J_q, S_q and L_q are the projections of total angular momentum, spin and OAM of quarks, respectively, on the z-axis. This decomposition may be useful for connecting the fundamental calculations in lattice QCD to quark models, which can be thought of as effective QCD models at much smaller scale $\mu < m_N$ [Tho08].

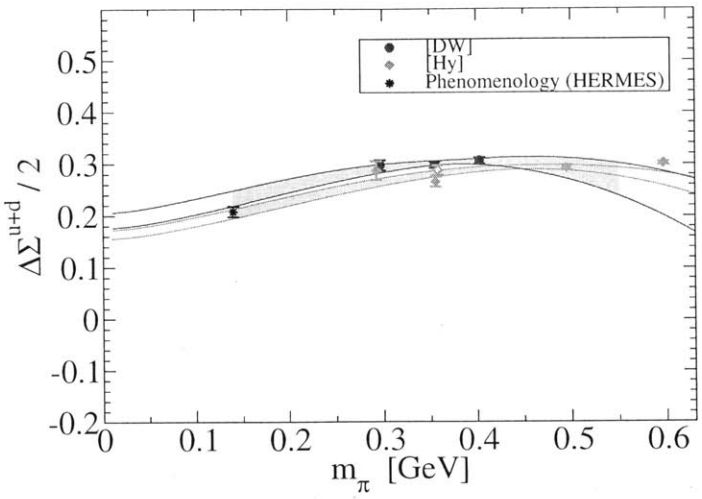

Figure 5-26: Comparison of the total quark spin contribution to the nucleon spin from the *Domain Wall* and *Hybrid* calculations. Disconnected contractions are not included.

The quark spin can be extracted from the forward value of the generalized form factor $\tilde{A}^q_{10}$,

$$S_q \equiv \frac{1}{2}\Delta\Sigma_q = \frac{1}{2}\langle 1\rangle_{\Delta q} = \frac{1}{2}\tilde{A}^q_{10}(0). \tag{5.27}$$

Note that the isovector combination $\Delta\Sigma_{u-d} = \langle 1\rangle_{\Delta u-\Delta d}$ is equal to the axial charge g_A that has already been discussed in Sec. 5.3.1, and in this section we will use the chiral extrapolation based on HBChPT+Δ presented there. In order to compute the individual quark spins, we perform chiral extrapolations of the isoscalar combination $\Delta\Sigma_{u+d} = \tilde{A}^{u+d}_{10}(0) = \langle 1\rangle_{\Delta u+\Delta d}$ using the HBChPT prediction [DMS07]

$$\tilde{A}^{u+d}_{n,0}(t=0) = \tilde{A}^{u+d,(0)}_{n,0}\Big[1 - \frac{3g_A^2 m_\pi^2}{(4\pi F_\pi)^2}\big(1 + \log\frac{m_\pi^2}{\mu_\chi^2}\big)\Big] + \tilde{A}^{u+d,(2,m)}_{n,0} m_\pi^2 \tag{5.28}$$

with two free parameters, $\tilde{A}^{u+d,(0)}_{n,0}$ and $\tilde{A}^{u+d,(2,m)}_{n,0}$, where μ_χ is a HBChPT scale. Figure 5-26 shows the comparison of the *Domain Wall* and *Hybrid* results as well as their chirally extrapolated values shown as the shaded bands. We collect the extrapolation results at the physical pion mass and in the chiral limit in Table 5.16. Note that the *Domain Wall* and *Hybrid* results show reasonable agreement.

Using the decomposition (5.26) above, we subtract the spin component from the quark angular momentum to obtain quark OAM. A summary of the results for both u

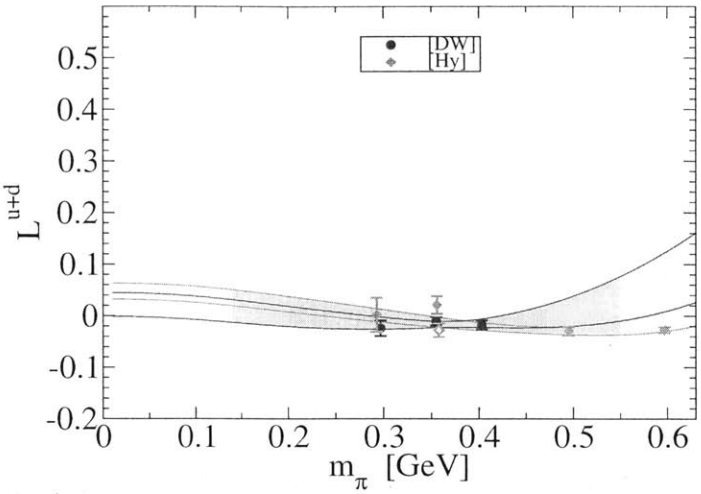

Figure 5-27: Comparison of the quark orbital angular momentum contributions to the nucleon spin from the *Domain Wall* and *Hybrid* calculations. Disconnected contractions are not included.

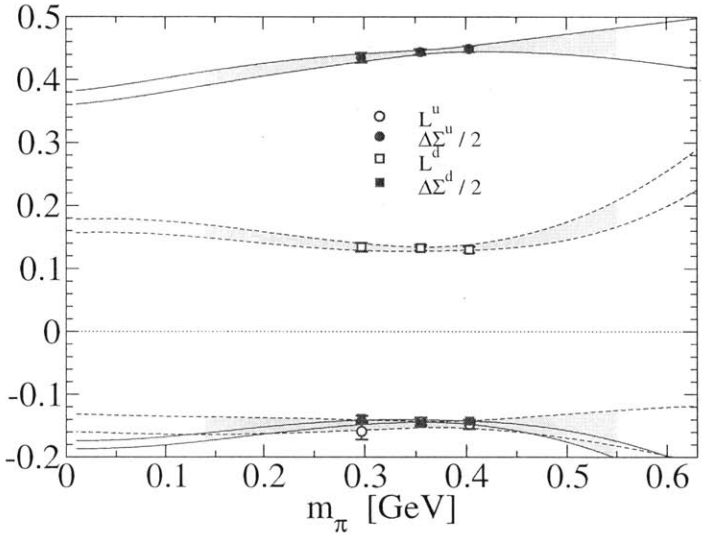

Figure 5-28: Contributions of the u and d quark spin and orbital angular momenta to the nucleon spin from the *Domain Wall* calculations. Disconnected contractions are not included.

and d quarks as well as their combinations is presented in Tab. 5.17. Again, we note that the results from the *Domain Wall* and *Hybrid* calculations reasonably agree. The small discrepancy between them can be explained either by the different lattice QCD actions, lattice spacings, or the renormalization procedures.

In Figure 5-28 we show the comparison of u and d quark spin and OAM contributions to the nucleon spin. We would like to discuss the decomposition of J^q into

Table 5.16: Covariant chiral perturbation theory extrapolations of the quark spin contributions to the nucleon spin.

	Domain Wall		*Hybrid*	
	$m_\pi = 140$ MeV	chiral limit	$m_\pi = 140$ MeV	chiral limit
$\frac{1}{2}\Delta\Sigma^{u-d}$	0.570(10)	0.552(9)	0.580(7)	0.564(6)
$\frac{1}{2}\Delta\Sigma^{u+d}$	0.234(14)	0.191(14)	0.204(9)	0.164(8)
$\frac{1}{2}\Delta\Sigma^{u}$	0.402(11)	0.372(10)	0.392(7)	0.364(6)
$\frac{1}{2}\Delta\Sigma^{d}$	−0.168(6)	−0.180(6)	−0.188(4)	−0.200(4)

$S^{u,d}$ and $L^{u,d}$ in detail because it demonstrates a number of peculiar features. First, as has been noted in the previous section, the total d-quark angular momentum is very small. However, its spin and OAM are not small separately, and J^d being small is a result of almost precise cancellation between the spin S^d and the OAM L^d of the d-quark, and

$$|J^d| \ll \{|S^d|, |L^d|\}.$$

Second, in Figure 5-27 we show the sum of u and d quark OAM. Again, although the individual quark orbital angular momenta $L^{u,d}$ are not small, they are opposite and compensate each other so that

$$|L^{u+d}| \ll |L^{u,d}|.$$

Both these observation are in complete agreement with the previous calculations in Ref. [H$^+$08] and [B$^+$10]. Similar observations in the *Domain Wall* and *Hybrid* calculations lead to the conclusion that this is indeed a physical effect and it should be accounted for in nucleon models.

Table 5.17: Covariant chiral perturbation theory extrapolations of the quark orbital angular momentum contributions to the nucleon spin. The renormalization scale is $\mu^2 = (2\ \text{GeV}^2)$.

	Domain Wall		*Hybrid*	
	$m_\pi = 140$ MeV	chiral limit	$m_\pi = 140$ MeV	chiral limit
L^{u-d}	−0.309(10)	−0.313(10)	−0.341(7)	−0.346(6)
L^{u+d}	0.009(21)	0.022(22)	0.035(15)	0.048(15)
L^{u}	−0.150(13)	−0.146(14)	−0.153(9)	−0.149(9)
L^{d}	0.159(10)	0.168(10)	0.188(8)	0.197(8)

5.5 Generalized form factors

In this section we present an overview of our results for the nucleon generalized form factors. In Section 5.4 we have already discussed the $n = 2$ unpolarized GFF A_{20} and B_{20}. Now we will discuss these and other generalized form factors in more detail. However, because the topic of the nucleon GFFs is vast, we only highlight their most peculiar features revealed by our calculations and demonstrate the precision we are able to achieve, and postpone the systematic discussion to future publications.

5.5.1 Momentum transfer dependence

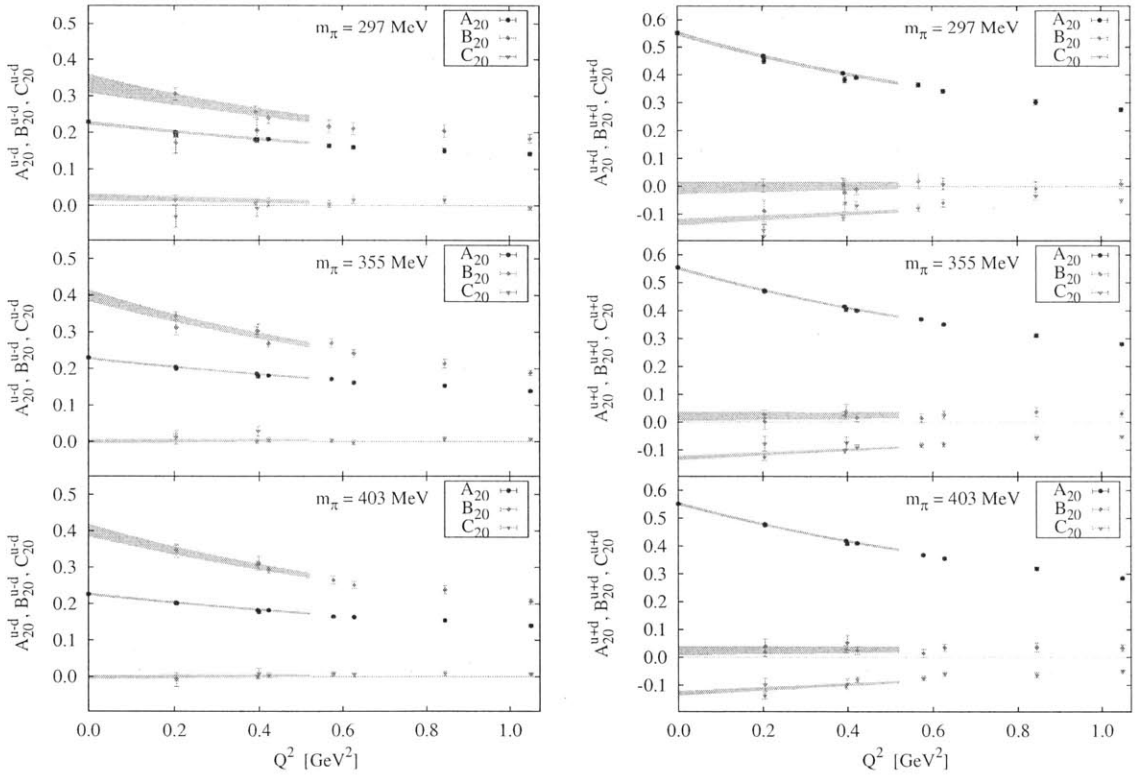

(a) Isovector (b) Isoscalar

Figure 5-29: $n = 2$ spin-independent generalized form factors from the *Domain Wall* calculation. Disconnected contractions are not included in the isoscalar parts.

In Figures 5-29 and 5-30 we present the dependence of the isovector and isoscalar GFFs A_{20}, B_{20} and C_{20} on the momentum transfer Q^2. We fit these form factors with a dipole form, with the resulting bands shown on the figures. The dipole form

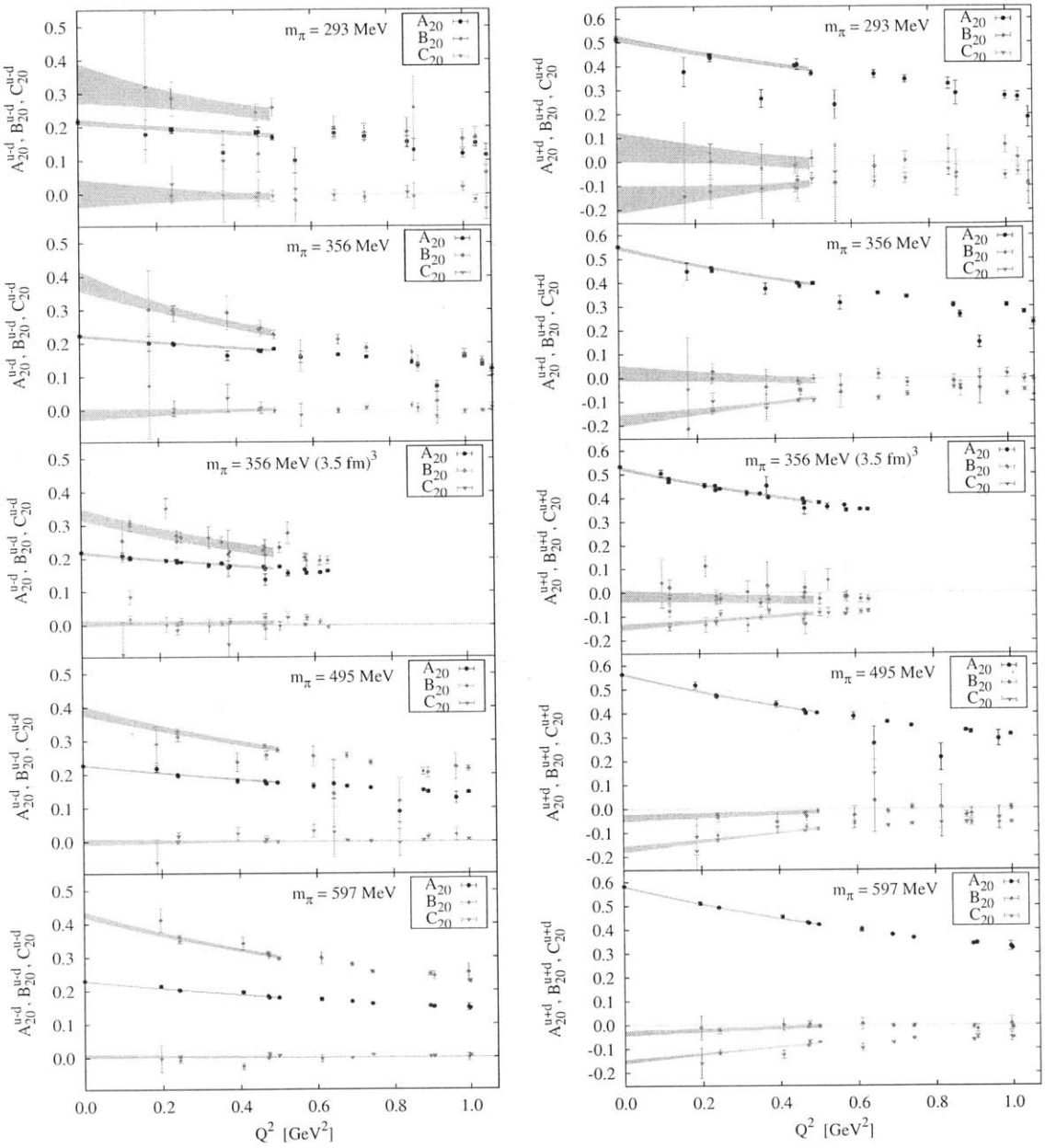

(a) Isovector

(b) Isoscalar

Figure 5-30: $n = 2$ spin-independent generalized form factors from the *Hybrid* calculation. Disconnected contractions are not included into the isoscalar parts.

is chosen because it is also employed in various phenomenological parameterizations of the GFFs, e.g., in Ref. [GV98]. For the form factors B_{20}^{u+d} and C_{20}^{u-d} that are consistent within their error bars or very close to zero we resort to a linear form to guarantee the stability of fits.

Results of both the *Domain Wall* and *Hybrid* calculations demonstrate similar trends for the magnitude of $n = 2$ unpolarized GFFs,

$$|C_{20}^{u-d}| \ll |A_{20}^{u-d}| < |B_{20}^{u-d}|,$$
$$|B_{20}^{u+d}| \ll |C_{20}^{u+d}| < |A_{20}^{u+d}|.$$

The relative magnitude of the form factors is of interest because according to Eq. (1.21) $C_{20}(t)$ determines the dependence of the generalized moments $H^{n=2}(\xi, t)$ and $E^{n=2}(\xi, t)$ on the longitudinal momentum fraction ξ. The (approximate) independence of the $n = 2$ isovector generalized moments $H^{n=2}$ and $E^{n=2}$ may be a relevant constraint for phenomenological analyses of future experimental data.

In addition, comparing isovector and isoscalar GFFs, we find qualitative agreement with the large-N_c scaling rules [GPV01],

$$|A_{20}^{u-d}| \sim N_c \ll |A_{20}^{u+d}| \sim N_c^2,$$
$$|B_{20}^{u-d}| \sim N_c^3 \gg |B_{20}^{u+d}| \sim N_c^2,$$
$$|C_{20}^{u-d}| \sim N_c \ll |C_{20}^{u+d}| \sim N_c^2.$$

The data for spin-dependent form factors has generally more stochastic variation. In Figure 5-31 we show the Q^2-dependence of the spin-dependent generalized form factors $\tilde{A}_{20}$ and $\tilde{B}_{20}$. There is no spin-dependent counterpart of C_{20}. We fit $\tilde{A}_{20}$ with a dipole form and $\tilde{B}_{20}$ with a linear form in the entire available range $0 \leq Q^2 \lesssim 1$ GeV^2.

We also present our observations how the Q^2-dependence of the zero-skewness generalized moment $H^n(\xi = 0, Q^2) \equiv A_{n,0}$ changes with n. It is easy to see from Eq. (1.18) that increasing n leads to amplifying the contribution of the quarks with large longitudinal momentum fraction x to the $H^n(\xi = 0, Q^2)$ moment. On the other hand, the 2D Fourier transform of the distribution $H(x, \xi = 0, -Q^2)$ in the transverse plane

$$H(x, b_\perp^2) = \int \frac{d^2 q_\perp}{(2\pi)^2} e^{-ib_\perp \cdot q_\perp} H(x, \xi = 0, t = -q_\perp^2) \tag{5.29}$$

has a probability interpretation [Bur00] for a quark to be found at the transverse

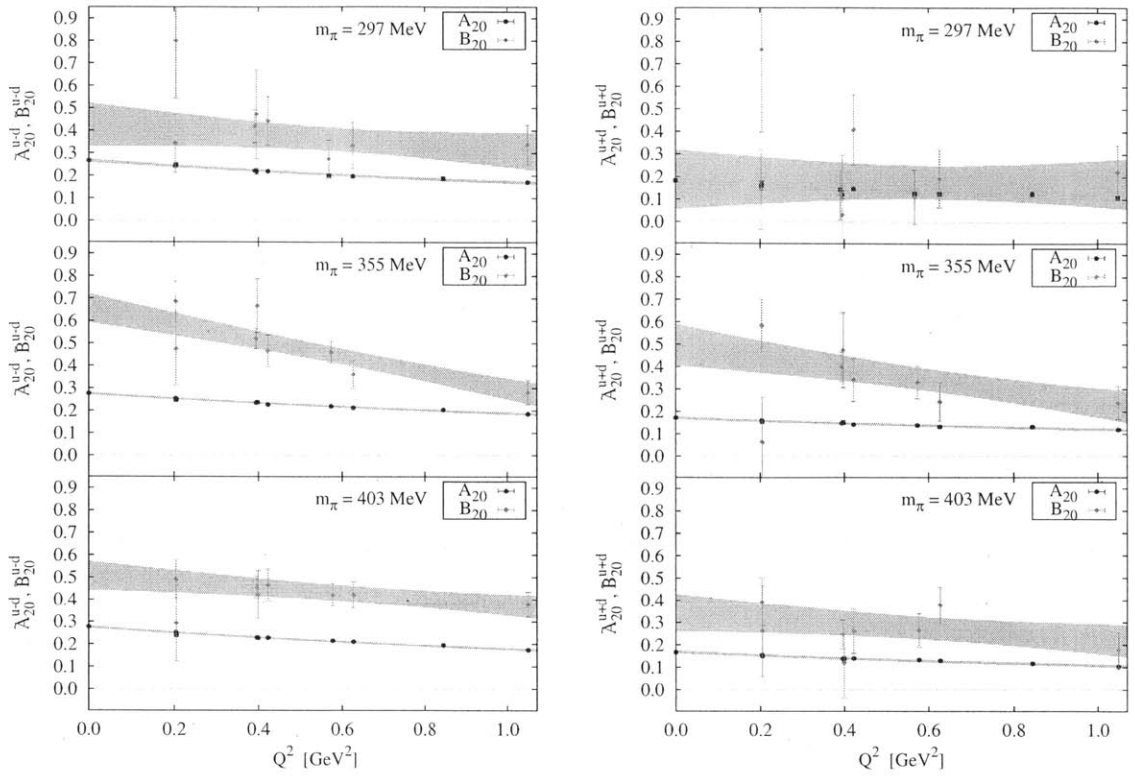

(a) Isovector (b) Isoscalar

Figure 5-31: $n = 2$ spin-dependent generalized form factors from the *Domain Wall* calculation. Disconnected contractions are not included into the isoscalar parts.

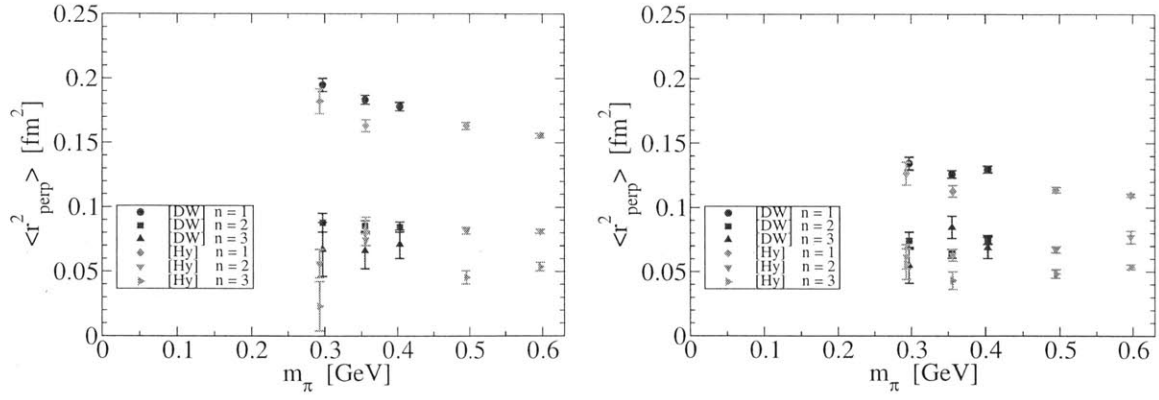

(a) Unpolarized radii (b) Polarized radii

Figure 5-32: Transverse isovector radii as extracted from dipole fits with momentum cut $Q^2 < 0.5$ GeV^2 to unpolarized A_{n0} and polarized $\tilde{A}_{n0}$ generalized form factors.

distance $b_\perp$ from the center of momentum of the nucleon. If one quark carries a significant portion of the nucleon momentum, the density distribution must be a

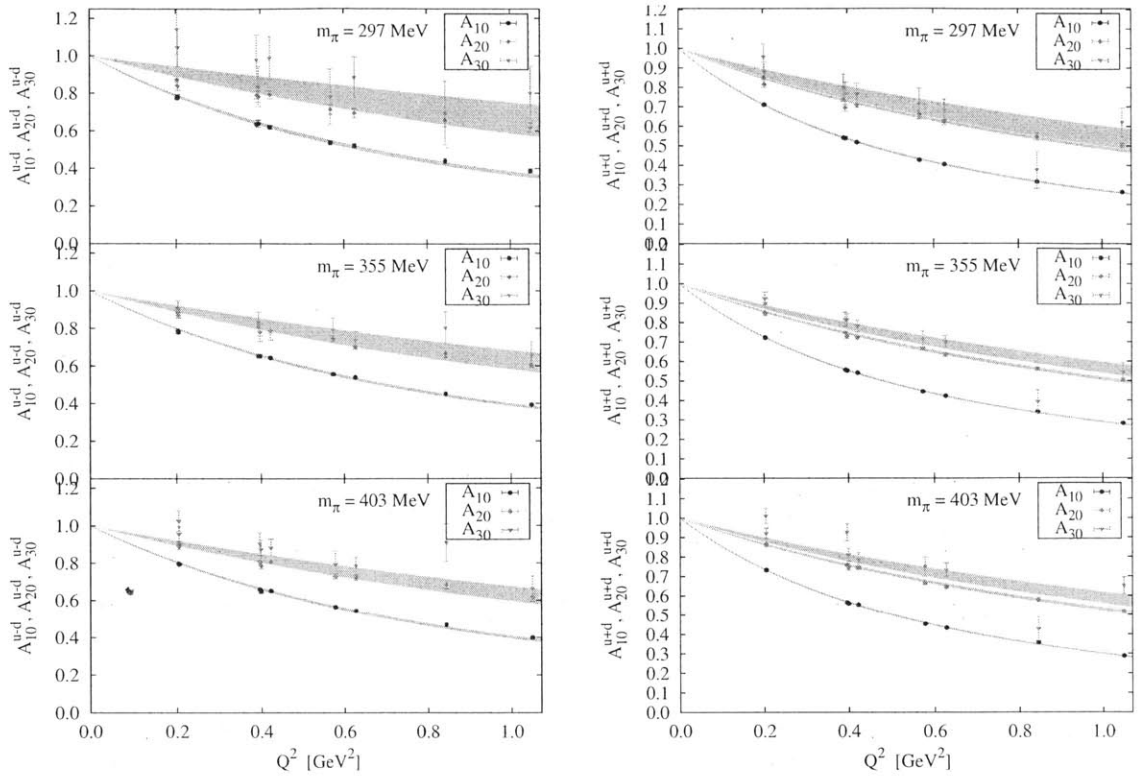

(a) Isovector

(b) Isoscalar

Figure 5-33: Dipole fits to the transverse "density" $H_q^n(\xi = 0, Q^2)$ from the *Domain Wall* calculations. Disconnected contractions are not included into the isoscalar parts.

narrow peak around zero, $H(x \to 1, b_\perp^2) \to \delta^2(b_\perp^2)$ [H$^+$08]. To study this question, similarly to Ref. [H$^+$08, B$^+$10, Ren04] we compute the transverse distribution radius $\langle r_{\perp,n}^2 \rangle$ defined as

$$H^n(\xi = 0, q_\perp^2) = H^n(\xi = 0, 0)(1 - \frac{1}{4}\langle r_{\perp,n}^2 \rangle \cdot q_\perp^2 + \mathcal{O}(q_\perp^4)),$$
$$\langle r_{\perp,n}^2 \rangle = -\frac{4}{H^n(\xi = 0, q_\perp^2 = 0)} \frac{dH^n(\xi = 0, q_\perp^2)}{dq_\perp^2}\Big|_{q_\perp^2=0} = \frac{8}{M_{\text{dipole},\perp,n}^2}$$

We present our dipole fits to the GFFs A_{10}, A_{20} and A_{30} in Fig. 5-33 and the extracted radii in Fig. 5-32. We find that the following rule holds approximately:

$$\langle r_{\perp,1}^2 \rangle > \langle r_{\perp,2}^2 \rangle \gtrsim \langle r_{\perp,3}^2 \rangle, \tag{5.30}$$

supporting the expectation that the distribution $H(x \to 1, b_\perp^2)$ becomes narrower

with $x \to 1$.

Finally, we note that the computed dependence of GFFs on the momentum transfer Q^2 has implications for phenomenological analyses of generalized parton distributions. Because of the lack of theoretical understanding of GPDs, one has to use various GPD Ansätze to analyze experimental data. Because the fall-off of nucleon GPDs is expected to be approximately as steep as the elastic form factors, the most often used form is a factorized Ansatz (e.g., in Ref. [GV98]) having separate Q^2- and x-dependence,

$$H_q(x,\xi,Q^2) = A^q_{10}(Q^2) H_q(x,\xi,0),$$
$$E_q(x,\xi,Q^2) = B^q_{10}(Q^2) E_q(x,\xi,0).$$

However, such an Ansatz contradicts our data. Otherwise, the Mellin moments (1.18) would demonstrate similar dependence on the momentum transfer Q^2. Our data, however, indicate that the Q^2-dependence is different even for small $Q^2 \ll 1$ GeV^2.

Chapter 6

Summary

In this work we have performed high-statistics, high-precision calculations of nucleon structure observables in the framework of lattice QCD. This is the first calculation of nucleon structure observables using QCD on a lattice with chiral quarks and pion masses as low as ≈ 300 MeV. We have carefully studied the systematic effects that can arise in computing nucleon matrix elements of quark operators, and applied optimization techniques to eliminate them as much as possible. As a result, we are able to reduce the Euclidean time distance in the nucleon correlation functions, which would otherwise be necessary to prevent systematic bias, and thus to improve considerably the signal-to-noise ratio in our calculations.

We perform our calculations using three different discretizations of the QCD action with *Domain Wall* (chiral sea and valence quarks), *Hybrid* (non-chiral sea and chiral valence quarks), and *Wilson-Clover*, (non-chiral valence and sea quarks), or *BMW*, fermions. The motivation to use the three different actions is twofold. First, a direct comparison of the results allows us to estimate systematic effects arising from simulating QCD on a lattice and assess the level at which different discretizations affect the observables we calculate. Second, *Wilson-Clover* action is significantly cheaper and allows us to obtain results at lighter pion masses at the expense of chiral symmetry breaking.

Because the differences in fundamental theory can lead to differences in effective theory parameters, one may not perform simultaneous chiral extrapolations of these

calculations Nevertheless, the results of both calculations agree reasonably well for all the observables we compute, and this fact reassures us that our methodology is correct and systematic effects are under control. In addition, since the lattice spacing is different in these two cases, the agreement of our results indicates that discretization errors in our calculations are small.

The results we report include the nucleon vector and axial form factors, the generalized form factors, the quark spin and angular momentum contributions to the nucleon spin. We observe that the dependence of the nucleon form factors on the momentum transfer is qualitatively similar to phenomenology and experiments. For example, we successfully use a dipole form to model the isovector Sachs electric form factor. However, the *size* parameters we extract from our calculations, such as the r.m.s. radii of charge, magnetization, and axial distributions in the nucleon, are considerably smaller than experimental values. This is not surprising since we are working with pion masses at least twice as heavy as the physical pion mass, and the nucleon is known to be surrounded by a virtual pion cloud, which contributes to the nucleon structure probed by experiments and our calculations.

The most precise results of our calculation, the nucleon vector form factors, provide a unique opportunity to test the predictions of chiral perturbation theory. Previously, either heavy pion masses or large stochastic variation prohibited testing predictions of ChPT, as well as extrapolating the results of lattice calculations to the physical pion mass reliably. Our new data indicate, however, that neither $\mathcal{O}(\epsilon^3)$ HBChPT+Δ (also known as small-scale expansion, or SSE) nor $\mathcal{O}(p^4)$ CBChPT effective theories can accommodate both our new lattice data *and* experimental results simultaneously. We draw the conclusion that these chiral perturbation theory calculations of Dirac and Pauli radii, at this specific order of approximation, cannot be valid in the range of pion masses above $m_\pi \gtrsim 300$ MeV.

One part of our results is renormalized non-perturbatively, and the other part is renormalized using perturbative lattice renormalization factors. We compare the perturbative renormalization factors to non-perturbative calculations, and estimate their difference as $\sim 10\%$. We thus establish a remarkable result that lattice perturbative

renormalization may introduce a systematic bias of order of 10%. This conclusion is an important enhancement of the previous studies of the nucleon structure reported in Refs. [H$^+$08, B$^+$10].

Finally, as has been discussed before, our calculations of nucleon structure are not complete yet. We do not compute the s-quark contribution to the nucleon structure, and omit disconnected diagrams contributing to nucleon isoscalar observables. However, the methods we developed to control the lattice systematic effects in nucleon matrix elements arising from excited state contributions will be necessary for reliable calculations of these quantities. Therefore, in this work we have laid essential foundation for studies of full quark contributions to nucleon structure in lattice QCD.

Appendix A

Lattice QCD simulation ensembles

A.1 Hybrid action ensembles

The *Hybrid* calculations are performed with the Asqtad action for sea quarks and domain wall action for valence quarks generated by the MILC collaboration [B+01]. The lattice spacing is $a = 0.1240(25)$ fm $= (1.591(32)\ \text{GeV})^{-1}$ as determined from heavy quark spectroscopy [A+04b]. The bare mass of *Domain Wall* valence quarks is tuned so that the mass of the pion [H+08] is equal to the Asqtad Goldstone boson mass. The gauge field was HYP-smeared to reduce the density of zero eigenmodes of the hermitian Wilson operator $H_W = \gamma_5 D_W$ to suppress the tunneling of fermion modes between the boundaries resulting from lattice artifacts. The parameters of the domain wall action are summarized in Ref. [H+08].

Table A.1: Summary of *Hybrid* ensembles.

Id	$L_s^3 \times L_t$	$am_{\text{sea}}^{\text{asqtad}}$	$am_{\text{val}}^{\text{DW}}$	$am'_{\text{res}} \times 10^3$	Z_A	# confs	# meas
Hy_{007}	$20^3 \times 64$	0.007/0.050	0.0081	1.58(1)	1.0839(2)	463	3704
$Hy_{010}^{20^3}$	$20^3 \times 64$	0.010/0.050	0.0138	1.57(1)	1.0849(1)	631	5048
$Hy_{010}^{28^3}$	$28^3 \times 64$	0.010/0.050	0.0138	1.58(1)	1.0850(1)	274	2192
Hy_{020}	$20^3 \times 64$	0.020/0.050	0.0313	1.23(1)	1.0986(1)	486	3888
Hy_{030}	$20^3 \times 64$	0.030/0.050	0.0478	1.016(7)	1.1090(1)	563	4504

We collect the size and parameters of the *Hybrid* gauge configuration ensembles in Tab. A.1 and the numerical results for the pion and nucleon masses and the pion

Table A.2: Hadron masses and decay constants in lattice and physical units in *Hybrid* ensembles.

Id	$(am)_\pi$	m_π [MeV]	$(af)_\pi$	f_π [MeV]	$(am)_N$	m_N [MeV]
Hy_{007}	0.1842(7)	292.99(111)	0.0657(3)	104.49(45)	0.696(7)	1107.1(111)
$Hy_{010}^{20^3}$	0.2238(5)	355.98(80)	0.0681(2)	108.31(34)	0.726(5)	1154.8(80)
$Hy_{010}^{20^3}$	0.2238(5)	355.98(80)	0.0681(2)	108.31(34)	0.726(5)	1154.8(80)
Hy_{020}	0.3113(4)	495.15(64)	0.0725(1)	115.40(23)	0.810(5)	1288.4(80)
Hy_{030}	0.3752(5)	596.79(80)	0.0761(2)	121.02(34)	0.878(5)	1396.5(80)

decay constant in Tab. A.2. The number of measurements for nucleon form factors ("# meas." column) includes a factor of 8 for each gauge configuration (a factor of 4 for m_π, F_π, m'_{res}).

The axial renormalization constant values in Tab. A.1 are determined from Eq. (2.30). Its variation over the range of pion masses is $\approx 3\%$, and its extrapolated value at $m_q + m'_{\text{res}} \to 0$ is $Z_A \approx 1.0750$.

A.2 Domain wall fermion ensembles

For our analysis we used one gauge configuration ensemble with *coarse* and three ensembles with *fine* lattice spacing. The former, *coarse*, ensemble was also used for setting the scale of *fine* ensembles, and to check the dependence on the lattice spacing. These configuration ensembles were generated by the RBC and UKQCD [A$^+$08a] collaborations. The coarse lattice spacing $a^{\text{coarse}} = 0.1141(18)$ fm $= (1.729(28)\ \text{GeV})^{-1}$ was determined in Ref. [A$^+$08a], and the fine lattice spacing $a^{\text{fine}} = 0.0840(14)$ fm $= (2.34(4)\ \text{GeV})^{-1}$ was determined in Ref. [S$^+$10]. The parameters of the domain wall action are summarized in Ref. [S$^+$10].

Table A.3: Summary of *Domain Wall* ensembles.

Id	$L_s^3 \times L_t$	a [fm]	T	# meas.	am_l/am_h	$am'_{\text{res}} \times 10^3$	Z_A
DW_{005}^{coarse}	$24^3 \times 64$	0.114	9	3208	0.005/0.04	3.15(1)	0.71724(5)
DW_{004}^{fine}	$32^3 \times 64$	0.084	12	4928	0.004/0.03	0.665(3)	0.74503(2)
DW_{006}^{fine}	$32^3 \times 64$	0.084	12	7064	0.006/0.03	0.663(2)	0.74521(2)
DW_{008}^{fine}	$32^3 \times 64$	0.084	12	4224	0.008/0.03	0.668(3)	0.74532(2)

Table A.4: Hadron masses and decay constants in lattice and physical units in *Domain Wall* ensembles.

Id	am_π	m_π [MeV]	aF_π	F_π [MeV]	aM_N	M_N [MeV]
DW_{005}^{coarse}	0.1901(3)	329(5)	0.06100(11)	105.5(1.7)	0.657(4)	1136(20)
DW_{004}^{fine}	0.1268(3)	297(5)	0.04400(15)	102.9(1.8)	0.474(4)	1109(21)
DW_{006}^{fine}	0.1519(3)	355(6)	0.04571(09)	107.0(1.8)	0.501(2)	1172(21)
DW_{008}^{fine}	0.1724(3)	403(7)	0.04755(18)	111.3(2.0)	0.522(2)	1221(21)

We collect the size and parameters of the gauge configuration ensembles in Tab. A.3 and the numerical results for the pion and nucleon masses and the pion decay constant in Tab. A.4. The number of measurements for nucleon form factors ("# meas." column) includes a factor of 8 for each gauge configuration. T is the source-sink separation in lattice units used in the calculation of three-point functions to obtain nucleon matrix elements.

The axial renormalization constant values in Tab. A.3 are determined from Eq. (2.30). Its variation over the range of pion masses is $< 0.1\%$, and its extrapolated value at $m_q + m'_{\text{res}} \to 0$ is $Z_A = 0.74470$.

A.3 Wilson-Clover ensembles

The gauge configuration ensembles with Wilson-Clover dynamical fermions generated by the BMW collaboration [D$^+$08, col] are used for exploratory purposes. The significantly lighter pion mass and different fermion action require additional efforts for tuning nucleon sources and renormalization. Below we summarize the ensembles used in Chap. 5.

Table A.5: Summary of *BMW* ensembles.

$L_s^3 \times L_t$	a [fm]	T	# meas.	am_l/am_h	m_π [MeV]
$24^3 \times 48$	0.116	10	2514	$-0.0953/-0.04$	≈ 250
$32^3 \times 48$	0.116	10	2520	$-0.0953/-0.04$	≈ 250
$32^3 \times 48$	0.116	10	2742	$-0.09756/-0.04$	≈ 200

Appendix B

Irreducible representations of the hypercubic group $H(4)$

Here we summarize the bases for tensors belonging to irreducible representations of the $H(4)$ group used in this work which are appropriate for the calculation of the twist-2 Wilson operators [G+96a]. These irreducible representations are generated by the rank $n = 2, 3, 4$ tensors, or $\left[\tau_1^{(4)}\right]^{\otimes n}$ reducible representations similar to rank-n tensors in $SO(4)$ group,

The discussion below does not include pseudotensors. For the rank-n operators including γ_5, one should choose an appropriate representation from $\left[\tau_1^{(4)}\right]^{\otimes n}$ based on symmetry and multiply it by $\tau_4^{(1)}$.

The representations for rank $n = 1$ tensors (vectors) do not split into separate irreducible representations under the $H(4)$ group action and do not require special treatment for renormalization, and are not discussed here.

Symmetric traceless rank-2 tensor irreducible representations:

$$\begin{aligned}
\tau_1^{(3)}: &\quad \tfrac{1}{2}(\mathcal{O}_{11}+\mathcal{O}_{22}-\mathcal{O}_{33}-\mathcal{O}_{44}),\quad \tfrac{1}{\sqrt{2}}(\mathcal{O}_{33}-\mathcal{O}_{44}),\quad \tfrac{1}{\sqrt{2}}(\mathcal{O}_{11}-\mathcal{O}_{22}),\\
\tau_3^{(6)}: &\quad \frac{1}{\sqrt{2}}(\mathcal{O}_{\mu\nu}+\mathcal{O}_{\nu\mu}),\quad 1\le\mu<\nu\le 4,
\end{aligned}$$

Symmetric traceless rank-3 tensor irreducible representations:

$$
\begin{aligned}
\tau_2^{(4)}: \quad & \sqrt{6}\mathcal{O}_{\{234\}}, \quad \sqrt{6}\mathcal{O}_{\{134\}}, \quad \sqrt{6}\mathcal{O}_{\{124\}}, \quad \sqrt{6}\mathcal{O}_{\{123\}}\ , \\
\tau_1^{(8)}: \quad & \sqrt{\tfrac{3}{2}}(\mathcal{O}_{\{122\}} - \mathcal{O}_{\{133\}}), \quad \tfrac{1}{\sqrt{2}}(\mathcal{O}_{\{122\}} + \mathcal{O}_{\{133\}} - 2\mathcal{O}_{\{144\}}), \\
& \sqrt{\tfrac{3}{2}}(\mathcal{O}_{\{211\}} - \mathcal{O}_{\{233\}}), \quad \tfrac{1}{\sqrt{2}}(\mathcal{O}_{\{211\}} + \mathcal{O}_{\{233\}} - 2\mathcal{O}_{\{244\}}), \\
& \sqrt{\tfrac{3}{2}}(\mathcal{O}_{\{311\}} - \mathcal{O}_{\{322\}}), \quad \tfrac{1}{\sqrt{2}}(\mathcal{O}_{\{311\}} + \mathcal{O}_{\{322\}} - 2\mathcal{O}_{\{344\}}), \\
& \sqrt{\tfrac{3}{2}}(\mathcal{O}_{\{411\}} - \mathcal{O}_{\{422\}}), \quad \tfrac{1}{\sqrt{2}}(\mathcal{O}_{\{411\}} + \mathcal{O}_{\{422\}} - 2\mathcal{O}_{\{433\}}),
\end{aligned}
$$

Antisymmetric traceless rank-2 tensor $\mathcal{O}_{[\mu\nu]}$:

$$
\tau_1^{(6)}: \quad \frac{1}{\sqrt{2}}(\mathcal{O}_{\mu\nu} - \mathcal{O}_{\nu\mu}), \quad 1 \le \mu < \nu \le 4,
$$

Mixed-symmetry traceless rank-3 tensor $\mathcal{O}_{[\mu\{|\nu|\rho\}]}$ (first symmetrized in ν, ρ, then antisymmetrized in μ, ρ, cf. Eq (4.19) and (4.9) in Ref. [G+96a]):

$$
\begin{aligned}
\tau_1^{(8)}: \quad & \tfrac{1}{2\sqrt{3}}(\mathcal{O}_{\langle\langle 122\rangle\rangle} - \mathcal{O}_{\langle\langle 133\rangle\rangle}), \quad \tfrac{1}{6}(\mathcal{O}_{\langle\langle 122\rangle\rangle} + \mathcal{O}_{\langle\langle 133\rangle\rangle} - 2\mathcal{O}_{\langle\langle 144\rangle\rangle}), \\
& \tfrac{1}{2\sqrt{3}}(\mathcal{O}_{\langle\langle 211\rangle\rangle} - \mathcal{O}_{\langle\langle 233\rangle\rangle}), \quad \tfrac{1}{6}(\mathcal{O}_{\langle\langle 211\rangle\rangle} + \mathcal{O}_{\langle\langle 233\rangle\rangle} - 2\mathcal{O}_{\langle\langle 244\rangle\rangle}), \\
& \tfrac{1}{2\sqrt{3}}(\mathcal{O}_{\langle\langle 311\rangle\rangle} - \mathcal{O}_{\langle\langle 322\rangle\rangle}), \quad \tfrac{1}{6}(\mathcal{O}_{\langle\langle 311\rangle\rangle} + \mathcal{O}_{\langle\langle 322\rangle\rangle} - 2\mathcal{O}_{\langle\langle 344\rangle\rangle}), \\
& \tfrac{1}{2\sqrt{3}}(\mathcal{O}_{\langle\langle 411\rangle\rangle} - \mathcal{O}_{\langle\langle 422\rangle\rangle}), \quad \tfrac{1}{6}(\mathcal{O}_{\langle\langle 411\rangle\rangle} + \mathcal{O}_{\langle\langle 422\rangle\rangle} - 2\mathcal{O}_{\langle\langle 433\rangle\rangle}),
\end{aligned}
$$

where $\quad \mathcal{O}_{\langle\langle\nu_1\nu_2\nu_3\rangle\rangle} = \mathcal{O}_{\nu_1\nu_2\nu_3} + \mathcal{O}_{\nu_1\nu_3\nu_2} - \mathcal{O}_{\nu_3\nu_1\nu_2} - \mathcal{O}_{\nu_3\nu_2\nu_1}$.

Appendix C

Renormalization of lattice operators

C.1 Structure of Born terms and corrections in lattice vertex functions

In this section I collect the spin structures of possible terms in vertex functions of operators for which we have to match lattice and perturbative calculations [Gra03b, Gra03a, Gra06].

Notations: symmetrization and antisymmetrization (chosen so that for a symmetric tensor the relation $X^{\{\mu_1\cdots\mu_n\}} \equiv X^{\mu_1\cdots\mu_n}$ and for an antisymmetric tensor the relation $Y^{[\mu_1\cdots\mu_n]} \equiv Y^{\mu_1\cdots\mu_n}$ hold):

$$X^{\{\mu_1\cdots\mu_n\}} = \frac{1}{n!}\sum_{\sigma} X^{\sigma(\mu_1\cdots\mu_n)}, \tag{C.1}$$

$$X^{[\mu_1\cdots\mu_n]} = \frac{1}{n!}\sum_{\sigma}(-1)^{\sigma} X^{\sigma(\mu_1\cdots\mu_n)} \tag{C.2}$$

The spin structure of the Wilson twist-2 $n = 2$ operator (also given in (4.13)):

$$\mathcal{O}^{[\gamma_5]}_{n=2} = \bar{q}[\gamma_5]\big[\gamma^{\{\mu} i\overleftrightarrow{D}^{\nu\}} - \langle\text{trace}\rangle\big]q, \tag{C.3}$$

$$[\Lambda^{\text{lat}}_{n=2}]^{\mu\nu}(p) = \Pi^{(11)}_{n=2}(p^2)\cdot[\Lambda^{(1)}_{n=2}]^{\{\mu\nu\}} + \Pi^{(12)}_{n=2}(p^2)\cdot[\Lambda^{(2)}_{n=2}]^{\{\mu\nu\}}, \tag{C.4}$$

where the tree-level structures are

$$\begin{aligned}\Big[\Lambda^{(1)}_{n=2}\Big]^{\{\mu\nu\}} &= [\gamma_5](\gamma^{\{\mu}p^{\nu\}} - \frac{1}{4}\not{p}\delta^{\mu\nu}),\\ \Big[\Lambda^{(1)}_{n=2}\Big]^{\{\mu\nu\}} &= [\gamma_5](\not{p}\frac{p^{\{\mu}p^{\nu\}}}{p^2} - \frac{1}{4}\not{p}\delta^{\mu\nu})\end{aligned} \tag{C.5}$$

where $[\gamma_5]$ means that the same structure holds for helicity-dependent operators.

Similarly, the spin structure of the Wilson twist-2 $n = 3$ operator is

$$\mathcal{O}^{[\gamma_5]}_{n=3} = \bar{q}[\gamma_5]\big[\gamma^{\{\mu} i\overleftrightarrow{D}^{\nu} i\overleftrightarrow{D}^{\rho\}} - \langle\text{traces}\rangle\big]q, \tag{C.6}$$

$$[\Lambda^{\text{lat}}_{n=3}]^{\mu\nu\rho}(p) = \Pi^{(11)}_{n=2}(p^2)\cdot[\Lambda^{(1)}_{n=2}]^{\{\mu\nu\rho\}} + \Pi^{(12)}_{n=2}(p^2)\cdot[\Lambda^{(2)}_{n=2}]^{\{\mu\nu\rho\}}, \tag{C.7}$$

where the tree-level structures are

$$\begin{aligned}\Big[\Lambda^{(1)}_{n=2}\Big]^{\{\mu\nu\rho\}} &= \gamma^{\{\mu}p^{\nu}p^{\rho\}} - \frac{1}{3}\not{p}p^{\{\mu}\delta^{\nu\rho\}} - \frac{1}{6}p^2\gamma^{\{\mu}\delta^{\nu\rho\}},\\ \Big[\Lambda^{(1)}_{n=2}\Big]^{\{\mu\nu\rho\}} &= \not{p}\frac{p^{\{\mu}p^{\nu}p^{\rho\}}}{p^2} - \frac{1}{2}\not{p}p^{\{\mu}\delta^{\nu\rho\}}\end{aligned} \tag{C.8}$$

Appendix D

Chiral extrapolation formulas

D.1 Electromagnetic structure

D.1.1 Small Scale expansion (HBChPT+Δ)

The small scale expansion (SSE) is a triple expansion in a combination of small parameters $\epsilon \in \{m_\pi, p, \Delta\}$ [HHK98], where $\Delta = M_\Delta - M_N$.

Isovector structure

The isovector anomalous magnetic moment to order $\mathcal{O}(\epsilon^3)$ is given by [BFHM98]

$$\begin{aligned}\kappa_v(m_\pi) &= \kappa_v^0 - \frac{g_A^2 m_\pi M_N}{4\pi F_\pi^2} \\ &\quad + \frac{2c_A^2 \Delta M_N}{9\pi^2 F_\pi^2}\left\{\sqrt{1-\frac{m_\pi^2}{\Delta^2}}\log\left[R(m_\pi)\right] + \log\left[\frac{m_\pi}{2\Delta}\right]\right\} + \mathcal{O}(m_\pi^2). \quad \text{(D.1)}\end{aligned}$$

In order to capture the most prominent $\mathcal{O}(m_\pi^2)$ corrections, Hemmert and Weise [HW02] proposed a modification of the standard SSE power counting to promote the leading term of the magnetic $N \to \Delta$ transition into the first order $N\Delta$ effective Lagrangian.

This leads to the following expression for $\kappa_v(m_\pi)$:

$$\begin{aligned}\kappa_v(m_\pi) =& \kappa_v^0 - \frac{g_A^2\, m_\pi M_N}{4\pi F_\pi^2} + \frac{2c_A^2 \Delta M_N}{9\pi^2 F_\pi^2}\left\{\sqrt{1-\frac{m_\pi^2}{\Delta^2}}\log\left[R(m_\pi)\right] + \log\left[\frac{m_\pi}{2\Delta}\right]\right\} \\ & - 8E_1^r(\lambda) M_N m_\pi^2 + \frac{4c_A c_V g_A M_N m_\pi^2}{9\pi^2 F_\pi^2}\log\left[\frac{2\Delta}{\lambda}\right] + \frac{4c_A c_V g_A M_N m_\pi^3}{27\pi F_\pi^2 \Delta} \\ & - \frac{8c_A c_V g_A \Delta^2 M_N}{27\pi^2 F_\pi^2}\left\{\left(1-\frac{m_\pi^2}{\Delta^2}\right)^{3/2}\log\left[R(m_\pi)\right] + \left(1-\frac{3m_\pi^2}{2\Delta^2}\right)\log\left[\frac{m_\pi}{2\Delta}\right]\right\},\end{aligned} \tag{D.2}$$

where c_V is the leading magnetic photon-nucleon-Δ coupling in the chiral limit and κ_v^0 denotes the anomalous magnetic moment in the $SU(2)$ chiral limit.

The $\mathcal{O}(\epsilon^3)$ SSE formulas for $(r_1^v)^2$ and $(r_2^v)^2$ can be derived from the chiral expressions for $F_{1,2}^v$, respectively, and are given by [BFHM98]

$$\begin{aligned}(r_1^v)^2 =& -\frac{1}{(4\pi F_\pi)^2}\left\{1 + 7g_A^2 + \left(10g_A^2+2\right)\log\left[\frac{m_\pi}{\lambda}\right]\right\} - \frac{12B_{10}^{(r)}(\lambda)}{(4\pi F_\pi)^2} \\ & + \frac{c_A^2}{54\pi^2 F_\pi^2}\left\{26 + 30\log\left[\frac{m_\pi}{\lambda}\right] + 30\frac{\Delta}{\sqrt{\Delta^2 - m_\pi^2}}\log\left[\frac{\Delta}{m_\pi} + \sqrt{\frac{\Delta^2}{m_\pi^2}-1}\right]\right\} + \mathcal{O}(m_\pi)\,,\end{aligned} \tag{D.3}$$

$$\kappa_v(m_\pi)\cdot(r_2^v)^2 = \frac{g_A^2 M_N}{8\pi F_\pi^2 m_\pi} + \frac{c_A^2 M_N}{9\pi^2 F_\pi^2\sqrt{\Delta^2 - m_\pi^2}}\log\left[\frac{\Delta}{m_\pi} + \sqrt{\frac{\Delta^2}{m_\pi^2}-1}\right] + \mathcal{O}(m_\pi^0). \tag{D.4}$$

Systematic disagreement of the ChPT prediction for the Pauli radius and lattice data because of insufficient approximation order motivates one to add the $\mathcal{O}(m_\pi^0)$ correction to the leading one-loop result of Eq. (D.4) (the so-called "core" contribution in Ref. [G$^+$05b]) to $\kappa_v\cdot(r_2^v)^2$, such that

$$\kappa_v(m_\pi)\cdot(r_2^v)^2 = \frac{g_A^2 M_N}{8\pi F_\pi^2 m_\pi} + \frac{c_A^2 M_N}{9\pi^2 F_\pi^2\sqrt{\Delta^2 - m_\pi^2}}\log\left[\frac{\Delta}{m_\pi} + \sqrt{\frac{\Delta^2}{m_\pi^2}-1}\right] + 24 M_N \mathcal{C}. \tag{D.5}$$

Isoscalar structure

The $\mathcal{O}(\epsilon^3)$ SSE expressions for the pion-mass and momentum transfer dependence of the isoscalar Dirac and Pauli form factors have been derived in [BFHM98]: Note that chiral dynamics in the isoscalar form factors of the nucleon starts at the 3-pion cut, i.e. at two-loop level [BFHM98]), corresponding to $\mathcal{O}(\epsilon^5)$ in the power-counting of SSE.

$$F_1^s(Q^2) = 1 + \tilde{B}_1 \frac{Q^2}{(4\pi F_\pi)^2}, \tag{D.6}$$

$$F_2^s(Q^2) = \kappa_s, \tag{D.7}$$

Low-energy parameters

The common low-energy constants (LECs) which enter the chiral Lagrangian to this order are the $SU(2)$ chiral limit values of F_π, the pion decay constant, g_A, the nucleon axial charge, c_A, the leading-order pion-nucleon-Δ coupling[1], and Δ, the $\Delta(1232)$-nucleon mass splitting. Additionally, Eq. (D.2,D.3,D.5) involve κ_v^0 and c_V LECs, as well as counter terms $B_{10}^r(\lambda)$ $E_1^r(\lambda)$ and $\mathcal{C}$. For more details on the effective Lagrangians and the definitions of the LECs, we refer the reader to [BFHM98].

Ideally we would like to determine all these constants from simultaneous fits to lattice results. However, this is not feasible with the limited number of measured observables and pion masses in the present calculation, and we thus fix some of the low-energy constants using their phenomenological values. We describe our choices for these values below.

The pion decay constant F_π convention is such that at the physical pion mass

$$F_\pi^{\text{phys}} = 92.4 \pm 0.3 \text{ MeV}. \tag{D.8}$$

In Ref. [CD04], Colangelo and Dürr analyze numerically the NNLO expression for the pion-mass dependence of F_π [BCT98]. They use available information from phenomenology to fix all low-energy constants but the chiral limit value of F_π, use the

[1] The coupling c_A corresponds to $\dot{g}_{\pi N\Delta}$ in the notation of Ref. [HHK98].

physical value (D.8) and obtain

$$F_\pi\big|_{\text{chiral limit}} = (86.2 \pm 0.5)\ \text{MeV}. \tag{D.9}$$

In the absence of reliable chiral extrapolations of both nucleon and $\Delta(1232)$ masses (see the discussion in Ref. [WL+09])[2], we identify the Δ-nucleon mass splitting in the chiral limit with its value at the physical m_π. The position of the $\Delta(1232)$ resonance pole in the total center-of-mass energy plane has been determined from magnetic dipole and electric quadrupole amplitudes of pion photoproduction. According to the Particle Data Group average [A+08b], the Δ-pole position leads to $M_\Delta = (1210 \pm 1)$ MeV and $\Gamma_\Delta = (100 \pm 2)$ MeV. If one instead defines the $\Delta(1232)$ mass and width by looking at the 90° πN phase shift in the spin-3/2 isospin-3/2 channel, the PDG averages give $M_\Delta = (1232 \pm 1)$ MeV and $\Gamma_\Delta = (118 \pm 2)$ MeV. With $M_N = 939$ MeV, one obtains, respectively,

$$\Delta = (271 \pm 1)\ \text{MeV}, \tag{D.10}$$

or

$$\Delta = (293 \pm 1)\ \text{MeV}. \tag{D.11}$$

The $\Delta(1232)$ decays strongly to a nucleon and a pion with almost 100% branching fraction. From the PDG values of masses and widths [A+08b] and from

$$\Gamma_{\Delta\to N\pi} = \frac{c_A^2}{12\pi\, F_\pi^2\, M_\Delta}\,(E_\pi^2 - m_\pi^2)^{3/2}\,(M_\Delta + M_N - E_\pi), \tag{D.12}$$

where

$$E_\pi = \frac{M_\Delta^2 - M_N^2 + m_\pi^2}{2M_\Delta}\,, \tag{D.13}$$

[2] For an analysis of the quark-mass dependence of nucleon and delta masses in the covariant SSE at order ϵ^4 we refer to [BHM05].

one obtains, respectively[3],

$$|c_A| = 1.50 \ldots 1.55 \qquad \text{if } \Gamma = (100 \pm 2) \text{ MeV and } \Delta = (271 \pm 1) \text{ MeV} \quad \text{(D.17)}$$

$$|c_A| = 1.43 \ldots 1.47 \qquad \text{if } \Gamma = (118 \pm 2) \text{ MeV and } \Delta = (293 \pm 1) \text{ MeV} \quad \text{(D.18)}$$

Chiral extrapolations of different sets of lattice results [HPW03, E$^+$06b, PMHW07, AK$^+$06] based on SSE at leading-one-loop accuracy lead to a chiral limit value for g_A of about 1.2. From the relativistic tree-level analysis of the process of pion photoproduction at threshold $\gamma p \to \pi^0 p$, one obtains [DMW91, HHK97] (for $c_A = 1.5$)

$$c_V = (-2.5 \pm 0.4) \text{ GeV}^{-1}. \quad \text{(D.19)}$$

D.1.2 Covariant Baryon ChPT (CBChPT)

In this section we collect the nucleon structure results obtained in the formulation of $SU(2)$ chiral effective field theory in the baryon sector, without explicit $\Delta\,(1232)$ degrees of freedom: covariant BChPT as introduced in Ref. [GSS88] with a modified version of infrared regularization ($\overline{\text{IR}}$-scheme). For details about the formalism and differences from the standard infrared regularization introduced by Becher and Leutwyler [BL99], we refer the reader to Refs. [DGH08, Gai07, GH].

[3] Calculating the strong decay width of $\Delta\,(1232)$ to leading order in (nonrelativistic) SSE kinematics, one obtains

$$\Gamma_{\Delta \to N\pi} = \frac{c_A^2}{6\pi F_\pi^2} (\Delta^2 - m_\pi^2)^{3/2}. \quad \text{(D.14)}$$

We note that this expression corresponds to the leading term in a $1/M_N$ expansion of the result given in Eq. (D.12), which utilizes the full covariant kinematics. Using the ranges of masses and decay widths mentioned above, this expression yields the lower values

$$|c_A| = 1.11 \ldots 1.14 \qquad \text{if } \Gamma = (100 \pm 2) \text{ MeV and } \Delta = (271 \pm 1) \text{ MeV;} \quad \text{(D.15)}$$

$$|c_A| = 1.04 \ldots 1.07 \qquad \text{if } \Gamma = (118 \pm 2) \text{ MeV and } \Delta = (293 \pm 1) \text{ MeV.} \quad \text{(D.16)}$$

Furthermore, $SU(4)$ spin-flavor quark symmetry gives $c_A = 3g_A/(2\sqrt{2}) = 1.34$.

Isovector structure

The expressions for the m_π dependence of the mean squared isovector Dirac and Pauli radii and the isovector anomalous magnetic moment have been derived in [Gai07] up to order p^4, *i.e.* at the next-to-leading one-loop accuracy and are collected below[4].

For the isovector mean squared Dirac radius, the expression is given as

$$(r_1^v)^2 = B_{c1} + \left[(r_1^v)^2\right]^{(3)} + \left[(r_1^v)^2\right]^{(4)} + \mathcal{O}(m_\pi^2), \tag{D.20}$$

where

$$B_{c1} = -12 d_6^r(\lambda),$$

$$\begin{aligned}\left[(r_1^v)^2\right]^{(3)} = &-\frac{1}{16\pi^2 F_\pi^2 M^4}\left[7g_A^2M^4 + 2(5g_A^2+1)M^4\log\frac{m_\pi}{\lambda} + M^4 - 15g_A^2m_\pi^2M^2\right.\\ &\left.+ g_A^2m_\pi^2(15m_\pi^2 - 44M^2)\log\frac{m_\pi}{M}\right]\\ &+\frac{g_A^2 m_\pi}{16\pi^2F_\pi^2M^4\sqrt{4M^2-m_\pi^2}}\left[15m_\pi^4 - 74m_\pi^2M^2 + 70M^4\right]\arccos\left(\frac{m_\pi}{2M}\right),\end{aligned}$$

$$\begin{aligned}\left[(r_1^v)^2\right]^{(4)} = -\frac{3c_6g_A^2m_\pi^2}{16\pi^2F_\pi^2M_0^4\sqrt{4M_0^2-m_\pi^2}}&\left[m_\pi(m_\pi^2-3M_0^2)\arccos\left(\frac{m_\pi}{2M_0}\right)\right.\\ &\left.+\sqrt{4M_0^2-m_\pi^2}\left[M_0^2 + (M_0^2-m_\pi^2)\log\frac{m_\pi}{M_0}\right]\right].\end{aligned}$$

The terms contributing up to and including $\mathcal{O}(p^i)$ are denoted by the superscript (i). Without any loss of generality, the regularization scale λ is set equal to M_0, the nucleon mass in the chiral limit. The low-energy constants d_6 and c_6 appear, respectively, in the third- and second-order πN effective Lagrangian. The mass function M must be identified with M_0 if one truncates the previous expression at $\mathcal{O}(p^3)$, whereas

[4] In Ref. [Gai07] the form factor slopes ρ_1^v and ρ_2^v are used, which are related to our notation for r_1^v and r_2^v by $\rho_1^v = \frac{1}{6}(r_1^v)^2$ and $\rho_2^v = \frac{1}{6}\kappa_v \cdot (r_2^v)^2$.

at order p^4, according to Ref. [Gai07], M should be replaced by [DGH08]

$$\begin{aligned} M_N(m_\pi) =& M_0 - 4c_1 m_\pi^2 + \frac{3g_A^2 m_\pi^3}{32\pi^2 F_\pi^2 \sqrt{4-\frac{m_\pi^2}{M_0^2}}}\left(-4+\frac{m_\pi^2}{M_0^2}+4c_1\frac{m_\pi^4}{M_0^3}\right)\arccos\left(\frac{m_\pi}{2M_0}\right) \\ &- \frac{3m_\pi^4}{128\pi^2 F_\pi^2}\left[\left(\frac{6g_A^2}{M_0}-c_2\right)+4\left(\frac{g_A^2}{M_0}-8c_1+c_2+4c_3\right)\log\left(\frac{m_\pi}{\lambda}\right)\right] \\ &+ 4e_1^r(\lambda)m_\pi^4 - \frac{3c_1 g_A^2 m_\pi^6}{8\pi^2 F_\pi^2 M_0^2}\log\left(\frac{m_\pi}{M_0}\right). \end{aligned} \tag{D.21}$$

where c_1, c_2 and c_3 are second-order low-energy constants and $e_1^r(\lambda)$ denotes an effective coupling consisting of a combination of fourth order low-energy constants. In our current analysis, we always include terms up to $\mathcal{O}(p^4)$, hence M in all the BChPT expressions presented here should be identified with $M_N(m_\pi)$.

The pion-mass dependence of the isovector Pauli radius is given by

$$\kappa_v(m_\pi)\cdot(r_2^v)^2 = \frac{M_N}{M_0}\left(B_{c2}+[\kappa_v\cdot(r_2^v)^2]^{(3)}+[\kappa_v\cdot(r_2^v)^2]^{(4)}\right)+\mathcal{O}(m_\pi), \tag{D.22}$$

where[5]

$$B_{c2} = 24M_0 e_{74}^r(\lambda),$$

$$\begin{aligned} \left[\kappa_v\cdot(r_2^v)^2\right]^{(3)} =& \frac{g_A^2 M_0}{16\pi^2 F_\pi^2 M^5(m_\pi^2-4M^2)}\Big[-124M^6+105m_\pi^2M^4-18m_\pi^4M^2 \\ &+6(3m_\pi^6-22M^2m_\pi^4+44M^4m_\pi^2-16M^6)\log\frac{m_\pi}{M}\Big] \\ &+\frac{g_A^2 M_0}{8\pi^2 F_\pi^2 M^5 m_\pi(4M^2-m_\pi^2)^{3/2}}\Big[9m_\pi^8-84M^2m_\pi^6+246M^4m_\pi^4 \\ &-216M^6m_\pi^2+16M^8\Big]\arccos\left(\frac{m_\pi}{2M}\right), \end{aligned}$$

[5] We note that $\mathcal{C}$ in Eq.(D.5) is equivalent to $e_{74}^r(\lambda)$.

$$\left[\kappa_v \cdot (r_2^v)^2\right]^{(4)} = -\frac{g_A^2 c_6 m_\pi^3}{16\pi^2 F_\pi^2 M_0^4 (4M_0^2 - m_\pi^2)^{3/2}}\left[4m_\pi^4 - 27m_\pi^2 M_0^2 + 42M_0^4\right]\arccos\left(\frac{m_\pi}{2M_0}\right)$$
$$+\frac{1}{16\pi^2 F_\pi^2 M_0^4 (m_\pi^2 - 4M_0^2)}\Bigg[16c_4 M_0^7 + 52g_A^2 M_0^6 - 4c_4 m_\pi^2 M_0^5 - 14c_6 g_A^2 m_\pi^2 M_0^4$$
$$-13g_A^2 m_\pi^2 M_0^4 + 8(3g_A^2 - c_4 M_0)(m_\pi^2 - 4M_0^2)M_0^4 \log\frac{m_\pi}{M_0} + 4c_6 g_A^2 m_\pi^4 M_0^2$$
$$-g_A^2(m_\pi^2 - 4M_0^2)(4c_6 m_\pi^4 - 3c_6 m_\pi^2 M_0^2 + 24M_0^4)\log\frac{m_\pi}{M_0}\Bigg].$$

For the isovector anomalous magnetic moment, the $\mathcal{O}(p^4)$ BChPT expression is

$$\kappa_v = \frac{M_N}{M_0}\left[c_6 - 16M_0 m_\pi^2 e_{106}^r(\lambda) + \delta\kappa_v^{(3)} + \delta\kappa_v^{(4)}\right] + \mathcal{O}(m_\pi^3), \tag{D.23}$$

where

$$\delta\kappa_v^{(3)} = \frac{g_A^2 m_\pi^2 M_0}{8\pi^2 F_\pi^2 M^3}\left[(3m_\pi^2 - 7M^2)\log\frac{m_\pi}{M} - 3M^2\right]$$
$$-\frac{g_A^2 m_\pi M_0}{8\pi^2 F_\pi^2 M^3\sqrt{4M^2 - m_\pi^2}}\left[3m_\pi^4 - 13M^2 m_\pi^2 + 8M^4\right]\arccos\left(\frac{m_\pi}{2M}\right),$$

$$\delta\kappa_v^{(4)} = -\frac{m_\pi^2}{32\pi^2 F_\pi^2 M_0^2}\Bigg[4g_A^2(c_6+1)M_0^2 - g_A^2(5c_6 m_\pi^2 + 28M_0^2)\log\frac{m_\pi}{M_0}$$
$$+4M_0^2(2c_6 g_A^2 + 7g_A^2 + c_6 - 4c_4 M_0)\log\frac{m_\pi}{\lambda}\Bigg]$$
$$-\frac{g_A^2 c_6 m_\pi^3}{32\pi^2 F_\pi^2 M_0^2\sqrt{4M_0^2 - m_\pi^2}}(5m_\pi^2 - 16M_0^2)\arccos\left(\frac{m_\pi}{2M_0}\right).$$

Note that $\frac{M_N}{M_0}c_6$ is equivalent to κ_v^0 in Eq.(D.2), where M_N is the physical nucleon mass and M_0 is the nucleon mass in the chiral limit.

Isoscalar structure

The BChPT formulas up to $\mathcal{O}(p^4)$ for $(r_1^s)^2$, $(r_2^s)^2$ and κ_s have been derived in [Gai07, GH]. Note that the NLO one-loop CBChPT results for the nucleon isoscalar form factors do not contain their dominant chiral dynamics arising from the 3-pion cut,

and such effects would only become visible at the two-loop level, i.e. starting at $\mathcal{O}(p^5)$ in BChPT.

$$(r_1^s)^2 = B_{c1}^s + \left[(r_1^s)^2\right]^{(3)} + \left[(r_1^s)^2\right]^{(4)}, \tag{D.24}$$

where

$$B_{c1}^s = -24 d_7,$$

$$\begin{aligned}\left[(r_1^s)^2\right]^{(3)} =& \frac{3 g_A^2 m_\pi^2}{16\pi^2 F_\pi^2 M^4 (m_\pi^2 - 4M^2)} \Bigg[5 m_\pi^2 M^2 - 18 M^4 \\ &+ \frac{m_\pi (5 m_\pi^4 - 34 M^2 m_\pi^2 + 54 M^4)}{\sqrt{4M^2 - m_\pi^2}} \arccos\left(\frac{m_\pi}{2M}\right) \\ &- (m_\pi^2 - 4M^2)(5 m_\pi^2 - 4M^2) \log\frac{m_\pi}{M} \Bigg],\end{aligned}$$

$$\left[(r_1^s)^2\right]^{(4)} = \frac{9 g_A^2 \kappa_s^0 m_\pi^2}{16\pi^2 F_\pi^2 M_0^4} \left[M_0^2 + (M_0^2 - m_\pi^2) \log\frac{m_\pi}{M_0} + \frac{m_\pi (m_\pi^2 - 3M_0^2)}{\sqrt{4M_0^2 - m_\pi^2}} \arccos\left(\frac{m_\pi}{2M_0}\right) \right].$$

Here, again, when the expression is truncated at $\mathcal{O}(p^3)$, M should be identified with M_0, while at $\mathcal{O}(p^4)$, it should be replaced by $M_N(m_\pi)$ in Eq. (D.21). Similarly, for $\kappa_s \cdot (r_2^s)^2$, we have

$$\kappa_s \cdot (r_2^s)^2 = \frac{M_N}{M_0} \left(B_{c2}^s + \left[\kappa_s \cdot (r_2^s)^2\right]^{(3)} + \left[\kappa_s \cdot (r_2^s)^2\right]^{(4)} \right), \tag{D.25}$$

with

$$B_{c2}^s = 48 M_0 e_{54},$$

$$\left[\kappa_s \cdot (r_2^s)^2\right]^{(3)} = \frac{3g_A^2 m_\pi^2 M_0}{16\pi^2 F_\pi^2 M^5 (4M^2 - m_\pi^2)} \left[\frac{m_\pi (6m_\pi^4 - 40M^2 m_\pi^2 + 60M^4)}{\sqrt{4M^2 - m_\pi^2}} \arccos\left(\frac{m_\pi}{2M}\right) \right.$$
$$\left. - 2\left(10M^4 - 3m_\pi^2 M^2 + (4M^2 - m_\pi^2)(2M^2 - 3m_\pi^2)\log\frac{m_\pi}{M}\right)\right],$$

$$\left[\kappa_s \cdot (r_2^s)^2\right]^{(4)} = \frac{3\kappa_s^0 g_A^2 m_\pi^2}{16\pi^2 F_\pi^2 M_0^4 (m_\pi^2 - 4M_0^2)} \left[- \frac{m_\pi (4m_\pi^4 - 27M_0^2 m_\pi^2 + 42M_0^4)}{\sqrt{4M_0^2 - m_\pi^2}} \arccos\left(\frac{m_\pi}{2M_0}\right) \right.$$
$$\left. + 14M_0^4 - 4m_\pi^2 M_0^2 + (m_\pi^2 - 4M_0^2)(4m_\pi^2 - 3M_0^2)\log\frac{m_\pi}{M_0}\right].$$

The BChPT expression for the isoscalar anomalous magnetic moment is written as

$$\kappa_s = \frac{M_N}{M_0}\left[\kappa_s^0 - 16M_0 m_\pi^2 \dot{e}_{105}^r(\lambda) + \delta\kappa_s^{(3)} + \delta\kappa_s^{(4)}\right], \tag{D.26}$$

where

$$\delta\kappa_s^{(3)} = -\frac{3g_A^2 m_\pi^2 M_0}{8\pi^2 F_\pi^2 M^3}\left[\frac{m_\pi(m_\pi^2 - 3M^2)}{\sqrt{4M^2 - m_\pi^2}}\arccos\left(\frac{m_\pi}{2M}\right) + M^2 + (M^2 - m_\pi^2)\log\frac{m_\pi}{M}\right],$$

$$\delta\kappa_s^{(4)} = \frac{3g_A^2 m_\pi^2}{32\pi^2 F_\pi^2 M_0^2}\left[4M_0^2 + \kappa_s^0(3m_\pi^2 - 4M_0^2)\log\frac{m_\pi}{M_0} - \kappa_s^0\frac{m_\pi(3m_\pi^2 - 8M_0^2)}{\sqrt{4M_0^2 - m_\pi^2}}\arccos\left(\frac{m_\pi}{2M_0}\right)\right].$$

Appendix E

Abbreviations

DWF	domain wall fermions
BMW	Budapest-Marseille-Wuppertal [collaboration]
(L)QCD	(lattice) quantum chromodynamics
CBChPT	covariant chiral perturbation theory
HBChPT	heavy-baryon chiral perturbation theory
SSE	small-scale expansion (HBChPT with Δ-resonance)
GPD	generalized parton distribution(s)
GFF	generalized form factor(s)

Bibliography

[A+88a] L. A. Ahrens et al. A study of the axial vector form-factor and second class currents in anti-neutrino quasielastic scattering. *Phys. Lett.*, B202:284–288, 1988.

[A+88b] J. Ashman et al. A measurement of the spin asymmetry and determination of the structure function g(1) in deep inelastic muon proton scattering. *Phys. Lett.*, B206:364, 1988.

[A+99] K. Ackerstaff et al. Flavor decomposition of the polarized quark distributions in the nucleon from inclusive and semi-inclusive deep- inelastic scattering. *Phys. Lett.*, B464:123–134, 1999.

[A+01] A. Airapetian et al. Measurement of the beam spin azimuthal asymmetry associated with deeply-virtual Compton scattering. *Phys. Rev. Lett.*, 87:182001, 2001.

[A+04a] J. Arrington et al. Two-photon exchange and elastic scattering of electrons / positrons on the proton. (Proposal for an experiment at VEPP-3). 2004.

[A+04b] C. Aubin et al. Light hadrons with improved staggered quarks: Approaching the continuum limit. *Phys. Rev.*, D70:094505, 2004.

[A+05] A. Aktas et al. Measurement of deeply virtual Compton scattering at HERA. *Eur. Phys. J.*, C44:1–11, 2005.

[A+07] P. Abbon et al. The COMPASS Experiment at CERN. *Nucl. Instrum. Meth.*, A577:455–518, 2007.

[A+08a] C. Allton et al. Physical Results from 2+1 Flavor Domain Wall QCD and SU(2) Chiral Perturbation Theory. *Phys. Rev.*, D78:114509, 2008.

[A+08b] C. Amsler et al. Review of particle physics. *Phys. Lett.*, B667:1, 2008.

[AK+04] A. Ali Khan et al. The nucleon mass in N(f) = 2 lattice QCD: Finite size effects from chiral perturbation theory. *Nucl. Phys.*, B689:175–194, 2004.

[AK+06] A. Ali Khan et al. Axial coupling constant of the nucleon for two flavours of dynamical quarks in finite and infinite volume. *Phys. Rev.*, D74:094508, 2006.

[AKNT06] C. Alexandrou, G. Koutsou, John W. Negele, and A. Tsapalis. The nucleon electromagnetic form factors from lattice QCD. *Phys. Rev.*, D74:034508, 2006.

[AMT07] J. Arrington, W. Melnitchouk, and J. A. Tjon. Global analysis of proton elastic form factor data with two-photon exchange corrections. *Phys. Rev.*, C76:035205, 2007.

[Are06] H. J. Arends. Overview of the physics at MAMI (Mainz). *AIP Conf. Proc.*, 870:481–485, 2006.

[B+73] Elliott D. Bloom et al. Measurements of inelastic electron scattering cross-sections near one pion threshold. *Phys. Rev. Lett.*, 30:1186, 1973.

[B+91] V. G. Bornyakov et al. The Density of monopoles in SU(2) lattice gauge theory. *Phys. Lett.*, B261:116–122, 1991.

[B+98] Claude W. Bernard et al. Quenched hadron spectroscopy with improved staggered quark action. *Phys. Rev.*, D58:014503, 1998.

[B+01] Claude W. Bernard et al. The QCD spectrum with three quark flavors. *Phys. Rev.*, D64:054506, 2001.

[B+02] T. Blum et al. Non-perturbative renormalisation of domain wall fermions: Quark bilinears. *Phys. Rev.*, D66:014504, 2002.

[B+04] T. Blum et al. Quenched lattice QCD with domain wall fermions and the chiral limit. *Phys. Rev.*, D69:074502, 2004.

[B+08a] P. A. Boyle et al. Parton Distribution Amplitudes and Non-Perturbative Renormalisation. *PoS*, LATTICE2008:165, 2008.

[B+08b] J. D. Bratt et al. Aspects of Precision Calculations of Nucleon Generalized Form Factors with Domain Wall Fermions on an Asqtad Sea. *PoS*, LATTICE2008:141, 2008.

[B+09] A. Bazavov et al. Full nonperturbative QCD simulations with 2+1 flavors of improved staggered quarks. 2009.

[B+10] Jonathan D. Bratt et al. Nucleon structure from mixed action calculations using 2+1 flavors of asqtad sea and domain wall valence fermions. 2010.

[BBCR95] Giuseppe Beccarini, Massimo Bianchi, Stafano Capitani, and Giancarlo Rossi. Deep inelastic scattering in improved lattice QCD. 2. The second moment of structure functions. *Nucl. Phys.*, B456:271 295, 1995.

[BCS09a] Gunnar Bali, Sara Collins, and Andreas Schafer. Strangeness and charm content of the nucleon. 2009.

[BCS09b] Gunnar S. Bali, Sara Collins, and Andreas Schafer. Effective noise reduction techniques for disconnected loops in Lattice QCD. 2009.

[BCT98] J. Bijnens, G. Colangelo, and P. Talavera. The vector and scalar form factors of the pion to two loops. *JHEP*, 05:014, 1998.

[BDHS] Claude W. Bernard, Terrence Draper, G. Hockney, and A. Soni. Calculation of weak matrix elements: some technical aspects. In *Wuppertal 1985, Proceedings, Lattice Gauge Theory*, 199-207.

[BEM02] Veronique Bernard, Latifa Elouadrhiri, and Ulf. G. Meissner. Axial structure of the nucleon. *J. Phys.*, G28:R1 R35, 2002.

[Ber08] J. C. Bernauer. Nucleon form factor measurements in Mainz: Past and future. *Lect. Notes Phys.*, 745:79–91, 2008.

[Bet09] Siegfried Bethke. The 2009 World Average of $\alpha_s(M_Z)$. *Eur. Phys. J.*, C64:689–703, 2009.

[BF75] Stanley J. Brodsky and Glennys R. Farrar. Scaling laws for large-momentum-transfer processes. *Phys. Rev. D*, 11(5):1309–1330, Mar 1975.

[BF89] Douglas S. Beder and Harold W. Fearing. Further comments on radiative muon capture in hydrogen and nucleon excitation. *Phys. Rev.*, D39:3493–3496, 1989.

[BFHM98] Veronique Bernard, Harold W. Fearing, Thomas R. Hemmert, and Ulf G. Meißner. The form factors of the nucleon at small momentum transfer. *Nucl. Phys.*, A635:121–145, 1998.

[BHM05] Veronique Bernard, Thomas R. Hemmert, and Ulf-G. Meißner. Chiral extrapolations and the covariant small scale expansion. *Phys. Lett.*, B622:141–150, 2005.

[BHM07] M. A. Belushkin, H. W. Hammer, and Ulf-G. Meißner. Dispersion analysis of the nucleon form factors including meson continua. *Phys. Rev.*, C75:035202, 2007.

[BHMS01] Stanley J. Brodsky, Dae Sung Hwang, Bo-Qiang Ma, and Ivan Schmidt. Light-cone representation of the spin and orbital angular momentum of relativistic composite systems. *Nucl. Phys.*, B593:311 335, 2001.

[Bis05] Bojan Bistrovič. *Perturbative renormalization of proton observables in lattice QCD using domain wall fermions.* PhD thesis, MIT, 2005.

[BJ97] Ian Balitsky and Xiang-Dong Ji. How much of the nucleon spin is carried by glue? *Phys. Rev. Lett.*, 79:1225 1228, 1997.

[BJY03] Andrei V. Belitsky, Xiang-dong Ji, and Feng Yuan. A perturbative QCD analysis of the nucleon's Pauli form factor F2(Q**2). *Phys. Rev. Lett.*, 91:092003, 2003.

[BKKM92] Veronique Bernard, Norbert Kaiser, Joachim Kambor, and Ulf G. Meissner. Chiral structure of the nucleon. *Nucl. Phys.*, B388:315–345, 1992.

[BKM94] V. Bernard, Norbert Kaiser, and Ulf G. Meissner. QCD accurately predicts the induced pseudoscalar coupling constant. *Phys. Rev.*, D50:6899–6901, 1994.

[BKM97] V. Bernard, Norbert Kaiser, and Ulf-G. Meißner. Determination of the low-energy constants of the next-to- leading order chiral pion nucleon Lagrangian. *Nucl. Phys.*, A615:483–500, 1997.

[BL99] Thomas Becher and H. Leutwyler. Baryon chiral perturbation theory in manifestly Lorentz invariant form. *Eur. Phys. J.*, C9:643–671, 1999.

[Bra09] J. D. Bratt. PhD thesis, MIT, 2009.

[Bur00] Matthias Burkardt. Impact parameter dependent parton distributions and off-forward parton distributions for zeta –¿ 0. *Phys. Rev.*, D62:071503(R), 2000.

[Bur03] Matthias Burkardt. Impact parameter space interpretation for generalized parton distributions. *Int. J. Mod. Phys.*, A18:173–208, 2003.

[C+93] Seonho Choi et al. Axial and pseudoscalar nucleon form-factors from low- energy pion electroproduction. *Phys. Rev. Lett.*, 71:3927 3930, 1993.

[C+03] S. Chekanov et al. Measurement of deeply virtual Compton scattering at HERA. *Phys. Lett.*, B573:46–62, 2003.

[CD04] Gilberto Colangelo and Stephan Dürr. The pion mass in finite volume. *Eur. Phys. J.*, C33:543–553, 2004.

[CKS97] K. G. Chetyrkin, Bernd A. Kniehl, and M. Steinhauser. Strong coupling constant with flavour thresholds at four loops in the MS-bar scheme. *Phys. Rev. Lett.*, 79:2184 2187, 1997.

[col] BMW collaboration. in preparation.

[CR00] K. G. Chetyrkin and A. Retey. Renormalization and running of quark mass and field in the regularization invariant and MS-bar schemes at three and four loops. *Nucl. Phys.*, B583:3 34, 2000.

[D+02] D. Dolgov et al. Moments of nucleon light cone quark distributions calculated in full lattice QCD. *Phys. Rev.*, D66:034506, 2002.

[D+08] S. Durr et al. Ab-Initio Determination of Light Hadron Masses. *Science*, 322:1224 1227, 2008.

[D+09] Takumi Doi et al. Nucleon strangeness form factors from $N_f = 2 + 1$ clover fermion lattice QCD. *Phys. Rev.*, D80:094503, 2009.

[DDG] Durham University (UK) Durham Database Group.

[dF+00] P. de Forcrand et al. Renormalization group flow of SU(3) lattice gauge theory: Numerical studies in a two coupling space. *Nucl. Phys.*, B577:263 278, 2000.

[DFJK05] M. Diehl, Th. Feldmann, R. Jakob, and P. Kroll. Generalized parton distributions from nucleon form factor data. *Eur. Phys. J.*, C39:1 39, 2005.

[DGH08] Marina Dorati, Tobias A. Gail, and Thomas R. Hemmert. Chiral Perturbation Theory and the first moments of the Generalized Parton Distributions in a Nucleon. *Nucl. Phys.*, A798:96 131, 2008.

[Die03] M. Diehl. Generalized parton distributions. *Phys. Rept.*, 388:41 277, 2003.

[DMS07] M. Diehl, A. Manashov, and A. Schafer. Generalized parton distributions for the nucleon in chiral perturbation theory. *Eur. Phys. J.*, A31:335 355, 2007.

[DMW91] R. M. Davidson, N. C. Mukhopadhyay, and R. S. Wittman. Effective Lagrangian approach to the theory of pion photoproduction in the Delta (1232) region. *Phys. Rev.*, D43:71 94, 1991.

[Dol00] D. Dolgov. *Calculation of the Structure of the Proton using Lattice QCD.* PhD thesis, MIT, 2000.

[E+06a] R. G. Edwards et al. Nucleon structure in the chiral regime with domain wall fermions on an improved staggered sea. *PoS*, LAT2006:121, 2006.

[E+06b] R. G. Edwards et al. The nucleon axial charge in full lattice QCD. *Phys. Rev. Lett.*, 96:052001, 2006.

[EHK98] R. G. Edwards, Urs M. Heller, and T. R. Klassen. The effectiveness of non-perturbative O(a) improvement in lattice QCD. *Phys. Rev. Lett.*, 80:3448–3451, 1998.

[EM02] D. R. Entem and R. Machleidt. Chiral 2pi exchange at order four and peripheral N N scattering. *Phys. Rev.*, C66:014002, 2002.

[FJ01] B. W. Filippone and Xiang-Dong Ji. The spin structure of the nucleon. *Adv. Nucl. Phys.*, 26:1, 2001.

[FMS98] Nadia Fettes, Ulf-G. Meißner, and Sven Steininger. Pion nucleon scattering in chiral perturbation theory. I: Isospin-symmetric case. *Nucl. Phys.*, A640:199–234, 1998.

[FPPT85] M. Falcioni, M. L. Paciello, G. Parisi, and B. Taglienti. Again on SU(3) glueball mass. *Nucl. Phys.*, B251:624–632, 1985.

[FW03] J. Friedrich and T. Walcher. A coherent interpretation of the form factors of the nucleon in terms of a pion cloud and constituent quarks. *Eur. Phys. J.*, A17:607–623, 2003.

[G+89] S. Güsken et al. Nonsinglet axial vector couplings of the baryon octet in lattice qcd. *Phys. Lett.*, B227:266, 1989.

[Gü90] S. Güsken. A Study of smearing techniques for hadron correlation functions. *Nucl. Phys. Proc. Suppl.*, 17:361–364, 1990.

[G+96a] M. Gockeler et al. Lattice Operators for Moments of the Structure Functions and their Transformation under the Hypercubic Group. *Phys. Rev.*, D54:5705–5714, 1996.

[G+96b] M. Gockeler et al. Perturbative Renormalization of Lattice Bilinear Quark Operators. *Nucl. Phys.*, B472:309–333, 1996.

[G+01] O. Gayou et al. Measurements of the elastic electromagnetic form factor ratio mu pGEp/GMp via polarization transfer. *Phys. Rev.*, C64:038202, 2001.

[G+02] O. Gayou et al. Measurement of G(E(p))/G(M(p)) in e(pol.) p$\rightarrow$ e p(pol.) to $Q^2 = 5.6$ GeV^2. *Phys. Rev. Lett.*, 88:092301, 2002.

[G+05a] M. Gockeler et al. Investigation of the second moment of the nucleon's g1 and g2 structure functions in two-flavor lattice QCD. *Phys. Rev.*, D72:054507, 2005.

[G+05b] M. Göckeler et al. Nucleon electromagnetic form factors on the lattice and in chiral effective field theory. *Phys. Rev.*, D71:034508, 2005.

[G+10] M. Gockeler et al. Perturbative and Nonperturbative Renormalization in Lattice QCD. 2010.

[Gai07] T. Gail. *Chiral Analysis and Baryon Form Factors.* PhD thesis, Technical University Munich, 2007.

[GH] T. A. Gail and T. R. Hemmert. Quark-mass dependence of the form factors of the nucleon near the photon point. forthcoming.

[Gia10] Paola Gianotti. The PANDA experiment at FAIR. *Nucl. Phys.*, A835:96–101, 2010.

[GPGASvB94] Margarita Garcia Perez, Antonio Gonzalez-Arroyo, Jeroen R. Snippe, and Pierre van Baal. Instantons from over - improved cooling. *Nucl. Phys.*, B413:535–552, 1994.

[GPV01] K. Goeke, Maxim V. Polyakov, and M. Vanderhaeghen. Hard Exclusive Reactions and the Structure of Hadrons. *Prog. Part. Nucl. Phys.*, 47:401–515, 2001.

[Gra92] J. M. Grandy. *Investigation of hadronic structure by solving QCD on a lattice.* PhD thesis, MIT, 1992.

[Gra03a] J. A. Gracey. Three loop anomalous dimension of non-singlet quark currents in the RI' scheme. *Nucl. Phys.*, B662:247–278, 2003.

[Gra03b] J. A. Gracey. Three loop anomalous dimension of the second moment of the transversity operator in the MS-bar and RI' schemes. *Nucl. Phys.*, B667:242–260, 2003.

[Gra06] J. A. Gracey. Three loop anomalous dimensions of higher moments of the non-singlet twist-2 Wilson and transversity operators in the MSbar and RI' schemes. *JHEP*, 10:040, 2006.

[GSS88] J. Gasser, M. E. Sainio, and A. Svarc. Nucleons with Chiral Loops. *Nucl. Phys.*, B307:779, 1988.

[GT58a] M. L. Goldberger and S. B. Treiman. Decay of the pi meson. *Phys. Rev.*, 110:1178–1184, 1958.

[GT58b] M. L. Goldberger and S. B. Treiman. Form-factors in Beta decay and muon capture. *Phys. Rev.*, 111:354–361, 1958.

[Gup97] Rajan Gupta. Introduction to lattice QCD. 1997.

[GV98] Pierre A. M. Guichon and M. Vanderhaeghen. Virtual Compton scattering off the nucleon. *Prog. Part. Nucl. Phys.*, 41:125–190, 1998.

[H+76] G. Höhler et al. Analysis of Electromagnetic Nucleon Form-Factors. *Nucl. Phys.*, B114:505, 1976.

[H+03] Philipp Hagler et al. Moments of nucleon generalized parton distributions in lattice QCD. *Phys. Rev.*, D68:034505, 2003.

[H+08] Ph. Hägler et al. Nucleon Generalized Parton Distributions from Full Lattice QCD. *Phys. Rev.*, D77:094502, 2008.

[HHK97] Thomas R. Hemmert, Barry R. Holstein, and Joachim Kambor. Systematic 1/M expansion for spin 3/2 particles in baryon chiral perturbation theory. *Phys. Lett.*, B395:89 95, 1997.

[HHK98] Thomas R. Hemmert, Barry R. Holstein, and Joachim Kambor. Chiral Lagrangians and Delta(1232) interactions: Formalism. *J. Phys.*, G24:1831–1859, 1998.

[HN94] P. Hasenfratz and F. Niedermayer. Perfect lattice action for asymptotically free theories. *Nucl. Phys.*, B414:785–814, 1994.

[HPW03] Thomas R. Hemmert, Massimiliano Procura, and Wolfram Weise. Quark mass dependence of the nucleon axial-vector coupling constant. *Phys. Rev.*, D68:075009, 2003.

[HW02] Thomas R. Hemmert and Wolfram Weise. Chiral magnetism of the nucleon. *Eur. Phys. J.*, A15:487–504, 2002.

[ILS+86] Ernst-Michael Ilgenfritz, M. L. Laursen, G. Schierholz, M. Muller-Preussker, and H. Schiller. First Evidence for the Existence of Instantons in the Quantized SU(2) Lattice Vacuum. *Nucl. Phys.*, B268:693, 1986.

[Iwa85] Y. Iwasaki. Renormalization Group Analysis of Lattice Theories and Improved Lattice Action: Two-Dimensional Nonlinear O(N) Sigma Model. *Nucl. Phys.*, B258:141 156, 1985.

[J+96] G. Jonkmans et al. Radiative muon capture on hydrogen and the induced pseudoscalar coupling. *Phys. Rev. Lett.*, 77:4512–4515, 1996.

[Ji97] Xiang-Dong Ji. Gauge invariant decomposition of nucleon spin. *Phys. Rev. Lett.*, 78:610–613, 1997.

[Ji98] Xiang-Dong Ji. Off-forward parton distributions. *J. Phys.*, G24:1181–1205, 1998.

[K+90] T. Kitagaki et al. Study of neutrino d → mu- p p(s) and neutrino d → mu- Delta++ (1232) n(s) using the BNL 7-foot deuterium filled bubble chamber. *Phys. Rev.*, D42:1331–1338, 1990.

[Kap92] David B. Kaplan. A Method for simulating chiral fermions on the lattice. *Phys. Lett.*, B288:342–347, 1992.

[Kel04] J. J. Kelly. Simple parametrization of nucleon form factors. *Phys. Rev.*, C70:068202, 2004.

[KLN+69] R. L. Kustom, D. E. Lundquist, T. B. Novey, A. Yokosawa, and F. Chilton. Quasielastic neutrino scattering. *Phys. Rev. Lett.*, 22:1014 1017, 1969.

[KN02] V. A. Korotkov and W. D. Nowak. Future measurements of deeply virtual Compton scattering at HERMES. *Eur. Phys. J.*, C23:455 461, 2002.

[LBO+08] Huey-Wen Lin, Tom Blum, Shigemi Ohta, Shoichi Sasaki, and Takeshi Yamazaki. Nucleon structure with two flavors of dynamical domain-wall fermions. *Phys. Rev.*, D78:014505, 2008.

[LCE+10] Huey-Wen Lin, Saul D. Cohen, Robert G. Edwards, Kostas Orginos, and David G. Richards. Lattice Calculations of Nucleon Electromagnetic Form Factors at Large Momentum Transfer. 2010.

[Lep] G. Peter Lepage. The analysis of algorithms for lattice field theory. Invited lectures given at TASI'89 Summer School, Boulder, CO, Jun 4-30, 1989.

[LHP] LHP collaboration. in preparation.

[LM93] G. Peter Lepage and Paul B. Mackenzie. On the viability of lattice perturbation theory. *Phys. Rev.*, D48:2250 2264, 1993.

[Lus77] M. Luscher. Construction of a Selfadjoint, Strictly Positive Transfer Matrix for Euclidean Lattice Gauge Theories. *Commun. Math. Phys.*, 54:283, 1977.

[LW90] Martin Luscher and Ulli Wolff. How to calculate the elastic scattering matrix in two-dimensional quantum field theories by numerical simulation. *Nucl. Phys.*, B339:222 252, 1990.

[M+98] B. D. Milbrath et al. A comparison of polarization observables in electron scattering from the proton and deuteron. *Phys. Rev. Lett.*, 80:452 455, 1998.

[MM] I. Montvay and G. Munster. Quantum fields on a lattice. Cambridge, UK: Univ. Pr. (1994) 491 p. (Cambridge monographs on mathematical physics).

[MMD96] P. Mergell, Ulf G. Meißner, and D. Drechsel. Dispersion-Theoretical Analysis of the Nucleon Electromagnetic Formfactors. *Nucl. Phys.*, A596:367 396, 1996.

[MPS+95] G. Martinelli, C. Pittori, Christopher T. Sachrajda, M. Testa, and A. Vladikas. A General method for nonperturbative renormalization of lattice operators. *Nucl. Phys.*, B445:81–108, 1995.

[NN81] Holger Bech Nielsen and M. Ninomiya. No Go Theorem for Regularizing Chiral Fermions. *Phys. Lett.*, B105:219, 1981.

[NN93] Rajamani Narayanan and Herbert Neuberger. Chiral fermions on the lattice. *Phys. Rev. Lett.*, 71:3251–3254, 1993.

[OLY09] OLYMPUS Collaboration. An Experiment to Definitively Determine the Contribution of Multiple Photon Exchange in Elastic Lepton-Nucleon Scattering. *http://web.mit.edu/olympus/*, 2009.

[OT99] Kostas Orginos and Doug Toussaint. Testing improved actions for dynamical Kogut-Susskind quarks. *Phys. Rev.*, D59:014501, 1999.

[OTS99] Kostas Orginos, Doug Toussaint, and R. L. Sugar. Variants of fattening and flavor symmetry restoration. *Phys. Rev.*, D60:054503, 1999.

[OY08] Shigemi Ohta and Takeshi Yamazaki. Nucleon structure with dynamical (2+1)-flavor domain wall fermions lattice QCD. 2008.

[P+01] T. Pospischil et al. Measurement of G(E(p))/G(M(p)) via polarization transfer at $Q^2 = 0.4$ GeV/c^2. *Eur. Phys. J.*, A12:125–127, 2001.

[P+05] V. Punjabi et al. Proton elastic form factor ratios to $Q^2 = 3.5$ GeV^2 by polarization transfer. *Phys. Rev.*, C71:055202, 2005.

[P+10] Randolf Pohl et al. The size of the proton. *Nature*, 466(7303):213–216, 2010.

[PMHW07] M. Procura, B. U. Musch, T. R. Hemmert, and W. Weise. Chiral extrapolation of g_A with explicit $\Delta(1232)$ degrees of freedom. *Phys. Rev.*, D75:014503, 2007.

[PMW+06] M. Procura, B. U. Musch, T. Wollenweber, T. R. Hemmert, and W. Weise. Nucleon mass: From lattice QCD to the chiral limit. *Phys. Rev.*, D73:114510, 2006.

[PS] A.V. Pochinsky and S. N. Syritsyn. In private communications.

[RBC07] RBC and LHP collaborations. Simulations with dynamical domain wall fermions. USQCD resource allocation proposal, 2007.

[Ren04] D. B. Renner. *Exploring Proton Structure using Lattice QCD.* PhD thesis, MIT, 2004.

[Rot05] H. J. Rothe. Lattice gauge theories: An Introduction. *World Sci. Lect. Notes Phys.*, 74:1–605, 2005.

[S+01] S. Stepanyan et al. First observation of exclusive deeply virtual Compton scattering in polarized electron beam asymmetry measurements. *Phys. Rev. Lett.*, 87:182002, 2001.

[S+09] C. Sturm et al. Renormalization of quark bilinear operators in a momentum- subtraction scheme with a nonexceptional subtraction point. *Phys. Rev.*, D80:014501, 2009.

[S+10] S. N. Syritsyn et al. Nucleon Electromagnetic Form Factors from Lattice QCD using 2+1 Flavor Domain Wall Fermions on Fine Lattices and Chiral Perturbation Theory. *Phys. Rev. D*, 81(3):034507, Feb 2010.

[Sha93] Yigal Shamir. Chiral fermions from lattice boundaries. *Nucl. Phys.*, B406:90–106, 1993.

[Sha07] Stephen R. Sharpe. Future of Chiral Extrapolations with Domain Wall Fermions. 2007.

[SN07] Sergey Syritsyn and John W. Negele. Oscillatory terms in the domain wall transfer matrix. *PoS*, LAT2007:078, 2007.

[Ste33] O. Stern. *Nature*, 132:169, 1933.

[SW85] B. Sheikholeslami and R. Wohlert. Improved Continuum Limit Lattice Action for QCD with Wilson Fermions. *Nucl. Phys.*, B259:572, 1985.

[Tho08] Anthony W. Thomas. Interplay of Spin and Orbital Angular Momentum in the Proton. *Phys. Rev. Lett.*, 101:102003, 2008.

[Vog04] Werner Vogelsang. QCD spin physics: Status, and prospects for RHIC. *Pramana*, 63:1251, 2004.

[W+98] D. H. Wright et al. Measurement of the induced pseudoscalar coupling using radiative muon capture on hydrogen. *Phys. Rev.*, C57:373–390, 1998.

[Wil74] Kenneth G. Wilson. Confinement of quarks. *Phys. Rev.*, D10:2445–2459, 1974.

[WL+09] A. Walker-Loud et al. Light hadron spectroscopy using domain wall valence quarks on an Asqtad sea. *Phys. Rev.*, D79:054502, 2009.

[Y+09] Takeshi Yamazaki et al. Nucleon form factors with 2+1 flavor dynamical domain-wall fermions. *Phys. Rev.*, D79:114505, 2009.

[Zic77] A. Zichichi, editor. *New Phenomena in Subnuclear Physics.* Plenum Press, 1977.